Structural and functional characterization of nanoporous thin films through advanced scanning-transmission electron microscopies and optical spectroscopies

(Caracterización estructural y funcional de películas delgadas nanoporosas mediante microscopías electrónicas de transmisión-barrido y espectroscopías ópticas)

Antonio Jesús Santos Izquierdo-Bueno

A Thesis submitted for the degree of Doctor from the University of Cádiz

Structural and functional characterization of nanoporous thin films through advanced scanning-transmission electron microscopies and optical spectroscopies

(Caracterización estructural y funcional de películas delgadas nanoporosas mediante microscopías electrónicas de transmisión-barrido y espectroscopías ópticas)

Antonio Jesús Santos Izquierdo-Bueno

Supervisors:

Prof. Dr. Francisco M. Morales Sánchez

Catedrático de Universidad

Departamento de Ciencia de los Materiales e Ingeniería Metalúrgica y Química Inorgánica

Dr. Bertrand Lacroix

Investigador Contratado

Departamento de Ciencia de los Materiales e Ingeniería Metalúrgica y Química Inorgánica

Thesis Committee

President:	**Prof. Dr. Daniel Araujo Gay** Full Professor University of Cádiz, Spain
Secretary:	**Dr. Ramón Escobar Galindo** Associate Professor University of Seville, Spain
Vocal:	**Prof. Dr. Somnath Bhattacharyya** Full Professor Indian Institute of Technology Madras, India

El Prof. Dr. Francisco Miguel Morales Sánchez, Catedrático de Universidad del Área de Conocimiento de Ciencia de los Materiales e Ingeniería Metalúrgica, y el Dr. Bertrand Lacroix, Investigador Contratado del mismo Área de Conocimiento, en calidad de Directores, AUTORIZAN la presentación a trámite de la Tesis Doctoral de Antonio Jesús Santos Izquierdo-Bueno titulada *Structural and functional characterization of nanoporous thin films through advanced scanning-transmission electron microscopies and optical spectroscopies (Caracterización estructural y funcional de películas delgadas nanoporosas mediante microscopías electrónicas de transmisión-barrido y espectroscopías ópticas).*

Puerto Real, 8 de julio de 2021

Vº. Bº.

Prof. Dr. Francisco Miguel Morales Sánchez

Dr. Bertrand Lacroix

Con todo mi amor, a mis dos Rosarios.

Sin vuestra fuerza y apoyo constante todo esto no hubiese sido posible.

Acknowledgments

¡Cómo pasa el tiempo! Parece que fue ayer cuando en marzo de 2017 el Prof. Dr. Francisco Miguel Morales Sánchez y el Prof. Dr. Rafael García Roja me animaban a que me moviese del sofá de mi casa para que incorporase a su Grupo de Investigación con el propósito de realizar una Tesis Doctoral. ¡Y finalmente me levanté del sofá, ya que de lo contrario hoy no estaría escribiendo estas líneas! No encuentro palabras para agradeceros todo lo que habéis hecho por mí. Gracias por abrirme los ojos y hacerme ver lo que yo era incapaz de ver. Gracias por abrirme la mente, por vuestros consejos y por devolverme la ilusión y la esperanza que, por aquel entonces, empezaba a perder.

Una vez subido a este barco, muchas han sido las personas que me han ayudado y que han hecho posible la realización de este trabajo. En este sentido, quiero agradecer, en primer lugar, la labor de mis directores de Tesis, el Prof. Dr. Francisco Miguel Morales Sánchez y el Dr. Bertrand Lacroix, así como la del responsable del grupo TEP-120, el Prof. Dr. Rafael García Roja. Gracias por vuestra formación, apoyo, confianza y dedicación. También me gustaría mencionar a los compañeros que he tenido en el departamento durante esta etapa, especialmente al Dr. Juan Jesús Jiménez Ríos. Desde que llegué, siempre me has ofrecido tu ayuda de una forma desinteresada. Tampoco me olvido de los buenos ratos vividos. Además de ser un gran investigador, eres buen compañero y amigo, noble y honesto como el que más. Igualmente, también me quiero acordar de José Manuel, Marta y Manu. Muchas gracias por la ayuda, consejos y momentos vividos. También quiero extender este agradecimiento a los Profesores Doctores Eduardo Blanco y Manolo Domínguez, del Departamento de Física de la Materia Condensada de la Universidad de Cádiz, por su formación y colaboración en la realización de estudios mediante técnicas de elipsometría y AFM, las cuales has sido de vital importancia para el desarrollo de la presente Tesis Doctoral.

I would like to thank the researchers from the Department Physics and Properties of Nanostructures – PPNa at the Pprime Intitute of the University of Poitiers, specially to Dr. Fabien Paumier and Dr. Simon Hurand, for the excellent reception received during my research stays and the productive discussions, as well as for the samples and complementary results which have been vital for the development of this Thesis.

Likewise, I would also like to express my gratitude to Dr. Víctor José Gómez from the Polytechnic University of Valencia (at that time linked to the Univeristy of Cardiff), and Prof. Dr. Nicolas Martin from the FEMTO-ST Institute of Besançon for the fruitful collaborations maintained during my predoctoral period. It has been an absolute pleasure and an honour to collaborate with you and I hope we can continue consolidating these relations in the near future.

También me gustaría agradecer el apoyo recibido por parte de las siguientes instituciones, las cuales han permitido la realización de este trabajo:

- El Ministerio de Universidades por la concesión de la beca-contrato de Formación de Profesorado Universitario (FPU) que me ha permitido realizar esta Tesis Doctoral, ref. FPU16/04386.
- La Universidad de Cádiz, especialmente el Instituto Universitario de Investigación en Microscopía Electrónica y Materiales (IMEYMAT) y la División de Microscopía Electrónica de los Servicios Centrales de Ciencia y Tecnología de la Universidad de Cádiz, por el uso de sus instalaciones e instrumentación.
- El Instituto Pprime de Poitiers (Francia), la empresa Safran Electronics and Defense, la Universidad de Cardiff (Reino Unido), y el Instituto FEMTO-ST de Besançon (Francia) por el suministro de los materiales investigados.

Y, por último, me gustaría cerrar esta sección agradeciendo el apoyo recibido por parte de mi familia. Sin vuestro apoyo esto no hubiese sido posible. Doy las gracias a mis padres y suegros, en especial a ti mamá, si hoy soy lo que soy lo aprendí de ti. Gracias por la educación y valores que me has dado. Rosario, amiga, compañera y confidente, gracias por dar sentido a mi vida, por tu comprensión, por ser la luz que me da fuerzas en mis días más difíciles, por tu cariño, por estar siempre ahí tanto para lo bueno como para lo malo. Gracias a todas aquellas personas que siempre apostaron por mí, y muy especialmente a mi tía Mari Carmen, gracias por todo lo que hiciste en vida y por lo que continúas haciendo desde donde quiera que estés.

The present PhD Thesis entitled *Structural and functional characterization of nanoporous thin films through advanced scanning-transmission electron microscopies and optical spectroscopies (Caracterización estructural y funcional de películas delgadas nanoporosas mediante microscopías electrónicas de transmisión-barrido y espectroscopías ópticas)* fulfills all the requirements to obtain the PhD title under the modality of *Thesis by Compendium of Publications* regulated by the regulations of UCA/CG06/2012, June 27, 2012.

The compendium of publications of this Thesis is constituted by the following articles:

I. A. J. Santos, B. Lacroix, F. Maudet, A. Corvisier, F. Paumier, C. Dupeyrat, T. Girardeau, R. García, F. M. Morales. *Surface oxidation of amorphous Si and Ge slanted columnar and mesoporous thin films: Evidence, scrutiny and limitations for infrared optics*, Applied Surface Science 493 (2019) 807–817.

II. F. Maudet, B. Lacroix, A. J. Santos, F. Paumier, M. Paraillous, C. Dupeyrat, R. García, F. M. Morales, T. Girardeau. *Towards perfect MWIR transparency using oblique angle deposition*, Applied Surface Science 470 (2019) 943–950.

III. F. Maudet, B. Lacroix, A. J. Santos, F. Paumier, M. Paraillous, S. Hurand, A. Corvisier, C. Dupeyrat, R. García, F. M. Morarles, T. Girardeau. *On the importance of light scattering for high performances nanostructured antireflective surfaces*, Acta Materialia 188 (2020) 386–393.

IV. F. Maudet, B. Lacroix, A. J. Santos, F. Paumier, M. Paraillous, S. Hurand, A. Corvisier, C. Marsal, B. Giroire, C. Dupeyrat, R. García, F. M. Morales, T. Girardeau. *Optical and nanostructural insights of oblique angle deposited layers applied for photonic coatings*, Applied Surface Science 520 (2020) 146312.

V. B. Lacroix, A. J. Santos, S. Hurand, A. Corvisier, F. Paumier, T. Girardeau, F. Maudet, C. Dupeyrat, R. García, F. M. Morales. *Nanostructure and physical properties control of indium tin oxide films prepared at room temperature through ion beam sputtering deposition at oblique angles*, The Journal of Physical Chemistry C 123 (2019) 14036−14046.

VI. V. J. Gómez, A. J. Santos, E. Blanco, B. Lacroix, R. García, D. L. Huffaker, F. M. Morales. *Porosity control for plasma-assisted molecular beam epitaxy of GaN nanowires*, Crystal Growth and Design 19 (2019) 2461–2469.

VII. A. J. Santos, B. Lacroix, E. Blanco, S. Hurand, V. J. Gómez, F. Paumier, T. Girardeau, D. L. Huffaker, R. García, F. M. Morales. *Simultaneous optical and electrical characterization of GaN nanowire arrays by means of vis-IR spectroscopic ellipsometry*, The Journal of Physical Chemistry C 124 (2020) 1535−1543.

There are two additional manuscripts, both under review, which complement this Thesis:

- A. J. Santos, B. Lacroix, F. Maudet, F. Paumier, S. Hurand, C. Dupeyrat, V. J. Gómez, D. L. Huffaker, T. Girardeau, R.García, F. M. Morales. *Exploring the possibilities and alternatives offered by the application of (S)TEM methods for the study of porous nanostructured coatings* (under review in Microscopy and Microanalysis). We will refer to this document along the Thesis as *Manuscript VIII*.
- A. J. Santos, B. Lacroix, M. Domínguez, R. García, N. Martin, F. M. Morales. Controlled grain-size thermochromic VO_2 coatings by the fast oxidation of sputtered vanadium or vanadium oxide films deposited at glancing angles (under

review in Applied Surface Science). We will refer to this document along the Thesis as *Manuscript IX*.

The format used in the present Thesis is in agreement with the indications published in the item 6 of the article 23 of the regulations of UCA/CG06/2012, where the following chapters are required: a) Abstract, b) Introduction and justification of the Thesis thematic unit, c) Hypotheses and objectives, d) Critical analysis of the state of the art, e) Joint discussion of the results obtained in the different articles, d) Conclusions, indicating from which article they have been obtained and g) Prospects, references and appendices with the accepted articles or their justification of publication.

List of acronyms

Acronym	Description
1D	One Dimensional
ABEMA	Anisotropic Bruggeman Effective Medium Approximation
AFM	Atomic Force Microscopy
AR	Antireflective
ARC	Antireflective Coating
BEMA	Bruggeman Effective Medium Approximation
BF	Bright Field
CNW	c-shaped Nanowire
CTEM	Conventional Transmission Electron Microscopy
CVD	Chemical Vapour Deposition
DBR	Distributed Bragg Reflector
DC	Direct Current
DO	Drude Oscillator
EDX or EDS	Energy Dispersive X-ray Spectroscopy
EELS	Electron Energy Loss Spectroscopy
ET	Electron Tomography
FDTD	Finite-Difference Time Domain
FIB	Focused Ion-Beam
GLAD	Glancing Angle Deposition
GO	Gaussian Oscillator
HAADF	High-Angle Annular Dark Field
HNW	Hollow Nanowire
HRTEM	High-Resolution Transmission Electron Microscopy
IBS	Ion Beam Sputtering
ICP	Inductively Coupled Plasma
iDPC	Integrated Differential Phase Contrast
IR	Infrared
ITO	Indium Tin-doped Oxide
KPFM	Kelvin Probe Force Microscopy
LCD	Liquid-Crystal Display
LD	Laser Diode
LED	Light Emitting Diodes
LWIR	Long Wavelength Infrared
MBE	Molecular Beam Epitaxy
MIT	Metal-to-Insulator Transition
MWIR	Mid-Wavelength Infrared
NIR	Near-Infrared
NPF	Nanoporous Film
NR	Nanorod
NT	Nanotube
NW	Nanowire
OAD	Oblique Angle Deposition
OPS	Optical Spectroscopy
PAMBE	Plasma-Assisted Molecular Beam Epitaxy
PVD	Physical Vapour Deposition
RGPP	Reactive Gas Pulsing Process

RS	Raman Spectroscopy
SAED	Selected Area Electron Diffraction
SE	Spectroscopic Ellipsometry
SEM	Scanning Electron Microscopy
SI	Spectrum Image
SNW	Solid Nanowire
STEM	Scanning-Transmission Electron Microscopy
TCO	Transparent Conductive Oxide
TEM	Transmission Electron Microscopy
TLO	Tauc-Lorentz Oscillator
XPS	X-ray Photoelectron Spectroscopy
XRD	X-Ray Diffraction

Abstract

Nano-structuration of materials at the mesoscale to give rise to porosity-controlled coatings represents an important breakthrough in the area of Materials Science and Engineering, offering new and enhanced functionalities of interest in fields such as optics, optronics and optoelectronics. In order to optimize their performances, in-depth analyses are required: local information about the morphology, composition and atomic structure, the compactness distribution, but also layer homogeneity, interface and interpenetration between stacked layers or oxidation are extremely important factors that can ruin their way of operation. In this particular context, the objective of the present PhD Thesis is to make significant contributions to the study and development of multifunctional porous nanostructured systems, from their design and elaboration, to the maximum knowledge of their structure and properties, through advanced (S)TEM methods, including 3D reconstructions, elemental analyses at the nanoscale and atomic-scale imaging, combined with optical spectroscopy techniques.

In the first instance, given the great potential of the slanted nanostructures generated by means of oblique angle depositions, in which the refractive index gradient can be tuned by the columns tilt and density imposed via the growth angles and parameters, OAD broadband antireflective coatings based on Si, Ge or SiO_2 OAD films have been designed, manufactured, and extensively characterized with the aim of maximizing the performance of the optical elements in the vis-IR wavelength range. This same approach has also been implemented to enhance the antireflective capabilities of transparent conductive ITO thin films in the near-IR window without compromising too much their electrical response.

On the other hand, the advanced structural and functional characterization of porosity-controlled GaN NW arrays grown by plasma-assisted MBE through (S)TEM

methods and vis-IR SE elliposmetry, has helped not only to improve growth processes but also to optimize their resulting optical and electrical properties.

Finally, the knowledge and methodologies acquired during the study and optimization of the previous porous systems have been transferred to the development of a two-step procedure, based on the deposition and the subsequent fast oxidation of vanadium-based OAD films in open air atmosphere, for the synthesis of thermochromic VO_2 coatings of tunable metal-to-insulator response and controlled grain sizes and crystallinities.

Resumen

La nanoestructuración de materiales a la mesoescala para dar lugar a recubrimientos de porosidad controlada representa un avance importante en el área de Ciencia e Ingeniería de Materiales, ofreciendo funcionalidades nuevas y mejoradas de interés en campos como la óptica, la optrónica y la optoelectrónica. Para optimizar el rendimiento de estos sistemas, se requieren análisis que den información local sobre la morfología, composición y estructura atómica, grado de compactación, y de otros factores que pueden influir en las propiedades, tales como homogeneidad de las capas, calidad de las intercaras, interpenetración entre capas apiladas u oxidación. En este contexto, el objetivo de la presente Tesis Doctoral es realizar contribuciones significativas al estudio y desarrollo de sistemas nanoestructurados porosos y multifuncionales, desde su diseño y elaboración, hasta el máximo conocimiento de su estructura y propiedades, a través de la aplicación de métodos (S)TEM avanzados, entre los que se incluyen reconstrucciones 3D, análisis elementales a la nanoescala e imágenes a escala atómica, combinados con técnicas de espectroscopia óptica.

En primera instancia, dado el gran potencial de las nanoestructuras inclinadas generadas mediante las deposiciones en ángulo oblicuo, en las que el gradiente del índice de refracción puede ser adaptado por la inclinación de las columnas y la densidad impuesta a través de los ángulos y parámetros de crecimiento, se han diseñado, fabricado y caracterizado en detalle recubrimientos antirreflectantes de banda ancha basados en películas OAD de Si, Ge o SiO_2 con el objetivo de maximizar el rendimiento de los elementos ópticos en el rango de longitudes de onda vis-IR. Este mismo enfoque también se ha implementado para mejorar las capacidades antirreflectantes de películas delgadas conductoras y transparentes de ITO en el infrarrojo cercano sin llegar a comprometer demasiado su respuesta eléctrica.

Por otro lado, también se ha llevado a cabo la caracterización estructural y funcional avanzada de matrices de nanohilos GaN de porosidad controlada, crecidas por MBE asistido por plasma, mediante métodos (S)TEM y eliposmetría vis-IR SE, lo cual no solo ha ayudado a mejorar los procesos de crecimiento sino también a optimizar las propiedades ópticas y eléctricas resultantes.

Finalmente, los conocimientos y metodologías adquiridas durante el estudio y optimización de los sistemas porosos anteriores se han trasladado al desarrollo de un procedimiento de dos etapas, basado en la deposición y posterior oxidación rápida de películas de OAD de vanadio en atmósfera de aire, para la síntesis de recubrimientos termocrómicos de VO_2 de respuesta metal-aislante sintonizable y de tamaños de grano y cristalinidades controladas.

Index

Chapter 1

Introduction and justification of the Thesis thematic unit

1. Introduction and justification of the Thesis thematic unit

Surface engineering is an area of Materials Science & Technology that has lately attracted great interest thanks to the possibility of modifying the properties of the material that is covered, functionalizing surfaces and, thus, providing some characteristics that make it ideal for a determined application in a simple and cost-effective way [1,2]. In this light, many different approaches have emerged, being the design and manufacturing of porosity-controlled coatings one of the most appealing. By tuning porosity, the physicochemical properties of coatings, like refractive index, surface roughness or surface area, can be modulated, endowing materials with improved and additional functionalities for applications in fields such as optics [3,4], optoelectronics [5,6], energy generation and storage [7,8], catalysis [9,10], and sensors [11,12].

Many efforts to attain materials with customized properties have generally focused on controlling the morphology and microstructure of the film during deposition. Nevertheless, in order to get maximum benefits from this approach, it has also become necessary to know accurately the structure of the porous deposited systems at different scales, as this will not only help to a better understanding of the fundamental processes involved in the generation of such type of nanostructured films, but also to go further into their performances optimization. In this context, the present PhD Thesis focuses on the comprehensive structural and functional characterization of porous materials for the development of multifunctional coatings by combining, at least, (scanning-)transmission electron microscopy ((S)TEM) techniques and optical spectroscopies (spectroscopic ellipsometry, Vis-IR spectrophotometry and Raman spectroscopy).

On the basis of the foregoing, this first Chapter has been organized as follows. First of all, the main deposition strategies conventionally used to achieve porosity-controlled

coatings will be briefly overviewed in section 1.1. Afterwards, the main material systems studied in this Thesis will be described in section 1.2, which include antireflective multilayers for infrared and visible optics (section 1.2.1), transparent conductive nanostructured films of indium tin-doped oxide (ITO) (section 1.2.2), GaN nanowire arrays with potential applications (section 1.2.3), and vanadium-based porous layers for switchable thermochromic applications (section 1.2.4). After that, the role of advanced electron microscopy techniques combined with optical spectroscopies as a powerful joint characterization tool for the development of porous multifunctional coatings is emphasized in section 1.3. Finally, the justification of the topical unity of the PhD Thesis is included in section 1.4.

1.1. Design and fabrication of porosity-controlled coatings

For the nanofabrication and functionalization of porous thin films, two main approaches referred as top-down and bottom-up can be employed. In a top-down approach like nanolithography or precision engineering, a process or instrument is used to sculpture the surface of a bulk material down to the nanoscale, giving rise to the fabrication of complex designs at high level of accuracy. On the contrary, in bottom-up approaches such as self-assembly combined with chemical synthesis, atoms and molecules arrange themselves into ordered nanoscale structures. Although it is still not as mature as other top-down processes, the bottom-up technology is preferred since it enables to manufacture well-defined morphologies, shapes, and patterns in a faster and more easily scalable and cost-effective ways.

Among the different bottom-up methods to fabricate porous structures, such as sol-gel [13], template synthesis [14], and layer-by-layer [15], oblique angle deposition (OAD) – alternatively called glancing angle deposition (GLAD) – has emerged as an innovative

and promising technology for attaining 3D micro- and mesoporous architectures of controlled structures and properties [16–21]. This particular geometry, combined with physical vapour deposition (PVD) processes, gives rise to tilted columnar and highly porous films and nanostructures which are promoted by shadowing effects that occurs at the surface of the substrate behind initially nucleated islands, when the incident flux of particles arrives at an oblique angle (Figure 1). This approach provides a great flexibility in the range of nanostructures that can be achieved, allowing not only to deposit many types of materials (single elements, compounds with complex stoichiometry, metals, oxides, semiconductors, dielectrics, etc.), but also to sculpt, with a nanometer precision, a variety of complex architectures with controlled geometries (inclined structures, vertical structures, graded density structures, zig-zag structures, helical structures, periodic arrays, etc.), simply by adjusting the process parameters during the deposition. Moreover, this method is not very high demanding in the vacuum and temperatures to be achieved in many cases. In this way, some outstanding properties, highly correlated to the architecture derived from OAD, have already been highlighted in various fields such as in optics (antireflective coatings, Bragg reflectors, surface enhanced Raman scattering) [22–24], in transparent gas sensing devices [25], or in thermochromic materials for smart windows [26].

Alternatively, the manufacture of fine-controlled self-assembled nanoporous films by molecular beam epitaxy (MBE) or chemical vapour deposition (CVD) methods has also shown to be a good choice on these purposes, even though the architectures achieved by these two techniques are different from those generated by OAD methods, being the most significant those formed by single-crystalline nanorod (NR) or nanowire (NW) arrays of semiconducting materials with controlled size, composition, porosity and shape [27–32].

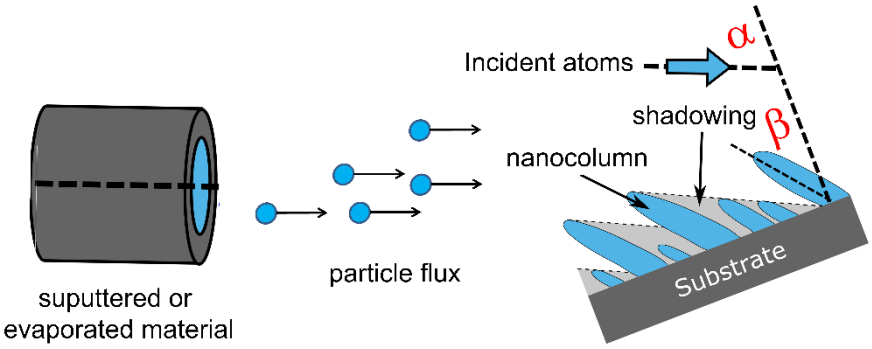

***Figure 1**. Scheme of the experimental setup of the OAD technique: α and β represent the deposition angle and the angle of the nanocolumns relative to the substrate normal, respectively.*

Within the framework of the development of nanostructures for ultra-high performance multifunctional devices, the present PhD Thesis will focus on uncompact thin films deposited by OAD and plasma-assisted molecular beam epitaxy (PAMBE) techniques, since, among other advantages, both bottom-up approaches permit to finely tailor three-dimensional nanoarchitectures of controlled porosity and shape, which endows materials with new or enhanced properties.

1.2. Advanced porous coatings studied in this PhD Thesis

This section includes the different types of nanostructured materials that have been investigated in the present PhD Thesis, which have been classified according to their properties and applications.

1.2.1. Nanostructured antireflective films for infrared and visible optics

The mid-wavelength infrared (MWIR) spectral band (3–5 μm) is known to be one of the most important atmospheric transmission windows used for thermal imaging systems [33]. Because of their transparency in the infrared (IR) region, silicon and germanium are two materials of common election to produce IR optical components (lenses, windows)

requiring high levels of transmittance. Si and Ge are usually found in high-resolution optical systems allowing to use a minimum number of lenses. Besides their IR transparency, each of them also have good thermal conductivity, excellent surface hardness, and high strength, that make them the favourite choices for optical designers of high performance infrared objectives for thermal imagers [34]. However, these dense materials suffer from important optical losses (> 30% at each interface with the air) due to their high refractive indices [35], which can limit the device performance. Since Si and Ge are among the few transparent solid elements in the IR, cutting down the light reflection on them to increase their transmittance in this spectral range has become a critical issue. This can be achieved, however, by using antireflective (AR) coatings**.**

In this context of thin AR surface design, a well-known approach to reduce the effective refractive index of Si and Ge consists in manufacturing porous films. For that matter, oblique angle deposition has demonstrated to be a powerful technique in optics, since the effective refractive index (*n*) of the deposited coatings can be tuned by controlling the porosity through parameters such as the deposition angle [20,23]. This principle has been applied for the fabrication of graded-index broadband antireflection coatings presenting smooth sequential variations of their *n* values, in order to reduce index mismatches at the interfaces between the substrate and the air close to the surface, and thus eliminating Fresnel reflections. This approach has appeared as an advantageous alternative to the conventional interferential AR coatings generally made of complex stacks alternating low and high refractive index layers at the surface of a substrate in order to obtain destructive interferences (Figure 2). This same principle can be implemented to remove reflections over the visible and near-infrared (NIR) domains (up to about μm) [23,36]. Within this wavelength window, silicon dioxide (SiO_2) stands out as a reference

photonic material which can be nanostructured by OAD to obtain the very low refractive index that is needed for a high-performance antireflective coating.

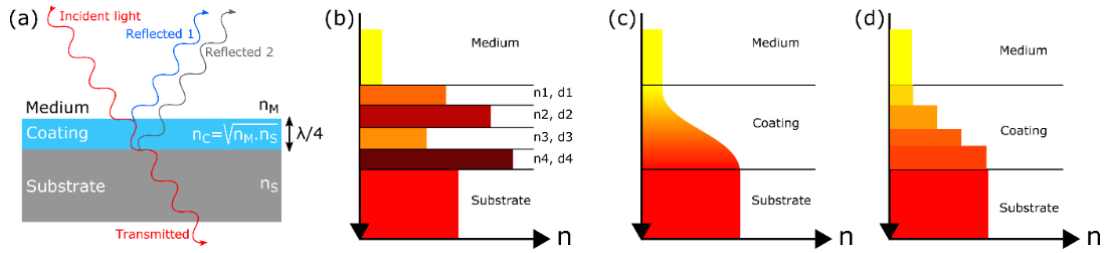

***Figure 2**. Different AR approaches. Interferential coatings using (a) a single layer, or (b) complex multilayer alternating low and high refractive index materials. The smoother transition of "n" is achieved by (c) continuous or (d) discrete gradient-index coatings.*

In this PhD Thesis, a comprehensive structural and optical characterization of Si, Ge and SiO_2 photonic coatings deposited by means of the electron-beam evaporation OAD technique has been conducted for the purpose of investigating and optimizing their physical properties.

1.2.2. Transparent conductive ITO films

With high optical transmissions in the visible range and simultaneously great electrical conductivities, transparent conductive oxides (TCOs) arise as very attractive materials in the field of (opto)electronics, offering a wide variety of applications, including transparent contacts in optoelectronic devices (solar cells, light-emitting diodes, flat-panel displays, touch screens), low emissivity, and smart windows for buildings, heat reflectors, static dissipation, airplane windshield de-icing systems, or electromagnetic shielding [37–42]. In these materials, transparency and conductivity are however intricately linked since TCOs generally exhibit strong absorption and reflection (and hence low transmission) of light in the infrared range due to the free-carrier plasma. Moreover, any effort to increase the carrier density for improving the conductivity σ (proportional to the product of the carrier mobility μ and the carrier density N) will

produce a shift of the plasma resonance toward the visible region, leading to substantial narrowing of the transmission window in this spectral domain [43]. Such antagonism between the electrical and optical properties is an important limitation for further implementation of TCOs in devices requiring both optical transparency across a wide portion of the electromagnetic spectrum and low electrical resistivity. In photovoltaics, for example, transparent electrodes with large optical access and low resistance are needed to make better use of the solar spectrum [41]. Besides broad-band transparency, the use of TCOs presenting low resistivity would be of great interest for providing other essential functionalities in these systems to ensure optimal performances in a variety of environmental conditions: heating capability to prevent fog and frost formation in critical regions exposed to humidity and low temperatures, or shielding against electromagnetic interferences [37,39,44].

Within this class of materials, indium tin-doped oxide (ITO) is certainly the best candidate for those applications because this n-type degenerate semiconductor combines the highest available transmissivity for visible light with the lowest electrical resistivity due to its high free-carrier density [45]. Nevertheless, finding the best compromise between reasonably low resistivity and sufficiently high IR transmittance in a spectral domain as wide as possible is far from being straightforward. This is due not only to the inherent electro-optical antagonism of TCOs but also to the limitations of the current fabrication technologies.

In order to get a better understanding for the development of tin-doped indium oxide nanostructures as well as to overcome the current difficulties related to the optimization of their electro-optical properties, the present PhD Thesis contributes to the aim of enhancing the antireflective capabilities of ITO thin films in the NIR range without compromising too much the carrier density by combining room temperature ion beam

sputtering (IBS), a type of PVD method, and OAD modality. For this purpose, deep insights into these systems are provided by coupling nanostructural and optical characterizations.

1.2.3. GaN nanowire arrays with optoelectronic applications

Gallium nitride (GaN) is a III-nitride wide bandgap semiconducting material extensively used in optoelectronics and power electronics due to its high Young's modulus, thermal conductivity, electron mobility, high melting point, and low chemical reactivity [46]. Among the different GaN nanostructures attained to date, nanoporous films (NPFs) have specially attracted the attention of the scientific community not only due to their large surface-to-volume ratio but also to their unique electrical and optical properties [47–49]. Comparing with their compact counterparts, GaN NPFs have demonstrated improved properties in diverse applications such as photoelectrochemical water splitting [50,51], supercapacitors for energy storage [52,53], light emitting diodes (LEDs) [54,55] or distributed Bragg reflectors [56].

The vast majority of reports on the synthesis of GaN NPFs are focused on different kind of etching of thin films or GaN-sapphire templates, such as electroless etching [56], electrochemical etching [57], or high-temperature annealing [52,53]. Likewise, the fabrication of ordered NPFs has been demonstrated using inductively coupled plasma (ICP) etching using an anodic alumina template as etching mask [58]. The main drawbacks of the etching (top-down) approach are the difficulties of controlling the porosity level and shapes on the films. Therefore, a way to produce high-quality NPFs in a bottom-up approach with direct control over the composition, porosity, and shape as well as low-cost routes to scale it to large areas for industrial transfer would be highly desirable.

In this context, GaN nanowire arrays, a type of NPF, grown by molecular beam epitaxy postulate as one of the best bottom-up alternatives. By varying the growth conditions, the size, shape and density of the nanowires, the porosity can be tuned, thus allowing to modulate the optical and electrical properties of the system. Thanks to its high surface-to-volume ratio, high crystalline quality, strain-free nature, tuneable refractive index and bandgap, high light extraction efficiency and quantum efficiency, NPFs of GaN nanowire arrays have been erected as a promising material for the development of optoelectronic and optical devices [59–62]. Nonetheless, for the optimization of such GaN nanostructures, it is not only essential to explore them at micro- and nanoscale, but also to jointly evaluate their optical and electrical properties. On this basis, this Thesis pursues to correlate the morphology, structure and composition of GaN nanowire arrays grown by PAMBE with their optical and electrical properties and growth conditions.

1.2.4. Vanadium-based films for switchable thermochromic applications

Vanadium is a transition element with an uncompleted electronic structure and a consequent availability of multiple valences. Upon oxidation of V, the products can progress to mixes of vanadium oxides (VO_x), which have become one of the most studied materials for many years due to their unique properties and technological applications. In this framework, vanadium (IV) oxide (VO_2) has specially attracted the attention of the scientific community since it experiments a reversible metal-to-insulator phase transition (MIT) between insulating monoclinic VO_2 (M1) to metallic rutile VO_2 (R) at a temperature of ~68 ºC, which implies drastic changes in the optical and electrical properties [63–66]. This makes VO_2 an attractive thermochromic material for

applications in smart windows [67–69], resistive switching elements [70,71], storage devices [72], and sensors [12].

Nevertheless, the fabrication of VO_2-based systems has become a real challenging issue not only due to the complexity of the vanadium-oxygen reactive system but also because of the narrow stability range of the dioxide, which can lead to the formation of other more thermodynamically stable oxides such as V_2O_3 and V_2O_5, mixtures of various stoichiometries, or even the appearance of several VO_2 metastable crystalline polymorphs [64–66,73–75]. Hence, it is clear that the preparation of high purity VO_2 systems requires a precise control of the deposition parameters as well as the exploration of novel manufacturing strategies and alternatives.

Aware of this opportunity, and taking advantage of the superior reactivity of high surface-to-volume porous nanostructures, this PhD Thesis proposes a two-step procedure to attain the formation of pure VO_2 films, which comprises the initial deposition of DC magnetron-sputtered vanadium or vanadium oxide films by the combination of oblique angle deposition and, if needed, reactive gas pulsing process (RGPP), followed by the fast oxidation of such layers in air atmosphere at high temperatures. Likewise, the comprehensive characterization of such structures before and after oxidation, as well as the evaluation of the MIT response, are also within the scope of these studies.

1.3. Advanced electron microscopies and optical spectroscopies

As pointed out earlier, the correlation between the design, deposition parameters, structural features and functional properties is a fundamental aspect for the development and optimization of porous thin films. Therefore, it is essential to apply, in a systematic way, characterization methodologies that also allow a complementary finer description of these systems. In this context, *transmission electron microscopy* (TEM), and its related

techniques, postulates as the appropriate candidate, which is known to be a powerful and fast-growing analytical tool to probe not only the local structure but also the local chemistry and morphology of materials. In the past few years, the integration of efficient and multiple signal detectors combined with the arrival of aberration correctors for the electron lenses have enabled significant improvements in TEM microscopes related to elemental detection sensitivity and dramatic reduction of the attainable resolution limits below the Angstrom, opening up new possibilities and challenges in the characterization of materials [76–78].

(S)TEM characterization techniques allow to perform a wide variety of surveys, including overall studies of the structures and morphologies generated at micro- and nanoscale, atomic-resolution imaging of crystalline structures, chemical analyses by combining imaging and spectroscopies, and 3D reconstructions of nanostructures. As a first approach, *conventional transmission electron microscopy* (CTEM) appears as the most viable option to explore the structure and morphology of porous films at micro- and nanoscale. The images collected through CTEM are formed by electrons of a parallel beam that have been transmitted, without interaction or diffracted at a low angle, when it passes through the electron-transparent prepared specimen.

When a thin film presents a polycrystalline organization of its atoms, the orientation of its grains can determine the macroscopic properties of the system. These periodic lattice features can be locally studied by combining *high-resolution transmission electron microscopy* (HRTEM) and *selected area electron diffraction* (SAED) methods. In HRTEM, phase contrast images are obtained as a consequence the multiple interferences between the beams involved in its creation. It is a technique that can currently reach hundredths of nanometer in resolution, which allows observing a projection of the columns of atoms of a material under study, and, thus, enables structural characterization

at an atomic level. However, the formation of the image is very sensitive to many factors (orientation of the sample, thickness variations, aberrations of the microscope lenses ...), so its interpretation must be carried out with prudence. On the other hand, by using an aperture to collect the signal coming from an isolated electron-transparent region, a SAED pattern of the electron interacting with the sample can be obtained. In crystalline systems, these interferences are reflected constructively in a plane as periodically ordered spots (single crystals) or rings (poly crystals) that correspond to beams diffracted by families of crystalline planes, and are distributed around the direct beam with an intensity that is attenuated in all radial directions. Properly interpreted, the SAED patterns enable to obtain structural information at the local level of the material under observation, including its reticular parameters, epitaxial relationships, symmetry, structural defects, etc.

Scanning transmission electron microscopy (STEM) is a modality of TEM microscopy, in which the electron beam is converged forming a probe of nanometric or subnanometric size, which offers new capabilities and alternatives for studying the chemical features of materials. When operating in STEM mode under dark field conditions, the image obtained using a *high-angle annular dark field* (HAADF) detector is solely and exclusively due to electrons that have been incoherently scattered from their path through matter at a sufficiently high angle. Since the HAADF technique is very sensitive to the atomic number of the irradiated elements (Z-contrast), the resulting STEM-HAADF image will present an intensity approximately proportional to the square of the average atomic number of the atoms in scanned region, as the heavier atoms will have a greater capacity to inelastically scatter electrons at higher angles due to bigger electrostatic interactions between their nuclei and the electron beam. This means that qualitative information about the chemical composition of a sample can be obtained, since the contrast in the HAADF images can be associated with a difference in the effective

atomic number. Nonetheless, it must be considered that variations in thickness also significantly affect the intensity of the HAADF signal, which should be taken into account so as not to misinterpret the information contained in the HAADF image.

Nevertheless, what really makes the TEM a very powerful analytic tool is the combination of STEM imaging and spectroscopy. In this sense, the most common TEM-based spectroscopy techniques are *Energy Dispersive X-ray Spectroscopy* (EDX or EDS) and *Electron Energy Loss Spectroscopy* (EELS). STEM-EDX is based on the inelastic interaction (with loss of energy) of the electrons of the beam with those existing in the constituent atoms of the material. If the energy transferred to these electrons is high enough, one of the electrons closest to the nucleus will be ejected from the atom. Thus, a hole is left that will be quickly occupied by one of the electrons located at a higher energy level, such as those of valence. The result of this occupation is the emission of an X-ray quantum whose energy is characteristic of a specific element. This analytical technique is especially useful to uncover, by means of spectrum images (SIs), the qualitative or quantitative distribution of the elements that compose a sample but also to know relevant information on how the interfaces are developed or, for example, if the exposed surfaces are subjected to spontaneous oxidation. Another alternative way to carry out chemical nature studies at nanometer scale consists of measuring the loss of energy from the inelastic interactions between the incoming electron beam and a thin specimen. That loss of energy in the transmitted beam will be associated with different characteristic electronic transitions of the constituent elements of a sample, allowing their identification and even their quantification. This is the basis of the STEM-EELS technique which, compared to EDX, provides improved signal, spatial resolution, energy resolution and sensitivity for low atomic number elements [79,80]. In addition to the above-mentioned, EELS information can also be used to characterize chemical bonding configurations,

oxidation states, valence and conduction band electronic properties or even sample thickness.

Electron Tomography (ET) is another TEM-based technique that specifically allows to reconstruct the three-dimensional structure of a specimen from a set of two-dimensional images recorded at various tilt angles (tilt-series) which are then processed off-line using different reconstruction algorithms [81–86]. Among the different ET variants, STEM tomography has become one of the most powerful. As 3D characterizations at the nanoscale represent valuable insights into the design of nanomaterials, STEM tomography examinations of thin films are becoming increasingly popular for material scientists, being the HAADF signal preferred to bright-field (BF) because of its monotonic dependence on the sample thickness [87,88]. In this sense, STEM-HAADF tomography reconstructions can supply relevant geometric features such as 3D morphologies and textures, distribution and interaction between nanostructures, anisotropy, and also provide quantitative information about the porosity distribution and profiles within coatings.

Specimen preparation appears to be a crucial step in the investigation of porous thin films by TEM methods. The lower consistency of these porous architectures when compared to their compact equivalents makes the collection of electron-transparent sections of submicron thicknesses (lamellae) a challenging issue, becoming one of the main reason why there are very few studies of these systems through (scanning-)transmission electron microscopy. Moreover, both the relative fragility of the mesoporous systems to be analysed and the type of analysis to be carried out (imaging, tomography, spectroscopies up to the atomic scale), impose great demands when preparing thin lamellae. Hence, it is desirable to avoid conventional preparation techniques like mechanical grinding plus dimpling, which are generally used for studies

of denser thin films. Keeping this in mind, it is thought that thinning down by *tripod polishing* plus low-energy *ion milling* is one of the most suitable approaches to achieve large electron-transparent regions of porous and delicate thin films. This sample preparation methodology allows to carefully thin down the specimen up to a few microns, leading to a much softer mechanical thinning than that achieved with SiC sandpapers, avoiding the dimpling stage and reducing the time required for the final thinning step by Ar^+ ion milling, which is not only recommended to reduce sample damage but also to prevent the amorphization of the electron transparent area. Since this method is not highly spread and not many groups have a high control of its effective handling, it is worth noting that the Thesis author was able to achieve and master high-quality tripod preparations, based in partly own-developed tools, as that shown in Figure 3. *Focused ion-beams* (FIB) specimen preparation technique is another more expensive but simple and straightforward alternative to collect electron-transparent lamellae of porous nanostructured films. A FIB system is almost identical to a scanning electron microscope (SEM), but with the difference that the probe is a beam of ions (usually Ga^+), which is used for milling the specimen, rather than electrons. This technique not only provides the capability to prepare TEM samples with minimum levels of damage and contamination but is also capable of preparing samples either along particular orientations or in specific areas with a few nanometer precision [89]. This equipment also allows to carry out 3D reconstructions of localized regions within a sample by overlapping the SEM-like images (or compositional maps) of the planes that are sliced consecutively, which is known as FIB tomography (slice and view) [90]. In this sense, it must be noted that optical and SEM microscopies were also used in many stages of the performed studies within this Thesis. SEM bases on probing an electron beam on the surface, and give topographic or compositional

information depending on the used mode. X-ray diffraction (XRD) had also a key role in specific studies of ITO structures.

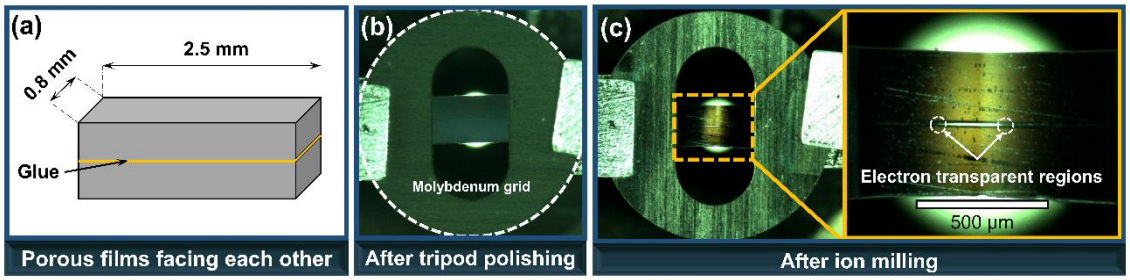

***Figure 3**. Different stages involved in preparing delicate TEM specimens using the tripod method. (a) Scheme of a glued staked specimen before polishing. Pictures of the specimen, once attached to a 3 mm TEM molybdenum grid, after tripod polishing (b) and after ion milling (c). The inset of (c) places emphasis on the developed electron-transparent region.*

In contrast to (S)TEM, for the purpose of carrying out a comprehensive structural and functional characterizations of such porous coatings, all the data acquired from electron microscopy have been contrasted and confronted to those obtained by means of *optical spectroscopies*. In this way, visible-IR *spectroscopic ellipsometry* (SE) is a powerful and precise tool for the simultaneous optical and electrical characterization of thin films. The basis of this non-destructive technique is the measuring of the changes in the state of polarization of the light after having impinged on a surface subject to study, and the subsequently fitting of the acquired data to ellipsometric models. Because it is very sensitive to the composition and capable of detecting very thin films, visible-IR SE is considered as an ideal complementary tool to TEM: the structural (morphology, thickness, porosity, etc.) and chemical information (composition, interfaces, etc.) provided by (S)TEM methods is indeed essential to validate and improve the models employed to describe the optical (refractive index, n; extinction coefficient, k) and electrical (N, μ) response as well as the anisotropy of nanostructured coatings. Additionally, other optical spectroscopies, such as vis-IR *optical spectroscopy* (OPS) and

Raman spectroscopy (RS), have been used in a more occasional manner to acquire complementary optical information (transmission and reflectance spectra by OPS) or as an alternative way to probe the chemical composition of materials (RS).

Briefly, it must be mentioned some techniques used sporadically to obtain complementary electrical properties of the studied material systems, such as Hall effect measurements that were important to characterize GaN systems, or Kelvin probe force microscopy (KPFM) measurements that suddenly appeared as a tool ideal to study VO_2-VO_x multilayers where optical spectroscopies had lower appropriateness to be used.

1.4. Justification of the Thesis thematic unit

The present PhD Thesis aims at contributing to the development of nanostructured porosity-controlled coatings with improved optical properties and additional functionalities (i.e. electrical) of interest in fields such as optics, optronics or optoelectronics, optimizing designs, fabrication processes and performances. For such purpose, the structure, chemistry and functional properties of the nanomaterials described in section 1.2 have been explored at different levels, from microscopic to atomic scale, by combining mostly advanced (S)TEM methods with optical spectroscopies.

The lower implicit consistency of the addressed materials when compared to their compact modality hinders the attainment of electron-transparent sheets, which becomes one of the main reasons for the scarcity of (S)TEM studies of these types reported in the literature to date. In this light, this PhD Thesis helps at filling this knowledge gap by demonstrating the unique opportunities and possibilities offered by (S)TEM methods, especially when combined with visible-IR SE, for the exhaustive scrutiny of porous nanostructured coatings. These studies allowed us to accomplish several of the pioneering works presented here, which not only represent valuable insights into the design of this

kind of nanomaterials but also relevant data to gain a better knowledge of their growth mechanisms and properties. Matters as the preparation of electron-transparent specimens and the advanced characterization of their structures, morphologies, interfaces and compositions are discussed thanks to the implementation of innovative approaches based on a variety of (S)TEM techniques, letting us obtain high resolution imaging, spectroscopies, or tomography, at both microscopic and nanoscopic levels. All collected information is not only then contrasted with the results obtained by optical spectroscopies but also can also be implemented in advanced ellipsometric models, enabling a comprehensive structural, chemical, optical and electrical characterization of such systems.

This Doctoral Thesis is presented as *Compendium of Publications*, and the corresponding articles can be found at appendices of this Thesis. Publications I and II are dedicated to Si and Ge OAD antireflective coatings for infrared optics. In these works, (S)TEM analyses, including EDX and EELS spectroscopies, were fundamental to provide key insights about the nanostructure of such systems that, once related and combined with ellipsometry and optical transmission measurements, contributed to the optimization of their optical performances. In publications III and IV, 3D reconstructions obtained by means of STEM-HAADF electron tomography experiments not only allowed to estimate the optical losses of an ultra-high performance SiO_2 OAD bilayer AR coating but also to get a precise comparison between optical properties and microstructure as well as to validate optical models. Publication V reports the structural and functional characterization of porous and crystalline ITO thin films deposited by ion beam sputtering deposition at oblique angles using either argon or xenon ions. Deep understanding of these systems are provided by coupling nanostructural (scanning and transmission electron microscopies, X-ray diffraction) and optical (spectroscopic ellipsometry,

reflectance optical spectroscopy) characterizations, which allows extracting important features of the films (porosity, refractive indexes, in-grain carrier densities, and mobilities). In publication VI, selected-area electron diffraction and scanning and high-resolution transmission electron microscopies evidenced the structure and epitaxial alignments of vertical GaN nanowire arrays epitaxially grown by PAMBE. In the line of the previous study, publication VII is associated to the simultaneous optical and electrical characterization of GaN nanowire arrays through vis-IR spectroscopic ellipsometry. With the aim not only of establishing (S)TEM as a reference tool, but also to provide better and new features that allow the optimization of the fabrication and design of porous nanostructured coatings, manuscript VIII accounts for the possibilities and alternatives offered by the application of (S)TEM methods for the study of such systems. Finally, applying the knowledge previously acquired during the study of porous thin films and taking advantage of the enhanced reactivity of the high surface-to-volume OAD structures, manuscript IX purposes the fabrication of controlled grain-size thermochromic VO_2 coatings by the fast oxidation of sputtered vanadium or vanadium oxide films deposited at glancing angles. The comprehensive characterization of as-deposited as well as the resultant oxidized systems is handled by scanning electron microscopy, Raman spectroscopy and scanning-transmission electron microscopy techniques, such as electron energy-loss spectroscopy.

In this light, the results shown throughout this PhD Thesis are expected to have a great impact on the development and optimization of porous multifunctional coatings, opening new horizons in the advanced characterization of such systems, simplifying methodologies and contributing to a better knowledge of deposition or growth processes and performances.

Chapter 2

Hypotheses and Objectives

2. Hypotheses and Objectives

The development of the present PhD Thesis is based on the following hypotheses:

- The performance of the multifunctional porous nanostructured coatings considered in this Thesis are closely linked to their morphologies, porosity, structures, interfaces and chemical compositions.
- Joint structural, chemical and functional characterizations at micro-, nano- and atomic scale by advanced (S)TEM techniques and optical spectroscopies can open new pathways in the design, development and optimization of porosity-controlled materials.
- The enhanced reactivity of high surface area porous films can promote the selective and quasi-instantaneous formation vanadium oxidized species of controlled grain size, composition and crystallinity.

The outcomes of the research addressed in this PhD Thesis support and confirm the validity of these hypotheses.

The main objective of this PhD Thesis is contributing to the development of design rules for the engineering of multifunctional porous nanostructured systems by optimizing their performances. To meet this goal, the advanced structural and compositional characterization of these materials through (S)TEM methods, including 3D reconstructions, elemental analysis at the nanoscale and atomic-scale imaging, combined with optical spectroscopy techniques such as vis-IR spectroscopic ellipsometry, is suggested for the purpose of not only directly correlating the constitutive characteristics and the functional properties of such coatings, but also with the design and manufacturing processes.

Particularly, the specific objectives are the following:

- Establish and apply (S)TEM methods as a central tool for the development of multifunctional porosity-controlled coatings. This specific objective also comprises the exploration of the most adequate procedures for the achievement of fine electron-transparent sheets of such materials that allow the achievement of the advanced studies addressed here (STEM-EDX and EELS analysis, STEM-HAADF imaging and tomography, ...).
- Investigation of the singular characteristics of OAD and PAMBE porous thin films which determine their functional properties: morphology and shape at nanoscale, porosity profiles extracted from 3D reconstruction, local composition at both micro- and nanoscale based on qualitative and quantitative analyses, nature and development of interfaces between layers, epitaxial alignments and crystalline features at atomic scale.
- Correlate and compare the information collected by (S)TEM methods with the functional properties evidenced by optical spectroscopies. This overall data will be then implemented into advanced ellipsometry models, which will not only allow to enhance and validate them, but also to address a comprehensive structural, chemical, optical and electrical characterization of such porous coatings, shedding light on the optimization of their designs, manufacturing process and, thus, performances.
- Transfer the methodology and knowledge acquired during the characterization and development of porous thin films to the synthesis of thermochromic VO_2 coatings of tuneable metal-to-insulator response by controlling grain sizes and crystallinity.

Chapter 3

Critical analysis of the state of the art

3. Critical analysis of the state of the art

This third Chapter discloses the state of the art of the materials addressed in this PhD thesis, including a critical review of the progresses made to date. In section 3.1, the current trends in porous thin-film nanotechnology, as well as the techniques used to characterize these structures are described. Thereafter, the main strategies to attain broadband omnidirectional AR coatings are explored in section 3.2. Sections 3.3 and 3.4 are about the best comprise solutions for improving the optical and electrical performances of ITO and GaN-based coatings, respectively. Finally, section 3.5 describes the current strategies to achieve thermochromic VO_2 films.

3.1. Porous thin-film nanotechnology

The fabrication of thin films with engineered structures of controlled porosity at the micrometer and nanometer scales is an exciting approach for the development of emerging technologies since it allows providing enhanced performances, novel properties and new functionalities [91]. Thanks to their high surface-to-volume ratio, lower refractive index, and ultra-low dielectric constant (ε) compared to their bulk modalities, uncompact coatings have been integrated in a large variety of devices with applications in fields such as energy, photocatalysis, sensors, optics and photonics, or thermal insulators [92–96]. Up to about a few years ago, most of the studies related to porous thin films, which are mainly based on etching processes or self-assembly templating, have been focused on elucidating the mechanisms behind the synthesis of this kind of materials as well as the design of novel architectures. Because of this, both the development of new and enhanced applications, as well as the establishment of the correlation between the structure and the functional properties of these systems have played a secondary role in the progress of this technology.

Nonetheless, the rise of simpler and more straightforward bottom-up strategies, such as the deposition of slanted columnar films at oblique angles or the growth of nanowire arrays by molecular beam epitaxy, has opened new possibilities for tuning, enhancing and creating porosity-controlled coatings. In this regard, OAD and MBE techniques have proved to be powerful tools for the elaboration and tailoring of nanostructures for ultra-high performance multifunctional devices since both permit to tune the effective refractive index of the deposited film by controlling the porosity of the system, enabling to manufacture broadband omnidirectional graded-refractive-index AR coatings [3,23,97–100]. Nevertheless, since the deep understanding of the structure-property relationship is the key to get the most of these two approaches, fine descriptions at different scales of the elaborated systems are needed.

From the outset of this nanotechnology, OAD and semiconducting NW films have been broadly studied through SEM [101–105], atomic force microscopy (AFM) [106–108], XRD [109–111], or X-ray photoelectron spectroscopy (XPS) [112–114]. These techniques have been applied to obtain information about the structure, morphology and composition of such systems, which are relevant data to take into account for a better description of their growth mechanisms and properties. However, it must be highlighted that all these methodologies provide microstructural information with a limited spatial resolution: several microns in the case of XRD and XPS and up to a few nanometers in the case of AFM (lateral resolution) and SEM.

According to Hawkeye et al. [21], “the future development of OAD technology requires further study of fundamental growth processes as well as continued investigation and optimization of the physical properties of OAD fabricated films”. Accordingly, because the structure and chemistry of these porous nanostructures intimately affect the functional properties they exhibit, it is necessary to study the characteristics of such

systems not only at the microscopic scale (pore distribution, layer morphology), but also at the nanoscale (composition of individual columns or nanowires, interlayers between layers) as well as the atomic scale (crystalline or amorphous nature, preferential crystal orientations). In this sense, (scanning-)transmission electron microscopy techniques are the most suitable tool to cover all these needs.

A thorough review of the state of the art dealing with the OAD processes indicates however that only a few studies have concerned the application of TEM, and most of them are restricted to basic TEM analyses, including, mainly, conventional TEM imaging, electron diffraction, or high-resolution TEM (see the recent references [115–122] as example), and do not take advantage of the full potential of the ultimate generation of electron microscopes including high spatial resolution imaging and spectroscopies or tomography for example.

Likewise, semiconducting nanowire films grown by MBE methods have barely been studied through TEM [123–127]. As with the OAD systems, these works are limited to high-resolution and electron diffraction TEM studies of very narrow areas, being often observed the side faces and interfaces of individual NWs but not being explored the entire film or different representative areas, which can be associated to the aforementioned difficulties that the achievement of electron-transparent sheets of regular widths for nanoporous structures implies.

Regarding the functional characterization of such nanostructured systems by optical spectroscopies, studies based on transmittance and reflectance as well as Raman spectroscopies have been found in the literature [107,128–131]. However, all of these reports lack of complementary structural and compositional characterizations at different levels, simply focusing on the evaluation of the system functionality and overlooking the

understanding of the structure-properties relationship in these materials. Something similar applies to the characterizations carried out by means of spectroscopy ellipsometry: either the SE optical responses are modelled through basic approximations and assumptions or the determined structural, optical or electrical properties are not validated and confronted with those experimentally obtained by means of other characterization techniques [132–137].

Therefore, given the absence of studies that address a structural, chemical and functional characterization of thin porous layers, bearing in mind the main objective of contributing to the progress and optimization of this technology, this PhD Thesis not only targets the joint characterization at different scales of such porous systems by means of (S)TEM microscopies and optical spectroscopies, but also the optimization of realistic ellipsometry models capable of evidencing the structural, optical and electrical behavior of porous coatings thanks to the incorporation of the data previously recorded through all the characterization techniques previously described.

3.2. Broadband antireflective coatings

The optimization of anti-reflective coatings (ARCs) has been a subject of intense research not only for the optical base function but also for more specific applications like photonics in which the optical transmission is usually a critical parameter [138–141]. In this context, the traditional approach to achieve antireflection, known as "*AR interferential technology*", consists in depositing multilayers alternating low and high refractive index layers at the surface of a substrate in order to obtain destructive interferences [142,143]. However, in addition to the antireflection limited to narrow wavelength ranges, this approach has become especially challenging due to the scarcity of material available as well as to the complexity of the layer assembly to deposit in order

to obtain high transmittance. In order to overcome these limitations, other solutions such as "*gradient-index antireflection coatings*" have been considered [97]. Based on the progressive decrease of the refractive index from that of the substrate to that of the air close to the surface, this approach allows obtaining an extended range of low reflectivity adapted for broadband wavelength applications. In this regard, numerical optimizations have determined that the optimal gradient is that close to the well-known quintic profile [144]. Nevertheless, because of the unavailability of optical materials with very low refractive indexes that closely match the refractive index of air, such broadband AR coatings are not realizable using standard deposition methods. Therefore, as conventional bulk materials with refractive index below 1.39 do not exist, the nanostructuration of ARCs, with the aim of reducing their refractive index through the introduction of porosity, is required. In this sense, staked systems with porous thin films presenting a decreasing index as going towards the surface (discrete ARCs) as well as moth eye architectures (continuously-graded ARCs) have been developed [144,145]. Since, according to the literature [146], discrete ARCs can outperform continuously-graded ARCs thanks to the interference effects, the manufacturing of porous nanostructured layers made by OAD has emerged as one of the simplest and most viable fabrication alternatives for attaining broadband discrete ARCs. By means of PVD methods such as electron beam evaporation, magnetron sputtering or ion-beam sputtering processes, this deposition strategy allows a fine-tuning of the effective refractive index of films through the insertion of voids, so that the higher the deposition angle, the higher the porosity and the lower the refractive index is [16,17]. In the light of this approach, many ARCs with remarkably low reflectivity or high transmittance over wide wavelength ranges have been developed [3,100,144,146,147].

In addition to the fabrication processes, the choice of materials to deposit is also an important issue since they must be transparent in the wavelength range in which they are aimed at operating. In the visible range, many candidates (in particular many oxides such as SiO_2, ITO or TiO_2) are compatible with the fabrication of gradient index AR coatings. In fact, OAD methods have been used many times for antireflective applications in the visible and near infrared ranges demonstrating remarkably low reflectivity or high transmittance over a large domain of wavelength [3,146,148–150]. For information, the best AR system already obtained for extended-visible applications, consisting of three TiO_2 and two SiO_2 OAD layers, presents reflectivity values as small as 0.1% [3]. Nevertheless, in the IR range, the number of candidates is much more limited so that the use of a technology like OAD to tune the refractive index of the layer is therefore essential.

As mentioned in previous chapters, Si and Ge are among the few materials used for MWIR instrumentation due to their wide transparency range in the IR. However, because silicon and germanium compact layers exhibit refractive indexes of 3.4 and 4 at 4 μm wavelength, respectively, reflecting more than the 30% of the light coming from the air, the design and fabrication of AR surfaces of such materials becomes a matter of vital importance. Up to date, the best ARCs reported in the literature for Si and Ge in the MWIR region based on multilayer stacks presents an average transmission of 98.5% over 3.6–4.9 μm [35]. Nonetheless, since these systems are aimed at being integrated in complex optical devices made of multiple diopters elements, gaining a few tenths of percent of transmitted light for each individual AR coatings will have a significant positive impact on the final device performances. For example, a 1.5% increase of transmittance of a single interface, from 98.5% to 99.97%, can lead to 21% of overall transmittance gain for an optical system composed of 8 lenses (16 interfaces). At this

juncture, the nanostructuration of silicon and germanium films through OAD methods can play a key role in the design of simpler and more efficient MWIR AR systems than those achieved by means of multilayer stacks of different materials, since it allows obtaining layers with adaptable refractive index values below that of the massive material counterpart. Indeed, from our own preliminary experience in the deposition of OAD systems, it was concluded that, at a wavelength of 4 μm, the refractive index of single OAD layers can be tuned from 4 to 1.6 for Ge, and from 3.4 to 1.5 for Si. Even though this principle has been used to prepare broadband silicon and germanium AR surfaces or distributed Bragg reflectors (DBRs) covering the visible and/or near-IR ranges [36,151–154], it must be pointed out that there are no scientific reports focused on the design of OAD ARCs for operating in the deeper IR region such as the MWIR band.

On the basis of the above, it is clear that discrete porous coatings manufactured by OAD methods postulates as the simplest and most promising alternative to produce and provide better optical performances. However, the future development and optimization of this technology will not only require a better understanding and control of the deposition parameters for a specific material, but also to accurately model the structure and optical response of these structures. Since both porosity and morphological anisotropy of OAD layers evolve during the growth [155,156], the use of advanced anisotropic models based on Bruggeman effective medium approximations, considering mixtures of dense material and voids, is needed [155]. Therefore, the knowledge of some key structural, compositional and morphological features (generally overlooked in the literature) at different scales, as well as the extraction of the porosity gradient within the film, will significantly contribute, along with optical spectroscopy measurements, to build, validate and hone these optical models. Keeping this in mind, this PhD Thesis addresses the characterization and modelling of Si, Ge and SiO_2 OAD systems, deposited

as mono or bilayers, through advanced (S)TEM methods in combination with vis-IR SE and transmittance optical spectroscopy measurements.

3.3. Transparent conductive oxide films

Indium tin oxide (ITO) is the most widely used transparent conductive oxide for the fabrication of multifunctional optoelectronic devices such as liquid-crystal displays (LCDs) [157], light emitting diodes (LEDs) [158] or solar cells [159], since it presents not only relevant optical properties (high transmittance in the visible range ~ 80-90%), but also important electrical properties (low resistivity ~10^{-4} Ω cm) and a low deposition temperatures [39,160]. However, due to the great interdependence between the mechanisms of electrical conduction and optical transmission in TCOs, high transmission ITO films can be only attained at the expense of the electrical properties and vice versa. Besides, the properties of ITO films are also strongly influenced by design and fabrication strategies, subsequent annealing treatments and tin concentrations, which ultimately affect their structure at micro- and nanoscales [160–163].

Indeed, although many carrier density (N) and electron mobility (μ) couples have been reported for compact polycrystalline ITO films prepared by standard PVD processes [150], none fulfil an acceptable compromise. In particular, carrier densities as high as $(1-2) \times 10^{21}$ cm^{-3}, obtained by Sn doping to levels of 5-10 at. %, promote resistivities as low as about 10^{-4} Ω cm, which is relevant for photovoltaic and electromagnetic shielding applications, but has deleterious effects on the optical properties due to a plasma resonance close to the visible range. On the other side, reducing N to $10^{18} - 10^{19}$ cm^{-3} for shifting plasma effects toward deeper IR cannot be considered here since conductivity (σ) becomes so low that it cannot be compensated by an increase of μ, even if monocrystalline layers – almost free of grain boundaries – would be used.

Regarding the preparation of ITO thin films, many different strategies, most of them based on PVD techniques, such as electron-beam evaporation [164], magnetron sputtering [165,166], or pulsed laser deposition [167], have been reported. However, these processes generally require heating the substrates at relatively high temperatures (>300°C) to ensure reasonable conductivity, which can lead to remarkable transmission drops, formation of intermixed layers, adhesion problems of the coatings, and substantial increase of production costs at industrial scale. Thanks to the great deal of control of the ion energy, flux and species combined with the possibility to operate at low pressure, ion beam sputtering (IBS) appears as an alternative and attractive technique for low-temperature deposition of ITO films with excellent properties ($\rho = 1.5 \times 10^{-4}$ Ω cm, visible transmittance > 80%) [168,169].

In addition to the choice of the growth process, the geometry is also an important parameter to take into account with a view to improving the film properties. In particular, oblique angle deposition of ITO thin films has been proposed in order to improve the transparency in the visible range and induce optical anisotropy [170–175]. Moreover, the OAD approach is of special interest when seeking to improve transparency in the near-infrared (NIR) range, close to the plasmon absorption edge, even at high electron doping. In this way, some studies report the OAD deposition of nanostructured ITO films by means of electron-beam evaporation [175–177] or magnetron sputtering [178,179]. However, there were not found works dealing with IBS deposition of ITO in the oblique geometry to date.

To fill this knowledge gap, with the ambition of achieving tin-doped indium oxides with controlled nanostructure and endowed with enhanced antireflective capabilities in the NIR range, without compromising too much the carrier density, this PhD Thesis investigates the possibilities offered by the fabrication at room temperature of ITO thin

films by combining IBS, using either Ar or Xe ions, and OAD processes. Special emphasis is placed on the relationship between the resulting physical properties (optical and electrical) of the deposited columnar ITO films and some vital details of their nanostructure such as the morphology, composition and porosity, as well as their crystallinity, grain size and orientation, or the amount of defects. For this purpose, comprehensive descriptions of the structure of these porous ITO layers are conducted combining advanced (S)TEM techniques with complementary SEM and XRD analyses, whereas the functional characterization of such systems is performed through vis-IR SE and spectral reflectometry.

3.4. GaN nanostructures

Due to its excellent properties, such as a wide direct and tunable band gap of 3.4 eV at room temperature, both thermal and chemical stability, high breakdown electric field and carrier mobility, GaN has become a reference material for optoelectronic and electronic applications in laser diodes (LDs), LEDs, FETs and sensors [180–183]. In recent years, GaN structures of controlled sizes, shapes and porosities have been shown to lead to superior optical and electrical properties than those obtained for traditional compact thin films [49,184–187]. In this way, GaN nanostructures such as wurtzite or zinc-blende nanotubes (NTs), nanowires (NWs) and nanorods (NRs) have been lately synthetized by methods as diverse as catalyst-free chemical vapor deposition (CVD) [188], or plasma-assisted molecular beam epitaxy (PAMBE) [189,190]. In turn, these one dimensional (1D) nanostructures can be found as single systems [191,192] or forming vertically-aligned porosity-controlled arrays [193–195]. Other potential GaN-based nanostructures are high surface area GaN nanoporous films (NPFs) attained by etching processes, which have also succeeded in enhancing properties in photoelectrochemical

water splitting [50,51] or supercapacitors for energy storage [52]. Hence, in the light of the above considerations, the best approach would be one that takes advantage of the benefits offered by GaN NTs, NWs or NRs and the technological attractiveness of NPFs, which can be achieved by synthesizing 1-D GaN nanostrucutures in a closed-packed manner that emulates the behavior of a NPF.

Conversely, the control over the porosity and shape of one dimensional GaN arrays lies in the precise control of growth parameters. For the specific case of 1D GaN arrays grown by PAMBE, it has been proved that the size, density and shape of such GaN nanostructures, and thus the optical and electrical properties of the film, strongly depend on substrate temperature and spontaneous nitridation as well as Ga, N and dopant fluxes during the growth [196–199]. As a result, it is essential to accurately know the structure of these arrangements at different levels, since this will not only help to a better appreciation of the mechanisms behind the formation of these nanoarchitectures but also to optimize growth processes according to the property or characteristic to be enhanced. In this context, (S)TEM microscopy is a powerful tool to obtain valuable insights into the structure and chemistry of 1D GaN nanostructured arrays. Although TEM methods have been successfully applied to unravel the mechanisms responsible for the singular morphology, shape and tilt of GaN NTs and NRs [196], it must be highlighted that most of the relatively few TEM-based studies found in the literature for arrays of 1D GaN nanostructures are limited to conventional and high-resolution TEM imaging [47,189,192,200].

Another important issue to be addressed is the functional characterization of these GaN nanostructured films. While the optical characterization of GaN arrays through SE [137], polarized-goniometry [201], or reflectivity spectroscopy [193] is well reported in the literature, the characterization of electrical properties related to conductivity, like

carrier concentration and mobility, presents some difficulties associated with the geometry of this kind of structures [202,203]. Up to now, the majority of the studies are focused on Hall effect and field effect measurements performed on single nanowires after fabricating multiple contacts [192,204–206]. Nevertheless, given the challenges aforementioned, very few studies based on the electrical characterization of complete 1D nanostructured films have been reported so far [207–209]. Therefore, the development of novel and alternative methodologies for the electrical characterization of these GaN arrays, such as noncontact THz spectroscopic measurements [210], is crucial.

In order to contribute to the development of GaN nanostructured films of controlled porosity, helping not only to improve growth processes but also to optimize their resulting optical and electrical properties, the present PhD Thesis purposes original methodologies for the advanced structural, compositional, optical and electrical characterization of PAMBE GaN NW arrays based on (S)TEM methods, FIB tomography, vis-IR SE and Hall effect measurements.

3.5. Thermochromic vanadium dioxide films

As mentioned in previous chapters, VO_2 is currently the most promising material for smart windows and switching electronic applications due to its thermally induced reversible metal-to-insulator transition (MIT) at near room temperature (~68 ºC), which is accompanied by dramatic changes in its optical properties in the near-IR range, from a low temperature transparent monoclinic (M1) phase to a more heat blocking rutile (R) phase at high temperature. For this reason, VO_2-based systems, fashioned in many different ways such as thin films, nanoparticles, NWs or microtubes, have been recently studied and developed [64–66,211,212].

In particular, for energy conservation applications, VO_2 thin films have stood out as the most suitable and straightforward alternative to directly coat glass substrates mounted in buildings [213]. Many different approaches, such as sol-gel [214], pulsed laser deposition [215,216], chemical vapor deposition [217], and polymer-assisted deposition [218], have succeeded in synthesizing VO_x films with high VO_2 yields, although the complexity and high cost involved in all these methods, which is closely linked to the complex chemistry of vanadium and its large number of stable oxidation states, become a critical limitation for practical applications. In this context, reactive direct current (DC) magnetron sputtering postulates as one of the most promising and simplest PVD techniques for depositing large-areas of vanadium or vanadium oxide films at low temperature [67,219–223], so that by adjusting oxygen injection times during the sputtering process, the proportions of V to O on the films can be controlled. As can be found in the literature [12,219,221–224], many different post-deposition annealing strategies, which are required to obtain VO_2 coats with desired compositions and morphologies, have been extensively implemented on magnetron sputtered V or VO_x films. However, several of these post-annealing treatments sometimes lack of precise control of key oxidation parameters like reaction temperatures and times or heating and cooling rates, either omitting or not proving accurate data on them, which seriously compromise their reproducibility. Others however, have the disadvantage of rigid experimental conditions that implies controlled O_2, N_2 or SO_2 partial pressures at high temperatures (> 450ºC) for reaction times longer than 1 hour. Therefore, the development of a simple, fast and cost-effective thermal treatment to carry out the effective oxidation of vanadium or vanadium oxide films for the fabrication of thermochromic VO_2 coatings has become a crucial issue.

Among the different limiting factors in the large-scale commercialization of VO_2-coated smart windows, the insufficient luminous transmittance (T_{lum}) in the visible rage becomes one of the most critical one, with typical reported values of about T_{lum}=30-50% or less [225], which are still quite far from ideal visible transmission above 60-70% for architectural and vehicles glazings [213,226]. A well-known strategy to overcome this restriction consists in engineering the morphology of VO_2 at micro- and nanoscale to attain ARCs. Some works have reported that the introduction of porosity can improve the antireflectivity properties of VO_2 coats, thanks to a modulation of the optical constants (n, k), leading to T_{lum} values higher than 40% [227–229]. In this sense, the manufacturing of porosity-controlled VO_2 thin films by OAD methods, which, as seen in previous sections, have been proved to succeed in finely tuning the refractive index of coatings to achieve excellent antireflection performances, are called to be the most suitable alternative to mitigate this problem. Besides, as a consequence of their high surface area, the enhanced reactivity of OAD coatings can result in an additional appeal for the synthesis of VO_2 ARCs through the fast oxidation of pure vanadium-based nanostructured films. However, very few works have tried to exploit the potential of OAD systems applied to VO_2 thermochromic coatings to date [26,219].

With regard to the characterization of these VO_2 thin films, although optical and electrical properties as well as MIT responses have been widely reported through temperature dependent resistivity [71,219] and vis-IR optical transmittance [217,220,230] measurements, structural and compositional characterizations are generally restricted to low magnification SEM and AFM micrographs or XRD, Raman and XPS analyses [73,214,216,220,231,232]. For that matter, it should be noted that both XRD and Raman techniques do not give local but global information about the coating, whereas XPS only provides quantitative information about the first 1-5 nm of layer

thickness. This translates into a significant lack of knowledge of the structure and composition of such VO_2 films at nanoscale, which is key not only to enhance deposition processes and subsequent thermal treatments, but also to optimize functional properties of the coating.

Covering all the aspects reviewed in this section, this Thesis describes a simple and straightforward post-deposition thermal treatment strategy for the effective oxidation of sputtered V or VO_x films deposited at oblique angles in order to obtain thermochromic VO_2 films of controlled crystallinity and grain size. To achieve this, SEM, Raman spectroscopy and (S)TEM techniques such as EELS and HRTEM, are used to evaluate in a pioneer manner the structure and composition such coatings at micro-, nano- and atomic scale, while MIT responses are investigated by temperature dependent Kelvin probe force microscopy (KPFM) measurements.

Chapter 4

Joint discussion of the results obtained in the different papers

4. Joint discussion of the results obtained in the different papers

As it has been introduced in previous chapters, the performance of materials currently used in infrared light detection and thermal imaging devices, like silicon and germanium, are significantly limited to the important light losses by reflection (>30%) due to their high refractive indexes. A simple way to overcome this issue consists in the nanostructuration of Si and Ge thin films by means of OAD methods accomplishing broadband ARCs on top of the optical elements. Nevertheless, such OAD nanostructures can also be subjected to limitations arising from their porosity. In particular, their large specific surface areas make them more reactive to environmental exposure, leading to the degradation of the device performance. In this light, Publications I and II deal with the design and optimization of nanostructured Si and Ge OAD antireflective coatings (ARCs) for the treatment of silicon-based optical components operating in the MWIR range (3.7–4.8 μm).

Publication I reports the studies of oxidation under atmospheric conditions of silicon and germanium single OAD layers made of slanted nanocolumns deposited by electron-beam evaporation. This work focuses on some features of the fabricated films such as the influence of the structure and the morphology on the oxidation rate, the effect of oxidation in their IR optical performances as well as the experimental validation of such oxidation and its extent by (S)TEM spectroscopy techniques. First, the porosity and the optical constants of Si and Ge OAD samples have been determined by means of infrared SE measurements using optical simulations based on the Bruggeman effective medium approximations (BEMA) [233], which predict that both Si and Ge porous layers are susceptible to oxidation, as previously reported in the literature [134,135], and water adsorption. Besides, studies performed on Si and Ge OAD 1 μm thick layers deposited in

a range of incidence angles from 60° to 82° have shown that the oxide and porosity percentages increase with respect to the incidence angle while the water amount decreases. This latter could be explained by an increase in the surface roughness with the deposition angle, which is also related to an increase in the water contact angle that makes the surface of the films more hydrophobic [234,235]. Thereafter, the effect that oxidation and water adsorption have on Si and Ge infrared optical properties was evaluated by optical transmittance spectroscopy. In this sense, BEMA simulations carried out by taking into account the presence of silicon or germanium plus voids and pollutants (oxidized species and water) have shown better fits but worse optical behaviors, revealing that the presence of pollutants generates absorption peaks that are significantly detrimental for the long wavelength infrared (LWIR) transmission window (8–14 μm). Nevertheless, these absorption bands observed in Si and Ge OAD systems are fortunately outside the MWIR range and, therefore, are not expected to degrade too much the AR performance in MWIR optics.

Additionally, XPS surface elemental analyses have evidenced that such oxidation is due to the formation of Si and Ge dioxides, while compositional analyses carried out by STEM-EDX have confirmed the widespread oxidation (macroscopically homogeneous but inhomogeneous at the nanoscale) of these thin films in proportions rather close to the predicted by the SE model. In order to go a little further in the characterization of the related nanostructures, local STEM-EELS quantitative analyses conducted in a Ge OAD film deposited at $\alpha = 75°$ have let us prove the formation of core-shell-type nanostructures, consisting of pure Ge surrounded by GeO_2, as a consequence of the superficial oxidation of germanium mesoporous architectures (Figure 1). Finally, STEM-EDX experiments carried out on samples undergone to different vacuum and water-free conditions have determined that the oxidation of these systems is mainly due to

spontaneous atmospheric oxidation because of air exposure, which can be slightly accentuated during water-based polishing TEM sample preparations as a consequence of the partially open porous structure of OAD layers. Therefore, the insights obtained through (S)TEM studies not only allowed us to validate the BEMA models used to describe the optical behavior of the system studied but also to collect accurate valuable information about the morphology, distribution, and composition of the nanocolumns that are part of OAD films to finally unravel the surface oxidation process of these architectures at the nanoscale.

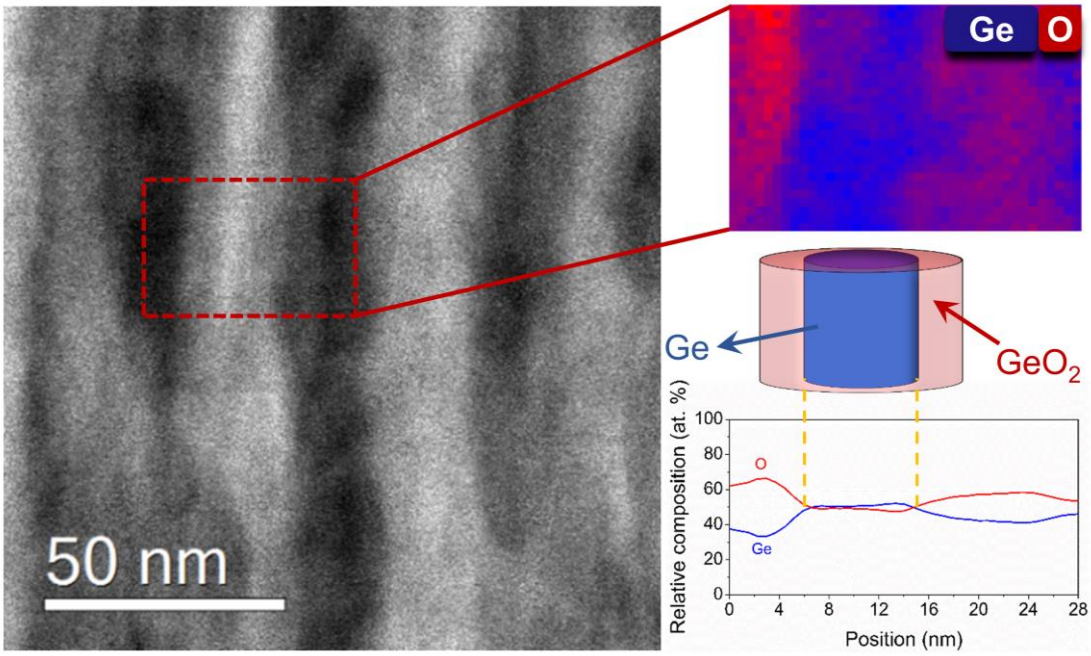

***Figure 1**. STEM-HAADF image and Dual-EELS Ge-versus-O composition map of an isolated Ge column along with its averaged compositional profile and the core-shell model proposed.*

In **Publication II**, the design and fabrication of a simple and highly efficient ARC in the MWIR region using the oblique angle deposition process have been addressed. Likewise, the role of important nanostructural and chemical aspects influencing the performance of such ARC has been considered based on studies by advanced (S)TEM methods, IR spectrophotometry, ellipsometry and optical simulations. Taking into

account fictive materials with effective refractive indexes, the design of a simple discrete bilayer ARC for a silicon substrate (both sides treated), consisting of two layers having refractive index target values of 2.52 and 1.37 and thicknesses target of 427 nm and 779 nm respectively, with 99.97% transmittance over the 3.7–4.8 μm atmospheric window has been simulated by using the commercial SCOUT software [236]. Among the materials able to meet these requirements, germanium has been chosen for the deposition of the first layer (n = 2.52) due to its large transparency in the infrared region as well as its high refractive index, which potentially permits to cover a wide range of effective refractive index using OAD geometries [153].

To reach a refractive index close to the design value, a calibration step of the effective refractive index obtained for Ge OAD is necessary. For this purpose, different germanium OAD films, deposited at angles ranging from 0º to 82º and fixed thicknesses of about 427 nm, have been studied by means of IR SE and optical transmittance spectroscopy. The observance of the refractive indexes extracted from BEMA approximations, considering the insertion of voids in the Ge layer to reproduce film porosity, determines that the Ge OAD layer deposited at 65° leads to the closest refractive index, even with slightly enhanced AR performance (n = 2.40), compared with the designed target. On the other hand, with the additional aim of ensuring the mechanical and chemical stability of the ARC as well as to minimize the adsorption or absorption of environmental pollutants, a second dense MgF_2 capping layer has been deposited in order to provide a refractive index in the MWIR that perfectly matches with the ideal one (n = 1.37).

At this stage, some chemical aspects of this study are considered. In this sense, as evidenced in Publication I, IR SE, spectrophotometry and STEM-EDX analyses have pointed out the remarkable presence of pollutants in the Ge OAD layer, more particularly GeO_2 and water, which lead to a degradation of the optical efficiency of the ARC in the

IR due to light absorption, especially in the LWIR region. More specifically, STEM-EDX analyses have provided relevant compositional information of the bilayer, not only confirming the generalized and slight oxidation of the Ge OAD (54 at.% of O) and MgF_2 (3 at.% of O) layers, respectively; but also evidencing the formation of an intermixing layer of about 50 nm thick at the interface between the Ge OAD and MgF_2.

Once highlighted the key role of the chemistry on the optical properties of the Ge OAD/MgF_2 system, a new bilayer has been fabricated in which the bottom Ge OAD layer has been annealed at 200ºC before being capped with MgF_2 to prevent water adsorption. This new optimized ARC presents a high maximum transmittance of 99.21% and very good average transmittance of 98.56% over MWIR, showing a better optical performance than typical commercial coatings (98% average transmission over 3.6–4.9 μm [237]) and similar efficiency compared with the best MWIR AR coating reported in the literature for Si and Ge optics [35]. Moreover, *in-situ* optical measurements conducted during vacuum annealing have showed that, simply by evaporating water, the performances of this ARC can be enhanced to 99.17%. However, water is readsorbed when exposed to atmospheric pressure. Finally, the set of all the information obtained through optical measurements and (S)TEM methods (presence of GeO_2, water, intermixing layer), not only has helped to establish and validate an advanced realistic model capable of simulating the optical response of the system, but also to point out the role of unwanted contamination (spontaneous surface oxidation and water adsorption) on the way toward perfect MWIR transparency.

Again on the basis of OAD approaches to attain antireflection surfaces, Publications III and IV describe the design, structure, optical behavior and modelling of a discrete broadband ARC aimed at covering a wide spectral range from the visible up the near infrared (NIR). This system consists in a SiO_2 bilayer deposited at oblique angles (α_1 =

65º; α_2 = 85º with an azimuthal rotation of Φ = 180° in between the layers) by electron-beam evaporation on a BK7 (optical glass) substrate (both sides coated). In the first instance, **Publication III** focuses on the study of different systems and routes to optimize the transparency, the design of the aforementioned bilayer system (which is carried out in the same way as in Publication II), as well as in the development of a method based on finite-difference time domain (FDTD) simulations to calculate the light scattering losses of these ARC nanostructures. In this sense, the complex 3D geometry of the SiO_2 bilayer system, whose knowledge is fundamental to accurately simulate the scattering cross-section of such ARC, has been experimentally determined from STEM-HAADF electron tomography experiments (see Figure 2(a)). The very good agreement between the experimental and simulated spectra confirms that this innovative approach combining the implementation of realistic 3D sample geometry with advanced simulation of light propagation is appropriate to account for optical losses, which are attributed to light scattering in the specific case of the SiO_2 bilayer.

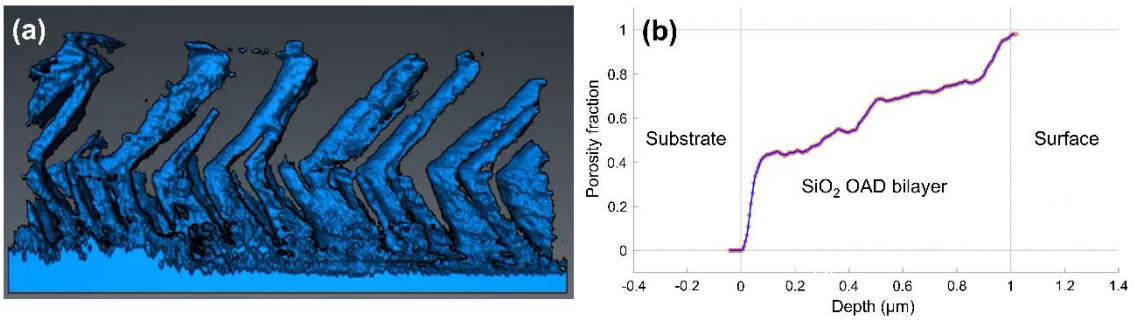

***Figure 2**. (a) 3D reconstruction of the SiO_2 OAD bilayer obtained from STEM-HAADF electron tomography experiments together with (b) its extracted porosity/depth profile.*

This same method has been used to evaluate the scattering behavior of gradient refractive index ARC SiO_2 moth eye [144] pyramid nanostructures of different width (w) and thickness (t), demonstrating that these systems must be sufficiently thick, at least 500 nm, to reach mean transmittance as high as that obtained for the SiO_2 OAD bilayer: 304 nm total thickness exhibiting a mean transmittance of 98.97% over the vis-NIR range

[400-1800 nm], which is quite close to the designed value (99.03%). From these simulations, it is concluded that, to limit scattering and keep on enhancing the transmittance, thick moth eye nanostructures with a high aspect ratio (t/w = 20) must be manufactured. However, such nanostructuration becomes challenging from a technological point of view, since the etching processes normally used to manufacture such architectures offer limited control over their widths. Therefore, this demonstrates that the development of discrete ARCs by the OAD approach should be preferred due to its simplicity to produce and provide high optical performances.

Conversely, **Publication IV** accounts for the optical and nanostructural characterization and modelling of different SiO_2 OAD systems which have been fundamental to develop the previously referred SiO_2 bilayer ARC. In agreement with the trends reported in the literature [156,238–241], the rise of both columns angle and porosity with respect to the deposition angle and film thickness, respectively, as well as the increase of the structural anisotropy and columnar broadening with the film thickness have been evidenced through cross-sectional and top-view SEM micrographs acquired from a series of SiO_2 samples deposited at different angles and thicknesses. On the basis of these key morphological features, an Anisotropic Bruggeman Effective Medium Approximation (ABEMA) optical model has been built [242] which incorporates a porosity gradient composed by 20 layers of variable porosity to reproduce the behavior observed at the microscopic scale. This method is then applied to model the generalized SE and transmittance optical spectroscopy measurements performed in different SiO_2 monolayers systems, revealing a good agreement between the simulations and the numerous optical and structural experimental data collected.

Once this approach was validated, a new bilayer model is used to optimize and describe the optical response of the SiO_2 bilayer ARC, establishing that, during the second

deposition, no material is deposited within the porosity of the first layer, and also taking into account the Φ angle between the first and the second layer. To get a precise comparison between optical properties and microstructure, STEM-HAADF electron tomography experiments (previously reported in Publication III) have been used for further quantitative extraction of the porosity gradient within the entire ARC (Figure 2(b)). The very fine agreement between the experimental porosity profile and that extracted from advanced optical simulations not only demonstrates the validity of the optical model used in this work, but also provides a simple and reliable way to describe the porosity profile of the system. This new type of information is crucial for further optimization of the optical design, by considering the porosity gradient naturally present in the OAD layer to optimize the optical function of such ARCs.

Publication V describes the nanostructure and physical properties of ITO OAD films prepared at room temperature, with varying $\alpha = 50°$, 70º and 85º, respectively, through ion beam sputtering using either argon or xenon ions. At first, SEM and (S)TEM micrographs evidence the two-layer character of each film where a dense layer presenting a uniform HAADF contrast is always detected, even for the greatest deposition angles, in the bottom part of the films. Moreover, as can be appreciated in Figure 3, the extension of this compact layer as well as the morphology of the entire film depend on both the deposition angle and the type of ions. (S)TEM-EDX elemental analyses performed on the Ar- and Xe-based films deposited at different angles have revealed a uniform distribution of indium, oxygen, and tin species, in concentrations very close to the nominal values. Nonetheless, it has been detected that ITO Ar-deposited films, in addition to presenting remarkable oxygen fluctuations, tend to trap small amounts of Ar (≥ 0.7 at. %) during the IBS process, which has been reported many times in other works [243,244].

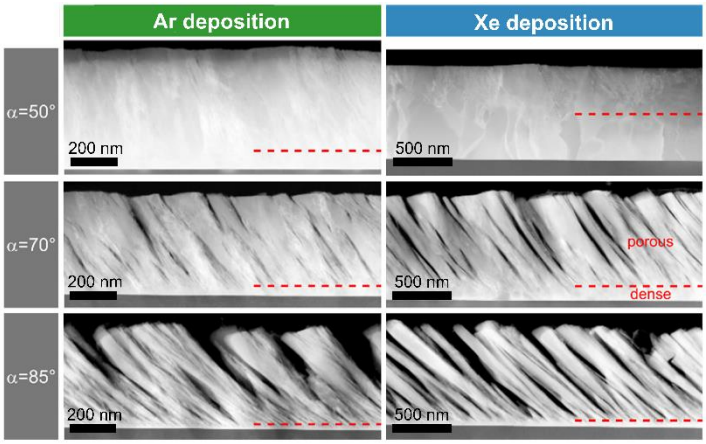

***Figure 3**. STEM-HAADF cross-sectional views of ITO films deposited during 120 min in different conditions. The dashed lines highlight the interfaces observed at high deposition angle between the bottom dense layer and the potential top porous layer (note here that the scales are different for Ar-deposited and Xe-deposited films).*

Further XRD and TEM experiments have determined that the structure and texture of the different samples are strongly affected by the deposition angle and the type of ions. In this sense, it has been observed that, although almost all the films are mainly (111)-textured, which is preserved over the full α range in the case of Ar deposition, a progressive switching in the preferential growth planes from (222) to (400) is detected for Xe deposition as α increases. Likewise, it has been realized that the 222 XRD reflection for both sets of Xe and Ar samples presents a slight shift of about 0.2−0.3° and 1° toward smaller 2θ values compared to the pure In_2O_3 cubic-C phase, respectively, which may be attributed to an increase of the lattice parameter due to the larger repulsive forces provided by the substitution of Sn^{4+} ions on the indium sites [245,246]. Bright-field and HRTEM images of ITO layers have also pointed out that IBS deposition with Xe leads to a better crystallinity (larger grains, lesser amount of grain boundaries, intragrain defects, and perturbed regions) than with Ar. On the other hand, reflectance optical spectroscopy measurements not only evidence an overall decrease of the reflectance in the visible range for both Ar- and Xe-deposited films as deposition angle increases, but also predict a much smaller carrier density in Ar-deposited layers (the onset

of free-carrier absorption appears at around 4 μm for Ar- and 2 μm for Xe-deposited films).

To go deeper into the understanding of these systems, an optical model has been developed and fitted onto the experimental data collected by UV-vis-IR ellipsometry and reflectance spectroscopies. In this way, the optical properties of ITO have been reproduced using a three-oscillator model: (i) a Tauc-Lorentz oscillator (TLO) centered close to 3.5 eV ($\lambda g \approx 360$ nm) modeling the direct band gap absorption of ITO; (ii) a Gaussian oscillator (GO) arbitrarily centered out of the measurement range at 8 eV to model all UV interband transitions; and (iii) a Drude oscillator (DO) modeling the free-carrier optical behavior in the NIR range. The best fits for the optical model are achieved when dividing the ITO film into two sublayers: the first sublayer at the bottom is always considered as compact, while porosity can be introduced in the second top sublayer in the framework of a BEMA approximation. In this sense, the optical constants in the UV-vis range (TLO and GO parameters) have been considered the same for both layers, while only the DO parameters (N and μ) are allowed to differ between the two sublayers. The good agreement between SEM and TEM analyses confirms that the two-layer optical model is suitable and physically meaningful to describe the optical properties of the OAD-IBS ITO films, as well as to extract other critical parameters such as porosity, refractive indexes, and in-grain carrier densities and mobilities. N and μ couples sourced from the optical model demonstrate the superior electrical behavior of Xe-deposited ITO films, which is in accordance with their higher crystallinity [247,248].

Finally, Monte-Carlo simulations, performed to reproduce the IBS experimental conditions, have supported the assumption that the significant difference between the morphology and crystallinity of ITO layers deposited with Ar and Xe is associated to the fact that ions with lower masses, such as Ar, are more subject to backscattering on the

target and are also more energetic, making Ar ions more prone to amplify the "atomic peening" effect and induce an "intrinsic" ion assistance during deposition. Overall, it has been concluded that, for transparent and conductive optical applications that would require a good compromise between broad-band antireflective capabilities over the extended visible range and electrical transport, deposition with Xe must clearly be preferred to Ar.

Moving to a different kind of porous surface, Publications VI and VII cover the fabrication, optimization and characterization of porosity-controlled GaN NW arrays grown on p-type Si(111) or (100) substrates by plasma-assisted molecular beam epitaxy (PAMBE). In order to explore the effect that the growth parameters have on the morphology, overall porosity, and optical properties of the resulting GaN-based systems, high-quality single crystalline GaN NW coats have been fabricated under different conditions of temperature (T_{subs}) and gallium (ϕ_{Ga}) and nitrogen (ϕ_N) fluxes (**Publication VI**). First of all, with the preliminary purpose of examining the effect of substrate orientation, the morphology and structure of samples referred as T2 and T2' (both growth at T_{subs} = 825ºC, $\phi_{Ga} = 8 \times 10^{14}$ at cm^{-2} s^{-1}, $\phi_N = 11 \times 10^{14}$ at cm^{-2} s^{-1}, but on Si(111) and Si(100) substrates, respectively) have been examined by means of SEM and (S)TEM microscopies. Cross-sectional and plan-view SEM micrographs not only show that these columnar nanostructures are grown straight and parallel to the surface normal direction on both substrates but also that the top morphology of these two specimens is a combination of solid NWs (SNWs) with well-developed hexagonal facets, most likely *m*-planes, hollow NWs (HNWs) with a hexagonal to dodecagonal shape, most likely a mixture of *m*- and *a*-planes, and c-shape NWs partially opened longitudinally.

Since the intensity on the HAADF images is proportional to the product of the effective atomic mass (the higher, the brighter) and the quantity of projected material,

STEM-HAADF cross-sectional studies have been carried out to elucidate up to which extent the nanostructures are hollow or solid. In this light, it has been found a higher HAADF intensity at the base of the nanostructures than at the tips, suggesting that the nanostructures bases (closer to the substrate) are more compact than at the tips of the HNWs and CNWs. The analysis of the HAADF intensity along what seems to be an individual HNW reinforce the idea that most of the uncompact NWs are actually composed by solid bases (or initially SNWs) that evolve some of them into hollow or most of them into c-shape structures as the growth proceeds.

Further insights into the nanostructure of T2 and T2' samples by HRTEM experiments show that single-crystalline wurtzite GaN S-, C- and H-NWs are grown with the *c*-axis perpendicular to the Si(111) and Si(100) planes, which coincides with results reported by other groups [189,200,249]. In the same way, the general epitaxial relationships between the GaN nanostructures and the underlying Si substrates collected through selected-area electron diffraction (SAED) patterns have been defined as GaN(0001)||Si(111) and GaN(10$\bar{1}$0)||Si(112) for GaN on Si(111), and GaN(0001)||Si(001) and GaN(11$\bar{2}$0)||Si(110) for GaN on Si(100). Figure 4 displays the plan-view HRTEM micrographs of single SNW and CNW together with their fast Fourier transform (FFT) (equivalent to a diffractogram), both indicating the 6-fold symmetry of the wurtzite crystal structure in the polar [0001] direction. As can be seen, while the SNW shows a well-developed hexagonal shape with {10$\bar{1}$0} side facets, the CNW shows five {10$\bar{1}$0} external side facets (parallel to the internal ones) together with a sixth opened one, forming an open hexagon with wall thickness of about 30 nm.

Once HNWs and CNWs have been identified and studied, it was time to find out what is the mechanism behind the formation this kind of structures. According to previous works, it could be due to three different explanations: firstly, the screw dislocation driven

model [196,250], which has been discarded because of the very low percentage of screw dislocations found after carrying out TEM studies in two-beam diffraction-contrast conditions; secondly the reduction of the nucleation barrier along the NW top facet boundary by introducing high Si-flux [197], which is not applicable in this case because of the absence of such silicon flux; and lastly, the growth under a locally Ga-limited regime [251,252].

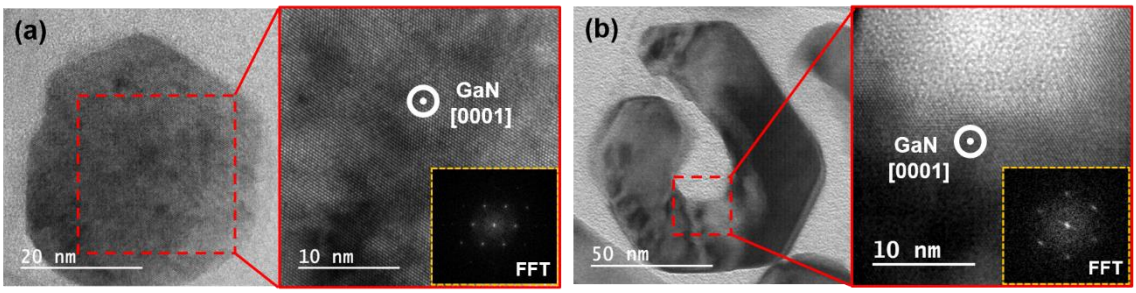

***Figure 4**. Plan-view HRTEM micrographs of a (a) SNW and a (b) CNW registered along their [0001] GaN zone axes. FFT images of both top-view HRTEM micrographs of the SNW and the CNW are shown in their respective insets.*

In order to consider this third mechanism, a comprehensive study of the influence of growth conditions on the morphology of these nanostructures has been performed. The observation of top view SEM micrographs of samples grown under different conditions allowed us to determine that, when Ga flux is smaller than the nitrogen flux, three competing processes take place: (i) the incorporation of Ga atoms on the top facets; (ii) the evaporation of Ga atoms from the top facet (*c*-plane) and side-walls (*m*-planes); and (iii) the incorporation of atoms on the *m*-plane to *c*-plane edges leaving a mixture of S-, H-, and C- NWs.

To conclude, taking advantage of methodologies developed in previous studies, vis-NIR SE analyses have been performed on three samples tagged as N3, N4 and N5 (all of them grown on Si(111) at T_{subs} = 850ºC and ϕ_{Ga} = 11 × 10^{14} at cm^{-2} s^{-1}, but at different nitrogen fluxes of ϕ_N = 19, 22 and 27 (× 10^{14} at cm^{-2} s^{-1})) to prove the impact of growth

under Ga-limited conditions on both the total porosity and the evolution of the optical constants along the thickness layer. For this purpose, the original BEMA model has been enhanced by separating the in-plane (X, Y) and out-of-plane (Z) optical responses (uniaxial anisotropy), whereas, to describe the columnar morphology of these nanostructures [135,253,254], the out-of-plane depolarization factor has been fitted to $q_z \approx 0$. The defined model shows a good agreement for the modeled and the experimental spectra, letting us know some further information about the studied systems. For instance, thanks to the increase of porosity arising from the identified NW morphologies, it has been observed that all these samples present a progressive refractive index decay (from the substrate to the surface) at 500 nm, which make them ideal for AR applications in the visible range. Besides, it is noticed that such refractive index decrease is more pronounced for greater MBE N_2 fluxes, which is directly related to the effect of the total density of nanostructures and the SNWs to CNWs proportion. In this sense, N4 and N5 samples present a faster drop in *n* within the first 100 nm, which could be related to the aforementioned structural change from SNWs to CNWs. This demonstrates that, by tuning the growth conditions, the density and shape of the nanostructures, and thus the porosity and optical performance of the array, can be finely controlled.

In this same line, **Publication VII** reports an original and straightforward method for the simultaneous optical and electrical characterization of such GaN nanowire arrays through vis-IR SE. With the additional purpose of examining the effect of substrate orientations on optical and electrical properties, this study is exclusively focused on the previously identified T2 and T2' samples. Firstly, because the presence of solid and hollow GaN NWs in different proportions makes the porosity profile along the Z direction uncertain and nonlinear, which in turn hinders the optical characterization of these systems, focused ion-beam (FIB) tomography experiments have been performed. Figure

5 illustrates the 3D reconstructions of representative areas of T2 and T2' samples together with their extracted porosity/depth profiles. Once more, the characteristic morphologies of GaN NWs (SNW, HNW, and CNW) are disclosed. As in Publication VI, the shapes of these two profiles only can be explained by considering that nanowires are composed by solid (filled) bases that evolve (or not) into hollow structures (HNW or CNW). On the other side, the initial drop in porosity in sample T2' has been associated to a possible the broadening of solid bases after attaining 100–150 nm of thickness.

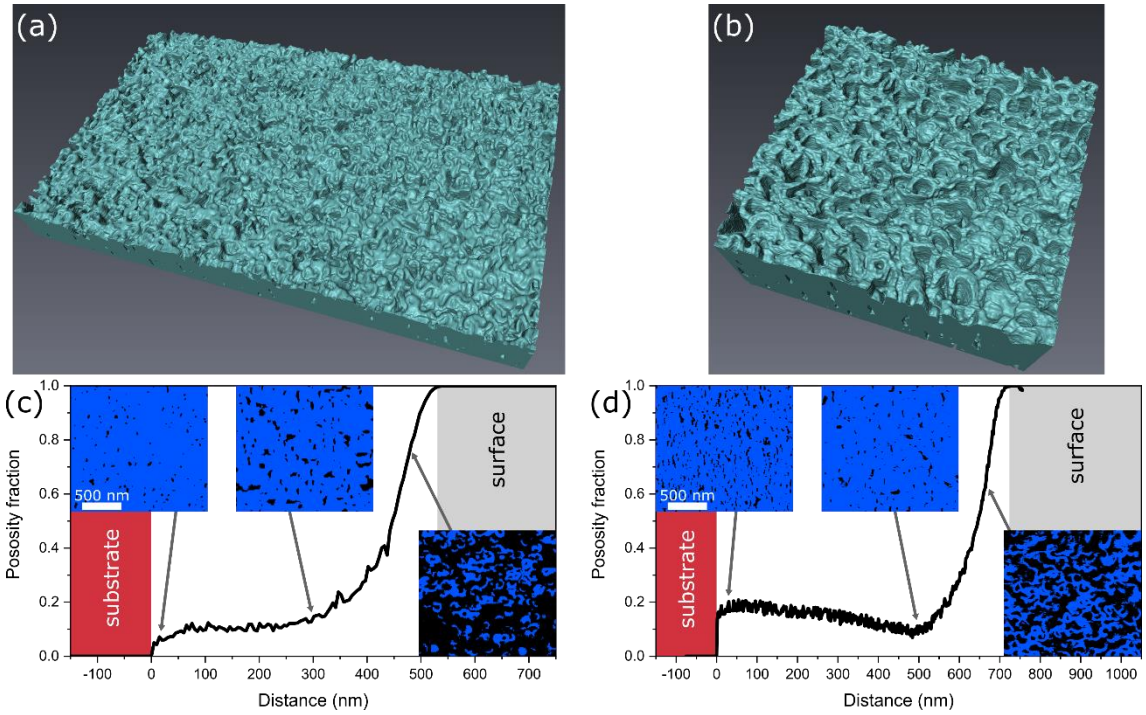

***Figure 5**. 3D reconstructions of the NW arrays in (a) T2 and (b) T2' samples through FIB tomography (slice and view). Porosity profiles of (c) T2 and (d) T2' samples extracted along the surface normal together with some planar views obtained by data segmentation at different depths.*

Thereafter, vis-IR SE measurements have been performed on T2 and T2' samples, which have then been fitted to an ABEMA model (similar to that defined in Publication VI) composed by a mixture of wurtzite GaN, whose optical constants have been modeled by those obtained from the literature [255], and voids. Nevertheless, although after incorporating the experimental porosity profiles this model has provided a fine agreement

to the experimental data in the visible range, it failed to reproduce the absorption in the IR range. In a similar manner as in Publication V, the optical constant of wurtzite GaN have been modelled by a multioscillator approach: (i) a TLO modeling the direct band gap (E_g) absorption of GaN [256], and (ii) a DO modeling the free-carrier behavior in the IR range [257].

The incorporation of these two oscillators to the ABEMA not only allows to improve the modelling of the IR oscillations, but also to determine, in addition to porosity, thickness, and optical constants, the carrier density and intragrain mobility of such nanostructures. In this sense, the N, μ couples extracted from the DO have evidenced the unintentional high doping level of both samples ($\approx 1 \times 10^{20}$ e^- cm^{-3}). Likewise, the N values measured for T2 and T2' samples by Hall effect measurements, which are directly comparable with those resulting from SE estimations, since they are not affected by the porosity [258], are in accordance with those predicted by ellipsometry, confirming the high n-doping level. With regard to electron mobility, great differences between the electrical behavior of T2 and T2' samples have been observed, with the T2' sample exhibiting a greater opposition to the flow of electric current than T2 (just over 1 order of magnitude). In this context, it should be noted that the reason why the mobility measured by Hall effect does not correspond with the one predicted by the SE model is because ellipsometry only provides information related to the free-carrier mobility within grains, while the Hall effect gives information about the total mobility of the layer, including the effects of grain boundaries as well as the porosity of the structure. Hence, the greater values of mobility predicted by the SE model, compared to those measured through Hall effect measurements, suggest that the mobility in GaN NW arrays is dominated (i.e. mostly affected) by intergrain barriers.

Further analyses by XRD, HRTEM and STEM-EDX support all these assumptions. The analyses of XRD rocking curves (ω and χ-scans) of 0002 GaN diffraction peaks for both samples not only indicate the good crystal quality of the NWs content in both samples, but also a more significant misorientation (although slight) in T2' than in T2, which explains its lower value of mobility obtained by the SE model. STEM-EDX elemental maps have revealed a remarkable presence of oxygen distributed throughout both films. Moreover, the fact that the oxygen signal becomes greater on the edges of the nanowires suggests that oxygen is mainly accumulated at NW surfaces. In addition, EDX qualitative analyses reveal that the amount of oxygen in T2′ is larger than the one detected in T2.

On the other hand, HRTEM micrographs recorded in individual NWs of T2 and T2' have evidenced the formation of amorphous layers of native oxide on their surfaces, being considerably thicker in the nanowire of T2' than that observed in the NW of T2. In the same way as in Publication I, this phenomenon is attributed to the spontaneous oxidation of these higher surface-to-volume ratio structures when exposed to air compared to compact GaN films. This issue has been previously reported by other authors [202,259], resulting in a detrimental effect on electrical properties since this oxide shell acts as a barrier for the motion of electrons among nanowires. According to similar studies [260,261], this fact might also provide an explanation for the high levels of electron concentration in these GaN nanostructures: part of the oxygen atoms could diffuse from the oxide layer into the GaN nanowire at room temperature, originating oxygen impurities. Furthermore, it has been proposed that both the native oxide layer formed on cylinder-like surfaces and porosity are the limiting factors on the global mobility of GaN nanowire array films. Finally, the nice agreement of the results predicted by the SE model with those obtained by combining Hall effect measurements, XRD, and (S)TEM, have

supported the validity of the proposed method, opening new horizons in the functional characterization of nanowire-based semiconducting layers.

Emphasizing the importance of the (S)TEM investigations conducted on the systems studied in previous publication, **Manuscript VIII** explores the possibilities that (S)TEM techniques provide to the study and development of porous nanostructured coatings. As mentioned in previous chapters, the fact that very few advanced TEM based studies were found for such nanostructured thin films, is closely linked to the difficulties encountered during the TEM sample preparation process of these uncompact and fragile coats.

In an attempt to lead the way for further TEM studies of porous nanostructured coatings, Manuscript VIII firstly addresses the challenging collection of electron-transparent lamellae of porous (multi)layers of different materials, architectures and hardness with methods of thinning down by tripod polishing plus ion milling, or focused ion beams (FIB). Throughout the manuscript, the viability of both approaches to collect electron-transparent regions of porous and delicate thin films has been evidenced, including recommendations (either based on own experience or on what has been reported in the literature) on which of the two alternatives to use depending on the type of (S)TEM study to be carried out. In this sense, since it has been the main preparation technique that has made possible the TEM studies included in this PhD Thesis, the role of the tripod polishing as a cheap and easily adaptable method for achieving good quality TEM preparations was highlighted. A proof of this is shown in Figure 6, in which the STEM-EELS relative thickness map of a SiO_2 OAD bilayer (Publications III and IV) prepared for TEM observations by means of tripod polishing plus ion-milling demonstrates that this approach offers extensive and homogeneous regions of electron transparency ($t/\lambda \approx 0.3$ over several microns, but extreme parts of the specimen exhibit reduced t/λ values) which is ideal to carry out a wide panel of (S)TEM experiments.

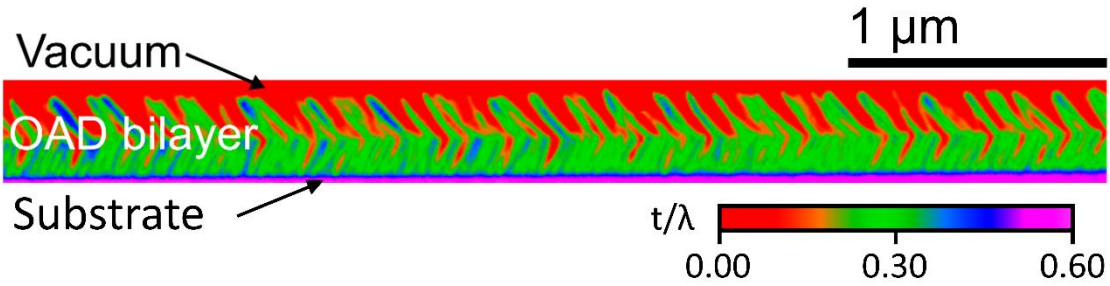

***Figure 6**. Large field-of-view (more than 4 μm width) STEM-EELS thickness-map of a SiO_2 OAD bilayer (about 300 nm thick). The colour scale represents the evolution of relative thickness of the specimen (t/λ) where t is specimen thickness and λ is the characteristic mean free path for inelastic scattering.*

Once this difficulty has been overcome, several advanced (S)TEM characterization techniques, such as HRTEM, STEM-HAADF, integrated differential phase contrast STEM (STEM-iDPC), STEM-EDX, STEM-EELS or ET, have been implemented to complete the study of some porous coatings. In this way, the implementation of new breakthroughs in (S)TEM imaging and spectroscopy has allowed us to accomplish some of the pioneering studies presented in this PhD Thesis, emphasising the versatility and capabilities that TEM methods offer to the extensive characterization of porous nanostructures. Issues, such as (i) the morphology, porosity, crystal structure and composition of individual columns or nanowires, local regions and entire layers; (ii) the nature, morphology, composition and thickness of transitions between layers; and (iii) the 3D reconstruction of such porous structures have been finely explored by (S)TEM methods, providing, at the same time, both local and overall data.

Based on the evidences shown throughout Manuscript VIII, it is intended to make materials scientists aware of the niche of opportunity that (S)TEM methods represent for the advanced characterization of porous nanostructured systems, opening new horizons, since they allow to examine the structure and composition of miscellaneous materials at scales and levels of detail that other techniques do not reach, simplifying methodologies, as they allow to obtain, by using a single equipment, equivalent results to those that could

be acquired thorough the combination of SEM, AFM, XPS and XRD analyses, and contributing to a better knowledge of growth mechanisms and properties of multimaterials.

Lastly, putting into practice the knowledge and methodologies acquired during the characterization and development of the porous systems previously studied, **Manuscript IX** reports an original strategy to attain thermochromic uncompact VO_2 coatings of controlled grain size and crystallinity by means of the initial deposition by DC magnetron-sputtering of vanadium or vanadium oxide films, combining the OAD and reactive gas pulsing process (RGPP) approaches, and the subsequent fast oxidation of such layers in air atmosphere at high temperatures and short reaction times.

In the first instance, taking advantage of the enhanced reactivity of such porous nanostructures, which are expected to lead to the selective and quasi-instantaneous formation of vanadium oxidized species, pure vanadium or vanadium oxide (VO_x) OAD films have been deposited on silicon substrates at $\alpha = 85°$, while oxygen has been pulsed during the deposition, varying the oxygen injection time (t_{ON}) from 0 to 8 s. In this regard, five samples have been deposited which were named as V0 ($t_{ON} = 0$s), V2 ($t_{ON} = 2$ s), V4 ($t_{ON} = 4$ s), V6 ($t_{ON} = 6$ s), and V8 ($t_{ON} = 8$ s). Afterwards, cross-sectional and planar view SEM micrographs have been acquired so as to evaluate the effect of the oxygen injection time on the structure and the morphology of as-deposited samples. Overall, it has been observed that as oxygen injection time increases, samples gradually become thicker and columns are more and more narrow, which not only promotes the connection between the columns but also leads to a decrease in the total porosity. Additionally, with the aim of disclosing the crystal structure and the predominant species present in the as-deposited films, V0 and V8 samples were prepared for TEM observations. As evidenced by SEM, the V0 overlayer presents a more porous structure when compared to that of V8. Also

noteworthy is the great difference between the column angles (β) values for both samples, being indeed double for the non-oxidized one (β = 52° for V0, and β = 26° for V8). Besides, HRTEM and SAED studies not only demonstrate that the V0 sample is crystalline after deposition at room temperature but also it is mainly composed by the pure vanadium cubic phase. By contrast, the vanadium oxide OAD layer (V8) presents a less crystalline structure constituted by a mixture of cubic VO and tetragonal $V_{16}O_3$.

Once disclosed the nature, morphology and structure of the as-deposited vanadium or vanadium oxide OAD films, their fast heating has been conducted. For the first series of thermal treatments, the only oxidation of pure vanadium samples has been performed, at fixed heating rates (h_r = 42ºC s^{-1}) and reaction temperatures (T_r = 550ºC), with reaction times (t_r) ranging from 1 to 300 s, followed by the subsequent instantaneous cooling in air. Raman spectroscopy analyses of these oxidized samples determined that, as reaction time increases, VO_2 (M1) peak signatures gradually become more significant, reaching a typical pure VO_2 (M1) signal for t_r = 45 s which perfectly matches with other Raman VO_2 spectra previously reported in the literature [262–265]. However, from this point forward, longer reaction times only promote the formation of the α-V_2O_5 phase (according to Ref. [265]), turning into the predominant phase for t_r > 75 s. The structure and morphology of all these annealed samples have then been explored by means of plan-view SEM micrographs, which have not only allowed us to appreciate a progressive widening of the grain size for reaction times between 1 and 45 seconds, but also to notice that t_r > 60 s leads to the gradual growth of these grains along the axial direction, emerging a kind of micro-rod structures randomly distributed in all directions which are characteristic of the V_2O_5 [266,267]. Cross-sectional (S)TEM images disclose that oxidation initiates on the surface of the film and progresses towards the substrate as the reaction time increases. Similarly, it is also evidenced that the OAD morphology disappears as the oxidation of

the film evolves. Further HRTEM and STEM-EELS analyses verify that the mosaic subgrain-line reaction product that progresses from the surface of the layer towards the substrate for $t_r \leq 45$ s, with thicknesses between 120 to 400 nm, is the thermochromic VO_2 phase.

Once known how oxidation develops for pure vanadium OAD films, a thermal treatment consisting in a fast heating ramp of 42ºC s^{-1}, followed by keeping a constant temperature of 550ºC for 45 seconds, and a final cooling down to ambient temperature by exposing in air atmosphere, has been systematically applied to V2, V4, V6 and V8 samples. Plan-view SEM micrographs of these oxidized layers reveal a mosaic structure, quite similar to those presented in the V0 sample subjected to $t_r = 45$ s, but with remarkable differences regarding the undesired appearance of V_2O_5 micro-rod bundles on the surface, as well as the cracking (sample V6) or the final detachment (sample V8) of the coating associated to residual stresses favored by thermal expansion mismatches between sublayers. In the same vein, the measured Raman spectra for V2, V4 and V6 samples (V8 sample could not be studied as result of its detachment and loss) show the characteristic Raman bands of the VO_2 (M1) phase together with other weaker signals associated to different V_2O_5 polymorphs. Nonetheless, TEM and STEM-EELS analyses confirm the good results obtained for the oxidized V2 sample, showing the formation of VO_2 (M1) multilayers of about 570 nm total thick (Figure 7(a)). In such way, it has been distinguished a most superficial sublayer composed by larger and single-crystalline VO_2 subgrains, and a second inner sublayer characterized by smaller grains. Finally, the remarkable surface potential drops at heating recorded by temperature dependent Kelvin probe force microscopy (KPFM) measurements of the best thermally treated vanadium or vanadium oxide (see Figure 7(b) as an example) samples, which are considerably

greater than those reported in the literature to date for VO_2 thin films [268], have confirmed the outstanding MIT electronic response of the resulting VO_2 (M1) films.

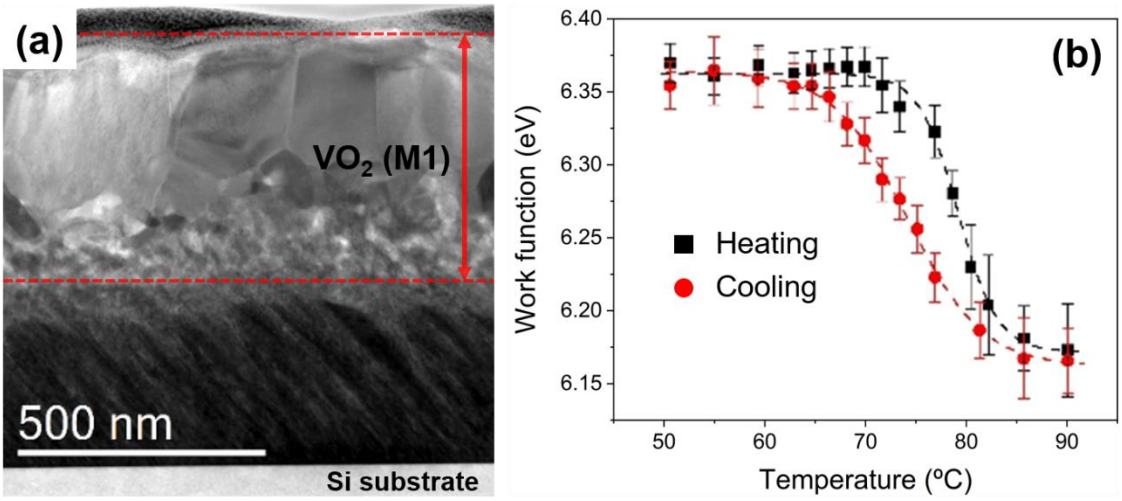

***Figure 7**. (a) Bright-field TEM overview of the V2 sample of VO_x after thermal treatment at 550ºC, h_r = 42ºC s^{-1} and t_r = 45 s demonstrating the appearance of thermochromic VO_2. (b) Work function of the surface potential versus sample temperature during heating (black squares) and cooling (red circles) for KPFM experiments performed on the V2 sample.*

In view of the foregoing, it is clearly demonstrated that the controlled and fast oxidation of V or VO_x OAD films in air atmosphere leads to the attainment of high-performance VO_2 thermochromic layers. Hence, given the VO_2 thicknesses achieved here for the different fast thermal treatments carried out, it is thought that the deposition and subsequent oxidation of vanadium or vanadium oxide OAD film thicknesses similar to those required for optical applications in smart windows (< 100 nm) would give rise to the exclusive formation of VO_2 (M1) layers of adjustable grain size and crystallinity by controlling (a) oxygen injection times during deposition ($t_{ON} \leq 2$ s); and (b) reaction times ($t_r \leq 45$s) for thermal treatments conducted at 550ºC and h_r = 42ºC s^{-1}.

Chapter 5

Conclusions

5. Conclusions

The results obtained in this PhD Thesis, which are framed in the development and optimization of multifunctional porous nanostructures, have led to the following general conclusions:

- The large surface-to-volume ratio of the Si and Ge nanostructures generated by OAD methods promotes the spontaneous surface oxidation of their columnar structures in air atmosphere as well as the adsorption of water. Both phenomena have proved to have a detrimental effect for their use in Si and Ge LWIR optics due to significant light absorption in this range. Furthermore, it has been evidenced that this surface oxidation leads to the formation of core-shell-type architectures consisting of pure Si or Ge surrounded by SiO_2 and GeO_2 species, respectively. (Publication I)
- Oblique angle deposition is the most suitable and simplest approach to manufacture broadband and high-performance ARCs for application in the MWIR range. Proof of this is the 98.56% average transparency for 3.7–4.8 μm achieved for a Si substrate when coated with a Ge OAD/MgF_2 bilayer. (Publication II)
- Light scattering is an important aspect to consider for the improvement of high transmittance ARCs. By means of FDTD simulations combined with STEM-HAADF electron tomography reconstructions, it has been possible to develop a method that takes into account this phenomenon, which also demonstrates that a discrete SiO_2 bilayer manufactured by OAD processes provides better optical performances than theoretical moth-eye nanoarchitectures. (Publication III)
- The study of the micro- and nanostructure of OAD systems through electron microscopies provides key insights to build and validate physically meaningful

optical models based on (A)BEMA approaches. When applied to ellipsometry and transmittance optical spectroscopy measurements, these models allow to optimize and describe the optical response of ARCs deposited by OAD. (Publications I, II, III and IV)

- The deposition at room temperature of ITO through IBS at oblique angles leads to the manufacture of crystalline films of controlled porosity. In addition, these films are also characterized by presenting two regions of different degree of porosity and crystallinity, and, thus, electro-optical properties. (Publication V)
- ITO OAD films deposited with Xe exhibit better crystallinity and larger porosity than those achieved using Ar ions, providing superior electrical transport properties and offering more flexibility in the design of broadband low-reflectivity surfaces. (Publication V)
- The growth under local Ga-limited conditions of GaN self-assembled NW arrays by PAMBE gives rise to a mixture of wurtzite GaN vertical nanostructures, from solid (SNW), to *c*-shaped (CNW) and hollow (HNW) nanowires, with their [0001] directions perpendicular with respect to different surfaces of Si substrates. Besides, it has been demonstrated that these uncompact NWs are composed by solid bases (or initially SNWs) that evolve into hollow or c-shape structures as the growth proceeds. This fact allows that, by adjusting the growth conditions, the density and shape of these GaN nanostructures, and thus the porosity of the array, can be controlled. (Publication VI)
- The modeling of vis-IR SE measurements collected from porous semiconducting films by combining BEMA and multioscillator (TLO + DO) approaches is a straightforward method for simultaneously reproducing the optical and electrical response of these systems. The fine agreement of these results with those

experimentally obtained supports the validity of the proposed methodology. (Publication V and VII)

- The high n-doping levels found in GaN NW array films are associated with the oxygen impurities generated as a consequence of the diffusion of oxygen atoms from the amorphous oxide layer spontaneously formed on the surface of such structures. Likewise, the total mobility of these nanostructures is mainly limited by the combined effect of porosity and the native oxide layer formed on surfaces. (Publication VII)
- Both tripod polishing plus low-energy ion milling and FIB sample preparation processes are good approaches to collect electron-transparent regions of porous and delicate thin films for TEM observations. Nonetheless, as a function of the (S)TEM study to be addressed, one method can result more appropriate than the other. (Manuscript VIII)
- The application of advanced (S)TEM imaging techniques and spectroscopies has enabled the realization of several pioneering studies on the morphology, structure and chemistry of multifunctional porosity-controlled coatings, which have been not only essential to complete their characterization at micro-, nano- and atomic scales, but also for a better knowledge of their fabrication processes and properties. (Manuscript VIII)
- High-performance VO_2 (M1) coatings of adjustable grain size and crystallinity can be achieved by the post-deposition fast oxidation of vanadium-based samples deposited at oblique angles and oxygen injection times $t_{ON} \leq 2$ s when the subsequent fast thermal treatments are conducted in air at $h_r = 42^{\circ}C\ s^{-1}$, $T_r = 550^{\circ}C$, and $t_r \leq 45$ s. (Manuscript IX)

Conclusiones

Los resultados obtenidos en la presente Tesis Doctoral, los cuales se enmarcan en el desarrollo y optimización de nanoestructuras porosas multifuncionales, han llevado a las siguientes conclusiones generales:

- La elevada superficie específica de las nanoestructuras de Si y Ge generadas por los métodos OAD promueve la oxidación superficial espontánea de sus estructuras columnares en condiciones ambientales, así como la adsorción de agua. Ambos fenómenos han demostrado tener un efecto perjudicial en la respuesta óptica de los sistemas Si y Ge en el infrarrojo lejano. Además, se ha evidenciado que esta oxidación superficial conduce a la formación de arquitecturas de tipo "core-shell" que consisten en Si o Ge puros, rodeados por especies de SiO_2 y GeO_2, respectivamente. (Publicación I)
- La deposición en ángulo oblicuo es el enfoque más adecuado y más simple para fabricar recubrimientos antirreflectantes de banda ancha y alto rendimiento para aplicaciones en el infrarrojo medio. Prueba de ello es la transparencia promedio del 98,56% conseguida en el rango de longitudes de onda 3.7–4.8 μm para un sustrato de Si cuando se recubre con una bicapa de Ge OAD/MgF_2. (Publicación II)
- La dispersión de la luz es un aspecto importante a considerar para mejorar la alta transmitancia de recubrimientos antirreflectantes. Mediante simulaciones FDTD y reconstrucciones 3D mediante técnicas de tomografía electrónica STEM-HAADF, se ha podido desarrollar un método que tiene en cuenta este fenómeno, a través del cual también se demuestra que una bicapa discreta de SiO_2 fabricada mediante procesos OAD proporciona mejores rendimientos ópticos que las

nanoarquitecturas AR basadas en cálculos teóricos que simulan una topografía de tipo “ojo de polilla”. (Publicación III)

- El estudio de la micro- y nanoestructura de los sistemas OAD a través de microscopías electrónicas proporciona información clave para construir y validar modelos ópticos basados en aproximaciones (anisotrópicas) de medio efectivo de Bruggeman. Cuando se aplican al modelado de medidas experimentales de espectroscopía óptica de transmitancia y elipsometría, estos modelos permiten optimizar y describir la respuesta óptica de los recubrimientos antirreflectantes depositados mediante técnicas OAD. (Publicaciones I, II, III y IV)
- La deposición a temperatura ambiente de ITO a través de técnicas de dispersión de haces de iones en ángulos oblicuos conduce a la fabricación de películas cristalinas de porosidad controlada. Además, estas películas también se caracterizan por presentar dos regiones de diferente grado de porosidad y cristalinidad y, por tanto, con diferentes propiedades electro-ópticas. (Publicación V)
- Las películas ITO OAD depositadas con la asistencia de iones de Xe exhiben una mejor cristalinidad y una mayor porosidad que las obtenidas con iones de Ar, proporcionando propiedades superiores de transporte eléctrico y ofreciendo mayor flexibilidad en el diseño de superficies de banda ancha de baja reflectividad. (Publicación V)
- El crecimiento, en condiciones locales de déficit de Ga, de matrices de nanohilos autoensamblados de GaN mediante epitaxia de haces moleculares asistida por plasma da lugar a una mezcla de nanoestructuras verticales de GaN con estructura wurtzita, desde nanohilos sólidos (SNW) hasta en forma de C (CNW) y huecos (HNW), con sus direcciones [0001] perpendiculares a las diferentes superficies de

sustratos de Si. Además, se ha demostrado que estos nanohilos no compactos están compuestos por bases sólidas (o inicialmente SNW) que progresan hacia estructuras huecas o en forma de C a medida que avanza el crecimiento. Este hecho permite que, ajustando las condiciones de crecimiento, se pueda controlar la densidad y forma de estas nanoestructuras de GaN y, por tanto, la porosidad de la matriz. (Publicación VI)

- El modelado de las medidas de elipsometría vis-IR, recopiladas de películas semiconductoras porosas, mediante la combinación de aproximaciones de medio efectivo de Bruggeman y modelos de osciladores (Tauc-Lorentz + Drude) es un método sencillo y directo para reproducir, de forma simultánea, la respuesta óptica y eléctrica de estos sistemas. La buena correspondencia de estos resultados con los obtenidos experimentalmente respalda la validez de la metodología propuesta. (Publicación V y VII)
- Los altos niveles de dopado tipo n que presentan las películas formadas por matrices nanohilos de GaN están asociados con las impurezas de oxígeno generadas como consecuencia de la difusión de átomos de oxígeno desde la capa de óxido amorfo formada espontáneamente en la superficie de tales estructuras. Asimismo, la movilidad total de estas nanoestructuras está principalmente limitada por el efecto combinado de la porosidad y la capa de óxido nativo formada en las superficies. (Publicación VII)
- Tanto el pulido por trípode y posterior adelgazamiento iónico de baja energía como los procesos de preparación de muestras mediante FIB son buenos métodos para la obtención de lamelas electrón-transparentes de películas delgadas porosas y relativamente frágiles para estudios de microscopía TEM. No obstante, en

función del estudio (S)TEM que se pretenda llevar a cabo, un método puede resultar más apropiado que el otro. (Manuscrito VIII)

- La aplicación de técnicas avanzadas de imagen y espectroscopias (S)TEM ha permitido la realización de varios estudios pioneros sobre la morfología, estructura y naturaleza química de recubrimientos multifuncionales de porosidad controlada, los cuales no solo han sido imprescindibles para completar la caracterización de los mismos hasta la escala atómica, sino también para un mejor conocimiento de sus procesos de fabricación y propiedades. (Manuscrito VIII)
- Se pueden lograr recubrimientos de alto rendimiento de VO_2 (M1) de tamaño de grano y cristalinidad ajustables mediante tratamientos térmicos rápidos en atmósfera de aire, a velocidades de calentamiento de 42ºC s^{-1}, temperaturas de reacción de 550ºC, y tiempos de reacción $\leq$ 45 s, aplicados posteriormente a muestras de vanadio depositadas en ángulos oblicuos con tiempos de inyección de oxígeno $\leq$ 2 s. (Manuscrito IX)

Chapter 6

Prospects

6. Prospects

The versatility of porous thin film synthesis and processing has led to the development of a wide variety of solutions for a wide range of case studies and applications. However, there are some issues, such as the clear understanding of the structure-property relationship of these systems, which is key to the successful development and optimization of this technology, or the integration of these procedures at a large scale in the real manufacturing industry, which are still awaiting a solution. In this context, the fabrication of porosity-controlled coatings by means of self-assembled processes has stand out as one of the most cost-effective and promising alternatives to attain nanostructured materials with adaptable morphologies, structures, compositions and properties. Of all these processes, there is one that has proven to be efficiently transferred to the industrial scale: oblique angle deposition [269]. A proof of it is the massive fabrication of antireflective coatings for wire-grid polarizers [270,271] and substrate for surface-enhanced Raman spectroscopy [272,273] products by the OAD technique. However, although this demonstrates the applicability of OAD thin films, the reality is that there are not many industrial processes that have finished adapting this technology [16] . In this sense, it is expected that the definitive take-off and consolidation of OAD methods on an industrial scale will be closely linked, in addition to the reduction in cost to be competitive with alternative technologies, to the arrival, in the near future, of the so-called “smart coatings” to the construction and transportation sectors.

According to the *Clean energy for all Europeans package* of the *Energy strategy* framed in the climate and energy plans of the EU [274], the building sector is responsible for approximately 40% of the whole energy consumption and of 36% of the CO_2 emissions in the EU, making it the single largest energy consumer in Europe mostly due

to air conditioning and lighting. In the transportation sector, the intensive use of mobile air conditioning systems is also responsible for a significant energetic demand with about 20% extra fuel consumption [275]. The envelope of buildings and vehicles plays a pivotal role in their energy management performance. In particular, windows are regarded as the weaker point since they have high thermal transfer coefficients that cause significant heat losses during the colder seasons and undesired heat gains in warmer times [276]. Thanks to their capability to regulate the solar energy transmittance, smart windows based on VO_2 thermochromic coatings are considered as one of the most exiting routes to make construction and transportation sectors more energy-efficient and to achieve the governments energy and climate directives included in the *Paris Agreement*. These systems are smart in the sense that they can respond independently to external environmental conditions without the needs of external electrical power and user intervention, blocking the infrared light (solar heat source) when the outdoor temperature becomes too high to prevent overheating inside building rooms and vehicles cabins.

Nevertheless, finding an appropriate balance between the transition temperature, the visible transmittance, and the solar modulation ability of these VO_2-based thermochromic coatings is far from being straightforward. In particular, the current challenge is to achieve a thermochromic coating with a transition temperature around 25ºC, a transmission in the visible range greater than 80% and a solar energy modulation capacity of 30% or greater. Hence, to meet these requirements, the development of novel VO_2 nanostructures is needed. In this scenario, beyond postulating as the best alternative to tackle the antireflection issue, the OAD technique also presents interest in the search for new functionalities such as self-cleaning capabilities [234,277]: keeping these systems clean is necessary not only to ensure optimal transmittance but also to reduce the maintenance costs and environmental impacts. Of course, the application of the characterization

methodologies developed in the context of this present PhD Thesis (advanced (S)TEM methods and optical spectroscopies) will be crucial (i) to better understand the fabrication processes (OAD deposition, annealing, etc.) and the physical-chemical properties (transmittance, thermochromism, surface wetting, etc.) of the systems up to the nanoscale; (ii) to unravel the key limitations in their development; and also (iii) to provide relevant feedback for their optimization.

References

[1] J.M. Albella, Capas delgadas y modificación superficial de materiales, Consejo Superior de Investigaciones Científicas, Madrid, 2018.

[2] J.P. Davim, Materials and Surface Engineering: Research and Development, Woodhead Publishing, Cambridge, 2012.

[3] J.Q. Xi, M.F. Schubert, J.K. Kim, E.F. Schubert, M. Chen, S.Y. Lin, X. Liu, J.A. Smart, Optical thin-film materials with low refractive index for broadband elimination of Fresnel reflection, Nat. Photonics. 1 (2007) 176–179.

[4] C. Toccafondi, S. Uttiya, O. Cavalleri, G. Gemme, E. Barborini, F. Bisio, M. Canepa, Optical properties of nanogranular and highly porous TiO_2 thin films, J. Phys. D. Appl. Phys. 47 (2014) 485301.

[5] K. Choi, J. Jung, J. Kim, J. Lee, H.S. Lee, I.S. Kang, Antireflective transparent conductive oxide film based on a tapered porous nanostructure, Micromachines. 11 (2020) 1–6.

[6] C.B. Soh, C.B. Tay, R.J.N. Tan, A.P. Vajpeyi, I.P. Seetoh, K.K. Ansah-Antwi, S.J. Chua, Nanopore morphology in porous GaN template and its effect on the LEDs emission, J. Phys. D. Appl. Phys. 46 (2013) 365102.

[7] X.J. Li, Z. wei Song, Y. Zhao, Y. Wang, X.C. Zhao, M. Liang, W.G. Chu, P. Jiang, Y. Liu, Vertically porous nickel thin film supported Mn_3O_4 for enhanced energy storage performance, J. Colloid Interface Sci. 483 (2016) 17–25.

[8] E. Dislaki, S. Robbennolt, M. Campoy-Quiles, J. Nogués, E. Pellicer, J. Sort, Coercivity Modulation in Fe–Cu Pseudo-Ordered Porous Thin Films Controlled by an Applied Voltage: A Sustainable, Energy-Efficient Approach to Magnetoelectrically Driven Materials, Adv. Sci. 5 (2018) 1–8.

[9] A. Dubey, S.K. Kolekar, E.S. Gnanakumar, K. Roy, C.P. Vinod, C.S. Gopinath, Porous thin films toward bridging the material gap in heterogeneous catalysis, Catal. Struct. React. 2 (2016) 1–12.

[10] S. Abate, G. Centi, S. Perathoner, F. Frusteri, Enhanced stability of catalytic membranes based on a porous thin Pd film on a ceramic support by forming a Pd-Ag interlayer, Catal. Today. 118 (2006) 189–197.

[11] S. Mariani, L. Pino, L.M. Strambini, L. Tedeschi, G. Barillaro, 10000-Fold Improvement in Protein Detection Using Nanostructured Porous Silicon Interferometric Aptasensors, ACS Sensors. 1 (2016) 1471–1479.

[12] A.K. Prasad, S. Amirthapandian, S. Dhara, S. Dash, N. Murali, A.K. Tyagi, Novel single phase vanadium dioxide nanostructured films for methane sensing near room temperature, Sensors Actuators, B Chem. 191 (2014) 252–256.

[13] Y. Yan, S.R. Chaudhuri, A. Sarkar, Synthesis, characterizations, and optical properties of stacked porous thin films derived from sol-gel process, J. Am. Ceram. Soc. 79 (1996) 1061–1065.

[14] Y. Xie, D. Kocaefe, C. Chen, Y. Kocaefe, Review of Research on Template Methods in Preparation of Nanomaterials, J. Nanomater. 2016 (2016) 2302595.

[15] F.N. Crespilho, V. Zucolotto, O.N. Oliveira, F.C. Nart, Electrochemistry of layer-by-layer films: A review, Int. J. Electrochem. Sci. 1 (2006) 194–214.

[16] A. Barranco, A. Borras, A.R. Gonzalez-Elipe, A. Palmero, Perspectives on oblique angle deposition of thin films: From fundamentals to devices, Prog. Mater. Sci. 76 (2016) 59–153.

[17] M.M. Hawkeye, M.T. Taschuk, M. Brett, Glancing angle deposition of thin films, John Wiley & Sons Inc, New Delhi, (2014).

[18] H. van Kranenburg, C. Lodder, Tailoring growth and local composition by oblique-incidence deposition: a review and new experimental data, Mater. Sci. Eng. R. 11 (1994) 295–354.

[19] Y. He, Y. Zhao, Advanced multi-component nanostructures designed by dynamic shadowing growth, Nanoscale. 3 (2011) 2361–2375.

[20] K. Robbie, M.J. Brett, Sculptured thin films and glancing angle deposition: Growth mechanics and applications, J. Vac. Sci. Technol. a-Vacuum Surfaces Film. 15 (1997) 1460–1465.

[21] M.M. Hawkeye, M.J. Brett, Glancing angle deposition: Fabrication, properties, and applications of micro- and nanostructured thin films, J. Vac. Sci. Technol. A Vacuum, Surfaces, Film. 25 (2007) 1317.

[22] M.F. Schubert, J.Q. Xi, J.K. Kim, E.F. Schubert, Distributed Bragg reflector consisting of high- and low-refractive-index thin film layers made of the same material, Appl. Phys. Lett. 90 (2007) 141115.

[23] S.R. Kennedy, M.J. Brett, Porous broadband antireflection coating by glancing angle deposition., Appl. Opt. 42 (2003) 4573–4579.

[24] H.O. Chu, S. Song, C. Li, D. Gibson, Surface enhanced Raman scattering substrates made by oblique angle deposition: Methods and applications, Coatings. 7 (2017) 26.

[25] H.G. Moon, Y.S. Shim, D.H. Kim, H.Y. Jeong, M. Jeong, J.Y. Jung, S.M. Han, J.K. Kim, J.S. Kim, H.H. Park, J.H. Lee, H.L. Tuller, S.J. Yoon, H.W. Jang, Self-activated ultrahigh chemosensitivity of oxide thin film nanostructures for transparent sensors, Sci. Rep. 2 (2012) 1–7.

[26] Y. Sun, X. Xiao, G. Xu, G. Dong, G. Chai, H. Zhang, P. Liu, H. Zhu, Y. Zhan, Anisotropic vanadium dioxide sculptured thin films with superior thermochromic properties, Sci. Rep. 3 (2013) 2756.

[27] A. Kikuchi, K. Yamano, M. Tada, K. Kishino, Stimulated emission from GaN nanocolumns, Phys. Status Solidi Basic Res. 241 (2004) 2754–2758.

[28] Q. Wan, P. Feng, T.H. Wang, Vertically aligned tin-doped indium oxide nanowire arrays: Epitaxial growth and electron field emission properties, Appl. Phys. Lett. 89 (2006) 87–90.

[29] C. O'Dwyer, M. Szachowicz, G. Visimberga, V. Lavayen, S.B. Newcomb, C.M.S. Torres, Bottom-up growth of fully transparent contact layers of indium tin oxide

nanowires for light-emitting devices, Nat. Nanotechnol. 4 (2009) 239–244.

[30] H.G. Cha, C.W. Kim, Y.H. Kim, M.H. Jung, E.S. Ji, B.K. Das, J.C. Kim, Y.S. Kang, Preparation and characterization of α-Fe_2O_3 nanorod-thin film by metal-organic chemical vapor deposition, Thin Solid Films. 517 (2009) 1853–1856.

[31] P. Tyagi, C. Ramesh, B.S. Yadav, S.S. Kushvaha, M.S. Kumar, Laser molecular beam epitaxy of vertically self-assembled GaN nanorods on Ta metal foil: Role of growth temperature and laser repetition rate, CrystEngComm. 21 (2019) 5448–5454.

[32] R. Sun, G.G. Wang, Z.C. Peng, Fabrication and UV photoresponse of GaN nanowire-film hybrid films on sapphire substrates by chemical vapor deposition method, Mater. Lett. 217 (2018) 288–291.

[33] D.C. Harris, Materials for Infrared Windows and Domes: Properties and Performance, SPIE, Bellingham, 1999.

[34] A. Rogalski, K. Chrzanowski, Infrared devices and techniques, Metrol. Meas. Syst. 21 (2014) 565–618.

[35] M. Bhatt, B.B. Nautiyal, P.K. Bandyopadhyay, High efficiency antireflection coating in MWIR region (3.6–4.9 μm) simultaneously effective for Germanium and Silicon optics, Infrared Phys. Technol. 53 (2010) 33–36.

[36] J.W. Leem, J.S. Yu, Multi-functional antireflective surface-relief structures based on nanoscale porous germanium with graded refractive index profiles, Nanoscale. 5 (2013) 2520–2526.

[37] R.G. Gordon, Criteria for choosing transparent conductors materials properties relevant to transparent conductors optical and electrical performance of transparent conductors, MRS Bull. 25 (2011) 52–57.

[38] A.L. Dawar, J.C. Joshi, Semiconducting transparent thin films: their properties and applications, J. Mater. Sci. 19 (1984) 1–23.

[39] B.G. Lewis, D.C. Paine, Applications and processing of transparent conducting oxides, MRS Bull. 25 (2000) 22–27.

[40] T. Minami, Transparent conducting oxide semiconductors for transparent electrodes, Semicond. Sci. Technol. 20 (2005) S35.

[41] E. Fortunato, D. Ginley, H. Hosono, D.C. Paine, Transparent for photovoltaics transparent conducting oxides, Mrs Bull. 32 (2017) 242–247.

[42] H. Liu, V. Avrutin, N. Izyumskaya, Ü. Özgr, H. Morkoç, Transparent conducting oxides for electrode applications in light emitting and absorbing devices, Superlattices Microstruct. 48 (2010) 458–484.

[43] T.J. Coutts, D.L. Young, X. Li, Characterization of transparent conducting oxides, MRS Bull. 25 (2000) 58–65.

[44] G. Hass, J.B. Heaney, A.R. Toft, Transparent electrically conducting thin films for spacecraft temperature control applications, Appl. Opt. 18 (1979) 1488−1489.

[45] D.S. Ginley, H. Hosono, D.C. Paine, Handbook of Transparent Conductors, Springer, Boston, 2010.

[46] L. Liu, J.H. Edgar, Substrates for gallium nitride epitaxy, Mater. Sci. Eng. R. 37 (2002) 61–127.

[47] C.Y. Chen, G. Zhu, Y. Hu, J.W. Yu, J. Song, K.Y. Cheng, L.H. Peng, L.J. Chou, Z.L. Wang, Gallium nitride nanowire based nanogenerators and light-emitting diodes, ACS Nano. 6 (2012) 5687–5692.

[48] P.J. Pauzauskie, P. Yang, Nanowire photonics, Mater. Today. 9 (2006) 36–45.

[49] E. Barrigón, M. Heurlin, Z. Bi, B. Monemar, L. Samuelson, Synthesis and Applications of III−V Nanowires, Chem. Rev. 119 (2019) 9170–9220.

[50] S.W. Ryu, Y. Zhang, B. Leung, C. Yerino, J. Han, Improved photoelectrochemical water splitting efficiency of nanoporous GaN photoanode, Semicond. Sci. Technol. 27 (2012) 015014.

[51] J. Benton, J. Bai, T. Wang, Nanoporous GaN for enhanced solar hydrogen production, Proc. SPIE 9176, Solar Hydrogen and Nanotechnology IX, 91760K (7 October 2014).

[52] L. Zhang, S. Wang, Y. Shao, Y. Wu, C. Sun, Q. Huo, B. Zhang, H. Hu, X. Hao, One-step fabrication of porous GaN crystal membrane and its application in energy storage, Sci. Rep. 7 (2017) 44063.

[53] J. Yu, L. Zhang, J. Shen, Z. Xiu, S. Liu, Wafer-scale porous GaN single crystal substrates and its application in energy storage, CrystEngComm. 18 (2016) 5149−5154.

[54] A.P. Vajpeyi, S. Tripathy, S.J. Chua, E.A. Fitzgerald, Investigation of optical properties of nanoporous GaN films, Phys. E Low-Dimensional Syst. Nanostructures. 28 (2005) 141–149.

[55] J.J. Carvajal, J. Mena, J. Aixart, F. Díaz, M. Aguiló, Rectifiers, MOS diodes and LEDs made of fully porous GaN produced by chemical vapor deposition, ECS Trans. 80 (2017) 143–148.

[56] G-Y. Shiu, K-T. Chen, F-H. Fan, K-P- Huang, W-J. Hsu, J-J. Dai, C-F. Lai, C-F. Lin, InGaN light-emitting diodes with embedded nanoporous GaN distributed Bragg reflectors, Sci. Rep. 6 (2016) 29138.

[57] K.J. Lee, S.-J. Kim, J.-J. Kim, K. Hwang, S.-T. Kim, S.-J. Park, Enhanced performance of InGaN/GaN multiple-quantum-well light-emitting diodes grown on nanoporous GaN layers, Opt. Express. 22 (2014) A1164.

[58] Y.D. Wang, S.J. Chua, M.S. Sander, P. Chen, S. Tripathy, C.G. Fonstad, Fabrication and properties of nanoporous GaN films, Appl. Phys. Lett. 85 (2004) 816.

[59] J. Sun, M. Han, Y. Gu, Z. Yang, H. Zeng, Recent advances in group III–V nanowire infrared detectors, Adv. Optical Mater. 2018 (2018) 1800256.

[60] S. Gradečak, F. Qian, Y. Li, H. Park, C.M. Lieber, S. Grade, F. Qian, Y. Li, H. Park, C.M. Lieber, GaN nanowire lasers with low lasing thresholds, Appl. Phys. Lett. 87(2005) 173111.

[61] P.-C. Yeh, M.-C. Hwa, J.-W. Yu, H.-M. Wu, H.-L. Tsai, C.-M. Lai, J.-J. Huang, J.-R. Yang, L. H. Peng, Photon-assisted tunneling in GaN nanowire white light emitting diodes, Phys. Status Solidi. 6 (2009) S538–S540.

[62] H. Cha, H. Wu, M. Chandrashekhar, Y.C. Choi, S. Chae, G. Koley, M.G. Spencer, Fabrication and characterization of pre-aligned gallium nitride nanowire field-effect transistors, Nanotechnology. 17 (2006) 1264.

[63] J.B. Goodenough, The two components of the crystallographic transition in VO_2, J. Solid State Chem. 3 (1971) 490–500.

[64] K. Liu, S. Lee, S. Yang, O. Delaire, J. Wu, Recent progresses on physics and applications of vanadium dioxide, Mater. Today. 21 (2018) 875–896.

[65] S. Wang, M. Liu, L. Kong, Y. Long, X. Jiang, A. Yu, Recent progress in VO_2 smart coatings: Strategies to improve the thermochromic properties, Prog. Mater. Sci. 81 (2016) 1–54.

[66] V. Devthade, S. Lee, Synthesis of vanadium dioxide thin films and nanostructures, J. Appl. Phys. 128 (2020) 231101.

[67] C. Batista, V. Teixeira, J. Carneiro, Structural and morphological characterization of magnetron sputtered nanocrystalline vanadium oxide films for thermochromic smart surfaces, J. Nano Res. 2 (2008) 21–30.

[68] X. He, C. Gu, F. Chen, X. Xu, Vanadium dioxide thin films for smart windows: optical design and performance improvement, Eighth Int. Conf. Thin Film Phys. Appl. 9068 (2013) 90680G.

[69] Z. Chen, Y. Gao, L. Kang, J. Du, Z. Zhang, H. Luo, H. Miao, G. Tan, VO_2-based double-layered films for smart windows: Optical design, all-solution preparation and improved properties, Sol. Energy Mater. Sol. Cells. 95 (2011) 2677–2684.

[70] B.G. Chae, H.T. Kim, D.H. Youn, K.Y. Kang, Abrupt metal-insulator transition observed in VO_2 thin films induced by a switching voltage pulse, Phys. B Condens. Matter. 369 (2005) 76–80.

[71] S.A. Corr, M. Grossman, J.D. Furman, B.C. Melot, A.K. Cheetham, K.R. Heier, R. Seshadri, Controlled reduction of vanadium oxide nanoscrolls: Crystal structure, morphology, and electrical properties, Chem. Mater. 20 (2008) 6396–6404.

[72] T. Driscoll, H.T. Kim, B.G. Chae, B.J. Kim, Y.W. Lee, N.M. Jokerst, S. Palit, D.R. Smith, M. Di Ventra, D.N. Basov, Memory metamaterials, Science 325 (2009) 1518–1521.

[73] M.G. Krishna, Y. Debauge, A.K. Bhattacharya, X-ray photoelectron spectroscopy and spectral transmittance study of stoichiometry in sputtered vanadium oxide films, Thin Solid Films. 312 (1998) 116–122.

[74] A. Perucchi, L. Baldassarre, P. Postorino, S. Lupi, Optical properties across the insulator to metal transitions in vanadium oxide compounds, J. Phys. Condens. Matter. 21 (2009) 323202.

[75] E. Hryha, E. Rutqvist, L. Nyborg, Stoichiometric vanadium oxides studied by XPS, Surf. Interface Anal. 44 (2012) 1022–1025.

[76] G. McMullan, A.R. Faruqi, D. Clare, R. Henderson, Comparison of optimal performance at 300 keV of three direct electron detectors for use in low dose electron microscopy, Ultramicroscopy. 147 (2014) 156–163.

[77] Z.L. Wang, Picoscale science and nanoscale engineering by electron microscopy, J. Electron Microsc 60 (2011) 269–278.

[78] F. Hosokawa, H. Sawada, Y. Kondo, K. Takayanagi, K. Suenaga, Development of Cs and Cc correctors for transmission electron microscopy, J. Electron Microsc. 62 (2013) 23–41.

[79] G. Bertoni, J. Verbeeck, Accuracy and precision in model based EELS quantification, Ultramicroscopy. 108 (2008) 782–790.

[80] R.F. Egerton, M. Malac, EELS in the TEM, J. Electron Spectros. Relat. Phenomena. 143 (2005) 43–50.

[81] M. Weyland, P.A. Midgley, Electron tomography, Mater. Today. 7 (2004) 32–40.

[82] P.A. Midgley, R.E. Dunin-Borkowski, Electron tomography and holography in materials science, Nat. Mater. 8 (2009) 271–280.

[83] B. Goris, T. Roelandts, K.J. Batenburg, H. Heidari Mezerji, S. Bals, Advanced reconstruction algorithms for electron tomography: From comparison to combination, Ultramicroscopy. 127 (2013) 40–47.

[84] W. van Aarle, W.J. Palenstijn, J. De Beenhouwer, T. Altantzis, S. Bals, K.J. Batenburg, J. Sijbers, The ASTRA Toolbox: A platform for advanced algorithm development in electron tomography, Ultramicroscopy. 157 (2015) 35–47.

[85] D. Chen, B. Goris, F. Bleichrodt, H.H. Mezerji, S. Bals, K.J. Batenburg, G. de With, H. Friedrich, The properties of SIRT, TVM, and DART for 3D imaging of tubular domains in nanocomposite thin-films and sections, Ultramicroscopy. 147 (2014) 137–148.

[86] C. Kübel, A. Voigt, R. Schoenmakers, M. Otten, D. Su, T.C. Lee, A. Carlsson, J. Bradley, Recent advances in electron tomography: TEM and HAADF-STEM tomography for materials science and semiconductor applications, Microsc. Microanal. 11 (2005) 378–400.

[87] P.A. Midgley, M. Weyland, J. Meurig Thomas, B.F.G. Johnson, Z-contrast tomography: A technique in three-dimensional nanostructural analysis based on Rutherford scattering, Chem. Commun. (2001) 907–908.

[88] H. Friedrich, M.R. McCartney, P.R. Buseck, Comparison of intensity distributions in tomograms from BF TEM, ADF STEM, HAADF STEM, and calculated tilt series, Ultramicroscopy. 106 (2005) 18–27.

[89] J. Li, T. Malis, S. Dionne, Recent advances in FIB-TEM specimen preparation techniques, Mater. Charact. 57 (2006) 64–70.

[90] L. Holzer, M. Cantoni, Review of FIB tomography, in: Nanofabrication Using Focus. Ion Electron Beams, 2014: pp. 410–435.

[91] P. Innocenzi, L. Malfatti, Mesoporous thin films: Properties and applications, Chem. Soc. Rev. 42 (2013) 4198–4216.

[92] D. Carboni, D. Marongiu, P. Rassu, A. Pinna, H. Amenitsch, M. Casula, A. Marcelli, G. Cibin, P. Falcaro, L. Malfatti, P. Innocenzi, Enhanced photocatalytic activity in low-temperature processed titania mesoporous films, J. Phys. Chem. C. 118 (2014) 12000–12009.

[93] M. Winter, R.J. Brodd, What are batteries, fuel cells, and supercapacitors?, Chem. Rev. 104 (2004) 4245–4269.

[94] F. Chi, L. Yan, H. Yan, B. Jiang, H. Lv, X. Yuan, Ultralow-refractive-index optical thin films through nanoscale etching of ordered mesoporous silica films, Opt. Lett. 37 (2012) 1406.

[95] S.G. Choi, T.J. Ha, B.G. Yu, S. Shin, H.H. Cho, H.H. Park, Application of mesoporous TiO_2 as a thermal isolation layer for infrared sensors, Thin Solid Films. 516 (2007) 212–215.

[96] B.J. Melde, B.J. Johnson, P.T. Charles, Mesoporous silicate materials in sensing, Sensors. 8 (2008) 5202–5228.

[97] W.H. Southwell, Gradient-index antireflection coatings, Opt. Lett. 8 (1983) 584.

[98] O.L. Muskens, S.L. Diedenhofen, M.H.M. Van Weert, M.T. Borgström, E.P.A.M. Bakkers, J.G. Rivas, Epitaxial growth of aligned semiconductor nanowire metamaterials for photonic applications, Adv. Funct. Mater. 18 (2008) 1039–1046.

[99] C. O'Dwyer, C.M. Sotomayor Torres, Epitaxial growth of an antireflective, conductive, graded index ITO nanowire layer, Front. Phys. 1 (2013) 18.

[100] X. Guo, X. Quan, Z. Li, Q. Li, B. Zhang, X. Zhang, C. Song, Broadband anti-reflection coatings fabricated by precise time-controlled and oblique-angle deposition methods, Coatings. 11 (2021) 492.

[101] R.K. Debnath, R. Meijers, K. Jeganathan, T. Richter, T. Stoica, R. Calarco, H. Lüth, Self-assembled growth of GaN nanowires, J. Phys. Conf. Ser. 126 (2008) 012026.

[102] R. Alvarez, J.M. Garcia-Martin, A. Garcia-Valenzuela, M. Macias-Montero, F.J. Ferrer, J. Santiso, V. Rico, J. Cotrino, A.R. Gonzalez-Elipe, A. Palmero, Nanostructured Ti thin films by magnetron sputtering at oblique angles, J. Phys. D. Appl. Phys. 49 (2016) 045303.

[103] R. El Beainou, N. Martin, V. Potin, P. Pedrosa, M.A.P. Yazdi, A. Billard, Correlation between structure and electrical resistivity of W-Cu thin films prepared by GLAD co-sputtering, Surf. Coatings Technol. 313 (2017) 1–7.

[104] H. Chu, S. Song, C. Li, D. Gibson, Surface enhanced Raman scattering substrates made by oblique angle deposition: Methods and applications, Coatings. 7 (2017) 26.

[105] R.R. Reznik, K.P. Kotlyar, I.P. Soshnikov, S.A. Kukushkin, A. V. Osipov, G.E. Cirlin, MBE growth and structural properties of InAs and InGaAs nanowires with different mole fraction of In on Si and strongly mismatched SiC/Si(111) Substrates, Semiconductors. 52 (2018) 651–653.

[106] D. Mikulik, M. Ricci, G. Tutuncuoglu, F. Matteini, J. Vukajlovic, N. Vulic, E. Alarcon-Llado, A. Fontcuberta i Morral, Conductive-probe atomic force microscopy as a characterization tool for nanowire-based solar cells, Nano Energy. 41 (2017) 566–572.

[107] R.K. Jain, Y.K. Gautam, V. Dave, A.K. Chawla, R. Chandra, A study on structural, optical and hydrophobic properties of oblique angle sputter deposited HfO_2 films, Appl. Surf. Sci. 283 (2013) 332–338.

[108] A. Esfandiar, H. Savaloni, F. Placido, On the fabrication and characterization of graded slanted chiral nano-sculptured silver thin films, Phys. E Low-Dimensional Syst. Nanostructures. 50 (2013) 88–96.

[109] S. Larson, Y. Zhao, Tuning the composition of Bi_xW_yO nanorods towards zero bias PEC water splitting, Nanotechnology. 27 (2016) 255401.

[110] A.R. Shetty, A. Karimi, Texture mechanisms and microstructure of biaxial thin films grown by oblique angle deposition, Phys. Status Solidi Basic Res. 249 (2012) 1531–1540.

[111] T. Van Khai, M. Prachuporn, B.-G. Choi, H.-W. Kim, D.-S. So, J.-W. Lee, N.-H. Park, H. Huh, N.T. Tung, H. Ham, K.-B. Shim, High-quality ZnO nanowire arrays directly synthesized from Zn vapor deposition without catalyst, J. Korean Cryst. Growth Cryst. Technol. 21 (2011) 137–146.

[112] D.B. Polat, O. Keles, K. Amine, Well-aligned, ordered, nanocolumnar, Cu-Si thin film as anode material for lithium-ion batteries, J. Power Sources. 270 (2014) 238–247.

[113] P. Salazar, V. Rico, A.R. González-Elipe, Non-enzymatic hydrogen peroxide detection at NiO nanoporous thin film- electrodes prepared by physical vapor deposition at oblique angles, Electrochim. Acta. 235 (2017) 534–542.

[114] T.G.G. Maffeis, M.W. Penny, A. Castaing, O.J. Guy, S.P. Wilks, XPS investigation of vacuum annealed vertically aligned ultralong ZnO nanowires, Surf. Sci. 606 (2012) 99–103.

[115] W. Phae-ngam, M. Horprathum, C. Chananonnawathorn, T. Lertvanithphol, B. Samransuksamer, P. Songsiriritthigul, H. Nakajima, S. Chaiyakun, Oblique angle deposition of nanocolumnar TiZrN films via reactive magnetron co-sputtering technique: The influence of the Zr target powers, Curr. Appl. Phys. 19 (2019) 894–901.

[116] S. Liedtke-Grüner, C. Grüner, A. Lotnyk, J.W. Gerlach, M. Mensing, P. Schumacher, B. Rauschenbach, Crystallinity and texture of molybdenum thin films

obliquely deposited at room temperature, Thin Solid Films. 685 (2019) 8–16.

[117] S. Liedtke, C. Grüner, A. Lotnyk, B. Rauschenbach, Glancing angle deposition of sculptured thin metal films at room temperature, Nanotechnology. 28 (2017) 385604.

[118] S. Liedtke, C. Grüner, J.W. Gerlach, A. Lotnyk, B. Rauschenbach, Crystalline Ti-nanostructures prepared by oblique angle deposition at room temperature, J. Vac. Sci. Technol. B, Nanotechnol. Microelectron. Mater. Process. Meas. Phenom. 36 (2018) 031804.

[119] Z. Qi, J. Tang, J. Huang, D. Zemlyanov, V.G. Pol, H. Wang, Li_2MnO_3 Thin films with tilted domain structure as cathode for Li-Ion batteries, ACS Appl. Energy Mater. 2 (2019) 3461–3468.

[120] M. Auer, D. Ye, Facet-mediated growth of silver nanoparticles on biaxial calcium fluoride nanorod arrays, Nanotechnology. 28 (2017) 035301.

[121] C. Amaya, J.J. Prías-Barragán, W. Aperador, M.A. Hernández-Landaverde, M. Ramírez-Cardona, J.C. Caicedo, L.A. Rodríguez, E. Snoeck, M.E. Gómez, G. Zambrano, Thermal conductivity of yttria-stabilized zirconia thin films with a zigzag microstructure, J. Appl. Phys. 121 (2017) 245110.

[122] P. Nuchuay, T. Chaikeeree, M. Horprathum, N. Mungkung, N. Kasayapanand, C. Oros, S. Limwichean, N. Nuntawong, C. Chananonnawathorn, V. Patthanasettakul, P. Muthitamongkol, B. Samransuksamer, S. Denchitcharoen, A. Klamchuen, C. Thanachayanont, P. Eiamchai, Engineered omnidirectional antireflection ITO nanorod films with super hydrophobic surface via glancing-angle ion-assisted electron-beam evaporation deposition, Curr. Appl. Phys. 17 (2017) 222–229.

[123] S. Zhao, Z. Mi, Recent advances on p-type III-nitride nanowires by molecular beam epitaxy, Crystals. 7 (2017) 18–26.

[124] S. Morkötter, S. Funk, M. Liang, M. Döblinger, S. Hertenberger, J. Treu, D. Rudolph, A. Yadav, J. Becker, M. Bichler, G. Scarpa, P. Lugli, I. Zardo, J.J. Finley, G. Abstreiter, G. Koblmüller, Role of microstructure on optical properties in high-uniformity $In_{1-x}Ga_xAs$ nanowire arrays: Evidence of a wider wurtzite band gap, Phys. Rev. B - Condens. Matter Mater. Phys. 87 (2013) 1–9.

[125] E.A. Anyebe, M. Kesaria, A.M. Sanchez, Q. Zhuang, A comparative study of graphite and silicon as suitable substrates for the self-catalysed growth of InAs nanowires by MBE, Appl. Phys. A Mater. Sci. Process. 126 (2020) 427.

[126] N. Abdel All, M. Almokhtar, J. El Ghoul, Temperature dependence of photoluminescence from AlN/GaN-thin nanowires, J. Mater. Sci. Mater. Electron. 31 (2020) 5033–5039.

[127] B. V. Novikov, S.Y. Serov, N.G. Filosofov, I. V. Shtrom, V.G. Talalaev, O.F. Vyvenko, E. V. Ubyivovk, Y.B. Samsonenko, A.D. Bouravleuv, I.P. Soshnikov, N. V. Sibirev, G.E. Cirlin, V.G. Dubrovskii, Photoluminescence properties of GaAs nanowire ensembles with zincblende and wurtzite crystal structure, Phys. Status Solidi - Rapid Res. Lett. 4 (2010) 175–177.

[128] H.O.M. Chu, S. Song, D. Gibson, L. Porteous, Glancing angle deposition of silver nanostructures for use in surface enhanced Raman scattering, Opt. Syst. Des. 2015 Adv. Opt. Thin Film. V. 9627 (2015) 96271E.

[129] I. V. Anoshkin, I.I. Nefedova, I.S. Nefedov, D. V. Lioubtchenko, A.G. Nasibulin, A. V. Räisänen, Resistivity and optical transmittance dependence on length and diameter of nanowires in silver nanowire layers in application to transparent conductive coatings, Micro Nano Lett. 11 (2016) 343–347.

[130] G. Sauer, G. Brehm, S. Schneider, H. Graener, G. Seifert, K. Nielsch, J. Choi, P. Göring, U. Gösele, P. Miclea, R.B. Wehrspohn, In situ surface-enhanced Raman spectroscopy of monodisperse silver nanowire arrays, J. Appl. Phys. 97 (2005) 024308.

[131] M. Bordbari, M.J. Eshraghi, N. Naderi, A.S.A.H. Zadeh, Investigation of structural and optical properties of oblique angle sputter deposited barium strontium titanate nanostructures, Mater. Res. Express. 6 (2019) 025009.

[132] M. Benson, P. Shah, M. Marciniak, A. Sarangan, A. Urbas, Optical characterization of silver nanorod thin films grown using oblique angle deposition, J. Nanomater. 2014 (2014) 694982.

[133] B. Ge, S. Larson, H. Tu, Y. Zhao, Y. Fei, Generalized ellipsometry characterization of Ag nanorod arrays prepared by oblique angle deposition, Nanoscale. 31 (2020) 075705.

[134] G. Beydaghyan, C. Buzea, Y. Cui, C. Elliott, K. Robbie, Ex situ ellipsometric investigation of nanocolumns inclination angle of obliquely evaporated silicon thin films, Appl. Phys. Lett. 87 (2005) 153103.

[135] K. Kaminska, A. Amassian, L. Martinu, K. Robbie, Growth of vacuum evaporated ultraporous silicon studied with spectroscopic ellipsometry and scanning electron microscopy, J. Appl. Phys. 97 (2005) 013511.

[136] B. Fodor, T. Defforge, E. Agócs, M. Fried, G. Gautier, P. Petrik, Spectroscopic ellipsometry of columnar porous Si thin films and Si nanowires, Appl. Surf. Sci. 421 (2017) 397–404.

[137] J.H. Lee, B. Lee, J.H. Kang, J.K. Lee, S.W. Ryu, Optical characterization of nanoporous GaN by spectroscopic ellipsometry, Thin Solid Films. 525 (2012) 84–87.

[138] A.K. Sood, Y.R. Puri, M.D. Agency, D.C. Washington, D. Mto, N.F. Drive, G. Brill, P. Wijewarnasuriya, N. Dhar, J. Yehoda, S. Finke, Development of high performance radiation hardened antireflection coatings for LWIR and multicolor IR focal plane arrays, Infrared Technol. Appl. 6206 (2006) 620615.

[139] D.J. Poxson, M. Kuo, F.W. Mont, Y. Kim, X. Yan, R.E. Welser, A.K. Sood, J. Cho, S. Lin, E.F. Schubert, High-performance antireflection coatings utilizing nanoporous layers, MRS Bull. 36 (2011) 9–11.

[140] A.K. Sood, A.W. Sood, R.E. Welser, G.G. Pethuraja, Y.R. Puri, X. Yan, D.J. Poxson, J. Cho, E.F. Schubert, N.K. Dhar, D.L. Polla, P. Haldar, J.L. Harvey, Development of nanostructured antireflection coatings for EO/IR sensor and solar

cell applications, Mater. Sci. Appl. 3 (2012) 633–639.

[141] Y.M. Song, Y. Jeong, C. Il Yeo, Y.T. Lee, Enhanced power generation in concentrated photovoltaics using broadband antireflective coverglasses with moth eye structures, Opt. Express. 20 (2012) 916–923.

[142] A. Musset, A. Thelen, IV Multilayer antireflection coatings, Prog. Opt. 8 (1970) 201–237.

[143] H.A. Macleod, Thin-Film Optical Filters, CRC Press, Boca Raton, 2001.

[144] H.K. Raut, V.A. Ganesh, A.S. Nair, S. Ramakrishna, Anti-reflective coatings: A critical, in-depth review, Energy Environ. Sci. 4 (2011) 3779–3804.

[145] S. Chattopadhyay, Y.F. Huang, Y.J. Jen, A. Ganguly, K.H. Chen, L.C. Chen, Anti-reflecting and photonic nanostructures, Mater. Sci. Eng. R. 69 (2010) 1–35.

[146] M.F. Schubert, D.J. Poxson, F.W. Mont, J.K. Kim, E.F. Schubert, Performance of antireflection coatings consisting of multiple discrete layers and comparison with continuously graded antireflection coatings, Appl. Phys. Express. 3 (2010) 082502.

[147] J.W. Leem, D.-H. Jun, J. Heo, W.-K. Park, J.-H. Park, W.J. Cho, D.E. Kim, J.S. Yu, Single-material zinc sulfide bi-layer antireflection coatings for GaAs solar cells, Opt. Express. 21 (2013) A821.

[148] Y.J. Park, K.M.A. Sobahan, J.J. Kim, C.K. Hwangbo, Antireflection coatings with helical SiO_2 films prepared by using glancing angle deposition, J. Korean Phys. Soc. 55 (2009) 2634–2637.

[149] S. Sarkar, S.K. Pradhan, Silica-based antireflection coating by glancing angle deposition, Surf. Eng. 35 (2019) 982–985.

[150] K. Ellmer, R. Mientus, Carrier transport in polycrystalline ITO and ZnO:Al II: The influence of grain barriers and boundaries, Thin Solid Films. 516 (2008) 5829–5835.

[151] S.J. Jang, C.I. Yeo, Y.T. Lee, Amorphous silicon Bragg reflectors fabricated by oblique angle deposition, Mater. Res. Soc. Symp. Proc. 1396 (2012) 231–236.

[152] S.J. Jang, Y.M. Song, C. Il Yeo, C.Y. Park, Y.T. Lee, Highly tolerant a-Si distributed Bragg reflector fabricated by oblique angle deposition, Opt. Mater. Express. 1 (2011) 451.

[153] J.W. Leem, J.S. Yu, Broadband and wide-angle distributed Bragg reflectors based on amorphous germanium films by glancing angle deposition, Opt. Express. 20 (2012) 20576.

[154] J.W. Leem, J.S. Yu, Design and fabrication of amorphous germanium thin film-based single-material distributed Bragg reflectors operating near 22 μm for long wavelength applications, J. Opt. Soc. Am. B. 30 (2013) 838.

[155] F. Nita, C. Mastail, G. Abadias, Three-dimensional kinetic Monte Carlo simulations of cubic transition metal nitride thin film growth, Phys. Rev. B. 93 (2016) 064107.

[156] C. Lopez-Santos, R. Alvarez, A. Garcia-Valenzuela, V. Rico, M. Loeffler, A.R. Gonzalez-Elipe, A. Palmero, Nanocolumnar association and domain formation in porous thin films grown by evaporation at oblique angles, Nanotechnology. 27 (2016) 395702.

[157] X. Yan, F.W. Mont, D.J. Poxson, M.F. Schubert, J.K. Kim, J. Cho, E.F. Schubert, Refractive-index-matched indium-tin-oxide electrodes for liquid crystal displays, Jpn. J. Appl. Phys. 48 (2009) 120203.

[158] Y. Zhang, W. Guo, W. Gao, C. Li, T. Ding, Properties of the ITO layer in a novel red light-emitting diode, J. Semicond. 31 (2010) 043002.

[159] D. Choi, H. Yoon, K.H. Kim, H.D. Um, K. Seo, ITO-free carrier-selective contact for crystalline silicon solar cells, J. Mater. Chem. A. 7 (2019) 2192–2199.

[160] T.C. Gorjanc, D. Leong, C. Py, D. Roth, Room temperature deposition of ITO using R.F. Magnetron sputtering, Thin Solid Films. 413 (2002) 181–185.

[161] N. Danson, I. Safi, G.W. Hall, R.P. Howson, Techniques for the sputtering of optimum indium-tin oxide films on to room-temperature substrates, Surf. Coatings Technol. 99 (1998) 147–160.

[162] W.F. Wu, B.S. Chiou, Effect of annealing on electrical and optical properties of RF magnetron sputtered indium tin oxide films, Appl. Surf. Sci. 68 (1993) 497–504.

[163] R. Bel Hadj Tahar, T. Ban, Y. Ohya, Y. Takahashi, Tin doped indium oxide thin films: Electrical properties, J. Appl. Phys. 83 (1998) 2631–2645.

[164] I. Hamberg, C.G. Granqvist, Evaporated Sn-doped In_2O_3 films: Basic optical properties and applications to energy-efficient windows, J. Appl. Phys. 60 (1986) R123.

[165] Y. Shigesato, S. Takaki, T. Haranou, Crystallinity and electrical properties of tin-doped indium oxide films deposited by DC magnetron sputtering, Appl. Surf. Sci. 48–49 (1991) 269–275.

[166] S. Ray, R. Banerjee, N. Basu, A.K. Batabyal, A.K. Barua, Properties of tin doped indium oxide thin films prepared by magnetron sputtering, J. Appl. Phys. 54 (1983) 3497–3501.

[167] H. Kim, C.M. Gilmore, A. Piqué, J.S. Horwitz, H. Mattoussi, H. Murata, Z.H. Kafafi, D.B. Chrisey, Electrical, optical, and structural properties of indium-tin-oxide thin films for organic light-emitting devices, J. Appl. Phys. 86 (1999) 6451–6461.

[168] D. Kim, Y. Han, J.-S. Cho, S.-K. Koh, Low temperature deposition of ITO thin films by ion beam sputtering, Thin Solid Films. 377–378 (2000) 81–86.

[169] Y. Han, D. Kim, J.-S. Cho, S.-K. Koh, Y.S. Song, Tin-doped indium oxide (ITO) film deposition by ion beam sputtering, Sol. Energy Mater. Sol. Cells. 65 (2001) 211–218.

[170] J. Parra-Barranco, J.R. Sanchez-Valencia, F.J. Aparicio, F. Garcia-Garcia, F.J.

Ferrer, V. Rico, C. Lopez-Santos, A. Borras, A.R. Gonzalez-Elipe, A. Barranco, Plasma assisted oblique angle deposition of transparent and conductive in-plane anisotropic ITO thin films, ECS Trans. 77 (2017) 9–15.

[171] L.-C. Chen, C.-C. Chen, Y.-T. Sung, Y.-Y. Hsu, Oblique-angle sputtering effects on characteristics of nanocolumnar structure anisotropic indium tin oxide films, J. Electrochem. Soc. 156 (2009) H471.

[172] C.H. Chang, Y.P. Peichen, C.S. Yang, Broadband and omnidirectional antireflection from conductive indium-tin-oxide nanocolumns prepared by glancing-angle deposition with nitrogen, Appl. Phys. Lett. 94 (2009) 051114.

[173] B. Yosvichit, N. Siriphongsapak, M. Horprathum, P. Eiamchai, V. Patthanasettakul, S. Limwichean, P. Chindaudom, C. Oros, S. Denchitcharoen, High optical transmittance of indium tin oxide nanorods prepared by electron beam evaporation with glancing angle deposition technique, Chiang Mai J. Sci. 43 (2016) 271–275.

[174] G. Oh, S.P. Kim, K.S. Lee, E.K. Kim, Structural properties of indium tin oxide thin films by glancing angle deposition method, J. Nanosci. Nanotechnol. 13 (2013) 7149–7151.

[175] J.W. Leem, J.S. Yu, Glancing angle deposited ITO films for efficiency enhancement of a-Si:H/μc-Si:H tandem thin film solar cells, Opt. Express. 19 (2011) A258–A268.

[176] Y. Zhong, Y.C. Shin, C.M. Kim, B.G. Lee, E.H. Kim, Y.J. Park, K.M.A. Sobahan, C.K. Hwangbo, Y.P. Lee, T.G. Kim, Optical and electrical properties of indium tin oxide thin films with tilted and spiral microstructures prepared by oblique angle deposition, J. Mater. Res. 23 (2008) 2500–2505.

[177] C.-S. Yang, C.-M. Chang, P.-H. Chen, P. Yu, C.-L. Pan, Broadband terahertz conductivity and optical transmission of indium-tin-oxide (ITO) nanomaterials, Opt. Express. 21 (2013) 16670.

[178] Y.-C. Yao, M.-T. Tsai, H.-C. Hsu, L.-W. She, C.-M. Cheng, Y.-C. Chen, C.-J. Wu, Y.-J. Lee, Use of two-dimensional nanorod arrays with slanted ITO film to enhance optical absorption for photovoltaic applications, Opt. Express. 20 (2012) 1618–1621.

[179] J.W. Leem, J.S. Yu, Influence of oblique-angle sputtered transparent conducting oxides on performance of Si-based thin film solar cells, Phys. Status Solidi Appl. Mater. Sci. 208 (2011) 2220–2225.

[180] Y.-C. Chi, D.-H. Hsieh, C.-T. Tsai, H.-Y. Chen, H.-C. Kuo, G.-R. Lin, 450-nm GaN laser diode enables high-speed visible light communication with 9-Gbps QAM-OFDM, Opt. Express. 23 (2015) 13051.

[181] M. Micovic, P. Hashimoto, M. Hu, I. Milosavljevic, J. Duvall, P.J. Willadsen, W.S. Wong, A.M. Conway, A. Kurdoghlian, P.W. Deelman, J.S. Moon, A. Schmitz, M.J. Delaney, GaN double heterojunction field effect transistor for microwave and millimeterwave power applications, Tech. Dig.-Int. Electron Devices Meet. IEDM. (2004) 807–810.

[182] F.A. Ponce, D.P. Bour, Nitride-based semiconductors for blue and green light-emitting devices, Nature. 386 (1997) 351–359.

[183] D. Lee, J. Lee, Y. Lee, D. Lee, GaN thin films as gas sensors, Sensors Actuators, B. 89 (2003) 305-310.

[184] M.A.H. Khan, M. Rao, Gallium nitride (GaN) nanostructures and their gas sensing properties: A review, Sensors. 20 (2020) 3889.

[185] M. Sung, C. Lee, J. Beom, H. Yoo, G. Yi, Gallium nitride nanostructures for light-emitting diode applications, Nano Energy. 1 (2012) 391–400.

[186] T. Kente, S. Dalton, Gallium nitride nanostructures : Synthesis, characterization and applications, J. Cryst. Growth. 444 (2016) 55–72.

[187] R. Yan, D. Gargas, P. Yang, Nanowire photonics, Nat. Photonics. 3 (2009) 569–576.

[188] K. Lee, S. Chae, J. Jang, D. Min, J. Kim, O. Nam, Self-assembled growth of inclined GaN nanorods on nanoimprinted *m*-plane sapphire using catalyst-free metal-organic chemical vapor deposition, AIP Adv. 6 (2016) 045209.

[189] E. Calleja, J. Ristić, S. Fernández-Garrido, L. Cerutti, M. A. Sánchez-García, J. Grandal, A. Trampert, U. Jahn, G. Sánchez, A. Griol, B. Sánchez, Growth, morphology, and structural properties of group-III-nitride nanocolumns and nanodisks, Phys. Status Solidi Basic Res. 244 (2007) 2816–2837.

[190] M. Kesaria, S. Shetty, S.M. Shivaprasad, B. Gan, Spontaneous formation of GaN nanostructures by molecular beam epitaxy, J. Cryst. Growth. 326 (2011) 191–194.

[191] Y. Cui, Z. Zhong, D. Wang, W.U. Wang, C.M. Lieber, High performance silicon nanowire field effect transistors, Nano Lett. 2 (2003) 149–152.

[192] Y. Huang, X. Duan, Y. Cui, C.M. Lieber, Gallium nitride nanowire nanodevices, Nano Lett. 2 (2002) 101–104.

[193] H. Chen, H. Lin, C. Wu, W. Chen, J. Chen, S. Gwo, Gallium nitride nanorod arrays as low- refractive-index transparent media in the entire visible spectral region, Opt. Express. 16 (2008) 8106–8116.

[194] A. Wohlfart, A. Devi, E. Maile, R.A. Fischer, Morphology controlled growth of arrays of GaN nanopillars and randomly distributed GaN nanowires on sapphire using $(N_3)_2Ga[(CH_2)_3NMe_2]$ as a single molecule precursor, Chem. Commun. 2002 (2002) 998–999.

[195] M. Sobanska, Z.R. Zytkiewicz, G. Calabrese, L. Geelhaar, S. Fernández-Garrido, Comprehensive analysis of the self-assembled formation of GaN nanowires on amorphous Al_xO_y: in situ quadrupole mass spectrometry studies, Nanotechnology. 30 (2019) 154002.

[196] S. Shetty, M. Kesaria, J. Ghatak, S.M. Shivaprasad, The origin of shape, orientation, and structure of spontaneously formed wurtzite GaN nanorods on cubic Si(001) surface, Cryst. Growth Des. 13 (2013) 2407–2412.

[197] A.D. Bolshakov, A.M. Mozharov, G.A. Sapunov, I. V. Shtrom, N. V. Sibirev, V. V. Fedorov, E. V. Ubyivovk, M. Tchernycheva, G.E. Cirlin, I.S. Mukhin, Dopant-stimulated growth of GaN nanotube-like nanostructures on Si(111) by molecular beam epitaxy, Beilstein J. Nanotechnol. 9 (2018) 146–154.

[198] S. Fernandez-Garrido, V. Kaganer, K. Sabelfeld, J. Grandal, E. Calleja, L. Geelhaar, O. Brandt, GaN nanowires in molecular beam epitaxy Self-regulated radius of spontaneously formed GaN nanowires in molecular beam epitaxy, Nano Lett. 13 (2013) 3274–3280.

[199] A. Wierzbicka, Z.R. Zytkiewicz, S. Kret, J. Borysiuk, P. Dluzewski, M. Sobanska, K. Klosek, A. Reszka, G. Tchutchulashvili, A. Cabaj, E. Lusakowska, Influence of substrate nitridation temperature on epitaxial alignment of GaN nanowires to Si (111) substrate, Nanotechnology. 24 (2013) 035703.

[200] A. Wierzbicka, Z.R. Zytkiewicz, S. Kret, J. Borysiuk, P. Dluzewski, M. Sobanska, K. Klosek, a Reszka, G. Tchutchulashvili, a Cabaj, E. Lusakowska, Influence of substrate nitridation temperature on epitaxial alignment of GaN nanowires to Si(111) substrate, Nanotechnology. 24 (2013) 035703.

[201] A.-L. Henneghien, G. Tourbot, B. Daudin, O. Lartigue, Y. Désières, J.-M. Gérard, Optical anisotropy and light extraction efficiency of MBE grown GaN nanowires epilayers, Opt. Express. 19 (2011) 527.

[202] R. Gurwitz, I. Shalish, Method for electrical characterization of nanowires, Nanotechnology. 22 (2011) 435705.

[203] L.M. Mansfield, K.A. Bertness, P.T. Blanchard, T.E. Harvey, A.W. Sanders, N.A. Sanford, GaN nanowire carrier concentration calculated from light and dark resistance measurements, J. Electron. Mater. 38 (2009) 495–504.

[204] O. Hultin, G. Otnes, M.T. Borgström, M. Björk, L. Samuelson, K. Storm, Comparing Hall effect and field effect measurements on the same single nanowire, Nano Lett. 16 (2016) 205–211.

[205] K. Storm, F. Halvardsson, M. Heurlin, D. Lindgren, A. Gustafsson, P.M. Wu, B. Monemar, L. Samuelson, Spatially resolved Hall effect measurement in a single semiconductor nanowire, Nat. Nanotechnol. 7 (2012) 718–722.

[206] A. Motayed, M. Vaudin, A. V. Davydov, J. Melngailis, M. He, S.N. Mohammad, Diameter dependent transport properties of gallium nitride nanowire field effect transistors, Appl. Phys. Lett. 90 (2007) 043104.

[207] X. Wen, W. Wu, Y. Ding, Z.L. Wang, Seedless synthesis of patterned ZnO nanowire arrays on metal thin films (Au, Ag, Cu, Sn) and their application for flexible electromechanical sensing, J. Mater. Chem. 22 (2012) 9469–9476.

[208] Z.H. Chen, Y.B. Tang, Y. Liu, G.D. Yuan, W.F. Zhang, J.A. Zapien, I. Bello, W.J. Zhang, C.S. Lee, S.T. Lee, ZnO nanowire arrays grown on Al:ZnO buffer layers and their enhanced electron field emission, J. Appl. Phys. 106 (2009) 064303.

[209] S. Roddaro, K. Nilsson, G. Astromskas, L. Samuelson, L.-E. Wernersson, O. Karlstrom, A. Wacker, InAs nanowire metal-oxide-semiconductor capacitors, Appl. Phys. Lett. 92 (2008) 253509.

[210] P. Parkinson, C. Dodson, H.J. Joyce, K.A. Bertness, N.A. Sanford, L.M. Herz, M.B. Johnston, Noncontact measurement of charge carrier lifetime and mobility in GaN nanowires, Nano Lett. 12 (2012) 4600–4604.

[211] C. Zhao, S. Ma, Z. Li, W. Li, J. Li, Q. Hou, Y. Xing, Simple and fast fabrication of single crystal VO_2 microtube arrays, Commun. Mater. 1 (2020) 28.

[212] W. Zeng, N. Chen, W. Xie, Research progress on the preparation methods for VO_2 nanoparticles and their application in smart windows, CrystEngComm. 22 (2020) 851–869.

[213] Y. Gao, H. Luo, Z. Zhang, L. Kang, Z. Chen, J. Du, M. Kanehira, C. Cao, Nanoceramic VO_2 thermochromic smart glass: A review on progress in solution processing, Nano Energy. 1 (2012) 221–246.

[214] M.M. Seyfouri, R. Binions, Sol-gel approaches to thermochromic vanadium dioxide coating for smart glazing application, Sol. Energy Mater. Sol. Cells. 159 (2017) 52–65.

[215] H. Liu, O. Vasquez, V.R. Santiago, L. Diaz, A.J. Rua, F.E. Fernandez, Novel pulsed-laser-deposition-VO_2 thin films for ultrafast applications, J. Electron. Mater. 34 (2005) 491–496.

[216] Y.L. Wang, X.K. Chen, M.C. Li, R. Wang, G. Wu, J.P. Yang, W.H. Han, S.Z. Cao, L.C. Zhao, Phase composition and valence of pulsed laser deposited vanadium oxide thin films at different oxygen pressures, Surf. Coatings Technol. 201 (2007) 5344–5347.

[217] R. Binions, G. Hyett, C. Piccirillo, I.P. Parkin, Doped and un-doped vanadium dioxide thin films prepared by atmospheric pressure chemical vapour deposition from vanadyl acetylacetonate and tungsten hexachloride: The effects of thickness and crystallographic orientation on thermochromic properties, J. Mater. Chem. 17 (2007) 4652–4660.

[218] J. Du, Y. Gao, H. Luo, L. Kang, Z. Zhang, Z. Chen, C. Cao, Significant changes in phase-transition hysteresis for Ti-doped VO_2 films prepared by polymer-assisted deposition, Sol. Energy Mater. Sol. Cells. 95 (2011) 469–475.

[219] V. Collado, N. Martin, P. Pedrosa, J.Y. Rauch, M. Horakova, M.A.P. Yazdi, A. Billard, Temperature dependence of electrical resistivity in oxidized vanadium films grown by the GLAD technique, Surf. Coatings Technol. 304 (2016) 476–485.

[220] H. Zhang, Z. Wu, D. Yan, X. Xu, Y. Jiang, Tunable hysteresis in metal-insulator transition of nanostructured vanadium oxide thin films deposited by reactive direct current magnetron sputtering, Thin Solid Films. 552 (2014) 218–224.

[221] G. Rampelberg, B. De Schutter, W. Devulder, K. Martens, I. Radu, C. Detavernier, In situ X-ray diffraction study of the controlled oxidation and reduction in the V-O system for the synthesis of VO_2 and V_2O_3 thin films, J. Mater. Chem. C. 3 (2015) 11357–11365.

[222] Y.X. Ji, G.A. Niklasson, C.G. Granqvist, M. Boman, Thermochromic VO_2 films by thermal oxidation of vanadium in SO_2, Sol. Energy Mater. Sol. Cells. 144

(2016) 713–716.

[223] P. Pedrosa, N. Martin, R. Salut, M.A.P. Yazdi, A. Billard, Controlled thermal oxidation of nanostructured vanadium thin films, Mater. Lett. 174 (2016) 162–166.

[224] H.M.R. Giannetta, C. Calaza, L. Fraigi, L. Fonseca, Vanadium oxide thin films obtained by thermal annealing of layers deposited by RF magnetron sputtering at room temperature, in Modern technologies for creating the thin-film systems and coatings, by N. Nikitenkov, InTechOpen, London (2017).

[225] M. Kamalisarvestani, R. Saidur, S. Mekhilef, F.S. Javadi, Performance, materials and coating technologies of thermochromic thin films on smart windows, Renew. Sustain. Energy Rev. 26 (2020) 353–364.

[226] Y. Zhou, Y. Cai, X. Hu, Y. Long, Temperature-responsive hydrogel with ultra-large solar modulation and high luminous transmission for "smart window" applications, J. Mater. Chem. A Mater. Energy Sustain. 2 (2014) 13550–13555.

[227] X. Cao, N. Wang, J.Y. Law, S. Chye, J. Loo, S. Magdassi, Y. Long, Nanoporous thermochromic VO_2(M) thin films: Controlled porosity, largely enhanced luminous transmittance and solar modulating ability, Langmuir. 30 (2014) 1710−1715.

[228] M. Zhou, J. Bao, M. Tao, R. Zhu, Y. Lin, X. Zhang, Y. Xie, Periodic porous thermochromic VO_2(M) films with enhanced visible transmittance, Chem. Commun. 49 (2013) 6021−6023.

[229] L. Kang, Y. Gao, H. Luo, Z. Chen, J. Du, Z. Zhang, Nanoporous thermochromic VO_2 films with low optical constants, enhanced luminous transmittance and thermochromic properties, ACS Appl. Mater. Interfaces. 3 (2011) 135–138.

[230] L. Kang, Y. Gao, Z. Zhang, J. Du, C. Cao, Z. Chen, H. Luo, Effects of annealing parameters on optical properties of thermochromic VO_2 films prepared in aqueous solution, J. Phys. Chem. C 114 (2010) 1901–1911.

[231] Y. Huang, D. Zhang, Y. Liu, J. Jin, Y. Yang, T. Chen, H. Guan, P. Fan, W. Lv, Phase transition analysis of thermochromic VO_2 thin films by temperature-dependent Raman scattering and ellipsometry, Appl. Surf. Sci. 456 (2018) 545–551.

[232] M.A. Mamun, K. Zhang, H. Baumgart, A.A. Elmustafa, Evaluation of the nanomechanical properties of vanadium and native oxide vanadium thin films prepared by RF magnetron sputtering, Appl. Surf. Sci. 359 (2015) 30–35.

[233] D.A.G. Bruggeman, Berechnung verschiedener physikalischer konstanten von heterogenen substanzen. III. Die elastischen konstanten der quasiisotropen mischkörper aus isotropen substanzen, Ann. Phys. 421 (1937) 160–178.

[234] S. Chatterjee, M. Kumar, S. Gohil, T. Som, An oblique angle radio frequency sputtering method to fabricate nanoporous hydrophobic TiO_2 film, Thin Solid Films. 568 (2014) 81–86.

[235] R.K. Jain, J. Kaur, S. Arora, A. Kumar, A.K. Chawla, A. Khanna, Effects of oblique angle deposition on structural, electrical and wettability properties of Bi

thin films grown by thermal evaporation, Appl. Surf. Sci. 463 (2019) 45–51.

[236] W. Theiss, SCOUT Technical manual, (2014).

[237] 3-5µm AR Coated Silicon from EdmundOptics available on www.edmundoptics.com (accessed June 28, 2021).

[238] T. Karabacak, P. Singh, Y.P. Zhao, G.C. Wang, T.M. Lu, Scaling during shadowing growth of isolated nanocolumns, Phys. Rev. B - Condens. Matter Mater. Phys. 68 (2003) 125408.

[239] S. Mukherjee, D. Gall, Power law scaling during physical vapor deposition under extreme shadowing conditions, J. Appl. Phys. 107 (2010) 084301.

[240] D. Vick, T. Smy, M.J. Brett, Growth behavior of evaporated porous thin films, J. Mater. Res. 17 (2002) 2904–2911.

[241] R. Alvarez, C. Lopez-Santos, J. Parra-Barranco, V. Rico, A. Barranco, J. Cotrino, A.R. Gonzalez-Elipe, A. Palmero, Nanocolumnar growth of thin films deposited at oblique angles: Beyond the tangent rule, J. Vac. Sci. Technol. B, Nanotechnol. Microelectron. Mater. Process. Meas. Phenom. 32 (2014) 041802.

[242] D. Schmidt, M. Schubert, Anisotropic Bruggeman effective medium approaches for slanted columnar thin films, J. Appl. Phys. 114 (2013) 083510.

[243] B. Lacroix, F. Paumier, R.J. Gaboriaud, Crystal defects and related stress in Y_2O_3 thin films: Origin, modeling, and consequence on the stability of the C-type structure, Phys. Rev. B. 84 (2011) 014104.

[244] F. Meyer, D. Louchier, V. Stambouli, C. Pellet, C. Schwebel, G. Gautherin, Ion beam sputtering deposition of tungsten: Energy and mass effects of primary ions, Appl. Surf. Sci. 38 (1989) 286–294.

[245] M. Thirumoorthi, J. Thomas Joseph Prakash, Structure, optical and electrical properties of indium tin oxide ultra thin films prepared by jet nebulizer spray pyrolysis technique, J. Asian Ceram. Soc. 4 (2016) 124–132.

[246] G.B. González, J.B. Cohen, J. Hwang, T.O. Mason, J.P. Hodges, D. James, J.B. Cohen, J. Hwang, T.O. Mason, Neutron diffraction study on the defect structure of indium-tin-oxide, J. Appl. Phys. 89 (2001) 2550.

[247] Y.S. Jung, A spectroscopic ellipsometry study on the variation of the optical constants of tin-doped indium oxide thin films during crystallization, Solid State Commun. 129 (2004) 491–495.

[248] O. Tuna, Y. Selamet, G. Aygun, L. Ozyuzer, High quality ITO thin films grown by DC and RF sputtering without oxygen, J. Phys. D. Appl. Phys. 43 (2010) 055402.

[249] Ž. Gačević, A. Bengoechea-Encabo, S. Albert, A. Torres-Pardo, J. M. González-Calbet, E. Calleja, Crystallographically uniform arrays of ordered (In)GaN nanocolumns, J. Appl. Phys. 117 (2015) 035301.

[250] S.A. Morin, M.J. Bierman, J. Tong, S. Jin, Mechanism and kinetics of spontaneous

nanotube growth driven by screw dislocations, Science 328 (2010) 476–480.

[251] F. Schuster, M. Hetzl, S. Weiszer, J.A. Garrido, M. De La Mata, C. Magen, J. Arbiol, M. Stutzmann, Position-controlled growth of GaN nanowires and nanotubes on diamond by molecular beam epitaxy, Nano Lett. 15 (2015) 1773–1779.

[252] J. Park, A. Mandal, S. Kang, U. Chatterjee, J.S. Kim, Hydrogen generation using non-polar coaxial InGaN/GaN multiple quantum well structure formed on hollow n-GaN nanowires, Sci. Rep. 6 (2016) 31996.

[253] J. Gospodyn, J.C. Sit, Characterization of dielectric columnar thin films by variable angle Mueller matrix and spectroscopic ellipsometry, Opt. Mater. (Amst). 29 (2006) 318–325.

[254] S.B. Jones, S.P. Friedman, Particle shape effects on the effective permittivity of anisotropic or isotropic media consisting of aligned or randomly oriented ellipsoidal particles, Water Resour. Res. 36 (2000) 2821–2833.

[255] S. Adachi, Optical constants of crystalline and amorphous semiconductors, Springer, Boston, 1999.

[256] G.E. Jellison, F.A. Modine, Parameterization of the optical functions of amorphous materials in the interband region, Appl. Phys. Lett. 69 (1996) 371–373.

[257] H. Fujiwara, M. Kondo, Effects of carrier concentration on the dielectric function of ZnO:Ga and In_2O_3:Sn studied by spectroscopic ellipsometry: Analysis of free-carrier and band-edge absorption, Phys. Rev. B - Condens. Matter Mater. Phys. 71 (2005) 075109.

[258] J.W. Orton, M.J. Powell, The Hall effect in polycrystalline and powdered semiconductors, Reports Prog. Phys. 43 (1980) 1263–1307.

[259] N.J. Watkins, G.W. Wicks, Y. Gao, Oxidation study of GaN using X-ray photoemission spectroscopy, Appl. Phys. Lett. 75 (1999) 2602.

[260] R. Jakiela, E. Dumiszewska, P. Caban, A. Stonert, A. Turos, A. Barcz, Oxygen diffusion into GaN from oxygen implanted GaN or Al_2O_3, Phys. Status Solidi. 8 (2011) 1513–1515.

[261] S.J. Pearton, H. Cho, J.R. Laroche, F. Ren, R.G. Wilson, J.W. Lee, Oxygen diffusion into SiO_2-capped GaN during annealing, Appl. Phys. Express. 2939 (2012) 73–76.

[262] Y. Li, S. Ji, Y. Gao, H. Luo, M. Kanehira, Core-shell VO_2@TiO_2 nanorods that combine thermochromic and photocatalytic properties for application as energy-saving smart coatings, Sci. Rep. 3 (2013) 1370.

[263] P. Vilanova-Martínez, J. Hernández-Velasco, A.R. Landa-Cánovas, F. Agulló-Rueda, Laser heating induced phase changes of VO_2 crystals in air monitored by Raman spectroscopy, J. Alloys Compd. 661 (2016) 122–125.

[264] D. Louloudakis, D. Vernardou, E. Spanakis, M. Suchea, G. Kenanakis, M. Pemble, K. Savvakis, N. Katsarakis, E. Koudoumas, G. Kiriakidis, Atmospheric pressure

chemical vapor deposition of amorphous tungsten doped vanadium dioxide for smart window applications, Adv. Mater. Lett. 7 (2016) 192–196.

[265] P. Shvets, O. Dikaya, K. Maksimova, A. Goikhman, A review of Raman spectroscopy of vanadium oxides, J. Raman Spectrosc. 50 (2019) 1226–1244.

[266] M.M. Margoni, S. Mathuri, K. Ramamurthi, R.R. Babu, K. Sethuraman, Sprayed vanadium pentoxide thin films: Influence of substrate temperature and role of HNO_3 on the structural, optical, morphological and electrical properties, Appl. Surf. Sci. 418 (2017) 280–290.

[267] A. Baltakesmez, C. Aykaç, B. Güzeldir, Phase transition and changing properties of nanostructured V_2O_5 thin films deposited by spray pyrolysis technique, as a function of tungsten dopant, Appl. Phys. A Mater. Sci. Process. 125 (2019) 441.

[268] A. Sohn, T. Kanki, K. Sakai, H. Tanaka, D.W. Kim, Fractal nature of metallic and insulating domain configurations in a VO_2 thin film revealed by Kelvin probe force microscopy, Sci. Rep. 5 (2015) 10417.

[269] M. Suzuki, Practical applications of thin films nanostructured by shadowing growth, J. Nanophotonics. 7 (2013) 073598.

[270] M. Suzuki, A. Takada, T. Yamada, T. Hayasaka, K. Sasaki, E. Takahashi, S. Kumagai, Low-reflectivity wire-grid polarizers multilayered by the glancing-angle-deposition technique, J. Nanophotonics. 5 (2011) 051501.

[271] M. Suzuki, A. Takada, T. Yamada, T. Hayasaka, K. Sasaki, Antireflection coatings with $FeSi_2$ layer: Application to low-reflectivity wire grid polarizers, Thin Solid Films. 519 (2011) 8485–8489.

[272] M. Suzuki, W. Maekita, Y. Wada, Ag nanorod arrays tailored for surface-enhanced Raman imaging in the near-infrared region, Nanotechnology. 19 (2008) 265304.

[273] M. Suzuki, K. Nakajima, K. Kimura, T. Fukuoka, Y. Mori, Au Nanorod Arrays Tailored for Surface-Enhanced Raman, Anal. Sci. 23 (2007) 829–833.

[274] https://ec.europa.eu/energy/topics/energy-strategy/clean-energy-all-europeans_en (accessed July 3, 2021).

[275] https://glassforeurope.com/mobile-air-conditioning-systems-macs/ (accessed 3 July, 2021).

[276] E. Cuce, S.B. Riffat, A state-of-the-art review on innovative glazing technologies, Renew. Sustain. Energy Rev. 41 (2015) 695–714.

[277] S.B. Khan, H. Wu, J. Li, L. Chen, Z. Zhang, Bilayer SiO_2 nanorod arrays as omnidirectional and thermally stable antireflective coating, Adv. Eng. Mater. 20 (2018) 1700942.

Appendices

Appendices

In this section of the Thesis, Appendix I details the list of publications that do not form part of the main articles included in this Thesis. Afterward, Appendix II includes the list of works that are part of this *Thesis by Compendium of Publications*.

During this PhD Thesis, the author has participated as first author or co-author in 15 publications, a patent (presented on 10 June 2021) and 22 congress communications.

Appendix I

Publications

I. C. Fernández-Ponce, J. M. Mánuel, R. Fernández-Cisnal, E. Félix, J. Beato-López, J. P. Muñoz-Miranda, A. M. Beltrán, **A. J. Santos**, F. M. Morales, M. P. Yeste, O. Bomati-Miguel, R. Litrán, F. García-Cózar. *Superficial Characteristics and Functionalization Effectiveness of Non-Toxic Glutathione-Capped Magnetic, Fluorescent, Metallic and Hybrid Nanoparticles for Biomedical Applications*, Metals 11: 383 (2021).

II. P. Banerjee, C. Roy, S. K. De, **A. J. Santos**, F. M. Morales, S. Bhattacharyya. *Atomically resolved tomographic reconstruction of nanoparticles from single projection: Influence of amorphous carbon support*, Ultramicroscopy 221: 113177 (2021).

III. M. Beltrán, J. M. Mánuel, R. Litrán, E. Félix, **A. J. Santos**, F. M. Morales, O. Bomatí-Miguel. *(S)TEM structural and compositional nanoanalyses of chemically synthesized glutathione-shelled nanoparticles*, Applied Nanoscience 10: 2295–2301 (2020).

IV. García-Valenzuela, S. Muñoz-Piña, G. Alcalá, R. Álvarez, B. Lacroix, **A. J. Santos**, J. Cuevas, V. Rico, R. Gago, L. Vazquez, J. Cotrino, A. R. Gonzalez-Elipe, A. Palmero. *Growth of nanocolumnar thin films on patterned substrates at oblique angles*, Plasma Processes and Polymers 16: 1800135 (2019).

V. J. M. Mánuel, J. J. Jiménez, F. M. Morales, B. Lacroix, **A. J. Santos**, R. García, E. Blanco, M. Domínguez, M. Ramírez, A. M. Beltrán, D. Alexandrov, J. Tot, R. Dubreuil, V. Videkov, S. Andreev, B. Tzaneva, H. Bartsch, J. Breiling, J. Pezoldt, M. Fischer, J. Müller. *Engineering of III-nitride semiconductors on low temperature co-fired ceramics*, Scientific Reports 8: 6879 (2018).

There is an additional manuscript, submitted to Nanoscale:

VI. **A. J. Santos**, M. Escanciano, A. Suárez-Llorens, M. P. Yeste, F. M. Morales. *A novel route for the easy production of thermochromic VO_2 nanoparticles*.

Patent

INVENTORS: **A. J. Santos**, M. Escanciano, A. Suárez-Llorens, M. P. Yeste, F. M. Morales

TITLE: Fabricación directa de productos termocrómicos con alta carga de VO_2

PATENT NUMBER: P202130536

TITULAR ENTITY: University of Cadiz

Congresses

I. M. Escanciano, **A. J. Santos**, B. Lacroix, M. Figueroa, M. García, J. Perdigones, A. Suárez-Llorens, R. García, F. M. Morales. *Desarrollo y caracterización de un reactor de tratamientos térmicos de alta precisión*. VII Jornada de Investigación, Desarrollo e Innovación de la Escuela Politécnica Superior, November 4, 2020. Seville (Spain). *Poster Communication*.

II. E. Félix, O. Bomatí-Miguel, R. Litrán, J. M. Mánuel, A. M. Beltrán, **A. J. Santos**, F. M. Morales. *Empleo de técnicas (S)TEM para visualización de nanocapas amorfas de glutatión sobre nanopartículas semiconductoras*. VII Jornada de Investigación, Desarrollo e Innovación de la Escuela Politécnica Superior, November 4, 2020. Seville (Spain). *Poster Communication*.

III. **A. J. Santos**, B. Lacroix, E. Blanco, S. Hurand, V. J. Gómez, F. Paumier, T. Girardeau, D. L. Huffaker, R. García, F. M. Morales. *Crecimiento y*

caracterización avanzada de películas formadas por nanohilos epitaxiales de GaN. VI Jornada de Investigación, Desarrollo e Innovación de la Escuela Politécnica Superior, October 24–25, 2019. Seville (Spain). *Oral Communication*.

IV. S. Hurand, A. Corvisier, C. Dupeyrat, **A. J. Santos**, B. Lacroix, R. García, F. M. Morales, T. Girardeau, F. Paumier. *Investigation by spectroscopic ellipsometry, spectral reflectometry and electron microscopy of indium tin oxide thin films deposited at oblique angle by ion beam sputtering*. Journées Nationales 2019 du GDR OXYFUN, October 1–2, 2019. Caen (France). *Oral Communication*.

V. A. Corvisier, S. Hurand, F. Paumier, T. Girardeau, C. Dupeyrat, **A. J. Santos**, B. Lacroix. *Analyses by generalized ellipsometry of the anisotropy of an indium tin oxide metamaterial elaborated by ion beam sputtering in oblique angle deposition and suggestion of a two-layers optical model*. 8th International Conference on Spectroscopic Ellipsometry (ICSE8), May 26–31, 2019. Barcelona (Spain). *Poster Communication*.

VI. S. Hurand, A. Corvisier, F. Paumier, T. Girardeau, C. Dupeyrat, **A. J. Santos**, B. Lacroix. *Investigation by spectroscopic ellipsometry, spectral reflectometry and electron microscopy of indium tin oxide thin films deposited at oblique angle by ion beam sputtering*. 8th International Conference on Spectroscopic Ellipsometry (ICSE8), May 26–31, 2019. Barcelona (Spain). *Poster Communication.*

VII. F. Maudet, B. Lacroix, **A. J. Santos**, F. Paumier, M. Paraillous, C. Dupeyrat, R. García, F. M. Morales, T. Girardeau. *Nanostructured layers by oblique incidence deposition: microstructure and optical properties correlations for application to high-performance anti-reflection coatings*. 8th International Conference on Spectroscopic Ellipsometry (ICSE8), May 26–31, 2019. Barcelona (Spain). *Oral Communication*.

VIII. B. Lacroix, **A. J. Santos**, F. Maudet, A. Corvisier, F. Paumier, M. Paraillous, C. Dupeyrat, T. Girardeau, R. García, F. M. Morales. *Development of simple antireflective surfaces for IR optics using oblique angle deposition: from design to performances*. IBERTRIVA 2019, June 26–28, 2019. Seville (Spain). *Oral Communication*.

IX. S. Muñoz-Piña, A. García-Valenzuela, G. Alcalá, R. Álvarez, B. Lacroix, **A. J. Santos**, J. Cuevas-Maraver, V. Rico, R. Gago, L. Vázquez, J. Cotrino, A. R. González-Elipe, A. Palmero. *Magnetron sputtering depositions at oblique angles on patterned substrates for the development of sub-micron structural patterns*. IBERTRIVA 2019, June 26–28, 2019. Seville (Spain). *Oral Communication*.

X. **A. J. Santos**, V. J. Gómez, E. Blanco, B. Lacroix, R. García, D. L. Huffaker, F. M. Morales. *Structural studies and porosity control on GaN nanoporous films obtained from plasma-assisted molecular beam epitaxy self-assembled nanowires*. MATERIAIS 2019, XIX Congresso da Sociedade Portuguesa de Materiais and X International Symposium on Materials, April 14–17, 2019. Lisbon (Portugal). *Oral Communication*.

XI. **A. J. Santos**, B. Lacroix, F. Maudet, A. Corvisier, F. Paumier, C. Dupeyrat, T. Girardeau, R. García, F. M. Morales. *About the oxidation of antireflective nanoporous surfaces for optical applications in the infrared range*. MATERIAIS 2019, XIX Congresso da Sociedade Portuguesa de Materiais and X International Symposium on Materials, April 14–17, 2019. Lisbon (Portugal). *Poster Communication.*

XII. **A. J. Santos**, B. Lacroix, F. Maudet, M. Paraillous, F. Paumier, C. Dupeyrat, T. Girardeau, R. García, F. M. Morales. *Estudios basados en técnicas de microscopía (S)TEM avanzada para el desarrollo de sistemas nanoestructurados*

antirreflectantes fabricados mediante deposición en ángulo oblicuo. V Jornada de Investigación, Desarrollo e Innovación de la Escuela Politécnica Superior, October 30, 2018. Seville (Spain). *Oral Communication* (*awarded with the best presentation in the modality of PhD student*).

XIII. J. J. Jiménez, J. M. Mánuel, B. Lacroix, **A. J. Santos**, H. Bartsch, J. Pezoldt, J. Breiling, J. Müller, E. Blanco, M. Domínguez, D. Alexandrov, J. Tot, R. Dubreuil, V. Videkov, S. Andreev, B. Tzaneva, R. García, F. M. Morales. *Avances en la optimización del crecimiento a baja temperatura de heteroestructuras III-N/LTCC para electrónica de potencia basada en nitruros depositados sobre cerámicas multicapa*. V Jornada de Investigación, Desarrollo e Innovación de la Escuela Politécnica Superior, October 30, 2018. Seville (Spain). *Oral Communication*.

XIV. F. Paumier, S. Hurand, B. Lacroix, F. Maudet, **A. J. Santos**, C. Dupeyrat, M. Paraillous, A. Corvisier, R. García, F. M. Morales, Thierry Girardeau. *lndium Tin Oxide thin films deposited by Glancing Angle Deposition technique: Experimental and modelling of the anisotropic optical and electrical properties*. Materials Science and Engineering (MSE2018), September 26–28, 2018. Darmstadt (Germany). *Oral Communication*.

XV. F. Maudet, B. Lacroix, M. Paraillous, **A. J. Santos**, T. Girardeau, C. Dupeyrat, R. García, F. M. Morales, F. Paumier. *Comparative study of the transmittance and scattering behavior of continuously graded antireflective coatings and multiple discrete nanostructured layers deposited by Oblique Angle Deposition*. Materials Science and Engineering (MSE2018), September 26–28, 2018. Darmstadt (Germany). *Oral Communication*.

XVI. B. Lacroix, **A. J. Santos**, F. Maudet, M. Paraillous, F. Paumier, C. Dupeyrat, T. Girardeau, R. García, F. M. Morales. *Advanced (S)TEM applied on antireflective surfaces prepared by oblique angle deposition: a unique tool to establish new correlations between fabrication, nanostructure and performance*. Materials Science and Engineering (MSE2018), September 26–28, 2018. Darmstadt (Germany). *Oral Communication*.

XVII. **A. J. Santos**, B. Lacroix, F. Maudet, M. Paraillous, F. Paumier, C. Dupeyrat, T. Girardeau, R. García, F. M. Morales. *Advanced (S)TEM studies of nanostructured films grown by oblique angle deposition for efficient antireflective properties*. XV Congreso Nacional de Materiales (CNMAT2018), July 4–6, 2018. Salamanca (Spain). *Oral Communication*.

XVIII. J. J. Jiménez, J. M. Mánuel, B. Lacroix, **A. J. Santos**, H. Bartsch, J. Pezoldt, J. Breiling, J. Müller, E. Blanco, M. Domínguez, D. Alexandrov, J. Tot, R. Dubreuil, V. Videkov, S. Andreev, B. Tzaneva, R. García, F. M. Morales. *Progress in the optimization of low-temperature growth of III-N/LTCC heterostructures: towards multilayered ceramic-based nitrides power electronics*. XV Congreso Nacional de Materiales (CNMAT2018), July 4–6, 2018. Salamanca (Spain). *Oral Communication*.

XIX. B. Lacroix, **A. J. Santos**, S. Hurand, T. Girardeau, F. Maudet, C. Dupeyrat, R. García, F. M. Morales, F. Paumier. *Fabrication of transparent conductive indium-tin oxide films by oblique angle deposition: Relation between the growth parameters, nanostructure and properties for multispectral applications*. XV Congreso Nacional de Materiales (CNMAT2018), July 4–6, 2018. Salamanca (Spain). *Oral Communication*.

XX. F. Paumier, F. Maudet, B. Lacroix, **A. J. Santos**, C. Dupeyrat, S. Hurand, M. Paraillous, A. Corvisier, R. García, F. M. Morales, T. Girardeau. *Nanostructured thin films deposited by Oblique Angle Deposition for optronic applications: Influence of the nanostructuration on the optical properties and electrical conductivity mechanisms*. Journées Nationales 2018 du GDR OXYFUN, March 20–23, 2018. Piriac-Sur-Mer (France). *Oral Communication*.

XXI. F. M. Morales, M. A. Penela, L. Bey, **A. J. Santos**, A. J. García, M. Osorio, F. J. Puerto, R. García. *High-Temperature Degradation Mechanisms in some Stainless Steels (ferritic EN 1.4713 and austenitic EN 1.4571) and Nickel Superalloys (Monel 400)*. Microscopy at the Frontiers of Science 2017 (MFS2017), September 5–8, 2017. Zaragoza (Spain). *Oral Communication*.

XXII. B. Lacroix, F. Maudet, **A. J. Santos**, F.Paumier, C. Dupeyrat, T. Girardeau, R. García, F. M. Morales. *Contribution of advanced transmission electron microscopy in the studies of nanostructured layers fabricated by Oblique Angle Deposition for ultra-high performances anti-reflective coatings*. Microscopy at the Frontiers of Science 2017 (MFS2017), September 5–8, 2017. Zaragoza (Spain). *Oral Communication*.

Appendix II

Publication I

Surface oxidation of amorphous Si and Ge slanted columnar and mesoporous thin films: Evidence, scrutiny and limitations for infrared optics

A. J. Santos, B. Lacroix, F. Maudet, A. Corvisier, F. Paumier, C. Dupeyrat, T. Girardeau, R.García, F. M. Morales

Applied Surface Science 493 (2019) 807-817

Applied Surface Science 493 (2019) 807–817

Contents lists available at ScienceDirect

Applied Surface Science

journal homepage: www.elsevier.com/locate/apsusc

Full length article

Surface oxidation of amorphous Si and Ge slanted columnar and mesoporous thin films: Evidence, scrutiny and limitations for infrared optics

A.J. Santos[a,b], B. Lacroix[a,b], F. Maudet[c], A. Corvisier[c], F. Paumier[c], C. Dupeyrat[d], T. Girardeau[c], R. García[a,b], F.M. Morales[a,b,*]

[a] Department of Materials Science and Metallurgic Engineering, and Inorganic Chemistry, Faculty of Sciences, University of Cádiz, Spain
[b] IMEYMAT: Institute of Research on Electron Microscopy and Materials of the University of Cádiz, Spain
[c] Institut Pprime, UPR 3346 CNRS-Université de Poitiers-ENSMA, SP2MI, 86962 Futuroscope-Chasseneuil Cedex, France
[d] Safran Electronics and Defense, 26 avenue des Hauts de la Chaume, 86280 Saint-Benoît, France

ARTICLE INFO

Keywords:
Infrared optics
Oblique angle deposition
Surface oxidation
XPS
Transmission electron microscopy
Elemental analysis

ABSTRACT

Issues on the superficial oxidation of mesoporous amorphous silicon and germanium photonic layers generated at oblique angles are reported. Such films were designed to improve the transmittance of optical elements over the mid-IR window (3.6–4.9 μm) by removing the light reflection. These nanostructures were deposited on silicon substrates by e-beam evaporation at room temperature. IR ellipsometry and spectrophotometry studies combined with models based on effective medium approximations predicted the presence of silicon or germanium oxides. Such oxidation was evidenced by combining X-ray photoelectron spectroscopy and advanced (scanning-)transmission electron microscopy studies based on energy-dispersive X-rays and electron energy-loss spectroscopies. Both techniques also allowed to prove the formation of core-shell-type architectures consisting of pure Si or Ge surrounded by oxidized species, even for a Ge layer subsequently capped with a dense MgF_2 coating. The different approaches used for preparing electron transparent specimens (tripod polishing and focused ion-beams) confirmed a fast oxidation of the Ge nanocolumns even for short air exposure periods, and allowed comparing it with the level of oxidation promoted from other pollutant sources. This work sheds light on the spontaneous undesired oxidation in Si or Ge slanted nanorods which can diminish the performances and limit further development of optical devices.

1. Introduction

The mid-wavelength infrared (MWIR) spectral band (3–5 μm) is known to be one of the most important atmospheric transmission windows used for thermal imaging systems [1]. Because of their transparency in the infrared (IR) region, silicon and germanium are two materials of common election to produce IR optical components requiring high levels of transmittance. Si and Ge are usually found in high-resolution optical systems allowing to use a minimum number of lenses. Besides their IR transparency, each of them also have good thermal conductivity, excellent surface hardness, and high strength, that make them the favorite choices for optical designers of high performance infrared objectives for thermal imagers [2,3]. However, these dense materials suffer from important optical losses (> 30% at each interface with the air) due to their high refractive indices [4], which can limit the devices performances. Since Si and Ge are among the few transparent solid elements in the IR, cutting down the light reflection on them to increase their transmittance in this spectral range has become a critical issue. This can be achieved, however, by using anti-reflective (AR) coatings.

In this context of thin AR surface design, a well-known approach to reduce the effective refractive index of Si and Ge consists in manufacturing porous films. Among the different methods to fabricate porous structures, such as sol-gel [5], laser writing [6] and Metal-Catalyzed Electroless Etching (MCEE) [7], oblique angle deposition (OAD) stands out as a promising technology to remove efficiently unwanted light reflections. This bottom-up process provides tilted columnar and highly porous films which are influenced by atomic-scale shadowing effects when the incident flux of particles arrives at an oblique angle. Because it can be used to engineer self-organized architectures on surfaces with a fine control of their micro- and nano-structures, and their properties [8–11], and many fields have already benefitted from this technology, including sensing [12], magnetism [13], electrochemistry [14] and catalysis [15]. Oblique angle deposition has also demonstrated to be a

* Corresponding author at: Department of Materials Science and Metallurgic Engineering, and Inorganic Chemistry, Faculty of Sciences, University of Cádiz, Spain.
E-mail address: fmiguel.morales@uca.es (F.M. Morales).

https://doi.org/10.1016/j.apsusc.2019.07.064
Received 5 April 2019; Received in revised form 6 June 2019; Accepted 10 July 2019
Available online 10 July 2019
0169-4332/

powerful technique in optics, since the effective refractive index (n) of the deposited coatings can be tuned by controlling the porosity through parameters such as the deposition angle [16,17]. This principle has been applied for the fabrication of broadband antireflection graded-index coatings presenting smooth sequential variations of their n values, in order to reduce index mismatches at the interfaces between the substrate and the air and eliminate reflections over the visible and near-IR domains (up to about μm) [16,18,19]. This approach has appeared as an alternative to the conventional interferential AR coatings generally made of complex stacks of dense layers. As an example of devices in which the opposite effect is desired, OAD also allows to simplify the fabrication of distributed Bragg reflectors (DBRs), by using stacks of single materials (Si or Ge are extensively used) with different degree of porosities to provide a high n contrast, and thus to attain a high reflectivity and stop bandwidths [20–24]. Nevertheless, to the best of our knowledge, at the time of submission of this work, very few studies report the design of AR coatings based on OAD or DBRs in the MWIR range [25].

An important issue to be considered in the design and fabrication of OAD films for optical applications is their chemical stability and possible reactivity with atmospheric oxygen and water, note that this implies a similar environment to the operation conditions of many associated optical devices. A negative consequence of the oxidation is the detrimental effect on optical transmission and reflection that AR coatings can suffer due to the appearance of absorption peaks associated to the oxidized species. Several authors have studied the oxidation of silicon OAD coatings exposed to the air, reaching the conclusion that films are more or less partially oxidized depending on the quantity of exposed surface area [26–28]. According to these studies, the amount of silicon dioxide, which usually increases with the angle of incidence (level of porosity), can be estimated from optical measurements using effective medium approximations. The same applies to porous Ge systems [29,30]. Nonetheless, despite oxidation is a critical aspect for these structures, the way this process occurs is generally cleared up or is claimed without any verification and quantification by complementary experiments at the micro- and nano-scales.

In an attempt to gain a better understanding of OAD nanostructures, we report the studies of oxidation under atmospheric conditions of silicon and germanium single OAD layers designed to operate over the MWIR window, both grown at ranging incidence angles. In a first stage, the manufactured AR coatings were optically characterized by combining infrared spectroscopic ellipsometry (IRSE) and spectrophotometry studies. To elucidate the oxidation states for Si and Ge in the OAD structures, X-ray photoelectron spectroscopy (XPS) analyses were implemented. Finally, scanning-transmission electron microscopy (S)TEM techniques, which include elemental mapping methods like energy-dispersive X-ray spectroscopy (EDX) and electron energy-loss spectroscopy (EELS), were carried out in order to complement the previous studies but also to confirm and evaluate how oxidation takes place in Si and Ge OAD architectures. To identify the polluting agents that could be responsible for the presence of oxygen in the studied structures, a similar germanium OAD film to those previously studied, protected with a dense MgF_2 capping film to act as an oxygen seal, was again evaluated by (S)TEM techniques. To confirm that there could be various sources and degrees of oxidation, this sample was subjected to different methodologies of preparation of the electron-transparent lamellae that involve processes free of O_2 and H_2O, or the presence of oxygen, either with liquid water or with gaseous water.

2. Materials and method

2.1. Sample fabrication

The porous amorphous silicon (a-Si) and germanium (a-Ge) films were fabricated in an electron-beam evaporator placed into a physical vapour deposition (PVD) vacuum chamber. The process was carried out at room temperature with a base pressure of 2×10^{-6} mbar. The OAD layers were deposited at different angles of incidence (α) relative to the substrate normal from 50° to 85°, without substrate rotation, by adjusting the angle of the substrate holder with respect to a fixed evaporation direction. The aforementioned e-beam systems employed the evaporation of Si and Ge sources (Photonic sense© purity > 99.999%) onto 2 mm thick single crystalline (001) silicon substrates with a ~ 2 nm native oxide overlayer. With the aim of facilitating TEM studies, the substrates were placed on the holder with a ⟨110⟩ crystallographic axis normal to the incoming flux direction. The thickness was controlled and the deposition rate was maintained at 10 Å/s using a quartz crystal thickness monitor.

2.2. Optical studies

To evaluate the optical properties of each sample, the IRSE studies were carried out using a Woollam IR-VASE ellipsometer that permits to determine porosity, thickness and optical constants of the grown mesoporous layers by using advanced models based on effective medium approximations (EMA). Ellipsometric data were acquired at 65° and 75° angles of incidence with a spectral range from 2 to 14 μm. Otherwise, IR transmittance and reflectance measurements were taken with a Bruker Tensor 27 spectrometer for the same spectral window.

2.3. Nanostructural and chemical characterization

XPS analyses were carried out on a Kratos Axis Ultra DLD spectrometer equipped with monochromatized Al Kα radiation (1486.6 eV) with a selected X-ray power of 150 W. The spectrometer was operated in the constant analyzer energy mode, with pass energy of 80 eV for low resolution and wide range survey spectra, and 20 eV for high resolution and narrow core level spectra. Surface charging effects were compensated by using the Kratos coaxial neutralization system. Cross-sectional and plan-view scanning electron microscopy (SEM) images were acquired using a FEG 7001F-TTLS JEOL microscope operated at 30 kV, as a first approach to examine the general morphology and size of each film. More in-depth compositional and nanostructural studies were carried out using some advanced characterization techniques including high-angle annular dark-field imaging (HAADF), and local compositional analyses by EDX and EELS spectroscopies. On this purpose, two high resolution TEM microscopes (FEI Talos F200S and FEI Titan Cubed Themis 60–300) were used, working both in scanning mode at an accelerating voltage of 200 kV. EDX was implemented in the Talos microscope by using 2 Super-X windowless detectors, while a Gatan GIF Quantum ERS high energy resolution spectrometer and an energy filter were used for EELS in the Titan microscope. Due to the relative weakness of the mesoporous systems to be studied by TEM, the mechanical dimpling process must be avoided during the sample preparation process [31]. Taking this into account, cross-sectional OAD samples were progressively thinned down by a tripod polisher (Model 590 Tripod Polisher®) up to few microns, followed by Ar^+-ion milling in a Gatan PIPS system setting the acceleration energy of both guns to 3.5 keV (+7° top and − 7° bottom). As an alternative to the tripod process, a focused ion beam (FIB) sample preparation was carried out in a Zeiss Auriga FIB-SEM system. To highlight the originality and importance of the present studies, note that advanced (S)TEM techniques are not commonly devoted to OAD systems due to the difficulties of preparation of these mesoporous brittle materials, and there are only very few reports as the present one dedicated to such level of characterization till the nanoscale.

3. Results and discussion

The OAD layers were deposited at different incident angles in order to reduce the refractive index of silicon and germanium, respectively, and thus promote AR effects to increase their transmission levels in the

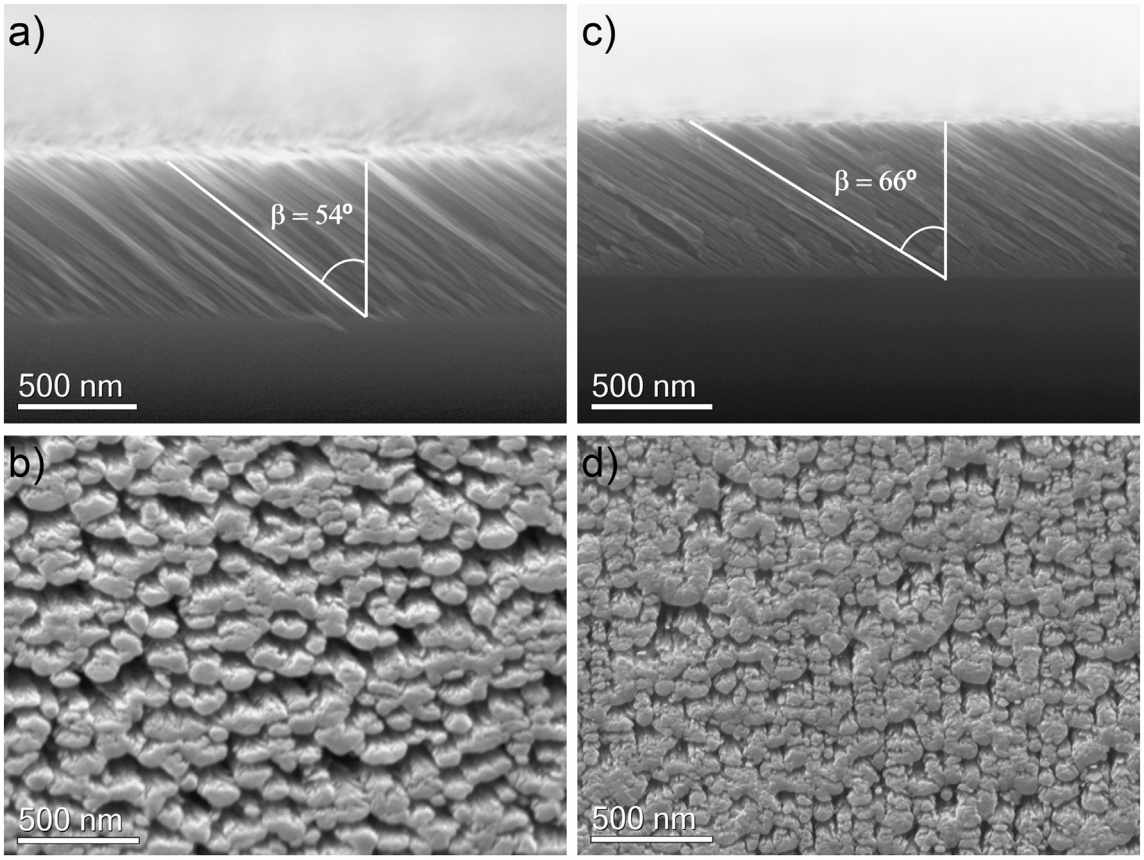

Fig. 1. SEM micrographs of OAD systems. Cross-sectional and top-view SEM images of a-Si (a and b) and a-Ge (c and d) samples deposited at α = 85° and 80° respectively).

MWIR window. Some aspects of the fabricated films were explored: (i) the relationship among factors such as deposition angle, porosity and reactivity to oxygen; (ii) the effect of oxidation in their IR optical properties; (iii) the experimental validation of oxidation, as well as its extent, present in the coatings.

3.1. Influence of the structure and the morphology on the oxidation rate

As examples of the achieved layers formed by slanted nanocolumns, Fig. 1 shows cross sectional and top-view SEM micrographs of a-Si and a-Ge films, deposited at incident vapour flux angles (α) of 85° and 80°, respectively. On the top surface, it can be observed the presence of empty spaces between bundled nanorods very similar to the model of columnar growth proposed by Messier et al. [32]. On the other hand, the cross-sections show homogenous OAD layers whose nanocolumns are not completely isolated even at these higher deposition angles. This can be associated to a combined growth mechanism in which the diffusion must be taken into account and a self-shadowing effect is not totally dominant. The columns tilt angle (β) with respect to the substrate normal, which amount increases with α, was found to be smaller than the deposition angle and strongly affected by the type of incoming atoms (in these micrographs, for Si grown at α = 85°, β is 54° whilst for Ge at α = 80°, β is 66°). Theoretical column angles (β) were calculated making use of heuristic expressions [33,34] but they differed from those measured because of its dependence on the chemical nature of the deposited material as well as on the deposition conditions [8,9].

The porosity of each sample and their optical constants were determined by means of IRSE and IR spectrophotometry using optical simulations based on the Bruggeman effective medium approximation (BEMA) [35]. This model allows describing the optical behavior of a heterogeneous medium with cavities of small sizes in regard of the probing wavelength.

For the purpose of determining the refractive index dispersion laws of both materials, Si and Ge dense samples deposited at normal incidence were measured and simulated. Then, in a first approach, assuming that individual nanocolumns exhibit the same behavior as the dense material, we simulated the resultant optical properties of the thin film by adding a volume fraction of porosity. The resulting ellipsometric simulations spectra are compared to the experimental ones in Fig. 2 for a silicon OAD coating deposited at α = 70°, for optical incidence angles (θ) of 65° and 75°. It can be noticed that there is a good agreement for the modeled spectra and the experimental ones except for short wavelengths and a singularity localized around 9 μm. This absorption band is characteristic of silica [36]. Thus to complete this optical model we have considered in a second time to add a volume fraction of silicon dioxide to the effective refractive index layer, but also water to account for the absorption features observed in Fig. 4 at about 2.9 and 6 μm. It can be appreciated that simulating IRSE with a Bruggeman's model, considering not only the presence of amorphous silicon (25%) mixed with voids (48%) but also silicon dioxide (20%) and water (7%), reproduces more closely the measured experimental data. In accordance to the above, the formation of silicon dioxide in Si layers prepared by OAD has been previously reported by other authors [26,27]. Those works proved that the amount of SiO_2 increases with the incidence angle up to a certain angle from which it starts to decrease due to a column surface-to-volume ratio reduction, suggesting that a silicon oxidation reaction takes places on the surface exposed to air. It is worth to note here that similar absorption features due to water and GeO_2 were observed and taken into account to describe satisfactorily the optical spectra for the Ge OAD layers.

Fig. 3(a) and (b) show the evolution of the volumetric fraction of oxidized species, water and air for Si and Ge OAD 1 μm thick layers

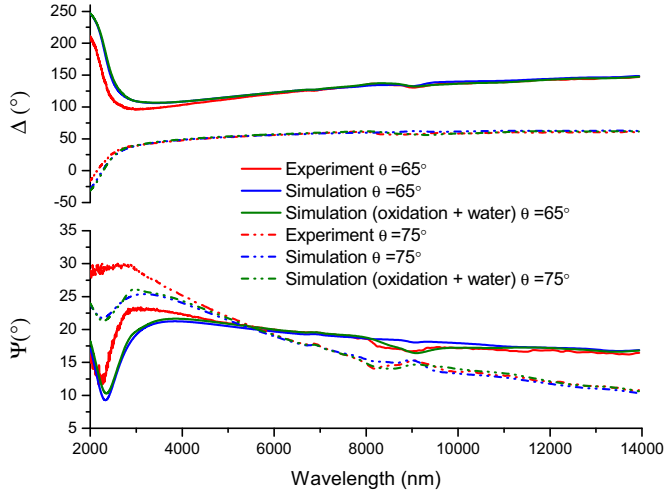

Fig. 2. Ellipsometric measurements for a reflection angle θ = 65° (solid lines) and 75° (dashed lines) of a α = 70° Si OAD film (red) and its simulations obtained with a simple Si/void BEMA optical model (blue) and after considering the presence of SiO_2 and water (green). (For interpretation of the references to colour in this figure legend, the reader is referred to the web version of this article.)

deposited in a range of incidence angles from 60° to 82°. As can be appreciated in both samples, the oxide and porosity percentages increase with respect to the incidence angle while the water amount decreases. This fact could be explained by an increase in the surface roughness with the deposition angle, which is also related to an increase in the water contact angle that makes the surface of the films more hydrophobic [37,38]. Besides, Fig. 3(c) illustrates the volumetric silicon and germanium dioxides percentages versus the porosity variation (implicating the change of incidence angles). Unlike the results obtained by the aforementioned authors, the amount of oxides increases with the deposition angle, which could be related to the texture of the layers: increasing the porosity implies greater surface-to-volume ratios. Note that in common OAD layers, the shadowing effect involves the formation of columns that become wider as they are thicker (see for example those at references [39,40]), implying the formation of big voids between them that increase the local and general porosity. Nevertheless, the columns reported in the present work are formed by packed groups of smaller cylinder-like nanorods that preserve their diameters, which suggest a weak tendency of angular broadening as well as a low surface trapping probability [9]. Increasing the deposition angle implies that the diameter of these bundles is getting smaller along a direction perpendicular to the incoming flux, increasing the general porosity, but not with bigger or smaller pores localized in some parts of the layer heights. This allows a fine control of gaps among nanocolumns that are somehow homogeneously distributed all over the layer, hence contributing to increase the surface-to-volume ratio.

After evaluating the IRSE results, it is concluded that the studied OAD layers have been subjected to a significant oxidation and some water absorption, which could have a crucial effect in their final optical properties.

3.2. Effect of oxidation in IR optics

Once established the relationship between both porosity and oxidation using a BEMA model, the effect that this oxidation has on silicon and germanium infrared transmittance properties has been evaluated. For instance, Fig. 4(a) shows the transmittance spectrum of a Si OAD structures deposited at α = 70°. Here again we simulated this transmittance spectrum with the BEMA when considering only porosity mixed with silicon in one hand and in the other considering silicon mixed with its dioxide, porosity and water. The same applies for the Ge

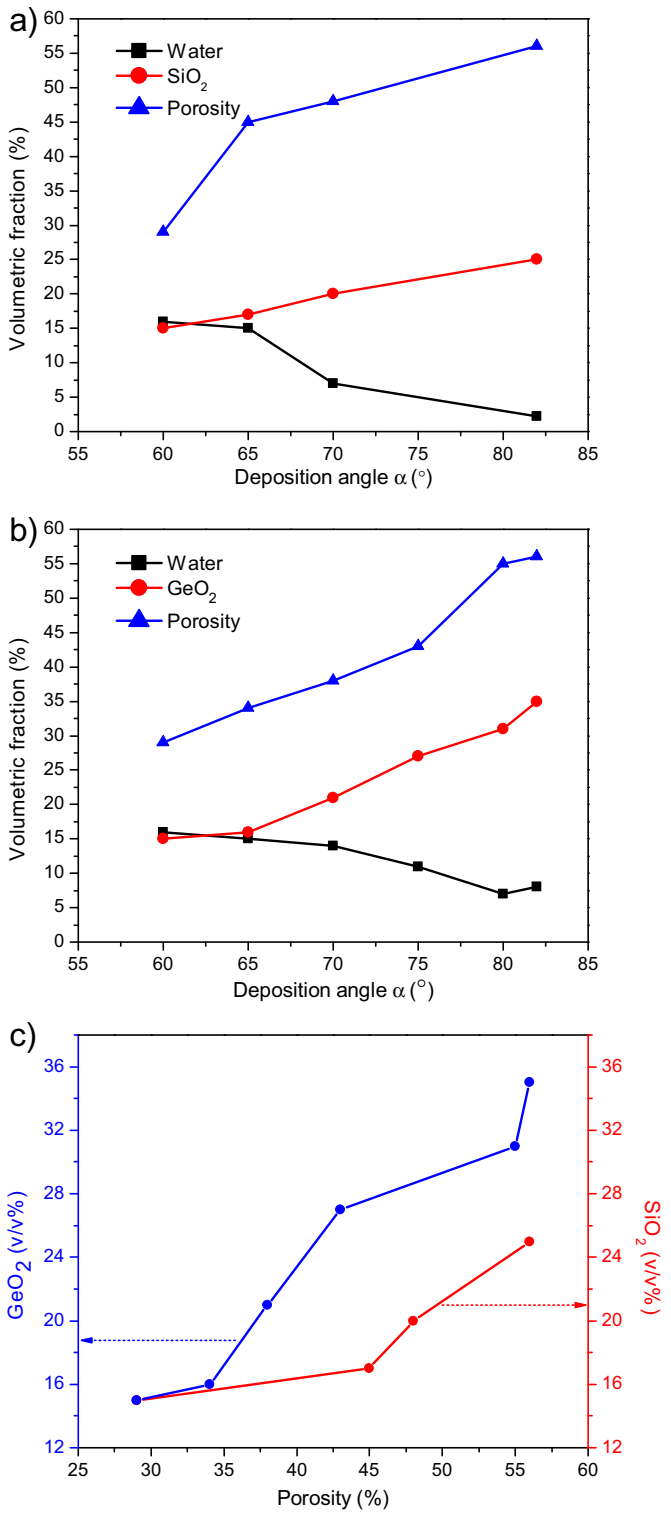

Fig. 3. Evolution of Si and Ge oxidation. Volumetric fraction of oxidized species, water and air for Si (a) and Ge (b) OAD versus the deposition angle and (c) Si (red) and Ge (blue) dioxides progression in function of the porosity percentage for 1 μm thick layers deposited in a range of incidence angles from 60 to 82° at 20 °C and 20 Å/s. (For interpretation of the references to colour in this figure legend, the reader is referred to the web version of this article.)

OAD layer. It is worthwhile to mention the remarkable fitting difference before and after incorporating oxidation and water pollution to the BEMA models (see pairs of dashed arrows in Fig. 4(a)). The simulations carried out by taking into account the only presence of silicon and voids

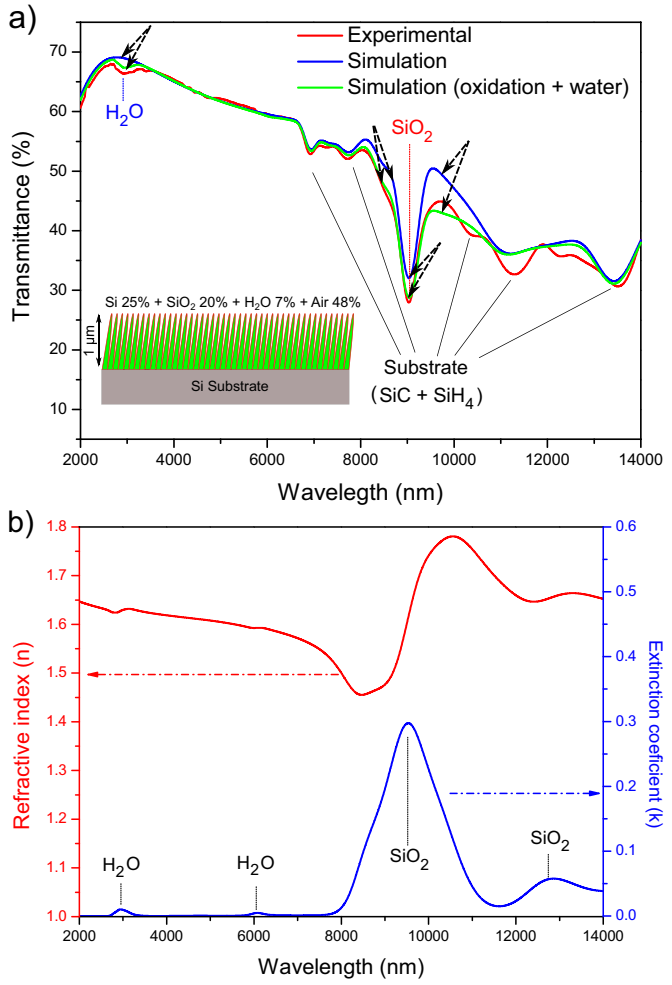

Fig. 4. (a) Spectrophotometric measurement of a α = 70° Si OAD film (red) and its simulations obtained before (blue) and after considering oxidation and water absorption in the BEMA optical model (green). Each pair of dashed arrows highlights the fitting improvement achieved after considering silicon dioxide and water. (b) Refractive index and extinction coefficient of the Si OAD layer deposited at α = 70° obtained from simulations using the optical model described in (a). (For interpretation of the references to colour in this figure legend, the reader is referred to the web version of this article.)

show a better optical behavior of that ideal system, which indicate that the presence of pollutants generates absorption peaks that are detrimental for IR optics as can be observed on the transmittance spectrum. In this way, transmission minima due to water (2.9 µm), silicon dioxide (9 µm) and others associated with the contamination of the substrate (SiC and SiH_4) were identified. On the other hand, the fits of the best models (presence of dioxides and water) for the extinction coefficients and the refractive indices in a part of the IR region (Fig. 4(b)) also shows corresponding absorption bands of water and SiO_2 which results in a transmittance drop. Moreover, the values of *n* oscillate between 1.4 and 1.8 for this region, and this is positive for approaching to the air index $n = 1$ in the goal of getting antireflectivity. Note that the expected value of refractive index for the dense Si in this region is about 3.42–3.44 [41]. These results are in agreement with our previous ellipsometric studies implemented on a germanium OAD layer in which germanium dioxide (GeO_2) and water absorption peaks could be identified [25]. Although the commented absorption peaks are luckily outside the MWIR range in both cases, the optical properties of Si and Ge would be severely depleted in the long wavelength infrared (LWIR) transmission window (8–14 µm) as a consequence of this optical absorption generated by the oxidized species.

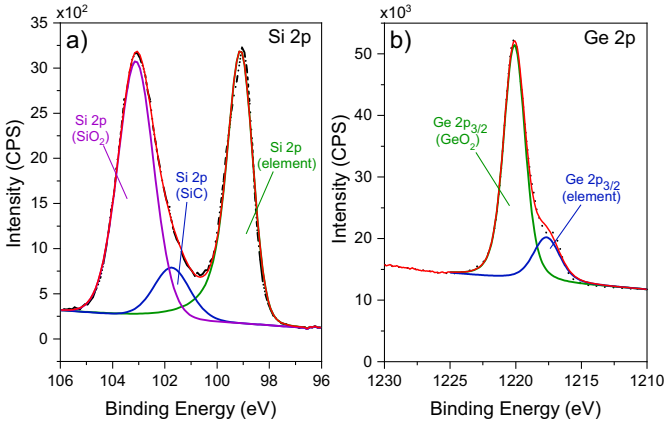

Fig. 5. High-resolution XPS spectra of (a) Si 2p and (b) Ge 2p for Si (α = 50°) and Ge (α = 75°) OAD films, respectively.

3.3. XPS characterization of the oxidation states of Si and Ge films

X-ray photoelectron spectroscopy analyses were performed in order to confirm the aforementioned spontaneous oxidation of Si and Ge OAD thin films predicted by SE as well as to determine their oxidation states. Initially, it could be thought that silicon and germanium dioxides should be the predominant oxidized species due to the fact that their formation reactions are more favored thermodynamically than those of their monoxides, i.e., the ΔG_f° of SiO_2 and GeO_2 compounds are −856 and − 521 kJ/mol respectively, whereas for SiO and GeO formation are −405 and − 237 kJ/mol [42,43]. Nevertheless, it should be noted that all the reactions are spontaneous since the values of their Gibbs free energy of formation are negative, which makes XPS studies adequate to clear up the dominant Si and Ge oxidized species present in the OAD nanostructures.

Fig. 5 shows the high-resolution spectra corresponding to Si 2p for Si OAD at α = 50° and Ge 2p for Ge OAD at α = 75°. In both cases, the binding energy scale was calibrated with respect to the C 1 s signal coming from adventitious carbon contamination and set at 284.8 eV. The CasaXPS software was used for spectra processing. Additionally, XPS survey spectra of these samples are shown in Fig. S1. The Si 2p spectrum (Fig. 5(a)) was deconvoluted into three components which correspond to Si elemental (99.1 eV), SiO_2 (103.1 eV) and SiC (101.7 eV) [44,45], whereas the Ge 2p deconvoluted spectrum (Fig. 5(b)) showed the presence of two signals which were attributed to elemental Ge (1217.6) and GeO_2 (1220.0 eV) species [46,47]. Here is important to highlight that the Ge 2p spectrum was considered instead of the Ge 3d one since the peak associated to the oxide component is more clearly seen in the former due to the higher surface sensitivity of the Ge 2p electrons [46]. Therefore, these results obtained from XPS studies let us prove the spontaneous formation of Si and Ge dioxides in the OAD nanostructures just like the BEMA model had anticipated.

On the other hand, the atomic percentages for Si (41% Si, 47% SiO_2 and 12% SiC) and Ge (19% Ge and 81% GeO_2) OAD samples were also estimated from the corresponding XPS spectra. However, these latter results should be interpreted carefully since they are only referred to the oxidation at the very top surface, which is much more exposed to the air. Thus, it is quite risky to extrapolate the result obtained here to the entire film.

3.4. (S)TEM studies: structural and compositional characterizations at micro- and nanoscale

Advanced (S)TEM studies were carried out with the aim of obtaining valuable information to thereby validate the presence of dioxides evidenced from optical and XPS measurements as well as to determine their distribution at the nanoscale and the way they are formed

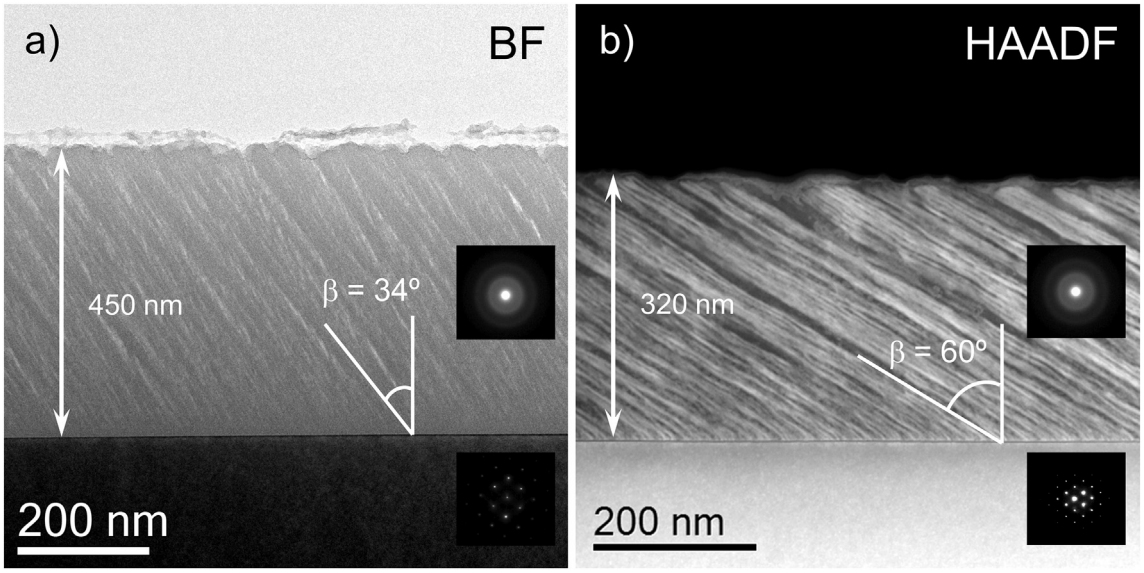

Fig. 6. (a) Bright-field TEM overview of the α = 50° Si OAD film. (b) High-angle annular dark-field STEM overview of the α = 75° Ge OAD film. The insets correspond to the SAED patterns recorded in the different regions.

within the films. These experiments will also help to improve the ellipsometry models used to simulate the optical response of these AR coatings in the IR range. To achieve the above, a sample of Si at α = 50° and another of Ge at α = 75° were prepared by tripod polishing for TEM observations along a ⟨110⟩ crystallographic direction of the Si substrate. Note that samples deposited at different angles were selected for TEM studies in order to explore how oxidation occurs at varying materials and porosity levels. Fig. 6(a) presents a bright-field (BF) TEM micrograph of the silicon OAD layer which gives information about the layer thickness, columns tilt angle and as well as the amorphous character of the slanted columns according to the selected area electron diffraction (SAED). Similar studies were carried out in the OAD Ge sample in which the oblique columnar amorphous structure of the film is evidenced (Fig. 6(b)).

3.5. (S)TEM-EDX overall elemental analyses

To obtain a better knowledge of the elements presence and distribution, STEM-EDX chemical analyses were carried out in both AR coatings. It is important to note that all samples studied through EDX and EELS techniques were previously introduced in a plasma cleaner so as to remove residual hydrocarbon contamination. At a micrometric scale, EDX elemental maps supported the presence of oxygen homogeneously distributed throughout the scaffolds of Si (Fig. 7(a)) and Ge (Fig.8(a)) nanocolumns just as the BEMA model predicted. Average quantifications of atoms amounts at both layers were obtained from these EDX spectra, recorded over many wide areas (430 × 430 nm^2 for Si, and 250 × 250 nm^2 for Ge) and at large integration times (several minutes) using a current probe of about 500 pA, beam convergence angles of 10.5 mrad and a dispersion of 5 eV/channel over 4000 channels. The FEI Velox™ software was used for data acquisition and processing. Quantification of the EDX data was performed using the standardless method. In order to minimize errors during this step, intensities of the different peaks were extracted with a great care after background subtraction with a multi-polynomial approach. We are aware that this approach can lead to inaccuracy in the composition determination, especially for low *Z* elements like O, but it should be noted that EDX measurements have been performed in the current study with the aim of demonstrating the Si and Ge OAD layers oxidation as well as the evolution of this fact after being undergone to different environments and sample preparation processes, and not for proving

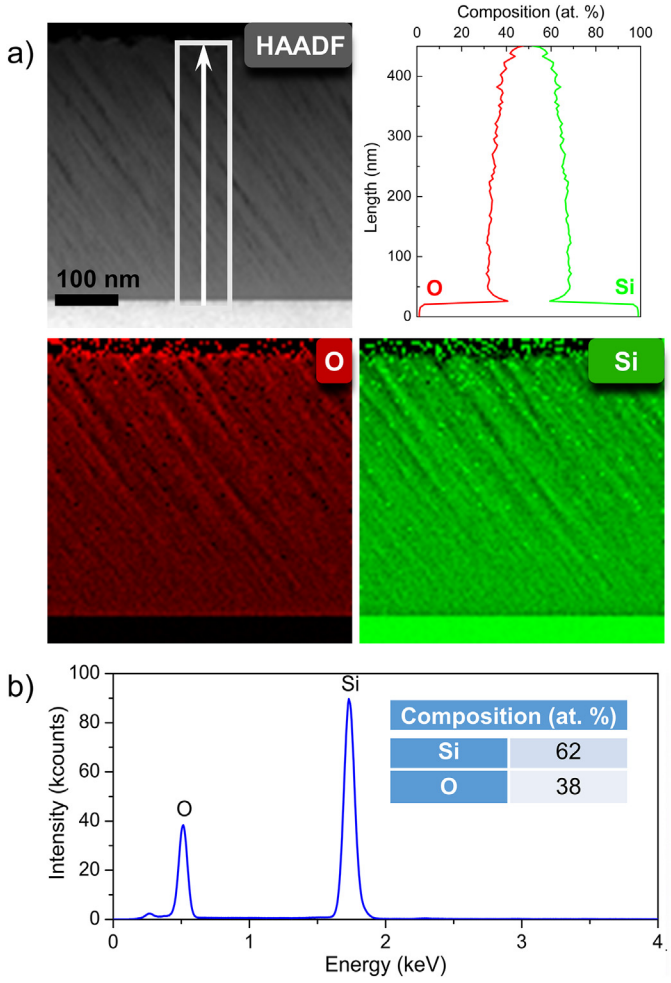

Fig. 7. STEM-EDX analysis of the α = 50° Si OAD film. HAADF image and elemental maps obtained for Si and O atoms are presented together with the elemental profile of the layer; (b) EDX integrated spectrum and associated quantitative analyses of composition for the Si OAD layer.

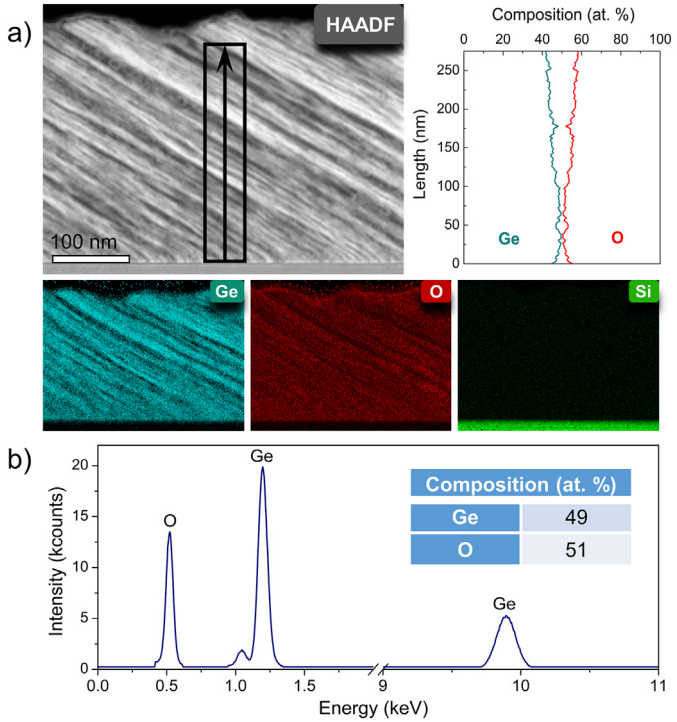

Fig. 8. STEM-EDX analysis of the α = 75° Ge OAD film. HAADF image and elemental maps obtained for Ge, O and Si atoms are presented together with the elemental profile of the layer; (b) EDX integrated spectrum and associated quantitative analyses of composition for the Ge OAD layer.

compositions with ultimate accuracies. Nevertheless, according to the literature, we may assume that our EDX compositional analyses conducted with the standardless method can provide results with relative errors between 4 and 10% [48,49]. Furthermore, similar compositional analyses carried out in other OAD sample made of compounds with defined stoichiometry (SiO_2 and TiO_2, results not published) showed relative measurement uncertainties below 5% for the values of oxygen quantification, supporting the validity of the analyses performed. Representative EDX integrated spectra are shown in Fig. 7(b) and Fig. 8 (b) which confirmed the homogeneous oxidation (at microscopic scale) of the Si (38 at. % of O) and Ge (51 at. % of O) OAD studied samples. Special attention must be paid to the implicit O/Si (0.61) and O/Ge (1.06) atomic ratios, since they are much lower than that obtained if they were pure dioxides (2 in SiO_2 and GeO_2). This difference in coefficient is an indication of a mixture of each pure elemental solid and its dioxide, that could be related to a feasible texture in which each column would be mainly oxidized at their surfaces, after a possible first stage of O decoration at the nanocolumns surface. Note that the measured oxide amount was much smaller in the more compact (Si, α = 50°) than in the more porous (Ge, α = 75°) OAD sample, even though the formation of the oxidized specie of Si is more favored thermodynamically than that of the Ge (the ΔG_f° of SiO_2 is −856 kJ/mol while the ΔG_f° of GeO_2 is −521 kJ/mol). Furthermore, the experimental activation energy for Si oxidation (1.23 eV), which occurs by the diffusion of the O_2 molecule along the channels of the a-SiO_2, is lower than for Ge oxidation (2.0 eV), which is controlled by the diffusion of interstitial network oxygen [50], letting us to conclude that in layers with similar thicknesses, the degree of porosity (estimated to be twice in Ge than in Si) increases dramatically the reactivity with oxygen and water, even for the less reactive atomic specie because of the higher surface-to-volume ratio.

3.5.1. (S)TEM-EELS elemental analyses at nanoscale

In order to go a little further in the characterization of related nanostructures, careful STEM-EELS nanoscale analyses were carried out in a similar Ge OAD film (400 nm thick, α = 75°) for demonstrating the formation of core-shell-type structures as a consequence of oxidation, and the oxidation extent depending on the ambient to which the specimen was exposed. Let us remind that this porous Ge film prepared at oblique incidence was briefly exposed to the air (during 30–60 min) before being evacuated and later sealed by a dense MgF_2 layer during a second e-beam deposition stage at normal incidence. The Ge/MgF_2 multilayer itself has a supplementary interest for IR optics [25] that is outside the scope of the present article, but we may not obviate that after the placement of this capping, a further Ge oxidation should be restricted. In consequence, one could expect that the OAD layer consists mainly of pure Ge this time.

For a tripod TEM preparation, a general BF-TEM bilayer overview and a more local annular dark-field (ADF) STEM Ge OAD micrograph are shown in Fig. 9(a). For this evacuated TEM lamella, two STEM-EELS spectrum images (SIs) were acquired simultaneously in two different ranges (the first from 470 to 982 eV and the second from 950 to 1462 eV, with a dispersion of 0.25 eV/channel over 2018 channels) using the Dual-EELS method [51] in order to record the O−K (532 eV) and the Ge-$L_{2,3}$ (1217–1248 eV) with sufficient signal and energy resolution for further analysis. These experiments were done with a sub-Angstrom probe size and integration times of 154 ms/pixel and 246 ms/pixel were used to record the first and second SIs, respectively. After aligning the two SIs separately using the O−K and Ge-$L_{2,3}$ edges as references and applying a multivariate statistical treatment to remove the noise (principal component analysis (PCA) approach with Hyperspy program [52]), both SIs were spliced together in order to get a continuous spectrum at each pixel position that contains both the O−K and Ge-$L_{2,3}$ edges (Fig. 9(c)). The EELS quantification was then applied by using the DigitalMicrograph™ software with hydrogenic cross-sections calculated for our experimental conditions (200 kV, convergence semi-angle of 19.5 mrad, collection semi-angle of 36.7 mrad). To minimize possible multiple scattering effects, O−K and Ge-$L_{2,3}$ edges were integrated over the same window width (60 eV). The procedure mentioned above, including instrumentations and techniques of last generation, was the key to ensure an accurate elemental quantification (the relative experimental error was assumed to be close to 3% according to the literature [53]). From the evidences associated to the quantification of the ADF portion and the associated elemental mapping presented in Fig. 9(b), the STEM-EELS analysis of a single Ge nanocolumn proves a subnanometric-scale inhomogeneous distribution of oxygen in the column, which is higher in the column outline and lower in the central region. According to these fluctuations, a core-shell structure with a higher quantity of O in the shells can be interpreted as the consequence of the surface oxidations of the nanocolumns. This suggests that the incorporation of oxygen is posterior to the film deposition process. Nevertheless, the composition integrated profiles carried out across the column width (Fig. 9(b)) point out that Ge composition grows until reaching a maximum from which it remains constant during certain distance to then decrease. This plateau distance could be considered as the unoxidized core diameter of the nanocolumn. Note that in these profiles, the Ge percentage remains smaller than the associated O signal even in the central position because it must be considered that the nanocolumn projection brings together contributions from the shell parts that are above and below the pure Ge mass, all of them crossed by the electron beam. Nevertheless, attending to this ADF image, assuming that the columns are pseudo-cylindrical, then that the projection crosses 22 nm of GeO_2 and 8 nm of pure Ge, this implies about 51% of Ge and 49% of O (taken from the elemental profile in Fig. 9(b)), while the shell cross section gives values of 33% of Ge and 66% of O, that are the those corresponding to the GeO_2 stoichiometry (this is especially clear in the Fig. 9(b), which is a portion of the nanocolumn closer to a pore). It is worth to note that similar observations were done on other nanocolumns. Consequently, these results provide an experimental confirmation of the formation of core-shell structures in germanium OAD systems due to atmospheric exposure. Nevertheless, since Si and Ge

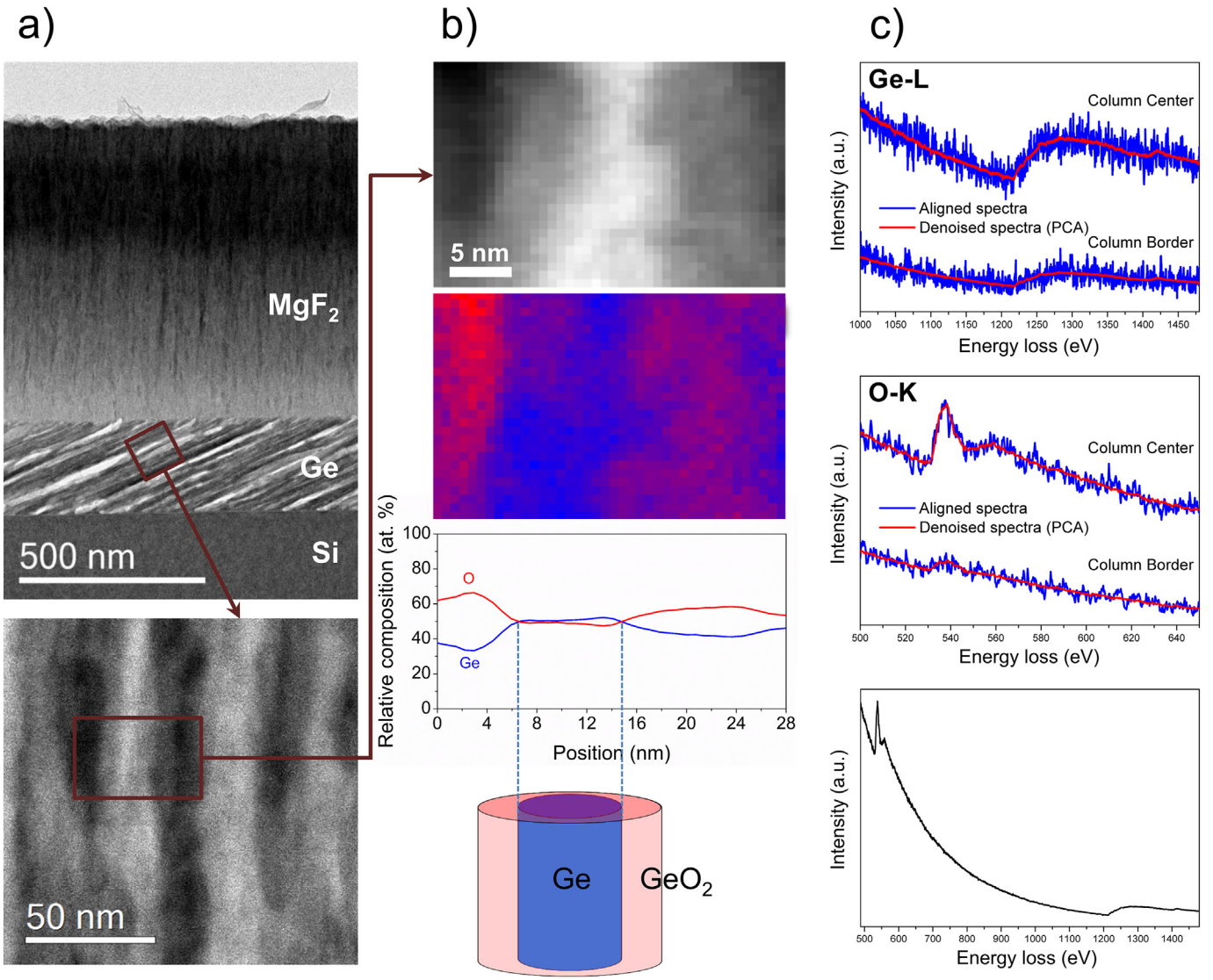

Fig. 9. STEM Dual-EELS analysis of Ge (α = 75°) OAD/MgF_2 sample. (a)Bright-field TEM overview of the bilayer together with HAADF image of several Ge α = 75° columns (bright contrast) separated by the porosity (dark contrast). (b) HAADF image and Dual-EELS Ge-versus-O composition map of an isolated Ge column along with its averaged composition profile and the core-shell model proposed. (c) EELS spectrum images obtained around the Ge-$L_{2,3}$ and O—K edges, before (blue) and after (red) removing the noise by PCA methods and the subsequently spliced spectrum. (For interpretation of the references to colour in this figure legend, the reader is referred to the web version of this article.)

layers present similar optical and nanostructural features, we may expect a similar oxidation behavior in Si OAD.

3.5.2. Oxidation rate dependence on TEM sample preparation and air/vacuum exposure

So as to be sure that this oxidation is not a product of our electron-transparent lamellae fabrication process (a wet TEM sample preparation with tripod water-based polishing in air), the same Ge/MgF_2 bilayer sample was prepared by FIB milling and kept in vacuum until TEM observations. For the tripod preparation, the STEM-EDX analysis gives an average percentage of 54% of O and 46% of Ge for the capped Ge OAD layer, not far of the previously commented 51/49 given by the uncapped one. For the FIB preparation, the sample was also studied by STEM-EDX before (without O_2 or H_2O, and whose EDX elemental map can be seen in Fig. 10(a)) and after being exposed to atmospheric conditions (with O_2 and *gas*-H_2O) for several weeks. In order to compare them in an accurate way, these analyses were executed under identical experimental conditions (the very same as in the previous EDX analyses for uncapped and capped samples prepared by tripod polishing) and covering similar porous Ge areas (300 × 300 nm^2). The elemental quantifications obtained for average O/Ge percentages for these two cases are 50/50 for the naturally aged FIB specimen, and 47/53 for the fresh (kept in vacuum) one. A brief overview of the results obtained from the elemental analyses performed in all studied samples can be found in Table.1. The EDX spectra of the Ge/MgF_2 sample, evaluated under the three different conditions previously mentioned (Fig. 10(b)), also evidence the same oxidation tendency as shown in the O—K peaks. Therefore, it is proved that the main amount of oxidation of the capped germanium OAD layer was quickly produced upon exposure to atmospheric oxygen and water vapour, as well as there is a small additional oxidation by natural aging, and during TEM sample preparation as a consequence of polishing in the presence of liquid water. This conclusion might be extrapolated to the oxidation of Si OAD systems. These EDX experimental data can also be confronted with the compositions estimated by the SE models for 1 µm OAD layers of Ge (α = 75°) and Si (α = 50°). For this purpose, considering only the respective volume fractions of Si and SiO_2, and of Ge and GeO_2, and their densities in amorphous states [54–57], when contributions of water and

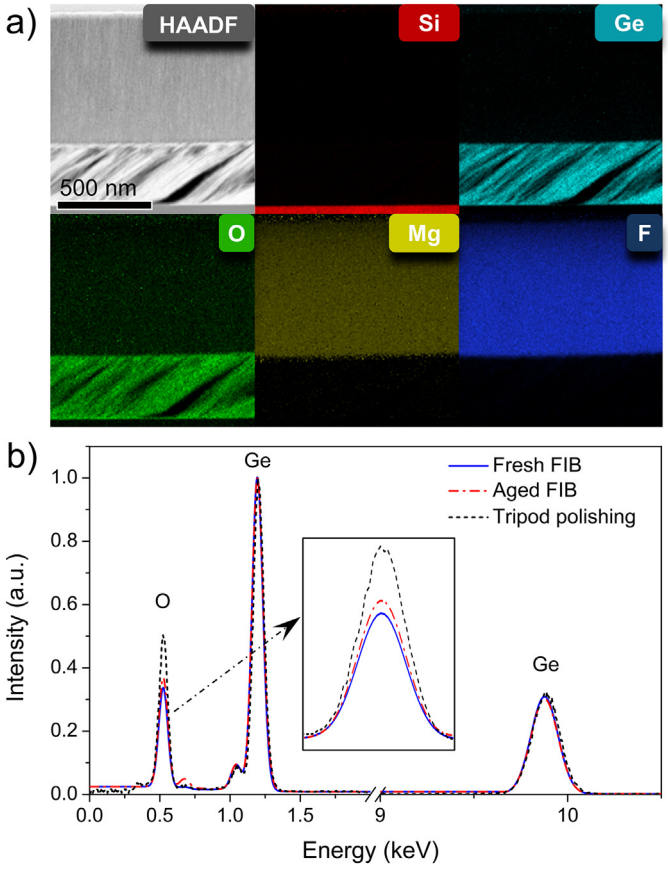

Fig. 10. STEM-EDX analyses of the Ge (α = 75°) OAD/MgF_2 bilayer under different conditions of preparation and preservation. (a) HAADF image of the fresh FIB sample and its EDX elemental maps obtained for Si, Ge, O, Mg and F atoms. (b) EDX spectra, normalized at the Ge-L_α peak (1.188 eV), for fresh (blue solid line) and aged (red dashed-dotted line) FIB preparation as well as for the prepared by tripod polishing (black dotted line). The inset correspond to the feature of the O-K_α peak (0.525 eV). (For interpretation of the references to colour in this figure legend, the reader is referred to the web version of this article.)

Table 1
Summary of (S)TEM-EDX and EELS compositional analyses for all studied samples. Note that values provided by EELS quantification (core and shell) are referred to the projected sections of a single nanocolumn.

Sample	TEM preparation	(S)TEM technique	Air/vacuum	Composition (at. %)		
				Si	Ge	O
Si (α = 50°) OAD	Tripod	EDX	Air	38	–	62
Ge (α = 75°) OAD	Tripod	EDX	Air	–	49	51
Ge (α = 75°) OAD/MgF_2	Tripod	EELS (core)	Air	–	51	49
		EELS (shell)		–	33	66
	Tripod	EDX	Air	–	46	54
	FIB	EDX	Air	–	50	50
	FIB	EDX	Vacuum	–	53	47

voids are discarded, the compositions of 55 at.% of Ge and 45 at. % of O, and 75 at. % of Si and 25 at. % of O are calculated for the Ge and Si OAD layers. Note that atomic compositions predicted by the BEMA model (obtained after conversion from volumetric fractions) are quite close to the measured by STEM-EDX for the uncapped, and the capped fresh and aged Ge OAD layers. Nevertheless, the slight differences

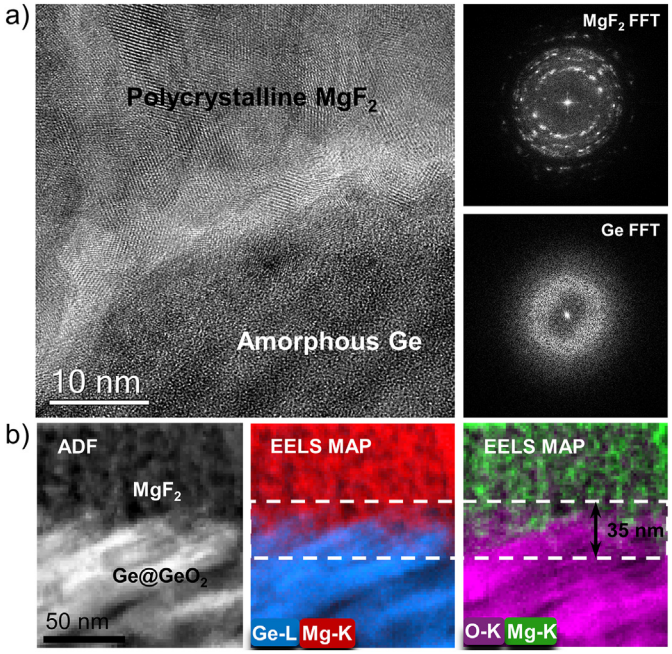

Fig. 11. Feature of the Ge (α = 75°) OAD/MgF_2 interface. (a) High-resolution TEM micrograph of the interface with the corresponding FFT diffraction of each layer; (b) STEM-ADF and STEM-EELS Ge-versus-Mg and O-versus-Mg elemental maps of the Ge OAD/MgF_2 interface.

between the oxygen compositions obtained by ellipsometry and EDX can be attributed to the additional oxidation produced during sample preparation by tripod polishing, and that they come from different groups of OAD deposited samples. Thereby, the similar tendency between the simulations and the information obtained through (S)TEM studies not only allowed us to validate the SE models used to describe the optical behavior of the system studied but also this accurate information about the morphology, distribution, composition and surface oxidation of nanocolumns, that could be used as key inputs to create an improved nanostructural-analytical model as close as possible to the physical reality through finite-difference time-domain (FDTD) advanced optical simulations.

Finally, it is worth mentioning that the MgF_2 capping layer can act as a real seal for the oxygen permeability because of its compact nature. High-resolution TEM micrographs of the Ge OAD/MgF_2 interface as well as the fast Fourier transform (FFT) diffractions (Fig. 11(a)) reveal a dense polycrystalline structure of the MgF_2 film and the porous amorphous structure of the Ge OAD layer. For EDX mappings of this interface (see example in Fig. 11(b)), it was found a residual homogeneously distributed presence of O in the amount of 3% together with Mg and F in a ratio proportional to the expected stoichiometry; besides the bilayer interface shows to be abrupt in their different compositions.

4. Conclusions

The oxidation of silicon and germanium AR single-layer coatings manufactured by the OAD technique and designed to operate over the MWIR range was investigated by combining ellipsometry, spectrophotometry, X-ray photoelectron spectroscopy and scanning-transmission electron microscopy studies. Simulations using a BEMA ellipsometric model predicted the oxidation of the deposited layers establishing, in addition, a proportional relation between the porosity and the oxidation rate of nanocolumns. The effect of this oxidation was evaluated through spectrophotometric measurement which proved that oxidized species (silicon and germanium dioxides) do not have significant negative effects in MWIR optics. Nevertheless, optical performances in the LWIR range may be degraded due to the absorption peaks

related with these dioxides. Such losses could drastically limit the performance of IR devices made of many optical elements. XPS surface elemental analyses evidenced that the oxidation of Si and Ge OAD films was due to the formation of silicon and germanium dioxides. Compositional analyses carried out by STEM-EDX confirmed the widespread oxidation (macroscopically homogeneous but inhomogeneous at the nanoscale) of these thin films in proportions rather close to the predicted by the SE model. Local STEM-EELS analyses let us demonstrate the formation of core-shell-type nanostructures, consisting of pure Ge surrounded by GeO_2, as a consequence of the superficial oxidation of germanium mesoporous architectures. This effect is also proposed for the Si OAD scenario. Additional experiments carried out under different vacuum and water-free conditions determined that the oxidation of these systems is the result of the combined effect of spontaneous atmospheric oxidation and water absorption during TEM sample preparation process, both favored by the strong porous structure of OAD layers. The validity of the ellipsometric model was supported by the close agreement with the combined XPS, STEM, EDX, and EELS investigations which also provide us with accurate and valuable data to be able to design and develop advanced optical models based on FDTD methods.

Acknowledgements

The authors would like to express their gratitude to J. J. Pérez Sagasti for his assistance in XPS analyses. A. J. Santos would like to thank the IMEYMAT Institute and the Spanish Ministerio de Educación y Cultura for the concessions of grants (ICARO-173873 and FPU16-04386). The “Talent Attraction Program” of the University of Cádiz is acknowledged by supporting B. Lacroix contract code E-11-2017-0117214. University of Cádiz and IMEYMAT are also agreed by financing the mutual facilities available at the UCA R&D Central Services (SC-ICYT), the UCA project reference “PUENTE PR2018-040”, and the IMEYMAT project reference “AGREGADOR 2018-1”. This work was supported by the DGA (Direction Générale de l'Armement), the French Defense Procurement Agency. This work has been partially supported by “Nouvelle Aquitaine” Region and by European Structural and Investment Funds (ERDF reference P-2016-BAFE-209): IMATOP project.

Appendix A. Supplementary data

Supplementary data to this article can be found online at https://doi.org/10.1016/j.apsusc.2019.07.064.

References

[1] D.C. Harris, Materials for Infrared Windows and Domes-Properties and Performance, SPIE, Bellingham, 1999.
[2] J.A. Savage, Infrared Optical Materials and their Antireflection Coatings, First edit, A. Hilger, Bristol, 1985.
[3] A. Rogalski, K. Chrzanowski, Infrared devices and techniques, Metrol. Meas. Syst. 21 (2014) 565–618, https://doi.org/10.2478/mms-2014-0057.
[4] M. Bhatt, B.B. Nautiyal, P.K. Bandyopadhyay, High efficiency antireflection coating in MWIR region (3.6–4.9 μm) simultaneously effective for germanium and silicon optics, Infrared Phys. Technol. 53 (2010) 33–36, https://doi.org/10.1016/j.infrared.2009.08.006.
[5] Y. Yan, S.R. Chaudhuri, A. Sarkar, Synthesis, characterizations, and optical properties of stacked porous thin films derived from sol-gel process, J. Am. Ceram. Soc. 79 (1996) 1061–1065, https://doi.org/10.1111/j.1151-2916.1996.tb08548.x.
[6] Y.L. Khung, S.D. Graney, N.H. Voelcker, Micropatterning of porous silicon films by direct laser writing, Biotechnol. Prog. 22 (2006) 1388–1393, https://doi.org/10.1021/bp060115s.
[7] Y. Hu, K. Peng, Z. Qiao, X. Huang, F. Zhang, R. Sun, X. Meng, S. Lee, Metal-catalyzed electroless etching of silicon in aerated HF/H_2O vapor for facile fabrication of silicon nanostructures, Nano Lett. 14 (2014) 4212–4219, https://doi.org/10.1021/nl500361u.
[8] M.M. Hawkeye, M.J. Brett, Glancing angle deposition: fabrication, properties, and applications of micro- and nanostructured thin films, J. Vac. Sci. Technol. A Vacuum, Surfaces, Film. 25 (2007) 1317, https://doi.org/10.1116/1.2764082.
[9] A. Barranco, A. Borras, A.R. Gonzalez-Elipe, A. Palmero, Perspectives on oblique angle deposition of thin films: from fundamentals to devices, Prog. Mater. Sci. 76 (2016) 59–153, https://doi.org/10.1016/j.pmatsci.2015.06.003.
[10] Y. He, Y. Zhao, Advanced multi-component nanostructures designed by dynamic shadowing growth, Nanoscale 3 (2011) 2361, https://doi.org/10.1039/c1nr10103j.
[11] H. van Kranenburg, C. Lodder, Tailoring growth and local composition by oblique-incidence deposition: a review and new experimental data, Mater. Sci. Eng. R 11 (1994) 295–354, https://doi.org/10.1016/0927-796X(94)90021-3.
[12] Z. Xie, X. Liu, W. Wang, C. Liu, Z. Li, Z. Zhang, Fabrication of TiN nanostructure as a hydrogen peroxide sensor by oblique angle deposition, Nanoscale Res. Lett. 9 (2014) 105, https://doi.org/10.1186/1556-276x-9-105.
[13] C. Li, G. Chai, C. Yang, W. Wang, D. Xue, Tunable zero-field ferromagnetic resonance frequency from S to X band in oblique deposited CoFeB thin films, Sci. Rep. 5 (2015) 1–7, https://doi.org/10.1038/srep17023.
[14] V. Kannan, A.I. Inamdar, S.M. Pawar, H.-S. Kim, H.-C. Park, H. Kim, H. Im, Y.S. Chae, Facile route to NiO nanostructured electrode grown by oblique angle deposition technique for supercapacitors, ACS Appl. Mater. Interfaces 8 (2016) 17220–17225, https://doi.org/10.1021/acsami.6b03714.
[15] M.J. Riley, B. Williams, G.Y. Condon, J. Borja, T.M. Lu, W.N. Gill, J.L. Plawsky, Photocatalytic properties of porous titania grown by oblique angle deposition, J. Appl. Phys. 111 (2012), https://doi.org/10.1063/1.3699370.
[16] S.R. Kennedy, M.J. Brett, Porous broadband antireflection coating by glancing angle deposition, Appl. Opt. 42 (2003) 4573–4579, https://doi.org/10.1364/AO.42.004573.
[17] K. Robbie, M.J. Brett, Sculptured thin films and glancing angle deposition: growth mechanics and applications, J. Vac. Sci. Technol. A 15 (1997) 1460–1465, https://doi.org/10.1116/1.580562.
[18] J.Q. Xi, M.F. Schubert, J.K. Kim, E.F. Schubert, M. Chen, S.Y. Lin, W. Liu, J.A. Smart, Optical thin-film materials with low refractive index for broadband elimination of Fresnel reflection, Nat. Photonics 1 (2007) 176–179, https://doi.org/10.1038/nphoton.2007.26.
[19] J.W. Leem, J.S. Yu, Multi-functional antireflective surface-relief structures based on nanoscale porous germanium with graded refractive index profiles, Nanoscale 5 (2013) 2520–2526, https://doi.org/10.1039/c3nr00286a.
[20] M.F. Schubert, J.Q. Xi, J.K. Kim, E.F. Schubert, Distributed Bragg reflector consisting of high- and low-refractive-index thin film layers made of the same material, Appl. Phys. Lett. 90 (2007) 1–4, https://doi.org/10.1063/1.2720269.
[21] S.J. Jang, C.I. Yeo, Y.T. Lee, Amorphous silicon Bragg reflectors fabricated by oblique angle deposition, MRS Proc. 1396 (2012), https://doi.org/10.1557/opl.2012.804 mrsf11-1396-o07-34.
[22] S.J. Jang, Y.M. Song, C. Il Yeo, C.Y. Park, Y.T. Lee, Highly tolerant a-Si distributed Bragg reflector fabricated by oblique angle deposition, Opt. Mater. Express. 1 (2011) 451, https://doi.org/10.1364/OME.1.000451.
[23] J.W. Leem, J.S. Yu, Broadband and wide-angle distributed Bragg reflectors based on amorphous germanium films by glancing angle deposition, Opt. Express 20 (2012) 20576, , https://doi.org/10.1364/OE.20.020576.
[24] J.W. Leem, J.S. Yu, Design and fabrication of amorphous germanium thin film-based single-material distributed Bragg reflectors operating near 22 μm for long wavelength applications, J. Opt. Soc. Am. B. 30 (2013) 838, https://doi.org/10.1364/JOSAB.30.000838.
[25] F. Maudet, B. Lacroix, A.J. Santos, F. Paumier, M. Paraillous, C. Dupeyrat, R. García, F.M. Morales, T. Girardeau, Towards perfect IR transparency using glancing oblique angle deposition, Appl. Surf. Sci. 470 (2018) 943–950, https://doi.org/10.1016/j.apsusc.2018.11.176.
[26] G. Beydaghyan, C. Buzea, Y. Cui, C. Elliott, K. Robbie, Ex situ ellipsometric investigation of nanocolumns inclination angle of obliquely evaporated silicon thin films, Appl. Phys. Lett. 87 (2005) 1–3, https://doi.org/10.1063/1.2084329.
[27] K. Kaminska, A. Amassian, L. Martinu, K. Robbie, Growth of vacuum evaporated ultraporous silicon studied with spectroscopic ellipsometry and scanning electron microscopy, J. Appl. Phys. 97 (2005), https://doi.org/10.1063/1.1823029.
[28] S. Asgharizadeh, M. Sutton, K. Robbie, T. Brown, X-ray reflectometry characterization of porous silicon films prepared by a glancing-angle deposition method, Phys. Rev. B - Condens. Matter Mater. Phys. 79 (2009) 1–8, https://doi.org/10.1103/PhysRevB.79.125405.
[29] N.R. Murphy, J.T. Grant, L. Sun, J.G. Jones, R. Jakubiak, V. Shutthanandan, C.V. Ramana, Correlation between optical properties and chemical composition of sputter-deposited germanium oxide (GeOx) films, Opt. Mater. (Amst). 36 (2014) 1177–1182, https://doi.org/10.1016/j.optmat.2014.02.023.
[30] E.B. Gorokhov, K.N. Astankova, I.A. Azarov, V.A. Volodin, A.V. Latyshev, New method of porous Ge layer fabrication: structure and optical properties, Semiconductors 52 (2018) 628–631, https://doi.org/10.1134/S1063782618050111.
[31] O. Unal, A.H. Heuer, T.E. Mitchell, Preparation of cross-sectional specimens of ceramic thermal barrier coatings for transmission electron microscopy, J. Electron Microsc. Tech. 14 (1990) 307–312, https://doi.org/10.1002/jemt.1060140404.
[32] R. Messier, A.P. Giri, R.A. Roy, Revised structure zone model for thin film physical structure, J. Vac. Sci. Technol. A Vacuum, Surfaces, Film. 2 (1984) 500–503, https://doi.org/10.1116/1.572604.
[33] R.N. Tait, T. Smy, M.J. Brett, Modelling and characterization of columnar growth in evaporated films, Thin Solid Films 226 (1993) 196–201, https://doi.org/10.1016/0040-6090(93)90378-3.
[34] J.M. Niewehuizen, H.B. Haanstra, Microfractography of thin films, Philips Tech. Rev. 27 (1966) 87–91.
[35] D.A.G. Bruggeman, Berechnung verschiedener physikalischer konstanten von heterogenen substanzen. III. Die elastischen konstanten der quasiisotropen mischkörper aus isotropen substanzen, Ann. Phys. 421 (1937) 160–178, https://

doi.org/10.1002/andp.19374210205.
[36] National Center for Biotechnology Information, PubChem Compound Database, CID = 24261 https://pubchem.ncbi.nlm.nih.gov/compound/24261 , Accessed date: 31 January 2019.
[37] R.K. Jain, J. Kaur, S. Arora, A. Kumar, A.K. Chawla, A. Khanna, Effects of oblique angle deposition on structural, electrical and wettability properties of Bi thin films grown by thermal evaporation, Appl. Surf. Sci. 463 (2019) 45–51, https://doi.org/10.1016/j.apsusc.2018.08.200.
[38] S. Chatterjee, M. Kumar, S. Gohil, T. Som, An oblique angle radio frequency sputtering method to fabricate nanoporous hydrophobic TiO_2 film, Thin Solid Films 568 (2014) 81–86, https://doi.org/10.1016/j.tsf.2014.08.005.
[39] C. Grüner, S. Liedtke, J. Bauer, S.G. Mayr, B. Rauschenbach, Morphology of thin films formed by oblique physical vapor deposition, ACS Appl. Nano Mater. 1 (2018) 1370–1376, https://doi.org/10.1021/acsanm.8b00124.
[40] S. Liedtke, C. Grüner, A. Lotnyk, B. Rauschenbach, Glancing angle deposition of sculptured thin metal films at room temperature, Nanotechnology 28 (2017) 385604, , https://doi.org/10.1088/1361-6528/aa7a79.
[41] D.F. Edwards, E. Ochoa, Infrared refractive index of silicon, Appl. Opt. 19 (1980) 4130, https://doi.org/10.1364/AO.19.004130.
[42] M. Nagamori, J.A. Boivin, A. Claveau, Gibbs free energies of formation of amorphous Si_2O_3, SiO and Si_2O, J. Non-Cryst. Solids 189 (1995) 270–276, https://doi.org/10.1016/0022-3093(95)00239-1.
[43] G. Rayner-Canham, T. Overton, Descriptive Inorganic Chemistry, 4th edition, W. H. Freeman & Co Ltd, New York, 2006.
[44] J.F. Moulder, W.F. Stickle, P.E. Sobol, K.D. Bomben, Handbook of X-Ray Photoelectron Spectroscopy: A Reference Book of Standard Spectra for Identification and Interpretation of XPS Data, Perkin-Elmer Corporation, Minnesota, 1992.
[45] Y. Hijikata, Physics and Technology of Silicon Carbide, InTech, Rijeka, 2013.
[46] K. Prabhakaran, T. Ogino, Oxidation of Ge(100) and Ge(111) surfaces: an UPS and XPS study, Surf. Sci. 325 (1995) 263–271, https://doi.org/10.1016/0039-6028(94)00746-2.
[47] B.V. Crist, Handbook of Monochromatic XPS Spectra, the Elements and Native Oxides, Wiley-VCH, New York, 2000.
[48] Y. Hua, Studies on quantification analysis of thin film layers (Si_3N_4, SiO_2, and TiW) in wafer fabrication using energy-dispersive X-ray microanalysis technique and SEC factors, J. Trace Microprobe Tech. 21 (2003) 25–34, https://doi.org/10.1081/TMA-120017889.
[49] R.F. Egerton, M. Malac, EELS in the TEM, J. Electron Spectros. Relat. Phenomena. 143 (2005) 43–50, https://doi.org/10.1016/j.elspec.2003.12.009.
[50] H. Li, J. Robertson, Germanium oxidation occurs by diffusion of oxygen network interstitials, Appl. Phys. Lett. 110 (2017) 222902, , https://doi.org/10.1063/1.4984805.
[51] J. Scott, P.J. Thomas, M. MacKenzie, S. McFadzean, J. Wilbrink, A.J. Craven, W.A.P. Nicholson, Near-simultaneous dual energy range EELS spectrum imaging, Ultramicroscopy 108 (2008) 1586–1594, https://doi.org/10.1016/j.ultramic.2008.05.006.
[52] F. de la Peña, T. Ostasevicius, V.T. Fauske, P. Burdet, E. Prestat, P. Jokubauskas, M. Nord, K.E. MacArthur, M. Sarahan, D.N. Johnstone, J. Taillon, A. Eljarrat, V. Migunov, J. Caron, T. Furnival, S. Mazzucco, T. Aarholt, M. Walls, T. Slater, F. Winkle, B. Martineau, G. Donval, R. McLeod, E.R. Hoglund, I. Alxneit, I. Hjorth, T. Henninen, L.F. Zagonel, A. Garmannslund, 5ht2, HyperSpy v1.4 (Version v1.4), Zenodo, 2018, https://doi.org/10.5281/zenodo.1407391.
[53] G. Bertoni, J. Verbeeck, Accuracy and precision in model based EELS quantification, Ultramicroscopy 108 (2008) 782–790, https://doi.org/10.1016/j.ultramic.2008.01.004.
[54] J.S. Custer, M.O. Thompson, D.C. Jacobson, J.M. Poate, S. Roorda, W.C. Sinke, F. Spaepen, Density of amorphous Si, Appl. Phys. Lett. 64 (1994) 437–439, https://doi.org/10.1063/1.111121.
[55] T. General, N. Si, The general properties of Si, Ge, SiGe, SiO_2 and Si_3N_4, Virginia Semiconductor https://www.virginiasemi.com/pdf/generalpropertiesSi62002.pdf, (2019) (31 January).
[56] M. Micoulaut, Structure of densified amorphous germanium dioxide, J. Phys. Condens. Matter. 16 (2004) L131–L138, https://doi.org/10.1088/0953-8984/16/10/L03.
[57] J.R. Blanco, P.J. McMarr, J.E. Yehoda, K. Vedam, R. Messier, Density of amorphous germanium films by spectroscopic ellipsometry, J. Vac. Sci. Technol. A Vacuum, Surfaces, Film. 4 (1986) 577–582, https://doi.org/10.1116/1.573851.

Publication II

Towards perfect IR transparency using glancing angle deposition

F. Maudet, B. Lacroix, A. J. Santos, F. Paumier, M. Paraillous,

C. Dupeyrat, R.Garcia, F. M. Morales, T. Girardeau

Applied Surface Science 470 (2019) 943–950

Applied Surface Science 470 (2019) 943–950

Contents lists available at ScienceDirect

Applied Surface Science

journal homepage: www.elsevier.com/locate/apsusc

Full Length Article

Towards perfect MWIR transparency using oblique angle deposition

F. Maudet[a,*], B. Lacroix[b,c], A.J. Santos[b,c], F. Paumier[a,*], M. Paraillous[d], C. Dupeyrat[d], R. García[b,c], F.M. Morales[b,c], T. Girardeau[a]

[a] Institut Pprime, Université de Poitiers – CNRS-SP2MI-BP 30179, 86962 Chasseneuil-Futuroscope, France
[b] Department of Materials Science and Metallurgic Engineering, and Inorganic Chemistry, Faculty of Sciences, University of Cádiz, Spain
[c] IMEYMAT: Institute of Research on Electron Microscopy and Materials of the University of Cádiz, Spain
[d] Safran Electronics and Defense, 86280 Saint-Benoît, France

ARTICLE INFO

Keywords:
Antireflective surface
Infrared
Oblique angle deposition
High transmittance
Effective medium approximation

ABSTRACT

This work reports the development of a perfect antireflective coating designed to operate over the 3.7–4.8 μm MWIR region, in order to improve the optics used in thermal detection systems. A simulated stack with 99.97% average transmittance is designed for a silicon support using an effective refractive index approach. This structure made of two layers is deposited by electron beam evaporation to achieve an optical transmittance as high as 99.21% and a 98.56% average. These performances are similar to that reported for the best MWIR interferential antireflective systems, but rely on a much simpler design. The first layer is fabricated by oblique angle deposition to obtain Ge nanocolumns that are then coated with a dense MgF_2 capping film. Because environmental pollution can cause light absorption in the infrared region, different techniques are combined to provide key insights about the nanostructure and the related optical properties: ellipsometry, spectrophotometry and scanning-transmission electron microscopy combined with energy-dispersive X-ray spectrometry. With this approach, essential chemical aspects like oxidation, water adsorption in the Ge layer and intermixing at the Ge/MgF_2 interface are evidenced. Advanced models based on effective medium approximation, considering this set of information, are addressed here to gain a better description of the optical response of the surface. In a context of performance optimization of this almost perfect antireflective bilayer, new routes and perspectives to limit or reduce these compositional issues are proposed.

1. Introduction

Infrared (IR) optics are used in a large variety of domains such as astronomy [1], building diagnostics [2] or agronomy [3]. In the IR region, the mid-wavelength-IR (MWIR) band covering the wavelengths from 3 μm to 5 μm plays a key role. This range forms one of the most important atmospheric transmission window [4] and it is particularly suitable for thermal imaging technologies in both civil and military applications related to navigation, targeting, surveillance and safety under all environmental conditions including fog, arctic, tropical, desert, sandstorm and maritime [5,6]. Unfortunately, materials currently used in the actual devices suffer from important reflection losses due to their high refractive index, which degrade significantly their performances. For example, at normal incidence, silicon with a refractive index of 3.4 will reflect about 30% of the light coming from the air at its interface. To limit light reflection, an antireflective (AR) coating can be deposed on top of the surface of interest [7,8]. Such treatment generally relies on destructive interferences created by the multiple reflections occurring when light encounters a material with a different refractive index. Up to date, the best AR coatings reported in the literature for Si and Ge optics in the MWIR region presents an average transmission of 98.5% over 3.6–4.9 μm [9]. For IR systems containing many optical elements and devoted to operate in a low light environment, further enhancement of the transmission at each interface even by only a few percent is essential. For example, a 1.5% increase of transmittance of a single interface, from 98.5% to 99.97%, can lead to 21% of overall transmittance gain for an optical system composed of 8 lenses (16 interfaces). However, the complexity of the interferential MWIR AR systems (multilayer stacks of different materials) and the small number of refractive indices available for transparent materials in the IR are currently limiting the design possibilities for improved MWIR optics.

To tackle this problem, a bottom-up process like oblique angle deposition (OAD) of thin films can be considered as an alternative since it has recently attracted much attention in the field of optics. By taking advantage of the self-shadowing effect, this method can be used to control the porosity rate at the nanoscale and thus to control the

* Corresponding authors.
E-mail addresses: florian.maudet@univ-poitiers.fr (F. Maudet), fabien.paumier@univ-poitiers.fr (F. Paumier).

https://doi.org/10.1016/j.apsusc.2018.11.176
Received 23 June 2018; Received in revised form 14 November 2018; Accepted 22 November 2018
Available online 23 November 2018
0169-4332/

effective refractive index of the deposited material [7]. The preparation of novel materials with tunable optical indices is suitable not only for the design of simpler and more efficient AR systems, but also for other coatings like distributed Bragg reflectors [10]. This OAD approach has been used many times to prepare AR surfaces covering the visible and/or near-IR ranges, mostly for photovoltaic applications, using SiO_2, TiO_2, ITO and Ge materials [11–13]. However, to our knowledge, there are no scientific reports that have already focused on OAD deposition for the engineering of AR coatings in the deeper IR region such as the MWIR band.

The paper reports for the first time the design and fabrication of a simple and highly efficient antireflective coating in the MWIR region (3.7–4.8 µm) using the oblique angle deposition process: a bilayer system composed of a germanium OAD film capped by a dense MgF_2 layer.

From advanced characterization, by transmission electron microscopy (TEM), IR spectrophotometry, ellipsometry and optical simulations, important nanostructural and chemical aspects influencing the AR MWIR properties are exposed. Combining these results generally overlooked in the literature, an advanced description for the optimization of the optical performances is presented.

2. Experimental section

2.1. Sample preparation

The experimental setup used for the deposition consists in a vacuum chamber (base pressure $2 \cdot 10^{-6}$ mbar) equipped with an electron-beam evaporator. Germanium OAD layers were deposited under a pressure of $2 \cdot 10^{-6}$ mbar with various angles of incidence from 0° to 82° by e-beam evaporation method using a germanium charge (Photonic sense© purity > 99.999%) on 2 mm thick (0 0 1) silicon substrates. The molten spot in the crucible has a diameter of 5 cm and the distance between the crucible and the sample is 70 cm leading to an angle deposition divergence of $\Delta\alpha = 4°$. Moreover, an estimated error of 10% of the deposition angle is assumed. To make easier further cross-sectional TEM observations of these samples, the substrates were intentionally placed with one ⟨1 1 0⟩ crystallographic axis perpendicular to the incoming deposition flux. A quartz crystal monitor was used to control the thickness and assure the deposition rate of 10 Å/s in normal incidence. Temperature of the deposition chamber was monitored and found to rise from 21 °C at the beginning of the evaporation to a value of 60 °C at the end of the process.

This elaboration set-up is not equipped with an in-situ adjustable orientation sample-holder, so the bilayer was made in two steps. For the first step, a germanium OAD layer was deposited at an angle of 65° with the condition of elaboration previously described. For the second step, the chamber was opened to modify the angle of incidence to a value of 0°. MgF_2 was then evaporated from pellets (Umicore© 99.99% purity) and deposited onto the germanium OAD layer. The deposition chamber was heated at a temperature of 200 °C to anneal the sample and MgF_2 layer was then grown at the same temperature and a deposition rate of 10 Å/s under a pressure of $2 \cdot 10^{-6}$ mbar. This whole process was repeated a second time to coat the silicon substrate on both sides.

2.2. Optical characterization

To access to optical properties of monolayer and bilayer, spectrophotometry and ellipsometry measurements were carried out for each sample. Transmittance and reflectance spectra were recorded with a Bruker Tensor 27 spectrometer. A great attention was dealt to assure a good parallelism for the silicon substrates as a non-parallel substrate can cause measurements to vary with the orientation of the sample. Transmittance and reflectance acquisitions were repeated 4 times for each sample giving a repeatability of 0.1%. The in-situ annealing transmittance measurement was made with a Woollam IR-Vase ellipsometer. Ellipsometry experiments were performed on the same Woollam IR-Vase ellipsometer.

2.3. Morphological and nanostructural characterizations

The overall morphology and thickness of the films were studied by scanning electron microscopy (SEM) using a FEG 7001F-TTLS JEOL microscope at an accelerating voltage of 30 kV.

To get additional insights about their nanostructure, transmission electron microscopy (TEM) experiments were conducted in a FEI Talos F200S microscope operated at 200 kV and equipped with a Super-X energy-dispersive X-ray spectrometry (EDX) system that includes two silicon drift detectors. Local compositional analyses were performed by combining high-angle annular dark field imaging (HAADF) and EDX acquisitions using the scanning (STEM) mode. EDX elemental maps of 100 × 100 pixels were obtained using a dwell time of 100 ms, energy resolution of 5 eV/channel over 4000 channels, and spatial drift correction. Cross-sectional specimens were thinned down by mechanical polishing using a tripod apparatus up to less than 10 µm followed by argon ion milling in a GATAN PIPS system (3.5 keV, ± 7° incidence). To minimize irradiation damage, the final step was performed at 2.5 keV, ± 5° during 5 min up to electron transparency.

3. Results and discussion

3.1. AR design for silicon substrate in the 3.7–4.8 µm range

AR coatings are usually designed with predefined materials, i.e. prefixed refractive indices. The thicknesses and number of layers are then optimized with a numerical iterative process to minimize the reflection at the interface, for a defined range of wavelength, by maximizing destructive interferences [14]. Herein we expected that the OAD technique could allow obtaining any effective refractive index values below that of the dense material counterpart. From this hypothesis, the optimization method used here for an AR coating can theoretically be used to improve the performance of any kind of optical thin film coating, for any substrate and any range of wavelength. In this paper, we have thus optimized a simple bilayer AR coating design for a silicon substrate (both sides treated) in the 3.7–4.8 µm region. Silicon was chosen because it is transparent in this infrared range, inexpensive, with well-known optical properties, and widely used in the industry. The AR optimizations were made with the commercial SCOUT software using the downhill simplex method with four free parameters for the bilayer coating (layer thickness and refractive index of each layer) [15].

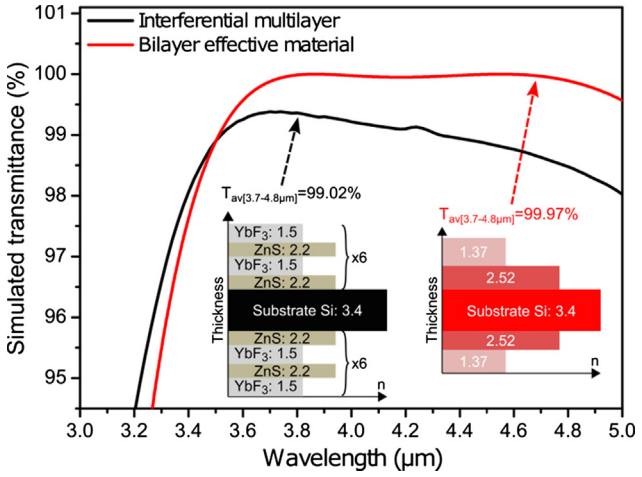

Fig. 1. Simulated transmittance spectra of an interferential (black) and an effective material bilayer (red) double sided AR coatings on silicon with their respective index profiles at λ = 4 µm.

Fig. 1 presents the transmittance spectrum of this optimized AR bilayer (with fictitious refractive index) compared with a conventional interferential system using dense materials: YbF_3/ZnS. This stack was designed with the Macleod software [14]. The optimal refractive indices of the optimized AR bilayer and those of the simulated classical interferential stack have been added on Fig. 1.

The simulated transmittance of the multilayer interferential stack is closed to the commercial specifications: 99.02% of average transmittance for the 3.7–4.8 μm range [16,17]. According to these simulations, it appears clearly that the transmittance of a silicon wafer can be increased significantly by reducing and controlling precisely the effective refractive index of the surface. In the present case, an average value of 99.97% over 3.7–4.8 μm may be reached with two layers having refractive index target values of 2.52 and 1.37 and thicknesses target of 427 nm and 779 nm respectively. This represents a 0.95% increase relative to the conventional interferential treatment. Among materials able to lead to these refractive indices, germanium was chosen because the latest is a well-known transparent material in the infrared region and because its high refractive index (n = 4 at λ = 4 μm) potentially permits to cover a wide range of effective refractive index using OAD geometries [18].

3.2. Ge OAD films: microstructural aspects and consequences on their refractive index as a function of deposition angles

To reach a refractive index close to the design value (n = 2.52 at λ = 4 μm), a calibration step of the effective refractive index obtained for Ge OAD is necessary. This was achieved by varying the deposition angle of Ge from α = 0° to a value of α = 82°. Fig. 2a shows a SEM cross-section and Fig. 2b is a plane view micrograph of a Ge OAD thin film taking, as an example, the thin film deposited with a deposition angle α = 65°. Pores and empty spaces are clearly seen on the top surface, which indicate the porosity of the films and the isolated nature of nanocolumns. The cross-section shows well separated inclined nanocolumns. This tilted angle β of the nanocolumns with respect to the Si surface depends on the deposition angle α: a value β = 62° was found in the present case for α = 65°. This tilt angle is higher than the one reported by Grüner et al. [19]. These differences may be ascribed to our large different setup chamber parameters as a higher divergence of the vapor flux, higher pressure in the chamber, effect of the temperature rise which can increase significantly the surface diffusion and to measurement errors of the deposition angle. However the objective being to calibrate the optical properties of a series of Ge, those uncertainties can be considered as acceptable. The porosity of OAD films increases with the deposition angle α due to an increasing shadowing effect and a lower ad-atom mobility on the film surface [20].

The effective refractive index of the Ge OAD thin films has been extracted from infrared ellipsometric and spectrophotometric measurements. For that purpose, we first determined the dispersion law

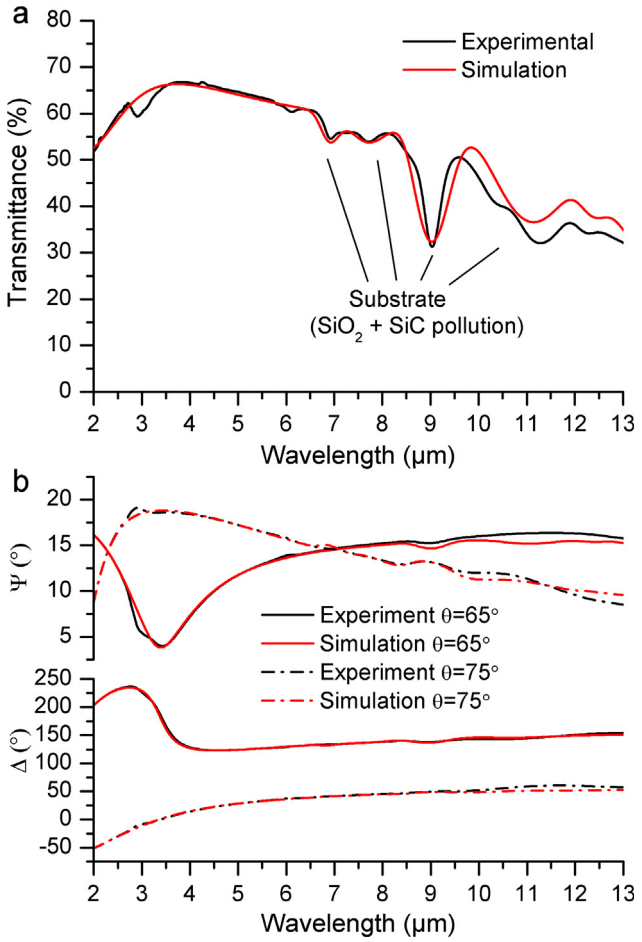

Fig. 3. (a) Spectrophotometric and (b) ellipsometric measurements for a reflexion angle θ = 65° and 75° (black) of a α = 65° Ge OAD thin film and its simulations (red) obtained with a simple Ge/void BEMA.

(Cauchy law) of the Ge thin film deposited at a normal incidence (α = 0°), considered as a dense and homogenous Ge thin film on silicon substrate. Then, taking into account the heterogeneous behavior of the nanostructured OAD thin films [21], a mixing law has been used (Bruggeman effective medium approximation BEMA) for each deposition angle. It is assumed here that the nanocolumns have the same optical behavior as the germanium dense material (obtained at α = 0°) so the mixing law is the result of a mixture of this bulk material and voids. The refractive index drop observed at higher deposition angle was simulated from BEMA model by taking into account the insertion of a volume fraction of air in the Ge layer, which is assumed to correspond to the film porosity.

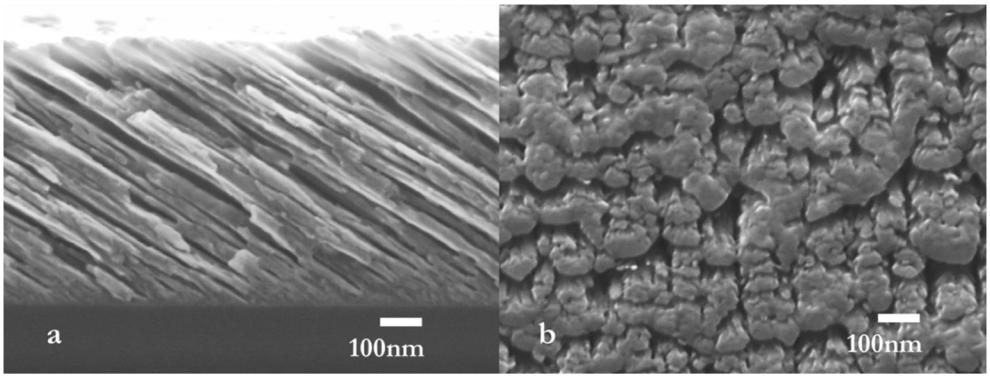

Fig. 2. (a) SEM cross-section view, (b) SEM tilted plane-view of a Ge OAD sample deposited at α = 65°.

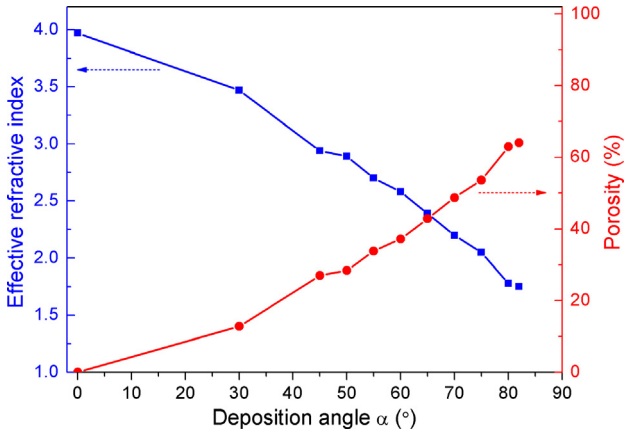

Fig. 4. Values of effective refractive index at λ = 4 μm and changing porosity of Ge OAD thin films extracted from simulations with the simple BEMA optical model for various deposition angles.

In the 2–6 μm spectral range, Fig. 3 shows a good fit of ellipsometric and spectrophotometric measurements on a Ge OAD thin film elaborated at α = 65° except for local discrepancies (located for example close to 3 μm and 10 μm), coming from pollution (discussed later). The simple BEMA optical model used for this simulation leads to 42.8% of porosity and an effective refractive index of n = 2.39 at λ = 4 μm. This model correctly fits the ellipsometric measurements for all deposition conditions. Fig. 4 presents the evolution of the porosity and effective refractive index of Ge OAD thin films at λ = 4 μm as function of the deposition angle. It shows that the effective refractive index of this material can be controlled from a value of 3.97 for α = 0° to a value of 1.75 for α = 82°. This also confirms that Ge is promising candidate to design AR films because it allows to cover a wide range of effective refractive indices using the OAD technique, as demonstrated by other authors [18].

3.3. Nanostructure and chemical analyses of the bilayer

In consideration of the preliminary results, the best experimental bilayer should be made using a germanium OAD bottom layer obtained with α = 60° or with α = 65° because these angles lead to the closest refractive index respectively (n = 2.58 and n = 2.40) compared with the designed target (n = 2.52). It must be added that the design was made with effective refractive indexes independent of the wavelength. By considering the dispersion law of the real refractive indexes, deposition of Ge OAD layer with α = 65° was preferred since it provides slightly enhanced AR performance. This ideal index of the top layer (n = 1.37) can be reached with this type of Ge nanostructuration (using an incident close to α = 88°, not presented here). Instead, a dense MgF_2 film deposited in normal incidence has been chosen as capping layer because its refractive index matches the ideal one (n = 1.37). In addition, this encapsulating layer can help ensuring the mechanical and chemical stability of the sample by minimizing the adsorption or absorption of environmental pollutants.

At this stage, chemical aspects of this study are considered because, as shown in Fig. 3, they can impact the optical performance of our stacks (refer for example to the singularities located at about 3 μm and 10 μm). This discussion is based on two experiments: the transmittance of the nanostructured Ge thin film (α = 65°) on the IR spectral range of 2–13 μm (Fig. 5) and an elemental analysis of the complete bilayer (including the nanostructured Ge thin film and the dense MgF_2 cap) from scanning TEM (STEM) energy-dispersive X-ray spectrometry (Fig. 7).

Various chemical features coming from pollutants can be observed on Fig. 5. The good match between the experimental spectrum and the simulation (described later in detail) attests that all of them have been

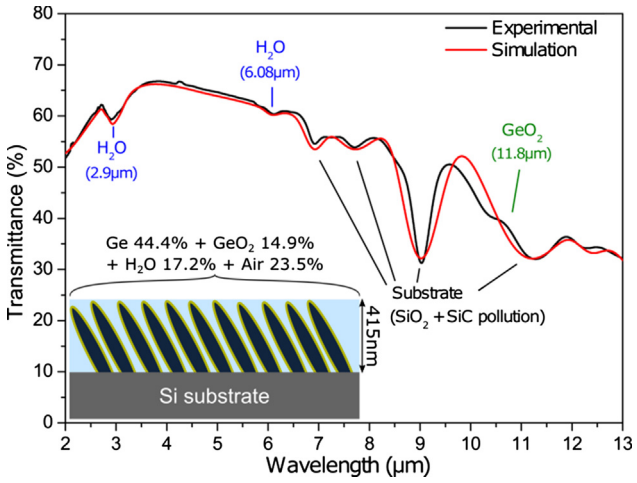

Fig. 5. Spectrophotometric measurement (black) of a α = 65° Ge OAD thin film and its simulation (red) with its BEMA model after considering water adsorption and oxidation.

identified. Those due to silicon contamination (referenced in black) are out of the range of interest 3.7–4.8 μm. Additional components coming from the nanostructured Ge thin film (referenced in blue and green) have been observed: two of them are attributed to water (located at 2.9 μm and 6 μm), the other one to germanium dioxide (located at 11.8 μm). According to PubChem [22], another absorption peak of GeO_2 should be present around 3.7 μm but its intensity is probably too small to identify it precisely. As demonstrated by other authors [23–25], these results show that, being a porous medium, the nanostructured Ge thin film is subjected to oxidation as well as water adsorption. These two elements were thus added in the BEMA mixing model and a regression was made on transmission (Fig. 5) and ellipsometry (Fig. 6a) spectra to determine the volume ratio of the different components. Thus, the germanium OAD layer deposited at α = 65° was found to be composed of 44.4% of Ge, 14.9% of GeO_2, 17.2% H_2O and 23.5% of air as illustrated on Fig. 5.

Finally, the resulting effective refractive index of this composite thin film is given in Fig. 6b. From the obtained extinction coefficient, we demonstrate that H_2O and GeO_2 will generate non-negligible absorption in the 3.7–4.8 μm range.

To gain further insights into the bilayer nanostructure and to confirm the chemical information extracted from optical spectroscopies, local analyses have been performed by TEM (Fig. 7). An overview of this system observed along a ⟨1 1 0⟩ direction of the Si substrate is shown in bright field in Fig. 7a. This observation confirms the morphology of the porous Ge OAD layer made of titled nanocolumns, and the dense character of the MgF_2 film. The selected area electron diffraction (SAED) patterns recorded in the different regions also indicate that the Ge nanocolumns are amorphous whereas the MgF_2 layer has a polycrystalline rutile structure, which is commonly observed after deposition by PVD processes [26]. Note that these TEM measurements were performed prior to the optimization of the thickness layers, which was done to match the designed performances. This explains why the layer thicknesses in Fig. 7 differ from the other results from SEM and ellipsometry, which were obtained on already optimized systems. However, the main purpose of TEM in this work was focused on the chemical characterization of the system which is expected to be unchanged after optimization.

The STEM-EDX analysis provides relevant compositional information of the bilayer. According to the elemental maps (Fig. 7b), a clear chemical evidence of Mg and F insertion inside the porosity of the bottom Ge layer is pointed out (see arrows), which contributes to form an intermixing layer at the interface between the Ge OAD and MgF_2 films. The extension of this interface layer is about 50 nm. The presence

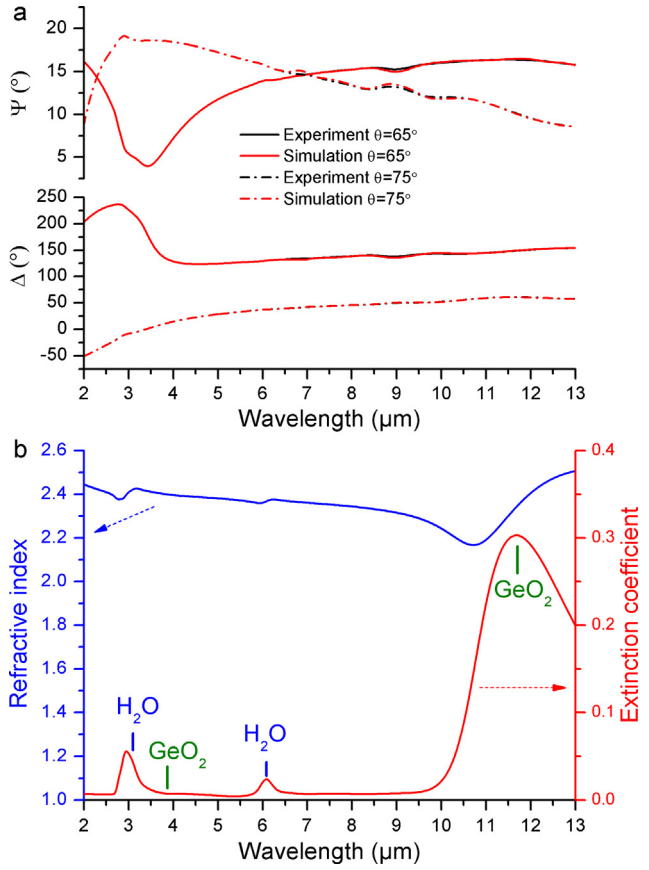

Fig. 6. (a) Ellipsometric measurements and simulations of Ge OAD film grown at a deposition angle of α = 65° for a reflexion angle θ = 65° and 75°. (b) Refractive index and extinction coefficient of the Ge OAD layer deposited at α = 65° obtained from ellipsometric (a), and spectrophotometric (Fig. 5) simulations using the optical model described by Fig. 5.

of oxygen is also visible in the Ge nanostructured film in agreement with the IR optical analysis predictions (Fig. 5). Quantitative data about the composition in the different layers has been obtained from EDX spectra, which were recorded by scanning areas of 150 × 200 nm^2 during 30 s with an electron probe of about 500 pA. Because sets of suitable standards materials are missing for our study, standardless analysis without thickness correction was performed using the FEI TEM Imaging and Analysis (TIA) software in order to evaluate the film composition. The K-lines were used to quantify O, F, Mg and Ge elements. Beforehand, the integral intensities of the different lines were extracted with a great care (subtraction of the background with a multi-polynomial approach, fitting of the peaks with a non-linear least square method). We are aware that this approach can lead to inaccuracy in the composition measurement, especially for light elements like O or F (systematic error of around 10–20% are generally admitted [27]), but it allows providing at least a general compositional tendency. The validity of the measurement is also supported by similar analyses we did on other systems presenting well-controlled stoichiometry (SiO_2 and TiO_2 OAD layers obtained by evaporation, results not published). The results shown in Fig. 7c not only confirm that the Ge is highly oxidized (54 at. % of O), but they also indicate that the MgF_2 layer contains oxygen in a minor amount (3 at.%). It is worth to note here that the F/Mg atomic ratio obtained from EDX is very close to 2, as expected for the MgF_2 layer. In the Ge OAD layer, the EDX analyses performed in different regions (from the bottom to the top) indicate that the oxygen content is constant (within the uncertainties of the measurement). Across the nanocolumns of the OAD layer, the O/Ge atomic ratio is substantially smaller than that of GeO_2 compound expected from the IR measurements. However, such differences may be explained by heterogeneous distributions of the oxide in each column (surface oxidation) or by uncertainties of the EDX measurements.

3.4. Optical performances and perspective of optimization of the Ge OAD/MgF_2 bilayer

The analyses presented in the previous section clearly highlight the key role of the chemistry on the optical properties of the Ge OAD/MgF_2 system. To optimize the transmittance, the presence of water and GeO_2 must be avoided since their absorption peaks are centered in (or close to) the range of interest, 3.7–4.8 μm (refer to Fig. 6b). For this, a new bilayer was fabricated in which the bottom Ge OAD has been annealed at 200 °C and was then, after opening the chamber to change the angle α to 0°, capped with MgF_2. These two layers were deposited on both sides of a thick silicon substrate (2 mm) for further optical characterizations and simulations. On Fig. 8c, the transmittance of the Ge OAD/MgF_2 bilayer is compared with the transmittance of the ideal AR design. The optimized Ge OAD/MgF_2 bilayer has a high maximum transmittance of 99.21% and very good average transmittance of 98.56% over 3.7–4.8 μm. This bilayer presents better performance than a typical commercial coating of 98% average transmission over 3.6–4.9 μm (representing a 0.56% transmittance average gain) [17] and similar efficiency compared with the best MWIR AR coating reported in the literature for Si and Ge optics [9]. However, simplicity of the design proposed in this paper enables a reduction of the manufacturing time and costs. Unfortunately, the experimental transmittance is still below the ideal design one.

To study other optimization paths of the Ge OAD/MgF_2 bilayer we have first simulated its optical characteristics (transmittance and ellipsometry). From the set of chemical information obtained by optical measurements and TEM, an optical model to simulate the behavior of the system was established. For the bottom layer, the model already described previously has been used: a BEMA, mixing Ge, GeO_2, water and void, using the optical properties of these compounds from literature. As pointed out from the STEM-EDX analysis, an intermixing layer is present between the Ge OAD and MgF_2 layer. This layer was also taken into account in the simulations using a BEMA mixing model. A graded concentration of MgF_2 mixed with Ge-GeO_2 has been assumed for this intermixing layer simulating the concentration by decomposing this region into 10 sublayers with various concentration rates of MgF_2. Finally, a MgF_2 layer was added on top of this intermixing layer. On Fig. 8b and Fig. 8c the optical simulation (ellipsometry and transmittance) of the experimental data using this model is presented. A schematic representation of this model is depicted on Fig. 8a.

As shown in Fig. 8b and Fig. 8c, the very good agreement between the simulation and the experimental measurements gives credibility to the model used and consequently demonstrates the coherence between chemical and optical analyses. From this simulation, we were able to determine that the 406 nm thick Ge OAD layer is composed of 12% of GeO_2, 44% of Ge, 40% of Air and 4% of water. The annealing process is thus able to reduce the amount of water present in the Ge OAD layer from a value of 11% to a value of 4% when sealed by a MgF_2 layer. The intermixing layer between the Ge OAD layer and the MgF_2 layer was found to be of a thickness of 39 nm with a MgF_2 volume fraction ranging from 55% at the bottom to 100% on top. Above it the MgF_2 layer was determined to be 672 nm thick.

Qualitatively, the TEM results are consistent with the optical model where the intermixing zone was determined to be 39 nm thick and with an MgF_2 concentration gradient. From a quantitative point of view, compositional information extracted from optical measurements and TEM are not directly comparable. In the case of ellipsometry, the simulations provide volume fractions of the different components present in the coating at a macroscopic scale (including porosity), while EDX gives elemental composition in individual nanocolumns. In order to compare these data, we can estimate roughly what should be the atomic

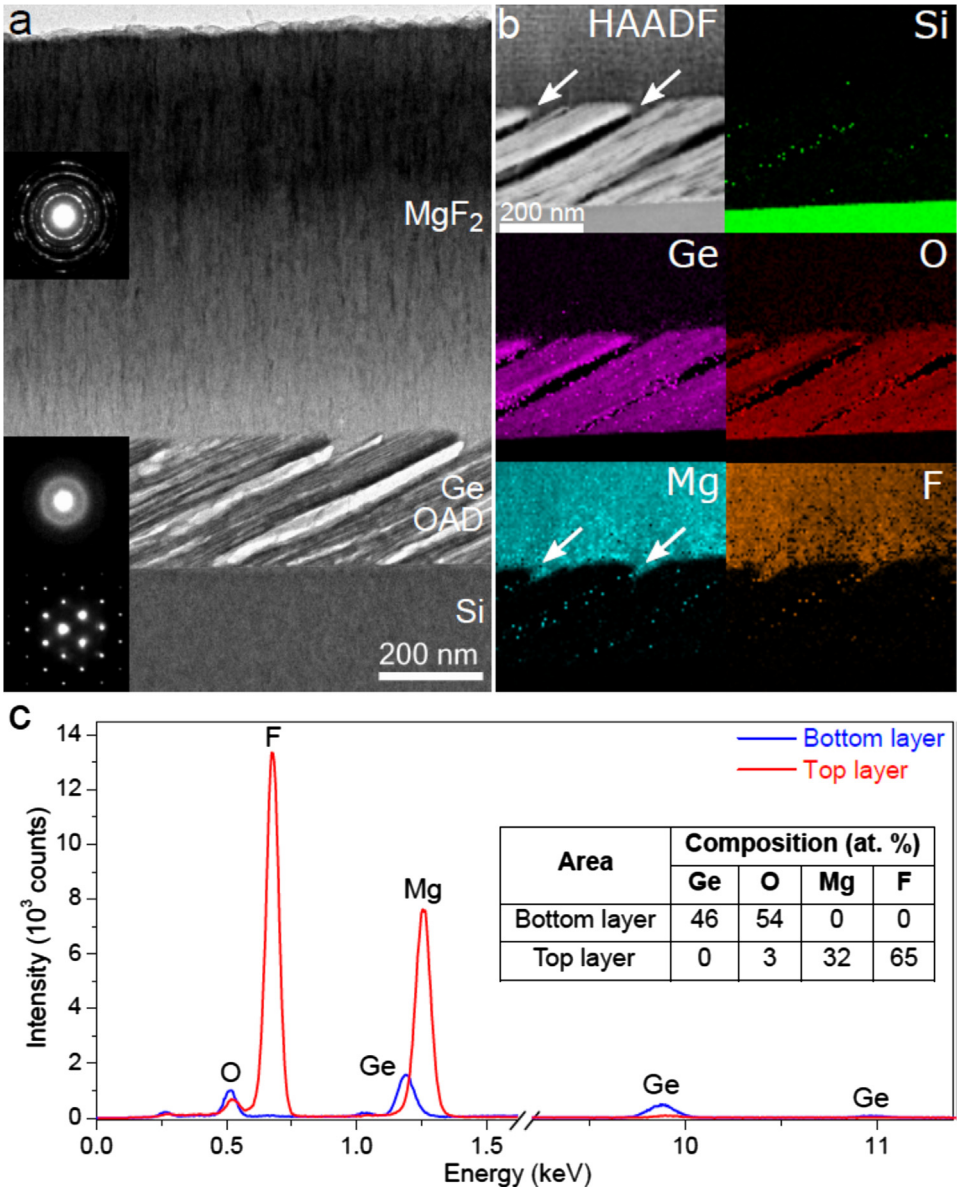

Fig. 7. (a) Bright field TEM overview of the bilayer on Si. The insets correspond to the SAED patterns recorded in the different regions. (b) STEM-EDX analysis at the vicinity of the Ge OAD/MgF_2 interface. HAADF image and elemental maps obtained for Si, Ge, O, Mg and F atoms are presented. (c) EDX spectra and associated quantitative analyses of composition in the bottom and top layers.

composition of Ge and O from the volume fractions given by ellipsometry. For that purpose, voids contribution has been discarded and densities of amorphous Ge and GeO_2 taken from the literature have been used [28,29]. With these assumptions, a composition of 65 at.% of Ge and 35 at.% of O is estimated. This oxygen content in the nanocolumns estimated from ellipsometry appears to be significantly lower than that obtained from EDX. These differences may be ascribed to the very local STEM-EDX technique.

In a context of optimization of the Ge OAD/MgF_2 bilayer, the sum of the simulated transmittance and absorption spectra (extracted from the optical model) are shown on Fig. 8. These data demonstrate that it is possible to enhance the optical performances of the AR by reducing the absorption sources present in the Ge OAD layer, i.e. GeO_2 and H_2O. To support this assumption, we performed an *in-situ* spectrophotometric measurement while annealing under vacuum the Ge OAD/MgF_2 layer to a temperature of 200 °C for 1 h (blue spectrum of the Fig. 8c). The obtained spectrum is close to the summed simulated spectrum (absorption + transmittance). This result proves that an annealing allows suppressing efficiently the absorption caused by H_2O, enhancing the average transmittance value from 98.56% to 99.17%. Unfortunately, water is readsorbed when exposing the annealed sample to atmospheric pressure, which suggests that the MgF_2 capping layer is probably not fully dense. The remaining difference between the design and the T + A spectrum is explained by the fact that the obtained refractive index of the Ge OAD layer (n = 2.40) is not the optimal one (n = 2.52).

Limiting the contamination and optimizing the refractive index of the Ge OAD layer will be the subject of further research. It will be made possible with the ongoing construction of a new home-made deposition chamber at the PPRIME Institute. This equipment, combining electron-beam and ion sputtering processes, will allow controlling finely and *in-situ* the deposition angle α. This approach will be considered in a close future to avoid oxidation phenomenon due to air exposure during the fabrication of the Ge OAD/MgF_2 system and to achieve a fine-tuning of the effective refractive indices.

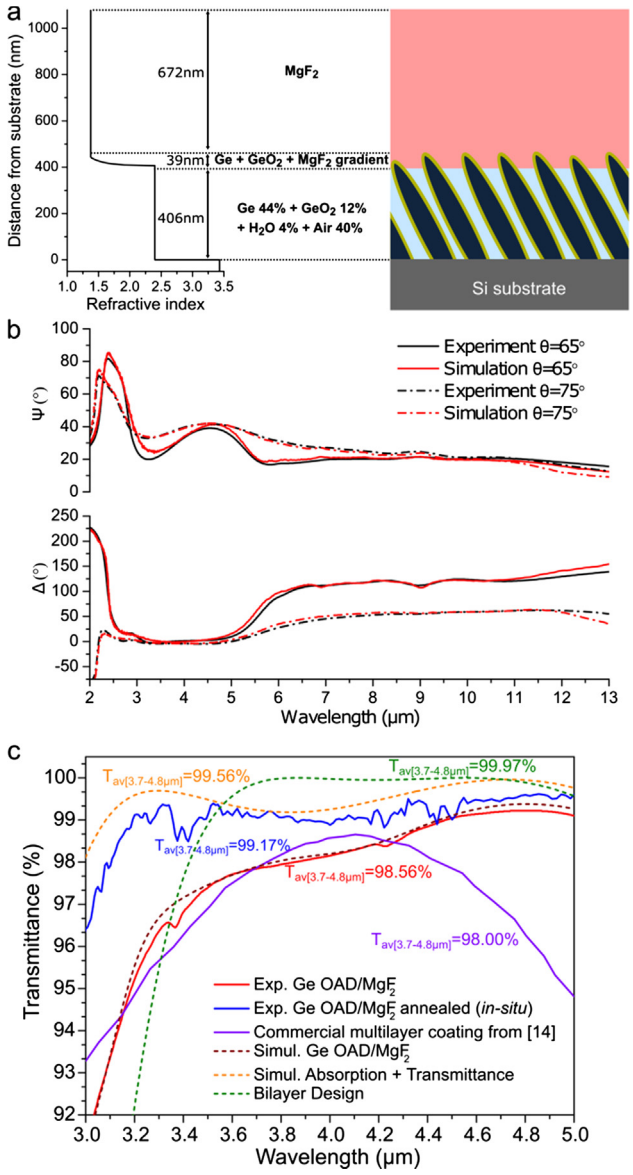

Fig. 8. Optical model of the Ge OAD/MgF_2 bilayer (a) simulating the ellipsometric (b) and spectrophotometric measurements (c).

4. Conclusion

In this work, we demonstrated that oblique angle deposition is a powerful approach to design and fabricate simple and high-performance antireflective surfaces for Si optics in the MWIR range. Taking into account fictive materials with effective refractive indices, we were able to design and simulate an AR coating with 99.97% transmittance over the 3.7–4.8 μm atmospheric window. This corresponds to a theoretical performance increase of about 2% compared to a standard AR system with dense materials. The optimization of the growth conditions, to obtain a bilayer made of a porous Ge OAD film with reduced effective refractive index and capped with a dense MgF_2 layer, allows achieving performances (98.56% average transmittance for 3.7–4.8 μm) similar to that of the best multilayered AR coatings reported in the literature, but with a much simpler structure suitable for large scale production. By combining IR ellipsometry, spectrophotometry and STEM-EDX analyses, it was pointed out that an important limiting factor for the transmittance is the presence of pollutants, more particularly GeO_2 and water, that lead to a degradation of the optical efficiency due to light absorption. *In-situ* optical measurements conducted during vacuum annealing showed that the performances of the AR system can be enhanced to 99.17% simply by evaporating water, opening new perspectives to achieve nearly perfect infrared transparency through the future improvements in the deposition process.

Acknowledgements

A. J. Santos thanks the financial support of the IMEYMAT Institute as well as the Ministerio de Ciencia, Innovación y Universidades and Ministerio de Educación y Formación Profesional in Spain for the concessions of grants (ICARO-173873 and FPU16-04386). The “Talent Attraction Program” of the University of Cádiz is also acknowledged by supporting B. Lacroix contract code E-11-2017-0117214. This work was supported by the DGA (Direction Générale de l’Armement), the French Defense Procurement Agency. This work has been partially supported by «Nouvelle Aquitaine» Region and by European Structural and Investment Funds (ERDF reference P-2016-BAFE-209): IMATOP project.

References

[1] G.G. Fazio, J.L. Hora, L.E. Allen, M.L.N. Ashby, P. Barmby, L.K. Deutsch, J.-S. Huang, S. Kleiner, M. Marengo, S.T. Megeath, G.J. Melnick, M.A. Pahre, B.M. Patten, J. Polizotti, H.A. Smith, R.S. Taylor, Z. Wang, S.P. Willner, W.F. Hoffmann, J.L. Pipher, W.J. Forrest, C.W. McMurty, C.R. McCreight, M.E. McKelvey, R.E. McMurray, D.G. Koch, S.H. Moseley, R.G. Arendt, J.E. Mentzell, C.T. Marx, P. Losch, P. Mayman, W. Eichhorn, D. Krebs, M. Jhabvala, D.Y. Gezari, D.J. Fixsen, J. Flores, K. Shakoorzadeh, R. Jungo, C. Hakun, L. Workman, G. Karpati, R. Kichak, R. Whitley, S. Mann, E.V. Tollestrup, P. Eisenhardt, D. Stern, V. Gorjian, B. Bhattacharya, S. Carey, B.O. Nelson, W.J. Glaccum, M. Lacy, P.J. Lowrance, S. Laine, W.T. Reach, J.A. Stauffer, J.A. Surace, G. Wilson, E.L. Wright, A. Hoffman, G. Domingo, M. Cohen, The Infrared Array Camera (IRAC) for the Spitzer space telescope, Astrophys. J. Suppl. Ser. 154 (2004) 10–17, https://doi.org/10.1086/422843.
[2] C.A. Balaras, A.A. Argiriou, Infrared thermography for building diagnostics, Energy Build. 34 (2002) 171–183, https://doi.org/10.1016/S0378-7788(01)00105-0.
[3] M. Shibayama, T. Akiyama, Seasonal visible, near-infrared and mid-infrared spectra of rice canopies in relation to LAI and above-ground dry phytomass, Remote Sens. Environ. 27 (1989) 119–127, https://doi.org/10.1016/0034-4257(89)90011-4.
[4] D.M. Gates, W.J. Harrop, Infrared transmission of the atmosphere to solar radiation, Appl. Opt. 2 (1963) 887–898, https://doi.org/10.1364/AO.2.000887.
[5] R. Breiter, T. Ihle, K. Mauk, M. Münzberg, W. Rode, Long range thermal weapon sights for the German future infantryman program IdZ, in: B.F. Andresen, G.F. Fulop, P.R. Norton (Eds.), Proc. SPIE 6542, Infrared Technology and Applications XXXIII, 2007, pp. 65422U. https://doi.org/10.1117/12.718424.
[6] A. Rogalski, K. Chrzanowski, Infrared devices and techniques (revision), Metrol. Meas. Syst. 21 (2014) 565–618, https://doi.org/10.2478/mms-2014-0057.
[7] K. Robbie, M.J. Brett, Sculptured thin films and glancing angle deposition: growth mechanics and applications, J. Vac. Sci. Technol. A Vacuum Surf. Film 15 (1997) 1460–1465, https://doi.org/10.1116/1.580562.
[8] C.K. Hwangbo, Y.J. Park, K.M.A. Sobahan, J.J. Kim, Antireflection coatings with helical SiO_2 films prepared by using glancing angle deposition, J. Korean Phys. Soc. 55 (2009) 2634–2637, https://doi.org/10.3938/jkps.55.2634.
[9] M. Bhatt, B.B. Nautiyal, P.K. Bandyopadhyay, High efficiency antireflection coating in MWIR region (3.6–4.9 μm) simultaneously effective for germanium and silicon optics, Infrared Phys. Technol. 53 (2010) 33–36, https://doi.org/10.1016/j.infrared.2009.08.006.
[10] M.F. Schubert, J.-Q. Xi, J.K. Kim, E.F. Schubert, Distributed Bragg reflector consisting of high- and low-refractive-index thin film layers made of the same material, Appl. Phys. Lett. 90 (2007) 141115, , https://doi.org/10.1063/1.2720269.
[11] M.F. Schubert, D.J. Poxson, F.W. Mont, J.K. Kim, E.F. Schubert, Performance of antireflection coatings consisting of multiple discrete layers and comparison with continuously graded antireflection coatings, Appl. Phys. Exp. 3 (2010) 082502, , https://doi.org/10.1143/APEX.3.082502.
[12] J.W. Leem, J.S. Yu, Glancing angle deposited ITO films for efficiency enhancement of a-Si:H/μc-Si:H tandem thin film solar cells, Opt. Exp. 19 (2011) A258–A269, https://doi.org/10.1364/OE.19.00A258.
[13] J.W. Leem, J.S. Yu, Multi-functional antireflective surface-relief structures based on nanoscale porous germanium with graded refractive index profiles, Nanoscale 5 (2013) 2520–2526, https://doi.org/10.1039/C3NR00286A.
[14] Optical Thin-Film Software: The Essential Macleod (Thin Film Center Inc., Version 8.18.0) <http://www.thinfilmcenter.com/essential.html> (accessed March 25, 2013).
[15] W. Theiss, G. Scout, Hard- and Software: Aachen, Technical Manual, 2014.
[16] Silicon AR coating from THORLABS available on www.thorlabs.com, (accessed October 1, 2018).
[17] Silicon AR coating from EdmundOptics available on www.edmundoptics.com, (accessed October 1, 2018).
[18] J.W. Leem, J.S. Yu, Broadband and wide-angle distributed Bragg reflectors based on

amorphous germanium films by glancing angle deposition, Opt. Exp. 20 (2012) 20576–20581, https://doi.org/10.1364/OE.20.020576.
[19] C. Grüner, S. Liedtke, J. Bauer, S.G. Mayr, B. Rauschenbach, Morphology of thin films formed by oblique physical vapor deposition, ACS Appl. Nano Mater. 1 (2018) 1370–1376, https://doi.org/10.1021/acsanm.8b00124.
[20] M.M. Hawkeye, M.J. Brett, Glancing angle deposition: fabrication, properties, and applications of micro- and nanostructured thin films, J. Vac. Sci. Technol. A Vacuum Surf. Film 25 (2007) 1317–1335, https://doi.org/10.1116/1.2764082.
[21] G.A. Niklasson, C.G. Granqvist, O. Hunderi, Effective medium models for the optical properties of inhomogeneous materials, Appl. Opt. 20 (1981) 26–30, https://doi.org/10.1364/AO.20.000026.
[22] National Center for Biotechnology Information. PubChem Compound Database; CID = 14796 <https://pubchem.ncbi.nlm.nih.gov/compound/14796>, <https://pubchem.ncbi.nlm.nih.gov>.
[23] K. Robbie, Y. Cui, C. Elliott, K. Kaminska, Oxidation of evaporated porous silicon rugate filters, Appl. Opt. 45 (2006) 8298–8303, https://doi.org/10.1364/AO.45.008298.
[24] A. Borrás, J.R. Sánchez-Valencia, J. Garrido-Molinero, A. Barranco, A.R. González-Elipe, Porosity and microstructure of plasma deposited TiO_2 thin films, Microporous Mesoporous Mater. 118 (2009) 314–324, https://doi.org/10.1016/j.micromeso.2008.09.002.
[25] A. Borrás, A. Barranco, A.R. González-Elipe, Design and control of porosity in oxide thin films grown by PECVD, J. Mater. Sci. 41 (2006) 5220–5226, https://doi.org/10.1007/s10853-006-0431-y.
[26] D. Jacob, F. Peiró, E. Quesnel, D. Ristau, Microstructure and composition of MgF_2 optical coatings grown on Si substrate by PVD and IBS processes, Thin Solid Films 360 (2000) 133–138, https://doi.org/10.1016/S0040-6090(99)00738-5.
[27] B.K.E. MacArthur, The use of annular dark-field scanning transmission electron microscopy for quantitative characterisation, Johnson Matthey Technol. Rev. 60 (2016) 117–131, https://doi.org/10.1595/205651316X691186.
[28] J.R. Blanco, P.J. McMarr, J.E. Yehoda, K. Vedam, R. Messier, Density of amorphous germanium films by spectroscopic ellipsometry, J. Vac. Sci. Technol. A Vacuum Surf. Film 4 (1986) 577–582, https://doi.org/10.1116/1.573851.
[29] M. Micoulaut, Structure of densified amorphous germanium dioxide, J. Phys. Condensed Matter. 16 (2004) L131–L138, https://doi.org/10.1088/0953-8984/16/10/L03.

Publication III

On the importance of light scattering for high performances nanostructured antireflective surfaces

F. Maudet, B. Lacroix, A. J. Santos, F. Paumier, M. Paraillous, S. Hurand, A. Corvisier, C. Dupeyrat, R. García, F. M. Morarles, T. Girardeau

Acta Materialia 188 (2020) 386–393

Acta Materialia 188 (2020) 386–393

Contents lists available at ScienceDirect

Acta Materialia

journal homepage: www.elsevier.com/locate/actamat

Full length article

On the importance of light scattering for high performances nanostructured antireflective surfaces

Florian Maudet[a,b,*], Bertrand Lacroix[c,d], Antonio J. Santos[c,d], Fabien Paumier[b], Maxime Paraillous[e], Simon Hurand[b], Alan Corvisier[b], Cyril Dupeyrat[e], Rafael García[c,d], Francisco M. Morales[c,d], Thierry Girardeau[b]

[a] Institute of Functional Thin Film Oxides for Energy-Efficient Future Information Technology, Helmholtz-Zentrum Berlin für Materialien und Energie Hahn-Meitner-Platz 1, 14109 Berlin, Germany
[b] Institut Pprime, UPR 3346 CNRS-Université de Poitiers-ENSMA, SP2MI, 86962 Futuroscope-Chasseneuil Cedex, France
[c] Department of Materials Science and Metallurgic Engineering, and Inorganic Chemistry, Faculty of Sciences, University of Cádiz, Spain
[d] IMEYMAT, Institute of Research on Electron Microscopy and Materials of the University of Cádiz, Spain
[e] Safran Electronics and Defense, 26 avenue des Hauts de la Chaume, 86280 Saint-Benoit, France

ARTICLE INFO

Article History:
Received 12 August 2019
Revised 25 January 2020
Accepted 7 February 2020
Available online 14 February 2020

Keywords:
Antireflective coating
Oblique angle deposition
Moth-eye
Gradient refractive index
Light scattering
Bruggeman effective medium approximation
FDTD
Electron tomography

ABSTRACT

An antireflective coating presenting a continuous refractive index gradient is theoretically better than its discrete counterpart because it can give rise to a perfect broadband transparency. This kind of surface treatment can be obtained with nanostructures like moth-eye. Despite the light scattering behavior must be accounted as it can lead to a significant transmittance drop, no methods are actually available to anticipate scattering losses in such nanostructured antireflective coatings. To overcome this current limitation, we present here an original way to simulate the scattering losses in these systems and routes to optimize the transparency. This method, which was validated by a comparative study of coatings presenting refractive indices with either discrete or continuous gradient, shows that a discrete antireflective coating bilayer made by oblique angle deposition allows reaching ultra-high mean transmittance of 98.97% over the broadband [400–1800] nm. Such simple surface treatment outperforms moth-eye architectures thanks to both interference effect and small dimensions nanostructures that minimize the scattering losses as confirmed by finite-difference time domain simulations performed on reconstructed volumes obtained from electron tomography experiments.

1. Introduction

Antireflective coatings (ARC) are indispensable features of high transmittance substrate with applications in a wide variety of domains of photonics as for example in optics or photovoltaic [1–4]. Particularly the need for a broadband ARC ensuring a high transparency glass substrate from the visible up the near infrared (NIR) is of interest accordingly to the available detectors [5]. Different approaches can be used to achieve broadband ARC. So far, the main way relies on the deposition of thin films forming a multilayer stack alternating materials with high and low refractive indices [6,7]. The refractive index (RI) and thickness of each layer are optimized to create destructive interference with the reflected wave [6,7]. However, for broadband wavelength applications this approach is challenging due to the lack of material available and to the complexity of the layer assembly to deposit in order to obtain high transmittance [3,6,7]. To go beyond these limitations, other approaches have been considered. As it is now well established, a gradient refractive index ARC (GRIARC) can suppress efficiently the light reflection over wide spectral ranges [8,9]. Recently, Kim and Park have demonstrated that it is indeed possible to perfectly remove the light reflection of any wavelength using a gradient profile of refractive index determined analytically [10]. From this analytical development it was established that perfect broadband antireflective property comes with a constraint on the dispersion law of the coating material. For thin GRIARC nanostructures in regard to the probing wavelength, it can be shown that perfect reflectance suppression comes with the use of anomalous dispersion materials. In order to obtain perfectly transparent ARC, this has to be avoided since the anomalous dispersion behavior of a material usually comes from an increasing extinction coefficient that will consequently lead to light absorption [10]. It may be noted however,

* Corresponding author at: Institute of Functional Thin Film Oxides for Energy-Efficient Future Information Technology, Helmholtz-Zentrum Berlin für Materialien und Energie Hahn-Meitner-Platz 1, 14109 Berlin, Germany.
E-mail address: florian.maudet@helmholtz-berlin.de (F. Maudet).

https://doi.org/10.1016/j.actamat.2020.02.014
1359-6454/

that the use of new metamaterials, still in the early development stage, could remove this constraint [11].

Nevertheless, the dispersion law becomes normal for sufficiently thick GRIARC structures. The optimal gradient profile is then close to the well-known quintic profile that was determined from numerical optimizations [12]. It can be derived from those calculations that using normal dispersion law material there will be a thickness dependency of the ARC efficiency.

In practice these ARC can be achieved by employing innovative nanostructuration methods to reduce the refractive index through the introduction of porosity, as conventional dense materials with RI below 1.39 do not exist [3]. GRIARC can be made by moth eye nanostructures (ME), called from their natural presence on the eyes of moths [13]. These biomorphic structures, consisting in pseudo-regular arrays of nanopillars, are mainly characterized by two parameters: their height, that is equivalent to the GRIARC thickness, and their width. Due to their shape, these ME structures present a gradually increasing porosity from their bases to their tips. If their dimensions are sufficiently small in regard of the probing light wavelength, the mixing result can be considered as a gradient effective RI that can be calculated from the Bruggeman effective medium approximation (BEMA). [14] Such structures are usually obtained by a reactive ion etching process although it can also be made from embossing process or other replicative methods [13,15–24]. These GRIARC follow behavior predicted by the BEMA for the long wavelength range, a thicker GRIARC is more efficient to suppress reflectance than its thinner counterpart [1,15,18,20,21,23,25]. On the contrary, on the short wavelength range a thicker GRIARC leads to higher optical losses that reduce the transmittance level [23]. This results in a necessary compromise to be found on the optimal thickness. Such compromise is usually determined empirically as the optical losses are not considered by the BEMA model.

Furthermore, it was pointed out that when a very low RI, or a high level of porosity, cannot be obtained, the performances of a discrete ARC can be higher than a continuous gradient thanks to the interference effects [26]. Such discrete ARC, can be made using oblique angle deposition (OAD) as it is a viable, flexible technique among all existing fabrication processes [13,27–35]. It allows a fine-tuning of the porosity inserted at the nanoscale through the adjustment of the deposition angle α, thus promoting a high control of the RI [36] .This method has been used many times for antireflective application demonstrating remarkably low reflectivity or high transmittance over a large domain of wavelength [8,27,28,37,38]. Enhancing the performances of these AR comes to the expanse of thicker stack with a higher porosity. However, to our knowledge the problem of light scattering that will arise on such OAD structures, limiting the transmittance performances, has not yet been specifically addressed.

In this article we aim to compare the transmittance performances of GRIARC with a discrete ARC made by OAD on the broadband range of [400–1800] nm. We specifically focus on the light scattering that may arise in these nanostructures as it hinders the transparency of thick ARC. An original method is presented to calculate those optical losses, making easier future designs and optimizations of nanostructured discrete ARC or GRIARC. Based on this approach, a discussion is made to understand the current limits of broadband nanostructured ARC performances and what problems need to be solved to lift them.

2. Experimental section

The experimental setup used for the oblique angle deposition consists in a vacuum chamber (base pressure 2.10−6 mbar) equipped with an electron-beam evaporator. For the calibration step of thickness and refractive index, SiO_2 OAD layers were deposited at various angles of incidence from 0° to 85° by e-beam evaporation method using SiO_2 (Umicore© purity>99.99%) in Mo crucible on 1 mm thick, 1 inch diameter BK7 glass substrates. A quartz crystal monitor was used to control the thickness and assure a deposition rate of 10 Å/s in normal incidence. The deposition was performed at room temperature. This elaboration set-up is not equipped with an in-situ adjustable orientation sample-holder, so the bilayer was made in two steps with an azimuthal rotation of Φ=180° in between. For the first step, a SiO_2 layer was deposited at an angle of 65° with the condition of elaboration previously described. For the second step, the chamber was opened to modify the angle of incidence to a value of 85°. The second layer of SiO_2 was then evaporated and deposited onto the first OAD layer. This whole process was repeated a second time to coat the BK7 substrate on both sides. Note that this bilayer was deposited at the same time on a (001) silicon substrate, which was intentionally placed with one ⟨110⟩ crystallographic axis perpendicular to the incoming deposition flux for further analyses by transmission electron microscopy (TEM [39]. The SiO_2 stoichiometry was confirmed through a STEM-EDX analysis on an OAD layer with the deposited angle of 75° and 85°.

To access the optical properties of monolayer and bilayer, spectrophotometry measurements were carried out for each sample. Transmittance and reflectance spectra were recorded with a Carry 5000 Varian spectrophotometer. Transmittance and reflectance acquisitions were repeated 4 times for each sample giving a repeatability of 0.1%. As anisotropic behavior may be expected from OAD nanostructures, measurements were made with a polarization both in the direction of the columns ($P_{//}$) and perpendicular ($P_{\perp}$) to it as illustrated in Fig. 2a.

The nanostructure of the OAD samples was analyzed by TEM experiments at an acceleration voltage of 200 kV. Bright-field TEM images were recorded in a JEOL 2010F microscope. The 3D morphology of the OAD SiO_2 bilayer was extracted from electron tomography in a FEI Titan Cubed Themis 60−300 microscope, using the high-angle annular dark-field scanning TEM (HAADF-STEM) imaging mode. For that purpose, a dedicated tomography holder operated by the FEI Xplore3D software was used to acquire tilt series every 2° from −60° to +60°. The FEI Inspect 3D software was then employed to align the projections using cross-correlation methods, and to perform reconstruction into a 3D volume using the conventional simultaneous iterative reconstruction technique (SIRT) with 30 iterations. The FEI Avizo program was used for 3D visualization and segmentation of the reconstructed volume. Specimen for TEM were prepared by soft and flat mechanical polishing of the two faces using a tripod apparatus (Model 590 Tripod Polisher) in order to control finely the thinning down to a few microns. This step was followed by a short Ar^+-ion milling step in a Gatan PIPS system (using an energy of 3.5 keV and an incidence angle of +/−7°). This procedure provides large and homogeneous electron transparent areas, which is suitable to limit the geometrical shadowing of the specimen at large tilt angles of the holder. Prior to insertion into the microscope, the specimen was cleaned in an Ar/O_2 plasma in order to remove the hydrocarbon contamination.

Finite-difference time domain (FDTD) simulations were carried out with the Lumerical© commercial software. The 3D reconstruction model of the SiO_2 bilayer obtained from electron tomography was slightly cropped to remove defects on the edges of the reconstruction and then converted into a surface file to be imported in the FDTD software. We then assumed that the refractive indexes of the material and porosity (empty space) components in the 3D reconstructed volume correspond to that of the dense SiO_2 film and of air, respectively. A simulation box of $800 \times 50 \times 500$ nm^3 with perfect matched layer boundaries and a mesh size of 1 nm was used. Total Field/Scattered Field source with slightly higher dimensions than the 3D bilayer was used to determine the scattering cross section of the structure. The source polarization was aligned with the direction of the columns (indicated by the red arrow in Fig. 2a) to respect the spectrophotometric measurements conditions.

The ME simulations were performed under the same conditions with a box size varying accordingly to the dimensions of the pyramid

structures. Five height dimensions of pyramid going from 500 to 2000 nm were tested with each 8 square bases dimensions ranging from 10 to 200 nm.

3. Results and discussions

3.1. Different theoretical approaches for broadband antireflective coatings

As previously stated, a GRIARC needs to be sufficiently thick to be efficient over a broadband. To emphasize this aspect, we present in Fig. 1a the simulated transmittance spectra on the wide [400–2000] nm range for different thicknesses of GRIARC on both sides of a glass (BK7) substrate following the quintic profile. The optical designs of the GRIARC systems are given in Fig. 1b.

Although thin GRIARC (400 and 500 nm) are relatively efficient for short wavelengths, it can be observed that the transmittance in the NIR wavelength range is limited by reflection of the light. To minimize optical losses in this domain, thicker GRIARC must be considered as demonstrated from simulations of the thicknesses of 1000 and 1500 nm. Actually, to obtain at least 99% mean transmittance over the 400–1800 nm range ($T_{m[400-1800]\ nm}$) a GRIARC coating thicker than 400 nm must be used.

The simulation of an optical design consisting in an interference-based bilayer implementing fictive values of refractive index was also performed and compared to the GRIARC systems. Those values are considered as fictive as they are free parameters of the simulation and might not correspond to the refractive indices of existing bulk materials. This numerically optimized bilayer is thinner (total thickness of 276 nm) than the presented GRIARC systems. It also presents high transmittance ($T_{m[400-1800\ nm]}$=99.03%), notably because it benefits from the interferential effect in the NIR range.

3.2. Experimental comparison of the transmittance performances of GRIARC and discrete ARC coatings

Because this bilayer design presents the appeal of simplicity and a high transmittance level, it has then been prepared using oblique angle deposition (OAD) technique. Prior to the fabrication of the bilayer, a preliminary step was devoted to the calibration of the refractive index and thickness of individual SiO_2 layers prepared by OAD at different deposition angles. After finding out the optimal deposition parameters, the ARC bilayer was then deposited on a BK7 substrate in a two-step process. First, a SiO_2 layer was deposited at α=65° with a targeted thickness of 134 nm and refractive index of n = 1.30. Then a second layer of SiO_2 was deposited at α=85° with a targeted thickness of 142 nm and refractive index of n = 1.16. An azimuthal rotation of 180° was performed in between the layers in order to minimize any material deposition within the porosity of the first layer during the deposition of the second one. A TEM bright-field micrograph of the resulting stack is presented in Fig. 2a. It can be observed that the obtained thicknesses are close from the targeted ones respectively 143 nm and 161 nm for the first and the second layer. As expected, the nanocolumns in the top layer are more tilted, yielding to higher porosity due to geometrical shadowing. This micrograph also clearly indicates that the OAD nanocolumns of the first layer act as nucleation sites for the second one. Fig. 2b and Fig. 2c, present spectrophotometric measurement of this bilayer at normal incidence with polarized light oriented both along the columns, $P_{//}$ as indicated with the red arrow in Fig. 2a and perpendicular to this direction, $P_{\perp}$ (orange dot). The ARC coating presents outstanding performances ($T_{m[400-1800]\ nm}$=98.97%). The resulting transmittance and reflectance spectra match almost perfectly with the design counterparts. Interestingly, the results are quite close to the performances obtained by Sood et al. demonstrating the reproducibility of this method [2]. The small mismatch present in the short wavelength range (below 500 nm) between the experimental and designed ARC coatings will be discuss further after. It can also be noted that a small difference is observed between the two polarizations. Indeed although SiO_2 deposited by OAD produces structures that are known to be anisotropic the weak refractive index of SiO_2 could explain this small difference. [40] To go deeper, we have compared the performance of our OAD bilayer with that of experimental GRIARC system based on ME structures according to Diao et al. (Fig. 2b and 2c) [23].

As predicted by the theory and demonstrated in Fig. 1, the use of thicker ME structures minimizes the reflectance thus increasing the transmittance in the NIR range as observed in Fig. 2c. However in counterpart, the transmittance level is lowered in the visible range for an increasing thickness of the ME (Fig. 2b), a behavior not described by BEMA simulations (Fig. 1a). This compromise between short and long wavelengths allows reaching a mean transmittance

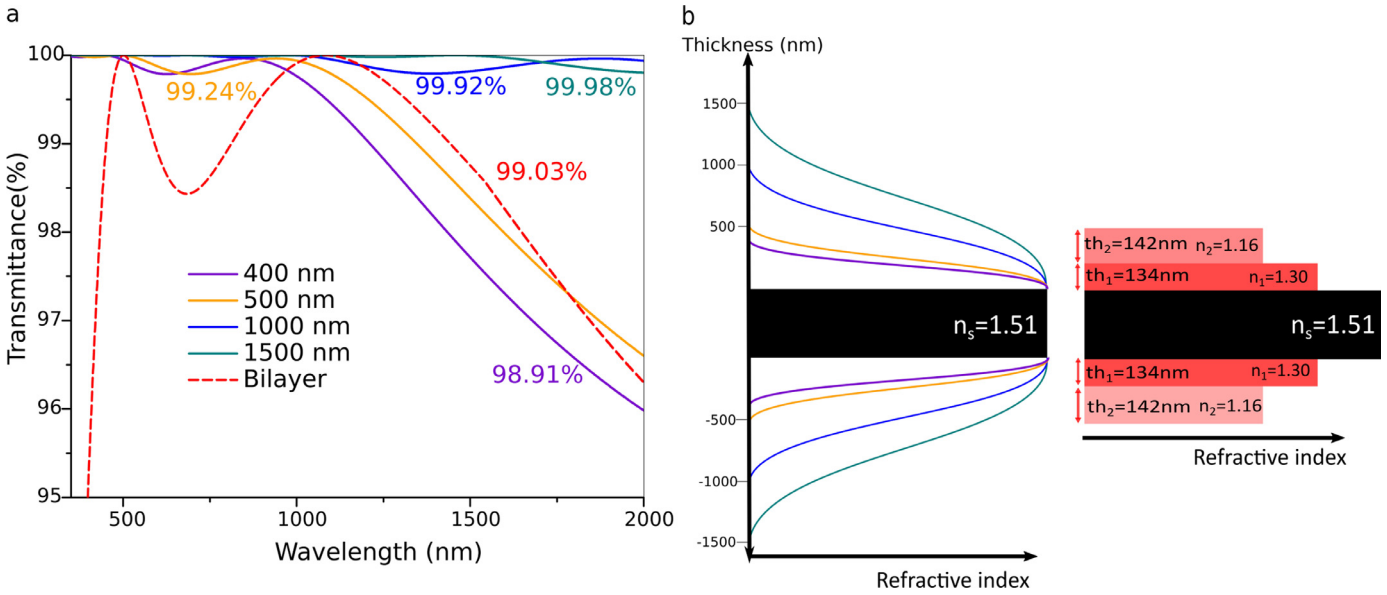

Fig. 1. (a) Transmittance spectra of GRIARC coatings of different thicknesses with a quintic profile compared with a bilayer interferential coating. The mean transmittance value of each spectrum is presented for the [400–1800] nm range. (b) Schematic representation of the optical design of the different coatings: GRIARC designs on the left, bilayer design on the right.

$T_{m[400-1800]\ nm}$=98.84% for the best GRIARC nanostructures, below that of the OAD bilayer prepared in this work.

To study the origin of low light transmittance in the short wavelength range, optical losses of the different systems (GRIARC and OAD bilayer) are presented in Fig. 2d. The optical losses considered here are deduced from transmittance and reflectance measurements as follows:

$$OpticalLosses(\lambda) = 1 - R(\lambda) - T(\lambda) \quad (1)$$

where R and T denotes, respectively, the reflectance and transmittance.

The OAD bilayer as well as the 450 nm ME present a low level of optical losses mostly in the UV range. However, thicker ME structures exhibit an increasingly high level of optical losses in this spectral range up to 80% at λ=350 nm for a thickness of 1520 nm. Therefore, optical losses are responsible for the weak transmittance in the short wavelength range for thick ME GRIARC. This demonstrates that the performances of ARC nanostructures cannot solely be determined from reflectance measurements and that optical losses by absorption or scattering must be assiduously considered.

As pointed out by Niklasson et al., a scattering behavior can be observed when the dimensions of the nanostructures are non-negligible in regards of the probing wavelength according to the Mie theory [14]. This therefore limits the validity of the BEMA for objects of small sizes and may explain the difference observed between designs and experiments in the short wavelength range. This point is supported by the diffuse scattering reported in the IR range for thick (several microns) ME structures [41].

3.3. A method to simulate scattering losses from nanostructured ARC

In order to consider the scattering behavior of the ARC nanostructures and anticipate the optical losses observed in the UV–vis range, we propose a method based on finite-difference time domain simulations. For a transparent medium, in absence of multiple scatterings (which is the case of weak scattering structures), the scattering efficiency Q_{scat} is related to the scattered intensity by [42]:

$$I_{scat}(\lambda) = 1 - I_{trans}(\lambda) = 1 - e^{-Q_{scat}(\lambda)} \text{ with } Q_{scat}(\lambda) = \frac{\sigma_{scat}(\lambda)}{S} \quad (2)$$

where σ_{scat} is the scattering cross section and S is the section area. The scattering cross section can be determined from FDTD simulations using total-field/scattered-field (TFSF) [43]. The studied structure is excited by a TFSF source, separating space into two regions: in the TFSF volume the total field is calculated, whereas outside the volume the scattered field is computed. The extinction, absorption, and

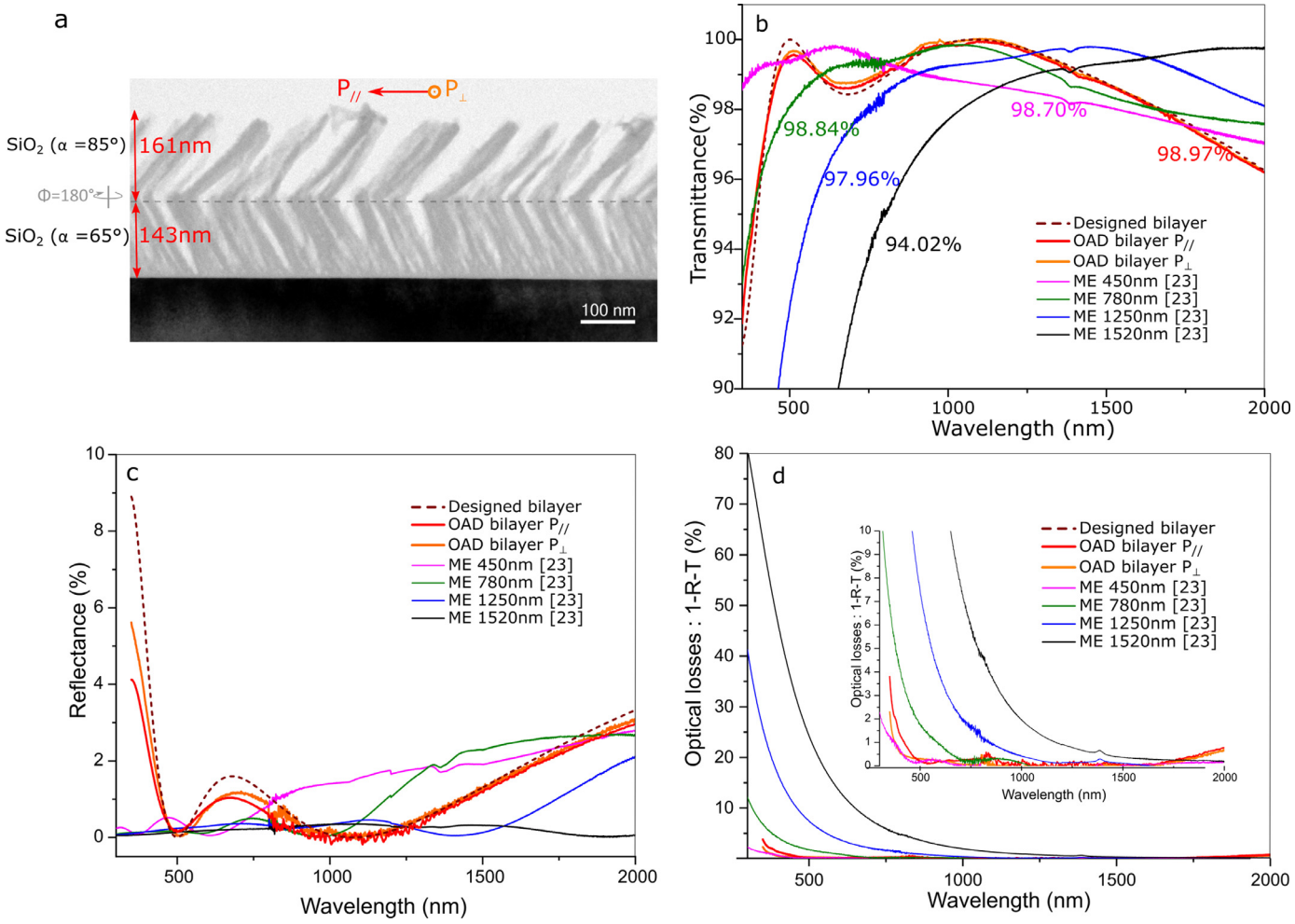

Fig. 2. (a) TEM bright field micrography of the ARC OAD bilayer composed of SiO_2 stacks deposited at α=65° and α=85° with azimuthal rotation between the two layers of Φ=180°. The observation was done along a ⟨110⟩ zone axis of the Si susbtrate. The red arrow presents the polarization direction of light $P_{//}$ and the orange one is for $P_{\perp}$. Transmittance (b), Reflectance (c) and optical losses (d) spectra of the OAD bilayer deposited on a glass substrate BK7 on two sides. The dashed lines in figure (b) and (c) present the transmittance and reflectance spectra of the optical design of the bilayer. The transmittance, reflectance and optical losses spectra of ME measured by Diao et al. [23] were added in, respectively, figure (b), (c) and (d). The mean transmittance value of each spectra is presented for the [400–1800] nm range. (For interpretation of the references to color in this figure legend, the reader is referred to the web version of this article.)

scattering cross section of the region enclosed can then be evaluated. Note that for the sake of simplicity, since the structures have a very low reflectivity, we only consider here the light attenuation due to scattering for the transmitted wave. In the case of a substrate coated on both sides, if we neglect light reflection at the interfaces, the corresponding total scattered intensity can be calculated as:

$$I_{scat}(\lambda) = 1 - e^{-2Q_{scat}(\lambda)} \quad (3)$$

3.4. Simulated and experimental scattering of nanostructured ARC

Firstly, we applied this method to estimate the optical losses of the ARC OAD bilayer. To simulate accurately the scattering cross section by FDTD, the complex 3D geometry of this system was determined experimentally from electron tomography (see Fig. 3a). The reconstructed volume, that includes morphological information of the coating of a wide spatial range (mostly the distribution of material and porosity components), was then used as an input parameter for the calculations, considering that the columns have the dielectric permittivity of SiO_2. This simulated scattered intensity is presented in Fig. 3a along with the experimental optical losses measured for this ARC OAD bilayer.

The very good agreement between the experimental and simulated spectra tends to confirm that this innovative approach combining the implementation of realistic 3D sample geometry with advanced simulation of light propagation is appropriate to account for optical losses. This result also validates that the optical losses can be attributed to the optical scattering of the nanostructures. The mismatch that is observed in the long wavelength regime comes from the substrate absorption that was not included in FDTD computation as only the upper interface is simulated. Knowing the scattering losses, we present in Fig. 3b the design spectra minimized from the simulated scattered intensity along with the experimental spectra of the OAD bilayer. It is possible to attribute the small mismatch between the designed spectra and the experimental OAD bilayer (pointed out before in Fig. 2b) to the scattering behavior of the ARC. Thus, the OAD bilayer forms a low scattering nanostructured film thanks to the small radius of the columns and its small thickness.

For comparison, we used the same method to evaluate the scattering behavior of SiO_2 ME nanostructures. For the sake of simplicity, these structures were approximated by square pyramids of width w and thickness t (as described in Fig. 4a). The scattered intensity was then deduced using Eq. (3) from the Mie scattering cross section for different thicknesses and a constant aspect ratio of $r = \frac{t}{w} = 10$. The resulting spectra are presented in Fig. 4a.

This figure shows that, for a constant aspect ratio of 10 and an increasing thickness of ME structures, the scattered intensity dramatically increases from a maximum value of 1.5% for a thickness of 500 nm up to 96% for 1625 nm. Interestingly the simulated scattered intensity reveals a similar behavior than the optical losses of ME nanostructures presented in Fig. 2d. This also confirms the scattering nature of the optical losses.

If we consider a GRIARC constituted of perfect periodic square based pyramids, the porosity for any position z, the vertical axis, can be calculated as:

$$P(z) = \left(1 - \frac{z}{t}\right)^2 \quad (4)$$

where t is the total thickness of the structure.

BEMA can be applied from this porosity profile by decomposing it to 100 layers of increasing porosity rate in order to calculate the transmittance spectra of ME square based pyramids. Then by combining the scattering results to BEMA simulations, we calculated the transmittance of ME structures. For that, both transmittance (BEMA) and scattering properties (FDTD) for different thicknesses of ME for a constant aspect ratio of $r = 10$ were considered.

The similarity between these results (Fig. 4b) and experimental transmission (Fig. 2b) confirms the validity of the approach adopted in this paper. This optical behavior, that consists in a transmittance diminution in the UV range coupled with an increasing transmittance in the IR range for an increasing thickness, is consistent with what can be found in literature [1,15,18,20,21,23,25].

To better understand the link between ME dimensions and the scattering losses, a contour plot of the mean transmittance $T_{m[400-1800]\ nm}$ of ME with different thicknesses and widths is presented in Fig. 4c. This figure is presented for a minimum thickness value of 500 nm because below, the GRIARC is not efficient to suppress long wavelength reflection in order to obtain a minimum of 99% mean transmittance. To facilitate the discussion three straight lines have been added corresponding to three different values of the constant aspect ratio: $r = 5$, 10 and 20. So Fig. 4b corresponds to a variation of thickness on the straight lines $r = 10$.

Fig. 4c shows that the width of the ME is the critical parameter to adjust in order to obtain a high broadband transmittance. A maximum width of 110 nm is required to obtain $T_{m[400-1800\ nm]} > 99\%$. If

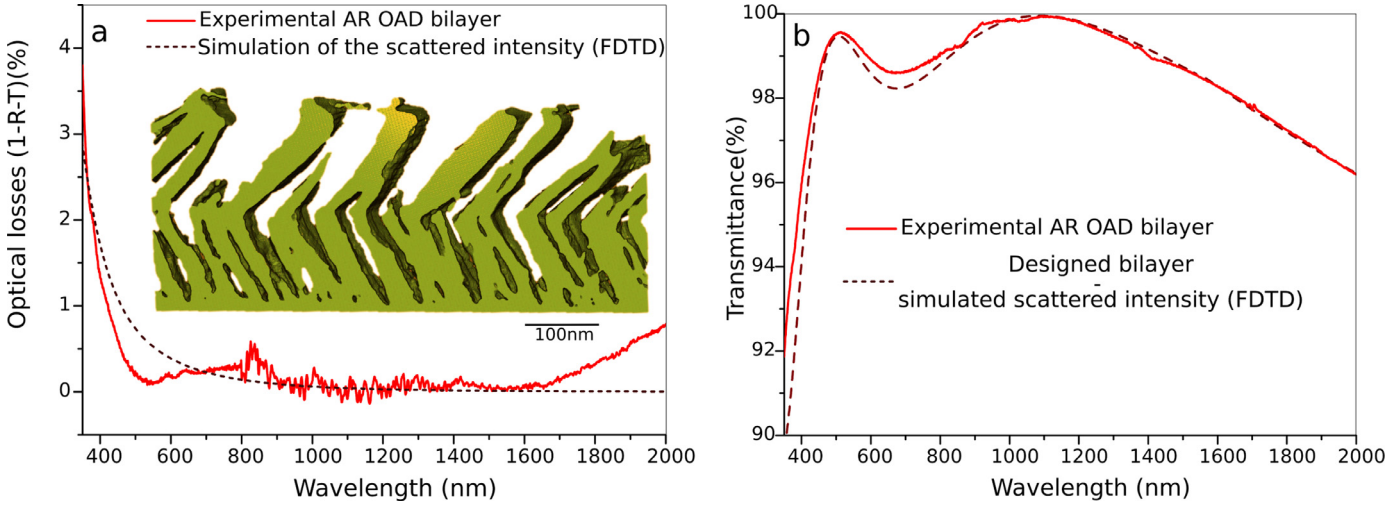

Fig. 3. (a) Optical losses of the SiO_2 OAD bilayer deposited on glass substrate measured experimentally (full line) and calculated from FDTD using the 3D reconstruction obtained from electron tomography (dashed line). (b) Transmittance spectra of the OAD bilayer measured experimentally (full line) and calculated by subtracting the simulated scattered intensity presented in figure a to the designed value (dashed line).

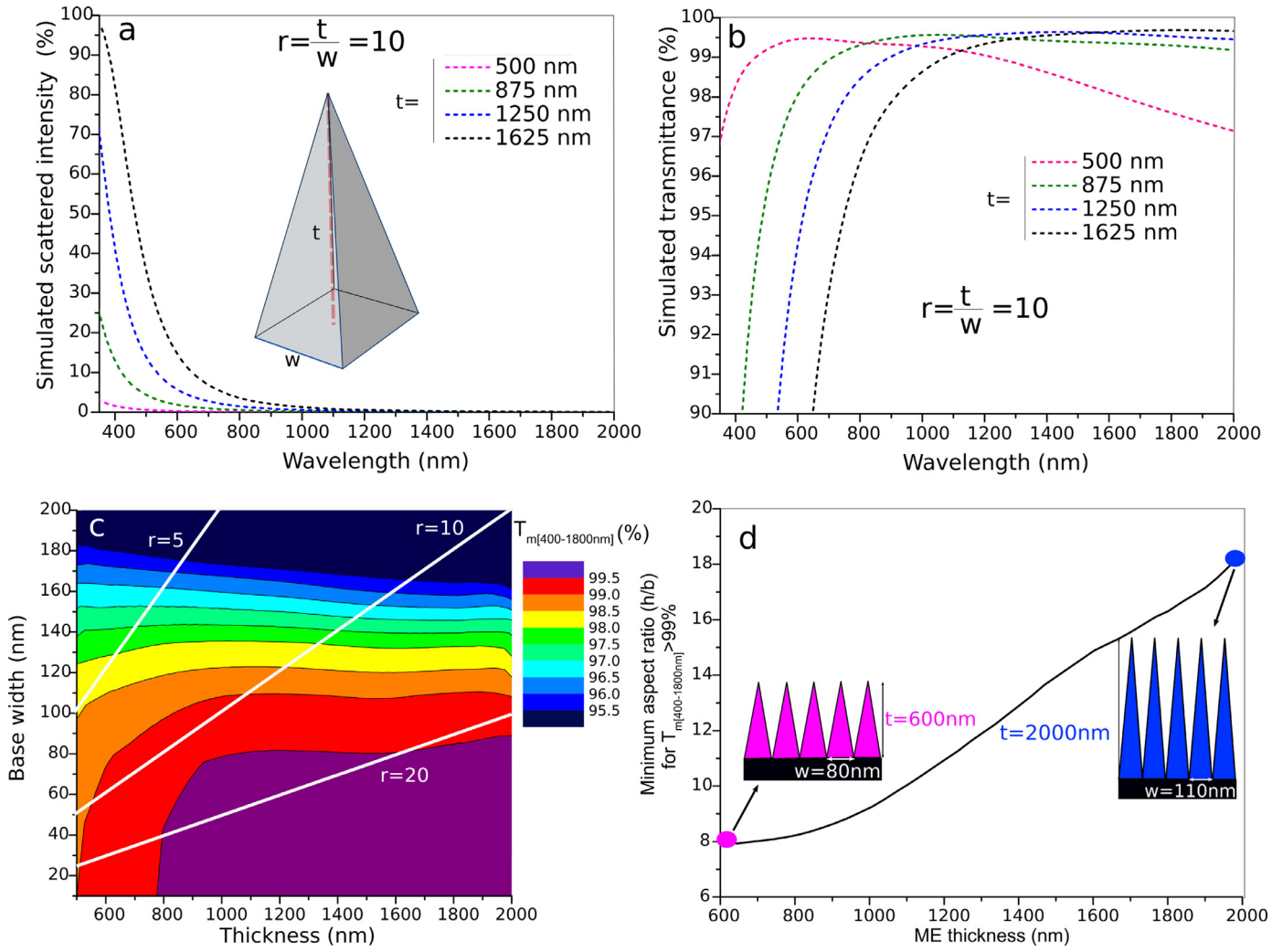

Fig. 4. (a) Simulated scattered intensity spectra from FDTD Mie scattering cross section of SiO_2 ME pyramid nanostructures with an aspect ratios of r = 10 for different thicknesses (b) Simulated transmittance of spectra SiO_2 ME pyramid nanostructures simulated by the BEMA for different thicknesses subtracting the scattered intensity presented in (a, c). Contour plot of $T_{m[400-1800\ nm]}$ simulated from the BEMA and taking into account the scattered intensity for pyramid ME of different thicknesses t and base widths (d) Minimum aspect ratio for $T_{m[400-1800]\ nm}$=99% for different thicknesses of ME SiO_2 pyramid nanostructures.

this width is kept constant, the performances are barely affected by an increase of the thickness if the GRIARC is sufficiently thick (thicker than 900 nm). So an increasing thickness will be beneficial only if the width is kept constant *i.e.* only if the aspect ratio increases. In other words, for an increasing thickness, an increasing aspect ratio of ME is needed to maintain a high $T_{m[400-1800\ nm]}$.

3.5. Discussion

Since the $T_{m[400-1800\ nm]}$ is equal to 99% for the OAD bilayer, we present in Fig. 4d the minimum aspect ratio of needed to obtain this mean transmittance for different thicknesses of pyramids ME structures. Interestingly, pyramid ME nanostructures with a thickness of 600 nm and an aspect ratio of 8 will have the same mean transmittance (99%) than pyramid ME of 2000 nm thickness and an aspect ratio of 18. Consequently, enhancing the mean transmittance of ME systems above 99% is in principle possible to the constraint of nanostructuring very high aspect ratio and thick architectures. However, beyond the mechanical instability that might be associated with high aspect ratio ME, such nanostructuration is challenging from the technological point of view. Indeed, the etching process usually employed to realize ME offers a limited control on the width of the structures. To increase the ME aspect ratio, it is necessary to minimize the dimension of the shadowing elements although these are already quite small. For example, Diao et al. reported the use of gold nanoparticles of 6 nm diameter as masks [23]. This therefore demonstrates clearly the interest of the OAD approach in the manufacturing of highly efficient antireflective coatings. By taking advantage of the interferences, the ARC bilayer coating developed in this work permits an efficient suppression of the reflectance with relatively small dimensions nanostructures thus avoiding undesirable light scattering. One could think of enhancing the performances of the OAD bilayer by adding supplementary layers. However, it is high likely that such stack will suffer from the scattering losses as the nanocolumns obtained from OAD deposition tend to broaden with the thickness [35,44]. The amelioration of optical ARC properties by OAD is feasible in a near future but will probably require the use of modified growth procedure to minimize the columns dimensions [40].

4. Conclusions

In summary, this paper demonstrates that light scattering is an important aspect to consider for the development of high transmittance ARC surfaces. A simple method to calculate light scattering losses of nanostructured coatings have been introduced. A detailed comparison of the performances of GRIARC and discrete gradient

ARC was done to evaluate those optical losses. We showed that a coating with a discrete gradient refractive index presents a very high transmittance level for a relatively small thickness by taking advantage of the interferences. This SiO_2 bilayer prepared by OAD deposition exhibits a mean transmittance $T_{m[400-1800\ nm]}$= 98.97% very close to the designed value. A very small amount of optical losses was measured (around 2% at 400 nm) and attributed to light scattering. The scattering behavior of this bilayer was confirmed from FDTD simulation which was performed on a 3D volume reconstruction obtained from electron tomography. On the other hand, continuous GRIARC nanostructures can in theory result in almost perfect transmittance. However, to be efficient on the long wavelength range, it is shown that these systems must be sufficiently thick, at least 500 nm, to reach mean transmittance as high as 99%. In practice, thick ME nanostructures will favor scattering losses mainly due to the too large width of those structures. Highlighting the presence of scattering demonstrates the need for a more in-depth study of this phenomenon through the use of integrating spheres. In order to limit scattering and keep on enhancing the transmittance, thick GRIARC nanostructures with a high aspect ratio must be manufactured. For technological reasons, this constraint represents a real challenge that may be hard to overcome. Therefore, considering the actual state-of-the-art of nanostructuring methods, development based on discrete gradient ARC should be preferred in the future as they are simpler to produce and provide better optical performances.

Declaration of Competing Interest

None.

Funding

This work was supported by the DGA (Direction Générale de l'Armement), the French Defense Procurement Agency. This work has been partially supported by « Nouvelle Aquitaine » Region and by European Structural and Investment Funds (ERDF reference P-2016-BAFE-209): IMATOP project. The "Talent Attraction Program" of the University of Cádiz is acknowledged for supporting B. Lacroix contract code E-11-2017-0117214. A. J. Santos also thanks the financial support of the IMEYMAT Institute as well as the Ministerio de Ciencia, Innovación y Universidades and Ministerio de Educación y Formación Profesional in Spain for the concessions of grants (ICARO-173873 and FPU16-04386).

References

[1] Y.M. Song, Y. Jeong, C.Il. Yeo, Y.T. Lee, Enhanced power generation in concentrated photovoltaics using broadband antireflective coverglasses with moth eye structures, Opt. Express 20 (2012) A916.
[2] A.K. Sood, A.W. Sood, R.E. Welser, G.G. Pethuraja, Y.R. Puri, X. Yan, D.J. Poxson, J. Cho, E.F. Schubert, N.K. Dhar, D.L. Polla, P. Haldar, J.L. Harvey, Development of nanostructured antireflection coatings for eo/ir sensor and solar cell applications, Mater. Sci. Appl. 03 (2012) 633–639.
[3] D.J. Poxson, M. Kuo, F.W. Mont, Y.-S. Kim, X. Yan, R.E. Welser, A.K. Sood, J. Cho, S. Lin, E.F. Schubert, High-performance antireflection coatings utilizing nanoporous layers, MRS Bull. 36 (2011) 434–438.
[4] A.K. Sood, Y.R. Puri, L. Becker, M.Z. Tidrow, R.S. Balcerak, G. Brill, P. Wijewarnasuriya, N. Dhar, P. Boieriu, C. Fulk, S. Sivananthan, J. Yehoda, S. Finke, in: B.F. Andresen, G.F. Fulop, P.R. Norton (Eds.), Development of high-performance radiation-hardened antireflection coatings for LWIR and multicolor IR focal plane arrays, 6206, Infrared Technology and Applications XXXII, 2006, p. 620615.
[5] A.K. Sood, R. Richwine, Y.R. Puri, N.K. Dhar, D.L. Polla, P.S. Wijewarnasuriya, Multispectral eo/ir sensor model for evaluating UV, visible, SWIR, mwir and lwir system performance, in: G.C. Holst (Ed.), Proceedings of the SPIE, 7300, The International Society for Optical Engineering, 2009, p. 73000.
[6] H.A. Macleod, Thin-film optical filters, CRC Press (2001) 110–117.
[7] A. Musset, A. Thelen, IV multilayer antireflection coatings, Prog. Opt. 8 (1970) 201–237.
[8] J.-Q. Xi, M.F. Schubert, J.K. Kim, E.F. Schubert, M. Chen, S.-Y. Lin, W. Liu, J.A. Smart, Optical thin-film materials with low refractive index for broadband elimination of fresnel reflection, Nat. Photonics 1 (2007) 176–179.
[9] S. Chattopadhyay, Y.F. Huang, Y.J. Jen, A. Ganguly, K.H. Chen, L.C. Chen, Anti-reflecting and photonic nanostructures, Mater. Sci. Eng. R: Rep. 69 (2010) 1–35.
[10] K.-H. Kim, Q-Han Park, Perfect anti-reflection from first principles, Sci. Rep. 3 (2013) 1062.
[11] K. Im, J.H. Kang, Q.H. Park, Universal impedance matching and the perfect transmission of white light, Nat. Photonics 12 (2018) 143–149.
[12] W.H. Southwell, Gradient-index antireflection coatings, Opt. Lett. 8 (1983) 584.
[13] H.K. Raut, V.A. Ganesh, A.S. Nair, S. Ramakrishna, Anti-reflective coatings: a critical, in-depth review, Energy Environ. Sci. 4 (2011) 3779.
[14] G.A. Niklasson, C.G. Granqvist, O. Hunderi, Effective medium models for the optical properties of inhomogeneous materials, Appl. Opt. 20 (1981) 26.
[15] F. Lora Gonzalez, L. Chan, A. Berry, D.E. Morse, M.J. Gordon, Simple colloidal lithography method to fabricate large-area moth-eye antireflective structures on Si, Ge, and GaAs for IR applications, J. Vac. Sci. Technol. B: Nanotechnol. Microelectron. Mater. Process. Meas. Phenom. 32 (2014) 051213.
[16] M. Motamedi, M.E. Warkiani, and R.A. Taylor, ";Transparent Surfaces Inspired by Nature," 1800091, 1–28 (2018).
[17] S. Ji, K. Song, T.B. Nguyen, N. Kim, and H. Lim, "Optimal Moth Eye Nanostructure Array on Transparent Glass Towards Broadband Antire FL Ection," (2013).
[18] F.L. Gonzalez, D.E. Morse, M.J. Gordon, Importance of diffuse scattering phenomena in moth-eye arrays for broadband infrared applications, Opt. Lett. 39 (2014) 13–16.
[19] P.I. Stavroulakis, S.A. Boden, T. Johnson, D.M. Bagnall, Suppression of backscattered diffraction from sub-wavelength 'moth-eye' arrays, Opt. Express 21 (2013) 1.
[20] S. Ji, J. Park, H. Lim, Improved antireflection properties of moth eye mimicking nanopillars on transparent glass: flat antireflection and color tuning, Nanoscale 4 (2012) 4603.
[21] L. Chan, A. Ghoshal, E.A. DeCuir, Y.P. Chen, D.E. Morse, M.J. Gordon, Fabrication and optical behavior of graded-index, moth-eye antireflective structures in cdte, J. Vac. Sci. Technol. B: Nanotechnol. Microelectron. Mater. Process. Meas. Phenom. 35 (2017) 011201.
[22] N.N. Lal, K.N. Le, A.F. Thomson, M. Brauers, T.P. White, K.R. Catchpole, Transparent long-pass filter with short-wavelength scattering based on morpho butterfly nanostructures, ACS Photonics 4 (2017) 741–745.
[23] Z. Diao, M. Kraus, R. Brunner, J.-H. Dirks, J.P. Spatz, Nanostructured stealth surfaces for visible and near-infrared light, Nano Lett. 16 (2016) 6610–6616.
[24] P.B. Clapham, M.C. Hutley, Reduction of lens reflexion by the "moth eye" principle, Nature 244 (1973) 281–282.
[25] S. J.I., K. Song, T.B. Nguyen, N. Kim, H. Lim, Optimal moth eye nanostructure array on transparent glass towards broadband antireflection, ACS Appl. Mater. Interfaces 5 (2013) 10731–10737.
[26] M.F. Schubert, D.J. Poxson, F.W. Mont, J.K. Kim, E.F. Schubert, Performance of antireflection coatings consisting of multiple discrete layers and comparison with continuously graded antireflection coatings, Appl. Phys. Express 3 (2010) 082502.
[27] J.W. Leem, D.-H. Jun, J. Heo, W.-K. Park, J.-H. Park, W.J. Cho, D.E. Kim, J.S. Yu, Single-material zinc sulfide bi-layer antireflection coatings for GaAs solar cells, Opt. Express 21 (2013) A821.
[28] J.W. Leem, J.S. Yu, Glancing angle deposited ITO films for efficiency enhancement of a-Si:H/μc-Si:H tandem thin film solar cells, Opt. Express 19 (2011) A258.
[29] M.S. Rodrigues, J. Borges, M. Proença, P. Pedrosa, N. Martin, K. Romanyuk, A.L. Kholkin, F. Vaz, Nanoplasmonic response of porous Au-TiO_2 thin films prepared by oblique angle deposition, Nanotechnology 30 (2019) 225701.
[30] L. González-García, J. Parra-Barranco, J.R. Sánchez-Valencia, A. Barranco, A. Borrás, A.R. González-Elipe, M.C. García-Gutiérrez, J.J. Hernández, D.R. Rueda, T.A. Ezquerra, Correlation lengths, porosity and water adsorption in TiO_2 thin films prepared by glancing angle deposition, Nanotechnology 23 (2012) 205701.
[31] J.R. Sanchez-Valencia, R. Longtin, M.D. Rossell, P. Groning, Growth assisted by glancing angle deposition: a new technique to fabricate highly porous anisotropic thin films, ACS Appl. Mater. Interfaces 8 (2016) 8686–8693.
[32] C. Lopez-Santos, R. Alvarez, A. Garcia-Valenzuela, V. Rico, M. Loeffler, A.R. Gonzalez-Elipe, A. Palmero, Nanocolumnar association and domain formation in porous thin films grown by evaporation at oblique angles, Nanotechnology 27 (2016) 395702.
[33] C. Grüner, S. Liedtke, J. Bauer, S.G. Mayr, B. Rauschenbach, Morphology of thin films formed by oblique physical vapor deposition, ACS Appl. Nano Mater. 1 (2018) 1370–1376.
[34] K. Li, Y. Dong, Modeling the influence of incident angle and deposition rate on a nanostructure grown by oblique angle deposition, J. Phys. D. Appl. Phys. 50 (2017) 065302.
[35] R. Álvarez, L. González-García, P. Romero-Gómez, V. Rico, J. Cotrino, A.R. González-Elipe, A. Palmero, Theoretical and experimental characterization of TiO_2 thin films deposited at oblique angles, J. Phys. D. Appl. Phys. 44 (2011) 385302.
[36] M.M. Hawkeye, M.T. Taschuk, M.J. Brett, Glancing Angle Deposition of Thin Films, John Wiley & Sons, Ltd, 2014.
[37] A.K. Sood, A.W. Sood, R.E. Welser, G.G. Pethuraja, Y.R. Puri, X. Yan, D.J. Poxson, J. Cho, E.F. Schubert, N.K. Dhar, D.L. Polla, P. Haldar, J.L. Harvey, Development of nanostructured antireflection coatings for EO/IR sensor and solar cell applications, Mater. Sci. Appl. 03 (2012) 633–639.
[38] S.R. Kennedy, M.J. Brett, Porous broadband antireflection coating by glancing angle deposition, Appl. Opt. 42 (2003) 4573–4579.
[39] F. Maudet, B. Lacroix, A.J. Santos, F. Paumier, M. Paraillous, C. Dupeyrat, R. García, F.M. Morales, T. Girardeau, Towards perfect mwir transparency using oblique angle deposition, Appl. Surf. Sci. 470 (2019) 943–950.
[40] D. Vick, T. Smy, M.J. Brett, Growth behavior of evaporated porous thin films, J. Mater. Res. 17 (2011) 2904–2911.

[41] F.L. Gonzalez, D.E. Morse, M.J. Gordon, Importance of diffuse scattering phenomena in moth-eye arrays for broadband infrared applications, Opt. Lett. 39 (2014) 13–16.
[42] C.F. Bohren, D.R. Huffman, Absorption and Scattering of Light by Small Particles, Wiley-VCH Verlag GmbH, 1998.
[43] Y. Nishijima, L. Rosa, S. Juodkazis, Long-range interaction of localized surface plasmons in periodic and random patterns of Au nanoparticles, Appl. Phys. A 115 (2014) 409–414.
[44] S. Mukherjee, D. Gall, Power law scaling during physical vapor deposition under extreme shadowing conditions, J. Appl. Phys. 107 (2010) 084301.

Publication IV

Optical and nanostructural insights of oblique angle deposited layers applied for photonic coatings

F. Maudet, B. Lacroix, A. J. Santos, F. Paumier, M. Paraillous, S. Hurand, A. Corvisier, C. Marsal, B. Giroire, C. Dupeyrat, R. García, F. M. Morales, T. Girardeau

Applied Surface Science 520 (2020) 146312

Applied Surface Science 520 (2020) 146312

Contents lists available at ScienceDirect

Applied Surface Science

journal homepage: www.elsevier.com/locate/apsusc

Optical and nanostructural insights of oblique angle deposited layers applied for photonic coatings

Florian Maudet[a,d,*], Bertrand Lacroix[b,c], Antonio J. Santos[b,c], Fabien Paumier[d], Maxime Paraillous[e], Simon Hurand[d], Alan Corvisier[d], Cecile Marsal[d], Baptiste Giroire[e], Cyril Dupeyrat[e], Rafael García[b,c], Francisco M. Morales[b,c], Thierry Girardeau[d]

[a] Institute Functional Thin Film Oxides for Energy-efficient Future Information Technology, Helmholtz-Zentrum Berlin für Materialien und Energie Hahn-Meitner-Platz 1, 14109 Berlin, Germany
[b] Department of Materials Science and Metallurgic Engineering, and Inorganic Chemistry, Faculty of Sciences, University of Cádiz, Spain
[c] IMEYMAT: Institute of Research on Electron Microscopy and Materials of the University of Cádiz, Spain
[d] Institut Pprime, UPR 3346 CNRS-Université de Poitiers-ENSMA, SP2MI, 86962 Futuroscope-Chasseneuil cedex, France
[e] Safran Electronics and Defense, 26 avenue des Hauts de la Chaume, 86280 Saint-Benoît, France

ARTICLE INFO

Keywords:
Oblique angle deposition
Gradient refractive index
Antireflective coating
Generalized ellipsometry
Spectrophotometry
Anisotropy
Anisotropic Bruggeman effective medium approximation
Electron tomography

ABSTRACT

Oblique angle deposition (OAD) is a nanostructuration method widely used to tune the optical properties of thin films. The introduction of porosity controlled by the deposition angle is used to develop the architecture of each layer. However, optical properties of these porous layers may differ greatly from those of dense layers due to the presence of anisotropy, refractive index gradient and scattering. This work focuses on OAD thin film of SiO_2 and it aims at considering all these effects to describe the optical response. For that, the nanostructure has been analyzed with a complete SEM study and key parameters like the porosity gradient profile and aspect ratio of the nanocolumns were extracted. The samples were then characterized by generalized ellipsometry to evaluate the influence of the microstructural properties on the optical response of the films. An original optical model is then presented to fit these new optical properties. A reliable correspondence is observed between the optical model parameters and the microstructure characteristics like the column angle and porosity gradient. This demonstrates that such complex microstructural parameters can be accessed solely from optical measurements. All the work has enabled us to develop a two-layer anti-reflective coating that demonstrate high transmission level.

1. Introduction

Oblique angle deposition (OAD) is a versatile method to obtain complex morphological nanostructures for a great variety of materials [1–6]. By changing the deposition angle, it is possible to take advantage of the self-shadowing effect to control the porosity rate at the nanoscale [7–9]. These OAD thin films, are generally made of slanted nanocolumns, that will exhibit tunable optical properties that differs from their bulk counterpart due to the presence of porosity and morphological anisotropy, making OAD very interesting for various applications like antireflective coatings, Bragg reflectors, solar cells or polarized optics [10–19]. However, both the anisotropy and porosity of the OAD films strongly depend on the growth mechanisms that may vary with the deposited material as well as the deposition parameters [20,21]. To engineer the optical properties of OAD thin films, it is thus necessary not only to understand and control the growth of a specific material in relation with the deposition parameters, but also to accurately model the optical response of these complex structures. In most cases, the conventional Bruggeman effective medium approximation (BEMA) is used to describe the optical properties of mesoporous layers that are generally considered as a mixture of dense material and air [10,22,23]. However, this simple interpretation does not take into account the morphological anisotropy specific of OAD layers, and more advanced models like the Anisotropic BEMA (ABEMA) should be used instead [24]. Moreover, as demonstrated from microstructural and simulation studies, the porosity and morphological anisotropy of OAD layers evolves during the growth [11,25]. Integrating anisotropy, porosity and their evolution in the optical description of thin films thus involves using a multilayered model with graded optical properties instead of a single homogenous effective layer as it is usually done. This approach can lead to a more accurate description of the optical response that provides information on the morphological parameters of the layers.

* Corresponding author.
E-mail addresses: florian.maudet@helmholtz-berlin.de (F. Maudet), fabien.paumier@univ-poitiers.fr (F. Paumier).

https://doi.org/10.1016/j.apsusc.2020.146312
Received 20 December 2019; Received in revised form 10 February 2020; Accepted 9 April 2020
Available online 18 April 2020

In this article, we aim at knowing to which extent such an optical model can describe the observed morphological properties of OAD thin films. We studied the case of SiO_2 because it is a reference photonic material and it can be nanostructured by OAD to obtain very low refractive index that is needed for a high-performance antireflective coating [26]. We demonstrate the interest of this knowledge by developing a SiO_2 antireflective bilayer presenting not only a low reflectance but also a high transmittance over a large band of wavelength.

We present herein first a SEM based microstructural study of a series of SiO_2 deposited by OAD made to extract key morphological features to help building an optical model. These microstructural observations and their possible physical origin are then discussed in regard of the existing literature. From those observations, an optical model is proposed and is then applied to model generalized ellipsometry and spectrophotometry measurements of the prepared films. The parameters extracted from the optical model are then compared to the morphological parameters observed for the SiO_2 series. To illustrate the optical model and its sensitivity to optical measurements a python code that calculates the ellipsometric and spectrophotometric response of the optical model is presented in Supplementary Material 1 of this article [27]. To conclude, this model is used to optimize and describe the optical response of a SiO_2 antireflective bilayer, the morphological parameters extracted from the optical model are compared to electron tomography observation.

2. Experimental details

The experimental setup used for the oblique angle deposition consists in a vacuum chamber (base pressure $2 \cdot 10^{-6}$ mbar) equipped with an electron-beam evaporator. SiO_2 OAD layers were deposited at various angles of incidence from 65° to 90° by e-beam evaporation method using SiO_2 grains (Umicore© purity > 99.99%) in a Mo crucible on 1 mm thick, 1-inch diameter BK7 glass substrates. The angle range was to chosen to be where the porosity is sufficiently high to be of interest for photonic application. The substrate is placed 70 cm from the crucible which diameter is 5 cm leading to angular broadening of $\Delta\alpha = 4°$. The SiO_2 stoichiometry was confirmed through a STEM-EDX analysis on an OAD deposited angle of 75° and 85°. For each deposition, a (0 0 1) silicon substrate was also placed, with one ⟨1 1 0⟩ crystallographic axis perpendicular to the incoming deposition flux for further analyses by scanning electron microscopy (SEM) and spectrometric ellipsometry studies. A quartz crystal monitor was used to control the thickness and ensure a nominal deposition rate of 10 Å/s at normal incidence. The depositions were all performed at room temperature. After calibration, a SiO_2 bilayer was deposited by OAD. Since our deposition set-up is not equipped with an in-situ adjustable orientation sample-holder, the bilayer was made in two steps with an azimuthal rotation of $\Phi = 180°$ in between on silicon glass (BK7) substrate. For the first step, a SiO_2 layer was deposited at an angle of 65° with the condition of elaboration previously described. For the second step, the chamber was opened to modify the angle of incidence to a value of 85°. The second layer of SiO_2 was then evaporated and deposited onto the first OAD layer. This whole process was repeated a second time to coat the BK7 substrate on both sides.

The microstructural study was performed by scanning electron microscopy (SEM) using a FEG 7001F-TTLS JEOL microscope at an accelerating voltage of 30 kV. To extract statistical data from the micrographs (Fig. 1), different types of filters were used to (i) correct and improve the quality of contrasts, (ii) highlight the contours of the nanocolumns, (iii) reduce image noise. Advanced image processing was then implemented. The SiO_2 columns were isolated by locally segmenting the image. After this segmentation, the void appears in dark contrast and the condensed matter in light contrast, which makes possible the easy identification of the columns or column agglomerates (Fig. 1b and c). Finally, we carried out a statistical analysis by adjusting an ellipse as closely as possible to the contour of the column or agglomerate; each ellipse being characterized by its area, ellipticity and orientation (Fig. 1d).

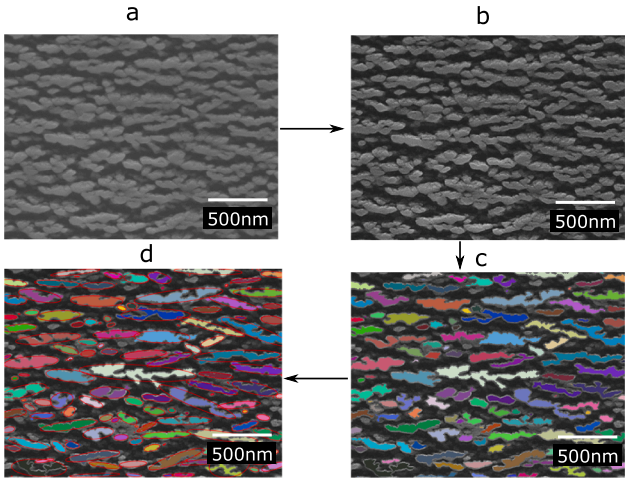

Fig. 1. SEM micrographs for different processing steps, (a) raw picture, (b) after cleaning with different filters, (c) after segmentation and column detection, (d) micrograph after column adjustment with ellipses.

To access the optical properties of monolayers and bilayers, spectrophotometry measurements were carried out for each sample. Transmittance and reflectance spectra were recorded with a Carry 5000 Varian spectrophotometer for the 350–2000 nm range with a fixed step of 1 nm. Transmittance and reflectance acquisitions were repeated 4 times for each sample giving a repeatability of 0.1%. To avoid problems coming from the anisotropic behavior of the samples, measurements were made with a light polarized in the direction perpendicular to the direction of deposition, i.e. along the elongation axis of the nanocolumns. Indeed, as we will see later, ellipsometry study of OAD samples show anisotropic character such as non-zero off diagonal coefficients per block of the Mueller matrix. Consequently, a generalized ellipsometry characterization was used to improve the optical model. This generalized ellipsometry characterization was performed with a Woolam M-2000, and the measurements were carried out with an incidence angle going from 55° to 80° with a 5° step for each azimuthal rotation angle going from 0° to 180° with a 5° step.

The nanostructure of the OAD samples was analyzed by TEM experiments at an acceleration voltage of 200 kV. Bright-field TEM images were recorded in a JEOL 2010F microscope. The 3D morphology of the OAD SiO_2 bilayer deposited on the substrate was extracted from electron tomography in a FEI Titan Cubed Themis 60-300 microscope, using the high-angle annular dark-field scanning TEM (HAADF-STEM) imaging mode. For that purpose, a dedicated tomography holder operated by the FEI Xplore3D software was used to acquire tilt series every 2° from −60° to +60°. The FEI Inspect 3D software was then employed to align the projections using cross-correlation methods, and to perform reconstruction into a 3D volume using the conventional simultaneous iterative reconstruction technique (SIRT) with 30 iterations. The FEI Avizo program was used for 3D visualization and segmentation of the reconstructed volume. Specimen for TEM were prepared by soft and flat mechanical polishing of the two faces using a tripod apparatus (Model 590 Tripod Polisher) in order to control finely the thinning down to a few microns. This step was followed by a short Ar^+-ion milling step in a Gatan PIPS system (using an energy of 3.5 keV and an incidence angle of ±7°). This procedure provides large and homogeneous electron transparent areas, which is suitable to limit the geometrical shadowing of the specimen at large tilt angles of the holder. Prior to insertion into the microscope, the specimen was cleaned in an Ar/O_2 plasma in order to remove the hydrocarbon contamination.

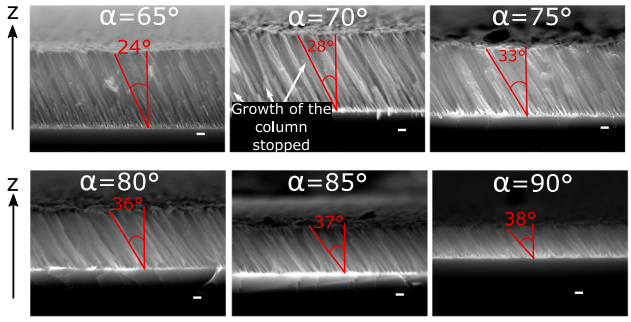

Fig. 2. Evolution of the column angle β_{col} with the deposition angle α for a SiO_2 series on Si. The scale bar is 100 nm.

3. Results and discussion

3.1. Microstructural characterization

In order to build an accurate optical model, we investigated at first the microstructural properties of the samples. As it is expected, the column angle β_{col} of our SiO_2 OAD layers increases with the deposition angle α, from $\beta_{col} = 24^\circ$ for $\alpha = 65^\circ$ up to $\beta_{col} = 38^\circ$ for $\alpha = 90^\circ$ (Fig. 2). These results matched the ones observed and predicted by Alvarez et al. for SiO_2 [20]. On the other hand, we observe that the growth of some columns has been stopped within the films due a competitive growth process wherein the largest columns are shading the smallest ones. This phenomenon contributes to the evolution of porosity as function of the depth inside the film [28].

As it is hard to get information on anisotropy or porosity evolution of the thin film solely from cross-sectional observations, SEM images were also captured in the direction of the columns. Under these conditions, four SEM micrographs of SiO_2 deposited at 85° with different thicknesses have been performed: 76 nm, 153 nm, 317 nm, 630 nm (Fig. 3). We qualitatively observe, with the increase in thickness, a coalescence of the columns leading to an anisotropic enlargement of the structures. These observations indicate increasingly anisotropic structures with the film thickness, in accordance with those made by Vick et al. and C. Lopez-Santos et al. [9,11].

To be more quantitative, we present on Fig. 4 the average area evolution of the columns agglomerates for different thicknesses using the method described in Part II (for more information see Supplementary Material 2 (colored image)). The linear growth of the

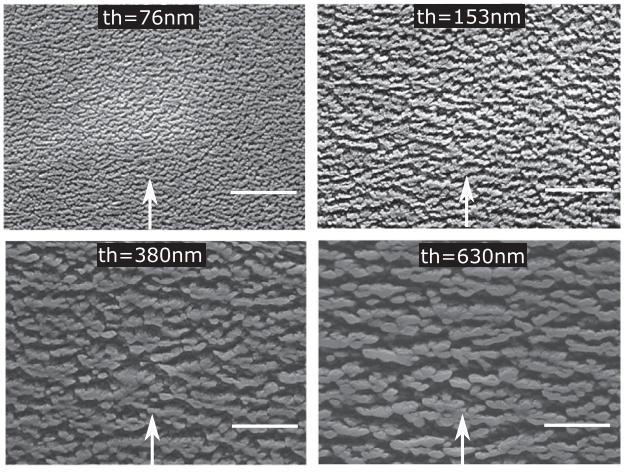

Fig. 3. SEM micrographs recorded along the column direction of the SiO_2 sample deposited by OAD at $\alpha = 85^\circ$ on silicon substrate, for different film thicknesses (indicated on top of each image). The arrows indicate the direction of the incoming species during the deposition process, the scale bar is 500 nm.

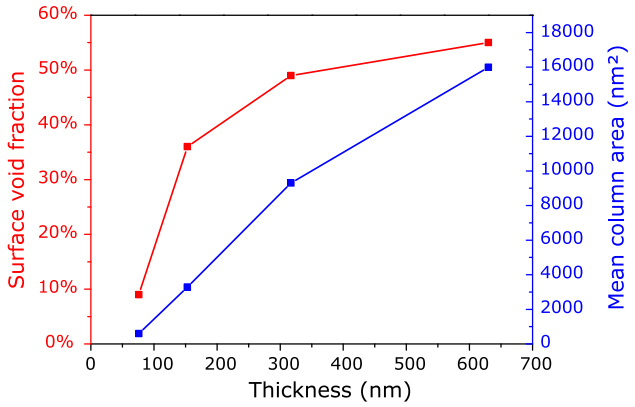

Fig. 4. Evolution of the surface porosity (red) and of the mean column area (blue) for a SiO_2 sample deposited at $\alpha = 85^\circ$ for different thicknesses.

average area of the columns section as a function of deposition thickness indicates a columnar broadening of structures deposited by OAD, which has been reported in other works [11,29,30]. This effect should lead to a decrease in porosity with thickness. The competitive growth phenomenon mentioned previously is expected to have an opposite effect, leading instead to a porosity increase with thickness. According to Fig. 4, the observed large increase in surface void fraction with the thickness of the thin film actually suggests that the latter phenomenon is dominant, at least over the thickness range studied. Furthermore, it can be noted that the surface void fraction increases faster for the first part of the growth process and slows down for the second part. This suggests that the early stage of the growth is dominated by the competitive growth process when for the second part this mechanism is balanced by the column broadening process.

Using the information extracted from the ellipses approximating the nanostructures observed on SEM images, the evolution of the anisotropic character as a function of the film thickness can also be highlighted in Fig. 5. To describe this anisotropy, a coordinate system (x′, y′, z′) linked to the columns is introduced, tilted from β angle along y axis of the laboratory system (x, y, z) (Fig. 6). These ellipses are characterized by their major axis l_b along y′ = y axis of Fig. 6, their minor axis l_a along x′ axis and the angle γ indicating the orientation of the ellipses with respect to the horizontal axis of Fig. 3. The evolution of the average length of these axes (Fig. 5a) clearly points out the development of morphological anisotropy as a function of thickness. Indeed, there is a slight increase in the average length of the short axis with thickness, while the average length of the long axis increases more rapidly. This reflects an anisotropic elongation of the structures during the film growth, as evidenced by the increase of the ratio l_b/l_a.

On the other hand, the increase in anisotropy is accompanied by a progressive alignment of the ellipses. This behavior is materialized by the probability distribution of the orientation of the ellipses increasingly centered on the horizontal axis as the thickness increases Fig. 5b).

3.2. Microstructural synthesis and discussion

To sum up, the microstructural characterizations have highlighted four morphological characteristics important for deepening the comprehension of the optical properties of OAD-formed thin films: (i) an increase of the columns angle β_{col} in respect to the deposition angle α, (ii) an increase in porosity rate during the growth, (iii) a broadening of the column section for an increasing thickness, (iv) an anisotropic growth of the nanostructures.

Thus, OAD deposition involves different competing growth processes. The shadowing effect favors the growth of the largest columns and the extinction of the growth of the smallest columns [28]. As highlighted in the work of F. Nita et al. [25], this process is responsible for the increase in porosity rate during thin film growth. These

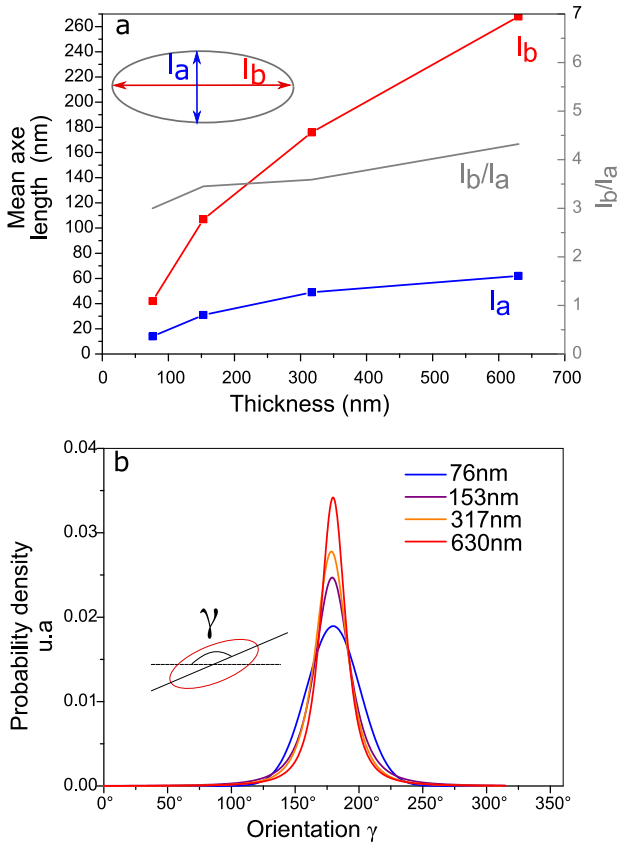

Fig. 5. (a) Evolution of the morphological parameters of SiO_2 nanocolumns (assimilated to ellipses with their minor and major axes Ia and Ib, respectively) as a function of the thickness of the SiO_2 OAD layers (b) Evolution of the probability density of the orientation γ with respect to the horizontal axis in Fig. 3.

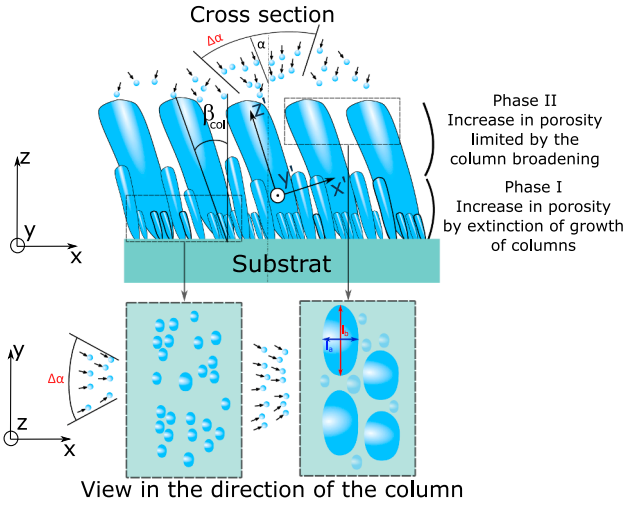

Fig. 6. Schematic view of the columns broadening occurring during OAD growth in cross section and plane view highlighting the different regime of porosity rate plane view. The coordinate system (x', y', z') linked to columns is introduced for a clearer description of the anisotropy.

observations characterize Phase I of the diagram presented in Fig. 6. However, the increase in porosity rate during growth is compensated by the columnar broadening mechanism, Phase II in Fig. 6. For low incident species energies, as it is the case for evaporation at room temperature, Alvarez *et al.* highlighted the importance of dispersion (Δα) of species incidence to explain the increase in column cross section [20]. Indeed, species deposited on the columns in different directions will not only contribute to increasing their length but also to their expansion. Thus the increase in angular aperture is accompanied by an acceleration of the columnar broadening [31]. However, this purely geometric explanation alone cannot explain the differences observed between materials.

C. Lopez-Santos et al. have highlighted the phenomenon of species captured passing near the columns [11]. By considering different capture radii (named the sticking coefficient in the reference) the authors were able to explain the differences in growth behavior specific to different materials[20]. They showed that this capture effect favors columnar enlargement and therefore the coalescence of the columns. This effect is also at the origin of anisotropic growth, for species with a large catch radius the expansion of the section is favored. This broadening favors the coalescence of the columns between them in the direction orthogonal to the flow because there is no shading effect. The resulting structure is an elongated ellipse orthogonally to the flow [11]. Our observations are thus in line with the OAD growth model of SiO_2.

3.3. Optical model

Usually OAD deposited layers are simulated as one thin heterogenous layer composed of porosity and dense material. This optical description is however very basic and it will fail to consider the porosity evolution as well as the anisotropic morphology that was pointed out in the previous section. In order to sense the influence of these crucial geometrical factors from the optical point of view, generalized ellipsometry characterization is used to measure the Mueller matrix of the samples. The simulation of the experimental data, which requires the use of a model taking into account the anisotropy, gives access to a lot of information. The model we used is the Anisotropic Bruggeman Effective Medium Approximation (ABEMA) model. This approximation was used over the so-called rigorous anisotropic Bruggeman effective medium approximation because for lossless material the results are identical [24]. This model determines the porosity ratio, the angle of inclination β_{col} of the optical axis (equivalent in our case to the angle of the columns) as well as the depolarization factors La, Lb and Lc at the origin of anisotropy associated with the shape factors of nanostructures along x′, y′ and z′ directions respectively.

To consider the porosity evolution along the thickness of the films (z axis) evidenced by the microscopic observations, a porosity gradient was applied by dividing the thin film into 20 layers of variable porosity. To best match the evolution shown in Fig. 4, this gradient was decomposed into two linear segments. A first segment adapted to the evolution of the porosity over 10% of the initial thickness of the film and a second segment adapted to the evolution of the porosity of the remaining thickness. The ordinate at the origin of the first segment and the slopes of the two segments are therefore the adjustable parameters of the porosity gradient. Although the microstructural study pointed out a morphological increase of the anisotropy as function of z, this was not implemented in the model considered in this article. We therefore assumed fixed depolarization factors representing the morphological anisotropy for the entire thin film. A detailed discussion on this topic can be found in Supplementary Material 3.

The ABEMA model is considered to be valid for nanostructure dimensions that are much smaller than the probing wavelength, typically $r/\lambda < 0.1$ where r is the radius of a spherical inclusion embedded in the host matrix and λ the wavelength. For inclusion dimensions that do not fulfil this criterion, diffusion mechanisms must be taken into account [22,32]. To account for the possible presence of diffusion close to the UV spectral range, an intensity attenuation was applied according to Urbach's rule [33]. Spectrophotometric measurements can only measure optical losses without distinguishing between scattering and absorption. The absorption of dense SiO_2 embedded in OAD nanostructure is assumed equal to the one evidenced on a dense sample deposited at $\alpha = 0°$. In this way, possible additional optical losses evidenced by OAD

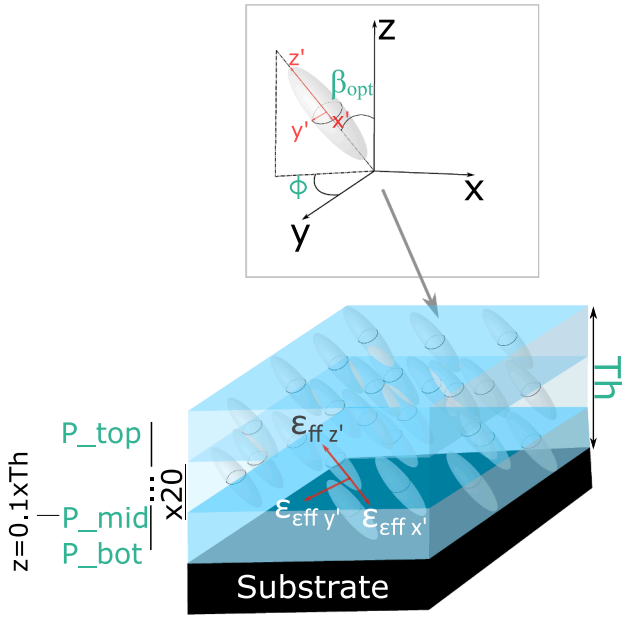

Fig. 7. Schematic picture of the model used to simulate OAD layer with fitted parameters highlighted in green.

nanostructures are assumed coming from diffusion. The validity of this hypothesis is discussed in Supplementary Material 4.

In summary, the adjustable parameters of the optical model are therefore: the thickness of the OAD layer Th; the volume fraction of air (porosity) near the substrate (z = 0), at 10% of the film thickness and on the surface of the layer (z = Th); the amplitude and slope of Urbach absorption (that in fact originates from diffusion); The depolarization coefficient Lc and the ratio of the depolarization coefficients La/Lb; the columns angle (optical axis) β_{opt} in respect with the y axis and Φ the azimuth angle of these columns in respect with the z axis. Fig. 7 presents a schematic view summing up the model. It should be noted that although our article is dedicated to the study of SiO2, a dielectric this method can also be used for the investigation of metals or semiconductors deposited by OAD. On figure is a schematic picture of the model.

To illustrate the model and its sensitivity to optical measurements a python code that allows the calculation of all optical simulation is presented in form of a Jupyter notebook on Supplementary Material 1.

3.4. Optical simulation of experimental OAD layers

As an example, we present on Fig. 8 the advanced optical characterization for an SiO_2 OAD thin film deposited at α = 70°. The generalized ellipsometry measurements (7c.) have been acquired with an incidence angle θ = 65° and with the optimal azimuthal angle for anisotropic contrast: Φ = 135° from x and y axis. These ellipsometry measurements are performed on SiO_2 layers deposited and silicon substrates when the layers analyzed by spectrophotometry are deposited on glass. The same model is applied for both SiO_2 OAD layers with the hypothesis that the substrate doesn't affect their growth behavior.

The very good agreement between the simulations and the numerous experimental measurements attests to the quality and robustness of the model used. The information about the anisotropy of the sample carried by the off diagonal block coefficients of the Mueller matrix makes possible the determination of the optical axis angle of the OAD layers: β_{opt} = 25° for this thin film deposited at α = 70°. From the depolarization coefficients L_a, L_b and L_c it is possible to determine the characteristic shape factor, considering a medium composed of aligned ellipsoids with the average aspect ratio of the SiO_2 OAD ellipsoids

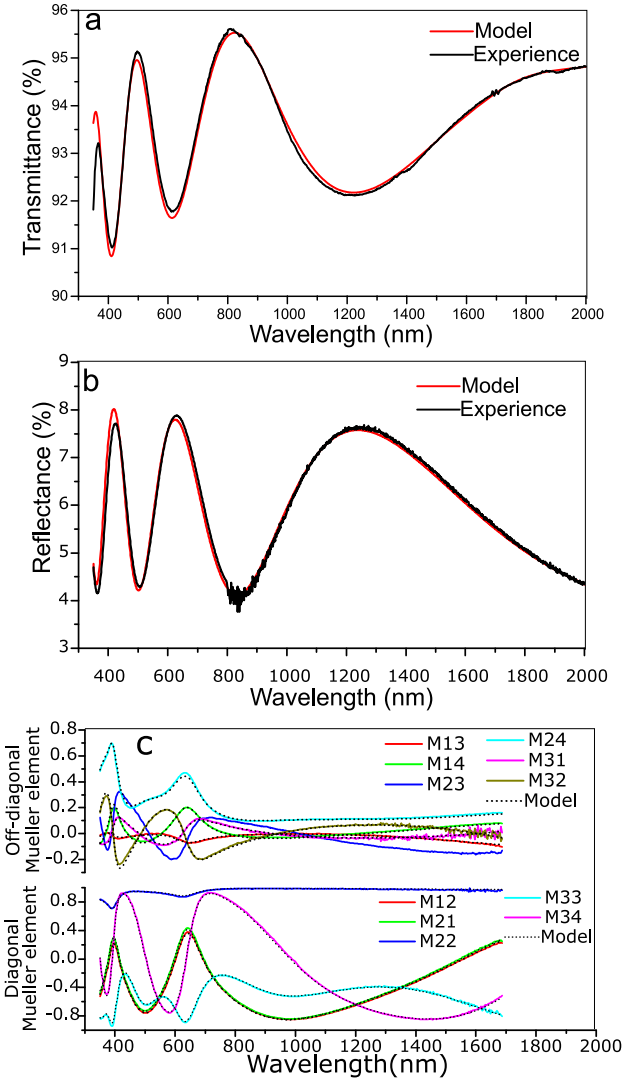

Fig. 8. Experimental and simulated optical spectra. (a) Normal transmission. (b) Quasi-normal reflection. (c) Off diagonal coefficients per block of the Mueller matrix determined by generalized ellipsometry at θ = 65° and φ = 135° or an SiO_2 OAD thin film deposited at α = 70°.

nanostructures [34]. In particular, the aspect ratio of the ellipses is in this case $r = l_b/l_a = 2.31$.

Since the model is anisotropic, the effective refractive index differs according to the three directions of the sample reference (x′, y′ and z′). These indices also change between the substrate and the interface with the surrounding environment due to the porosity gradient. This gradient extracted from the optical simulation is given in Fig. 9a. The evolution of the resulting refractive indices (Fig. 9b) is illustrated by their values at the ends of the OAD layer: positions marked by the arrows (z = 0 and z = Th) in Fig. 9a.

According to this figure, a significant increase in porosity is observed for the bottom part of the deposited layer followed by a slower rise for the remaining thicknesses. This trend is consistent with that observed in SEM (Fig. 4). The effective refractive indexes resulting from the OAD deposition are therefore highly dependent on the polarization direction and position in the thin film. A difference of 0.11 between $n_{z'}$(z = 0) and $n_{x'}$(z = Th) can thus be noted. Finally, the thickness for this thin film is obtained equal to Th = 537 nm and the azimuth angle Φ of the columns in respect with the x axis is close to zero. This last results confirms that the columns axes are aligned to the incident plane (x,z) of the evaporated species.

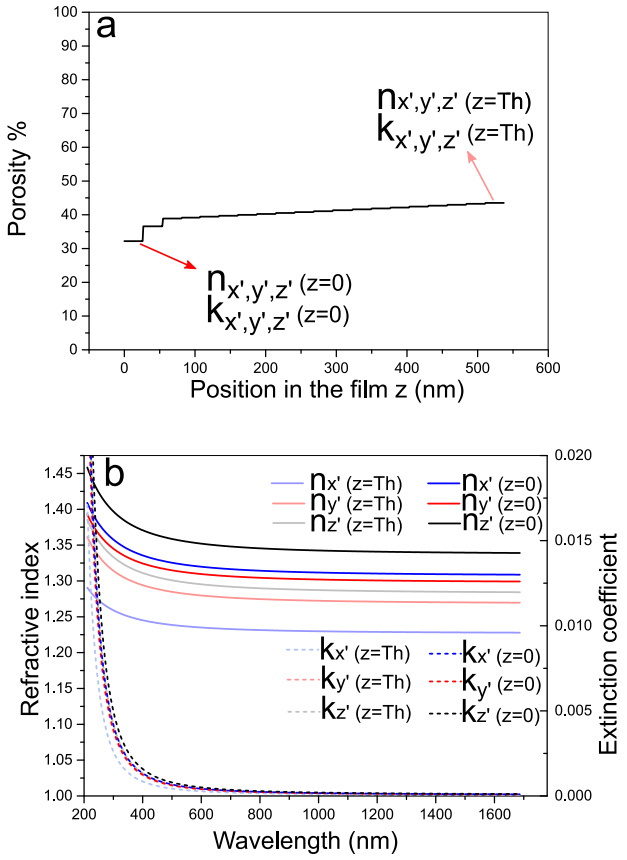

Fig. 9. Parameters extracted from generalized ellipsometry for the SiO_2 OAD thin film deposited at α = 70°: (a) Porosity gradient. (b) Refractive indexes associated with the three directions (x', y' and z') of the sample reference.

3.5. Comparison between optical properties and microstructural properties for OAD single layers

The same approach as that described in the previous section (Section 4) was carried out on a complete series of SiO_2 layers deposited by OAD from α = 65°–85° with step of 5°. The morphological information extracted from optical modeling have then been compared with microstructural studies. First, the order of magnitude and evolution of the optical axis angle β_{opt} with α are close to the measurements of the column tilts made from cross-sectional SEM observations (Fig. 10). We attribute the small discrepancies (maximum difference between the two methods of 8°) to the low refractive index of SiO_2 that leads to a small optical anisotropy making the optical simulation not so sensitive to anisotropic parameters.

Another morphological feature that can be extracted from the optical model is the porosity gradient within the different layers in function of the deposition angle α (Fig. 11a). As can be observed, the porosity level in the first growth steps increases faster for high deposition angles. This behavior is consistent with an increase of the competitive character (extinction of the smallest columns) of the growth with α. This evolution of porosity is qualitatively similar to that described by the SEM study added on the figure for the angle of 85°. Here again the low refractive index of SiO_2 causes a small influence of the porosity gradient on the optical properties that may explain part of the difference between the model and the microstructural observation. However, we argue that this cannot alone explain this significant discrepancy. We attribute another part of this difference to the nature of the SEM observation that lacks the depth information. The columns all appear to be on the same level on the micrograph, but some could be extinct due to neighbor shadowing but still appear leading to a

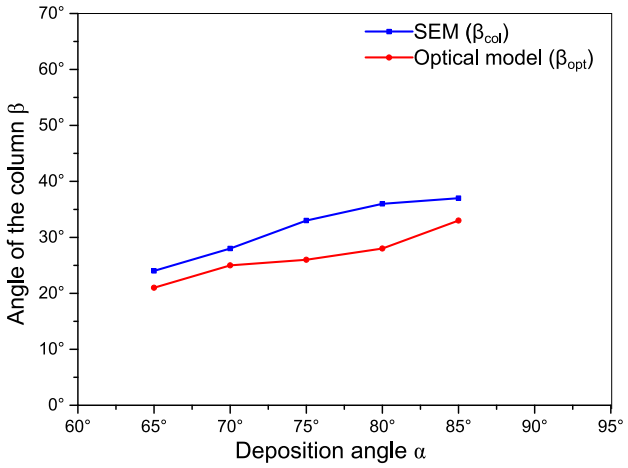

Fig. 10. Evolution of the angle β as a function of the deposition angle α determined by optical simulation (β_{opt}) and by SEM observation (β_{col}) for a series of SiO_2.

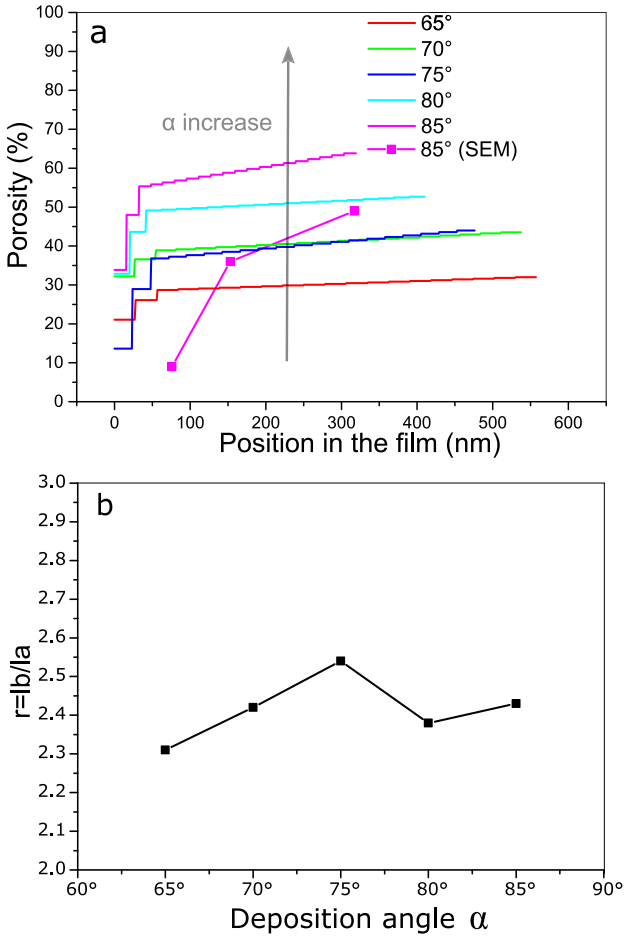

Fig. 11. (a) Porosity evolution as a function of z for several deposition angles α, extracted from optical modeling. The estimated surface porosity level extracted from SEM (layer deposited with α = 85°) is also shown for comparison. (b) Evolution of the aspect ratio as function of α.

minimization of the observed porosity level. Furthermore, due to the interaction volume of the electron, the porosity level inside the column isn't perceptible, despite its presence [35], but will affect the optical response. This effect may also contribute to the underestimation of the porosity level from the microstructural study.

Additionally, from the depolarization coefficients of the optical

model, the averaged aspect ratio of the inclusion, r, could be calculated, i.e. considering a medium composed of aligned ellipsoid with the same aspect ratio. The results are presented on Fig. 11b for the angle series. A small evolution of the aspect ratio with α is observed going from 2.30 to a maximal value of 2.54 for the angle of 75°. This tends to indicate a dependency of the column broadening mechanisms with the angle of deposition.

Those values can be compared to the average value of aspect ratio calculated from the microstructural study (Fig. 5) and more information on the method of calculation of the average of aspect ratio are given in Supplementary Material 3. Thus, for $\alpha = 85°$ an observed microstructural aspect ratio of $r = 2.15$ was found against $r = 2.43$ from the optical model. Here again, a comparable order of magnitude of the aspect ratio is observed between the two methods, although the discrepancy between them could also be due to the weak anisotropy of SiO_2. On Supplementary Material 3 the average on the thickness is avoided by considering the depolarizations gradient, and thus an aspect ratio gradient in the model.

3.6. Comparison between optical properties and microstructural properties for an OAD bilayer

From the previous optical models, the effective refractive indices accessible from the different SiO_2 OAD layers deposited from $\alpha = 0°$ to $\alpha = 85°$ have also been determined. By taking into account this information, an antireflective bilayer coating on glass substrate was designed for the 400–1800 nm range, and then numerically optimized using the refractive index and thickness of each layers as free parameters to maximize the transmittance. This AR was then experimentally achieved as follows: a SiO_2 layer was first deposited by OAD at $\alpha = 65°$ with a targeted thickness of 134 nm and refractive index of $n = 1.30$; then, a second SiO_2 layer was deposited at $\alpha = 85°$ with a targeted thickness of 142 nm and refractive index of $n = 1.16$. An azimuthal rotation of 180° was performed in between the layers in order to minimize any material deposition within the porosity of the first layer during the deposition of the second one.

To evaluate the performances of this bilayer antireflective coating, not only the reflectance (Fig. 12b) but also the transmittance (Fig. 12a) were measured in order to account for absorbance that might arise from the nanostructuration and that could minimize the transparency of the coating. According to Fig. 12a, the prepared bilayer presents high optical performances, in particular a very high and broadband transmittance: average transmittance of 98.97% over [400–1800 nm] range. It is also worth noting that the experimental transmittance is close to its original design. This demonstrate that by knowing precisely the effective refractive index of OAD, we were able to obtain the optical properties needed for our designed antireflective coating.

To go further, the previous model (Section 3) was used to describe with more details the optical properties of the bilayer. To make it more reliable, the optical model was constructed in two steps. On the first step, the first layer alone was optically measured and modelled from generalized ellipsometry and spectrophotometry. The obtained optical properties were then conserved, and a second layer was added to simulate the complete bilayer. The model is thus valid under the hypothesis that the optical properties of the first layer aren't change by the deposition of the second. In other words, no deposition of material should happen in the porosity of the first layer. The fitted parameters of the second layers are the same as described previously for the monolayers with the addition of the angle Φ, azimuthal angle between the first and the second layer, that was allowed to be fitted. The result of this optical simulation are presented on Fig. 12.

It can be noted that the model allows a very precise description of all optical measurements. *Via* the anisotropy information, we determined the column angles $\beta_{opt} = 25°$ and $\beta_{opt} = 36°$ respectively for the first and for the second layer. In addition, we were able to demonstrate that the optical axis of the second layer is not aligned in Φ

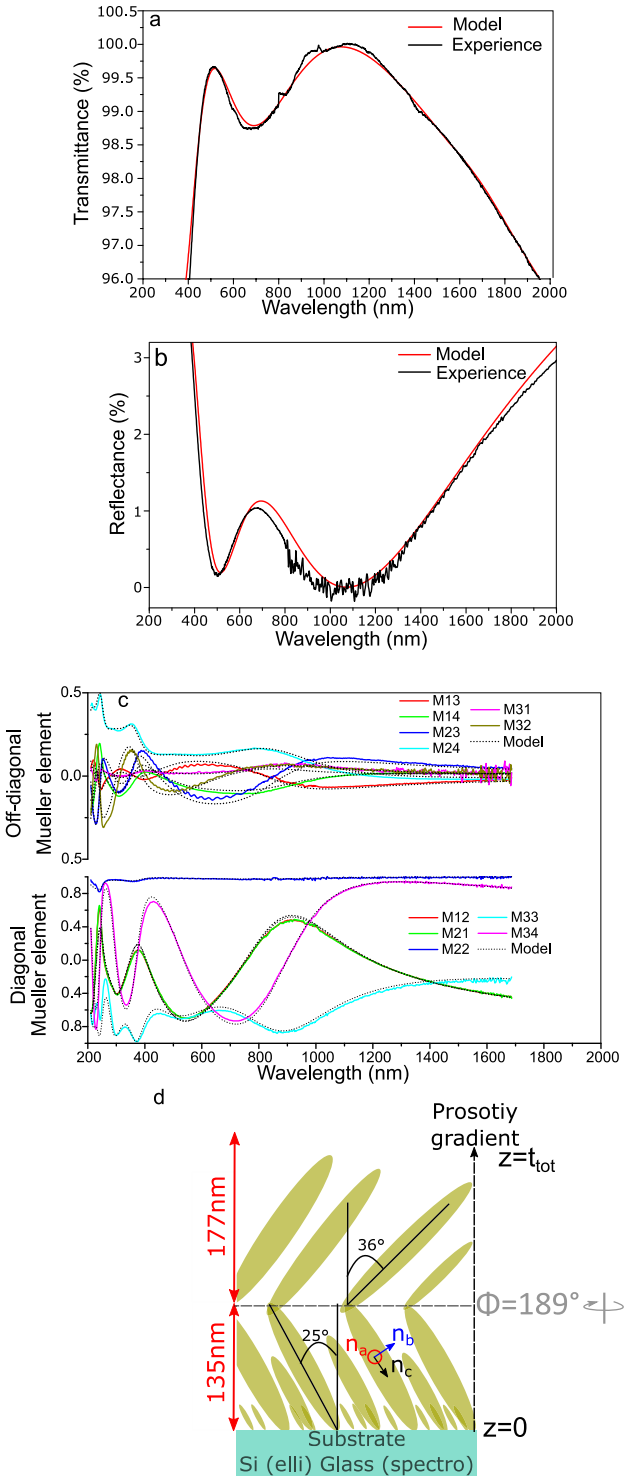

Fig. 12. Experimental and simulated (a) transmittance and (b) reflectance spectra of the OAD SiO_2 bilayer. (c) Mueller matrix determined by generalized ellipsometry at $\theta = 65°$ and $\Phi = 45°$ simulated from the model schematized in (d). The OAD bilayer consists of SiO_2 deposited at $\alpha = 65°$ and $\alpha = 85°$ with an azimuthal rotation between the two layers of $\Phi = 180°$.

with that of the first layer. An angle of $\Phi = 189°$ between the first and second layer is noted, which is close to the expected value ($\Phi = 180°$). A significant improvement in the mean square error (MSE), about 15%, is achieved by taking into account this parameter. Although anecdotal for stack transmission, the ability to access this value demonstrates the high sensitivity of generalized ellipsometry. In practice, this slight

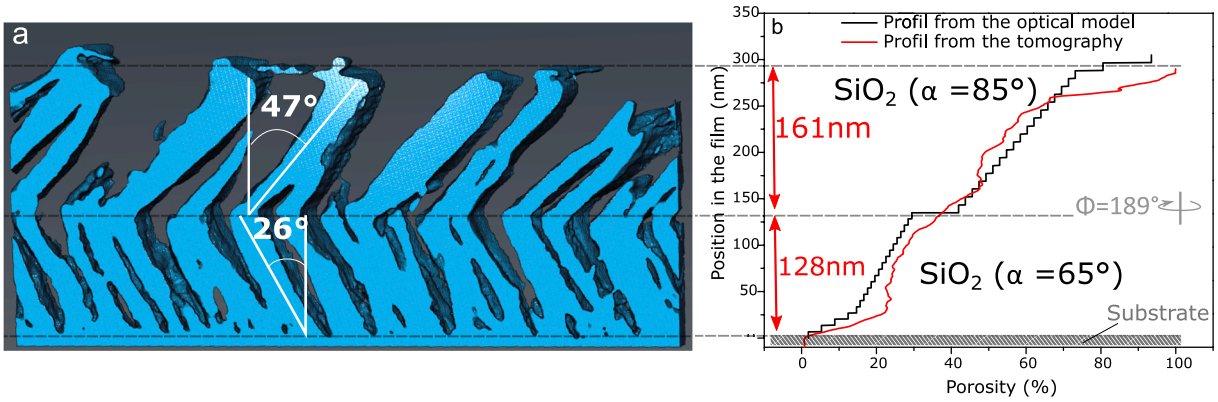

Fig. 13. (a) 3D view of the of the reconstructed OAD bilayer. (b) Associated porosity profile as a function of the depth of the film.

deviation can be explained by a slight disorientation of the sample during its placement at $\Phi = 180^{\circ}$ for the deposition of the second layer compared to the deposition of the first, this alignment being done approximately by the visual inspection.

To get a precise comparison between optical properties and microstructure, a 3D morphological analysis of the bilayer has been performed at the nanoscale from HAADF-STEM electron tomography experiments reported in our previous paper [36]. The 3D reconstruction is presented on Fig. 13a. Interestingly, the measured thicknesses of the first and second layers obtained from the 3D reconstruction (128 nm and 161 nm, respectively) are quite close to the ones extracted from the optical model (135 nm and 177 nm, respectively). Furthermore, the column angle in the first layer determined from electron tomography ($\beta_{col} = 26^{\circ}$) matches the one expected from the optical model ($\beta_{opt} = 25^{\circ}$). It should be noted however that the column angle of the second layer determined from the model, $\beta_{opt} = 26^{\circ}$, is quite different from the one observe, $\beta_{col} = 47^{\circ}$. This difference for the second layer might come as it was previously stated from the weak optical anisotropy of SiO_2. Interestingly this value is significantly higher than the value found for the same angle of deposition but grown on plane silicon substrate ($\beta_{col} = 37^{\circ}$). This highlights a difference of the growth behavior of the OAD layer when deposited on prepatterned thin film as it was previously demonstrated [37]. It can also be noted that, correspondingly to our hypothesis, no densification is observed at the interface between the first and the second layer.

Beside the extraction of the basic morphological information of the OAD coatings, like thicknesses and column tilts, electron tomography appears here as a powerful approach for further quantitative extraction of the porosity gradient within the full layer Fig. 13b. The very nice agreement of this porosity profile compared to that extracted from advanced optical simulations demonstrates the validity of the optical model used in this work, and indicate that it is possible to reliably describe the porosity profile from optical characterization. This type of information is crucial for further optical design optimization, by considering the porosity gradient naturally present in OAD layer to optimize optical function from such layer as antireflection for example.

4. Conclusions

In this work, we demonstrated by microstructural study that the growth process of OAD will produce nanocolumns with an anisotropic broadening of the section and an increasing porosity rate for an increasing thickness. These morphological aspects have an impact on optical properties that needs to be considered for practical applications. This was measured using generalized ellipsometry and spectrophotometry. Guided by the microstructural study, we established an optical model using the ABEMA combined with a gradient of porosity. This model describes with great accuracy both the generalized ellipsometry and spectrophotometry measurements. The parameters extracted from this model like the column angle, porosity rate and aspect ratio of the columns are close to the ones observed from the microstructural study which validate the merits of our model. Knowing with high accuracy the optical properties of OAD thin films allowed us to optimize precisely a SiO_2 antireflective bilayer that shows a very high level of transmittance. Finally, using electron tomography, we also confirmed that the optical model describes closely the morphological properties of the bilayer making it an interesting tool to get easy access to morphological parameters from optical measurements. Presented in the case of a SiO_2 mono and bilayer the model could also be used to precisely characterize semiconductors and metals deposited by OAD.

CRediT authorship contribution statement

Florian Maudet: Conceptualization, Methodology, Software, Validation, Formal analysis, Investigation, Data curation, Writing - original draft, Writing - review & editing, Visualization. **Bertrand Lacroix:** Conceptualization, Methodology, Validation, Investigation, Resources, Writing - review & editing. **Antonio J. Santos:** Investigation. **Fabien Paumier:** Conceptualization, Methodology, Resources, Supervision, Project administration, Funding acquisition. **Maxime Paraillous:** Validation, Investigation. **Simon Hurand:** Conceptualization, Validation, Writing - review & editing. **Alan Corvisier:** Investigation, Writing - review & editing. **Cecile Marsal:** Validation, Investigation. **Baptiste Giroire:** Validation, Investigation. **Cyril Dupeyrat:** Conceptualization, Validation, Resources, Funding acquisition, Project administration. **Rafael García:** Funding acquisition. **Francisco M. Morales:** Funding acquisition, Writing - review & editing. **Thierry Girardeau:** Conceptualization, Methodology, Validation, Formal analysis, Resources, Writing - original draft, Supervision, Project administration, Funding acquisition.

Declaration of Competing Interest

The authors declare that they have no known competing financial interests or personal relationships that could have appeared to influence the work reported in this paper.

Acknowledgements

This work was supported by the DGA (Direction Générale de l'Armement), the French Defense Procurement Agency. This work has been partially supported by « Nouvelle Aquitaine » Region and by European Structural and Investment Funds (ERDF reference P-2016-BAFE-209): IMATOP project.

A. J. Santos thanks the financial support of the IMEYMAT Institute and the Spanish Ministerio de Educación y Cultura for the concessions of grants (ICARO-173873 and FPU16-04386).

The “Talent Attraction Program” of the University of Cádiz is also acknowledged by supporting B. Lacroix contract code E-11-2017-0117214.

This work was carried out in the framework of the associate laboratory PRIMEO (“Partnership for Research and Innovation in Emerging Materials for phOtonics”) between Safran Electronics & Defense and Pprime Institute.

Appendix A. Supplementary material

Supplementary data to this article can be found online at https://doi.org/10.1016/j.apsusc.2020.146312.

References

[1] M.T. Taschuk, M.M. Hawkeye, M.J. Brett, Glancing Angle Deposition (2010).
[2] X. Xiao, et al., Structure and optical properties of Nb2O5 sculptured thin films by glancing angle deposition, Appl. Surf. Sci. 255 (5) (2008) 2192–2195.
[3] J.L. Bubendorff, et al., Nanostructuring of Fe films by oblique incidence deposition on a FeSi2 template onto Si(111): Growth, morphology, structure and faceting, Surf. Sci. 603 (2) (2009) 373–379.
[4] D.W. Flaherty, N.T. Hahn, D. Ferrer, T.R. Engstrom, P.L. Tanaka, C.B. Mullins, Growth and characterization of high surface area titanium carbide, J. Phys. Chem. C 113 (29) (2009) 12742–12752.
[5] J. Kim, Z. Dohnálek, B.D. Kay, Structural characterization of nanoporous Pd films grown via ballistic deposition, Surf. Sci. 586 (1–3) (2005) 137–145.
[6] Z. Dohnálek, et al., Structural and chemical characterization of aligned crystalline nanoporous MgO films grown via reactive ballistic deposition, J. Phys. Chem. B 106 (14) (2002) 3526–3529.
[7] K. Robbie, M.J. Brett, Sculptured thin films and glancing angle deposition: Growth mechanics and applications, J. Vac. Sci. Technol. A Vacuum, Surfaces, Film. 15(3) (1997) 1460–1465.
[8] D.J. Poxson, F.W. Mont, M.F. Schubert, J.K. Kim, E.F. Schubert, Quantification of porosity and deposition rate of nanoporous films grown by oblique-angle deposition, Appl. Phys. Lett. 93 (10) (2008) 2–4.
[9] D. Vick, T. Smy, M.J. Brett, Growth behavior of evaporated porous thin films, J. Mater. Res. 17 (11) (2011) 2904–2911.
[10] D.J. Poxson, F.W. Mont, M.F. Schubert, J.K. Kim, E.F. Schubert, Quantification of porosity and deposition rate of nanoporous films grown by oblique-angle deposition, Appl. Phys. Lett. 93 (10) (2008) 101914.
[11] C. Lopez-Santos, et al., Nanocolumnar association and domain formation in porous thin films grown by evaporation at oblique angles, Nanotechnology 27 (39) (2016) 395702.
[12] F. Maudet, et al., Towards perfect MWIR transparency using oblique angle deposition, Appl. Surf. Sci. 470 (2019) 943–950.
[13] M.F. Schubert, J.-Q. Xi, J.K. Kim, E.F. Schubert, Distributed Bragg reflector consisting of high- and low-refractive-index thin film layers made of the same material, Appl. Phys. Lett. 90 (14) (2007) 141115.
[14] D.A. Rider, et al., Indium tin oxide nanopillar electrodes in polymer/fullerene solar cells, Nanotechnology 22 (8) (2011) 085706.
[15] M. Wang, R. Salut, H. Lu, M.-A. Suarez, N. Martin, T. Grosjean, Subwavelength polarization optics via individual and coupled helical traveling-wave nanoantennas, Light Sci. Appl. 8(1) (2019).
[16] G. Oh, Y. Kim, S.J. Lee, E.K. Kim, Broadband antireflective coatings for high efficiency InGaP/GaAs/InGaAsP/InGaAs multi-junction solar cells, Sol. Energy Mater. Sol. Cells 207(October 2019) (2020) 110359.
[17] Z. Hu et al., TiO 2 nanocolumn arrays for more efficient and stable perovskite solar cells, 2020.
[18] A. Chargui, R. El Beainou, A. Mosset, S. Euphrasie, P. Vairac, N. Martin, Influence of thickness and sputtering pressure on electrical resistivity and elastic wave propagation in oriented columnar tungsten, Thin Films (2020).
[19] M.J.M. Jimenez, V.G. Antunes, L.F. Zagonel, C.A. Figueroa, D. Wisnivesky, F. Alvarez, Effect of the period of the substrate oscillation in the dynamic glancing angle deposition technique: A columnar periodic nanostructure formation, Surf. Coatings Technol. (2019) 125237.
[20] R. Alvarez, et al., Nanocolumnar growth of thin films deposited at oblique angles: Beyond the tangent rule, J. Vac. Sci. Technol. B, Nanotechnol. Microelectron. Mater. Process. Meas. Phenom. 32 (4) (2014) 041802.
[21] A. Barranco, A. Borras, A. R. Gonzalez-Elipe, A. Palmero, Perspectives on oblique angle deposition of thin films: From fundamentals to devices, Progress in Materials Science, vol. 76. Elsevier Ltd, pp. 59–153, 2016.
[22] G.A. Niklasson, C.G. Granqvist, O. Hunderi, Effective medium models for the optical properties of inhomogeneous materials, Appl. Opt. 20 (1) (1981) 26.
[23] J.R. Sanchez-Valencia, R. Longtin, M.D. Rossell, P. Gröning, Growth Assisted by Glancing Angle Deposition: A New Technique to Fabricate Highly Porous Anisotropic Thin Films, ACS Appl. Mater. Interfaces 8(13) (2016) 8686–8693.
[24] D. Schmidt, M. Schubert, Anisotropic Bruggeman effective medium approaches for slanted columnar thin films, J. Appl. Phys. 114(8) (2013).
[25] F. Nita, C. Mastail, G. Abadias, Three-dimensional kinetic Monte Carlo simulations of cubic transition metal nitride thin film growth, Phys. Rev. B 93 (6) (2016) 064107.
[26] J.-Q. Xi, et al., Optical thin-film materials with low refractive index for broadband elimination of Fresnel reflection, Nat. Photonics 1 (3) (2007) 176–179.
[27] Quikim, “Optic_lab: Initial release (Version v1.0). Zenodo,” 2019.
[28] M.M. Hawkeye, M.J. Brett, Glancing angle deposition: Fabrication, properties, and applications of micro- and nanostructured thin films, J. Vac. Sci. Technol. A Vacuum, Surfaces, Film. 25 (5) (2007) 1317.
[29] S. Mukherjee, D. Gall, Power law scaling during physical vapor deposition under extreme shadowing conditions, J. Appl. Phys. 107 (8) (2010) 084301.
[30] T. Karabacak, J.P. Singh, Y.-P. Zhao, G.-C. Wang, T.-M. Lu, Scaling during shadowing growth of isolated nanocolumns, Phys. Rev. B 68 (12) (2003) 125408.
[31] R. Álvarez, et al., Theoretical and experimental characterization of TiO 2 thin films deposited at oblique angles, J. Phys. D. Appl. Phys. 44 (38) (2011) 385302.
[32] M.M. Hawkeye, M.T. Taschuk, M.J. Brett, Glancing Angle Deposition of Thin Films, no. April, John Wiley & Sons Ltd, Chichester, UK, 2014.
[33] I. Studenyak, M. Kranj, M. Kurik, Urbach Rule in Solid State Physics, Int. J. Opt. Appl. 4 (3) (2014) 76–83.
[34] S. Giordano, Effective medium theory for dispersions of dielectric ellipsoids, J. Electrostat. 58 (1–2) (May 2003) 59–76.
[35] L. González-García, et al., Correlation lengths, porosity and water adsorption in TiO 2 thin films prepared by glancing angle deposition, Nanotechnology 23 (20) (May 2012) 205701.
[36] F. Maudet, et al., On the importance of light scattering for high performances nanostructured antireflective surfaces, pp. 1–15, Jun. 2019.
[37] M.O. Jensen, M.J. Brett, Periodically Structured Glancing Angle Deposition Thin Films, IEEE Trans. Nanotechnol. 4 (2) (Mar. 2005) 269–277.

Publication V

Nanostructure and physical properties control of indium tin oxide films prepared at room temperature through ion beam sputtering deposition at oblique angles

B. Lacroix, A. J. Santos, S. Hurand, A. Corvisier, F. Paumier, T. Girardeau, F. Maudet, C. Dupeyrat, R. García, F. M. Morales

The Journal of Physical Chemistry C 123 (2019) 14036−14046

THE JOURNAL OF PHYSICAL CHEMISTRY C

Article

Cite This: J. Phys. Chem. C 2019, 123, 14036−14046

pubs.acs.org/JPCC

Nanostructure and Physical Properties Control of Indium Tin Oxide Films Prepared at Room Temperature through Ion Beam Sputtering Deposition at Oblique Angles

B. Lacroix,*[,†,‡] A. J. Santos,[†,‡] S. Hurand,[§] A. Corvisier,[§] F. Paumier,*[,§] T. Girardeau,[§] F. Maudet,[§,⊥] C. Dupeyrat,[∥] R. García,[†,‡] and F. M. Morales[†,‡]

[†]Department of Materials Science and Metallurgic Engineering, and Inorganic Chemistry, University of Cádiz, E-11510 Puerto Real, Spain

[‡]IMEYMAT: Institute of Research on Electron Microscopy and Materials of the University of Cádiz, E-11510 Puerto Real, Spain

[§]PPRIME Institute, UPR 3346 CNRS - University of Poitiers - ENSMA, SP2MI, F-86962 Futuroscope-Chasseneuil, France

[∥]Safran Electronics and Defense, 26 avenue des Hauts de la Chaume, F-86280 Saint-Benoît, France

Supporting Information

ABSTRACT: In this paper, we report the fabrication of porous and crystalline tin-doped indium oxide (ITO) thin films at room temperature by ion beam sputtering deposition at oblique angles using either argon or xenon ions. Deep insights into these systems are provided by coupling nanostructural (scanning and transmission electron microscopies, X-ray diffraction) and optical (spectroscopic ellipsometry, spectral reflectometry) characterizations. This original approach allows extracting important features of the films (porosity, refractive indexes, in-grain carrier densities, and mobilities) not easy to reach locally by other techniques. We propose a model decomposing the complex film's nanostructure into two layers presenting different electro-optical properties, which are attributed to the shadowing effect, but also to the presence of growth defects and impurities due to the atomic peening. In particular, we demonstrate that ITO films deposited with Xe present a better crystallinity and larger porosity, providing superior in-grain carrier transport and offering more flexibility to design broad-band low-reflectivity surfaces. These results widen the possibilities to engineer transparent and conductive thin films at room temperature with enhanced properties, especially in the near-infrared range where oblique angle deposition allows a reduction of reflectivity even at high doping.

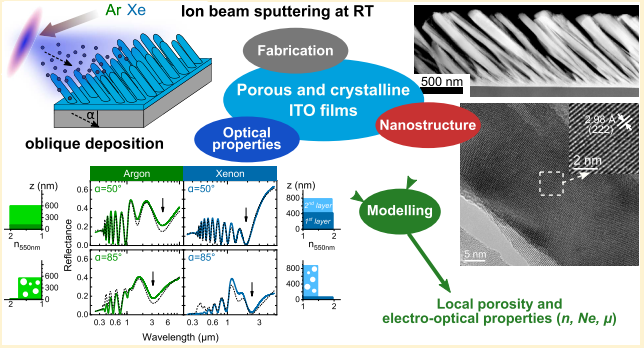

INTRODUCTION

With their high optical transmission in the visible range and simultaneously great electrical conductivity, transparent conducting oxides (TCOs) are very attractive materials in the field of (opto)electronics. They are playing an important role over a variety of applications, including transparent contacts in optoelectronic devices (solar cells, light-emitting diodes, flat-panel displays, touch screens), low emissivity, and smart windows for buildings, heat reflectors, static dissipation, airplane windshield deicer, or electromagnetic shielding.[1−6] In these materials, transparency and conductivity are however intricately linked since TCOs generally exhibit strong absorption and reflection (and hence low transmission) of light in the infrared (IR) range due to the free-carrier plasma. Moreover, any effort to increase the carrier density for improving the conductivity σ (proportional to the product of the carrier mobility μ and the carrier density N) will produce a shift of the plasma resonance toward the visible (vis) region, leading to substantial narrowing of the transmission window in this spectral domain.[7] Such antagonism between the electrical and optical properties is an important limitation for further implementation of TCOs in devices requiring both optical transparency across a wide portion of the electromagnetic spectrum and low electrical resistivity ($\rho = 1/\sigma$). In photovoltaics, for example, transparent electrodes with large optical access and low resistance are needed to make better use of the solar spectrum.[2] In other fields as diverse as security, surveillance, transportation, and environmental monitoring, TCOs also merit serious consideration for their integration in the optical components of multispectral and hyperspectral detectors, for instance.[8−10] Besides broad-band transparency, the use of TCOs presenting low resistivity would be of great

Received: March 27, 2019
Revised: May 14, 2019
Published: May 14, 2019

DOI: 10.1021/acs.jpcc.9b02885
J. Phys. Chem. C 2019, 123, 14036−14046

interest for providing other essential functionalities in these systems to ensure optimal performances in a variety of environmental conditions (ground, air, space, aquatic): heating capability to prevent fog and frost formation in critical regions exposed to humidity and low temperatures or shielding against electromagnetic interferences.[4,6,11]

Within this class of materials, tin-doped indium oxide (ITO) is certainly the best candidate for those applications because this n-type degenerate semiconductor combines the highest available transmissivity for visible light with the lowest electrical resistivity due to its high free-carrier density.[12] Nevertheless, finding the best compromise between reasonably low resistivity and sufficiently high IR transmittance in a spectral domain as wide as possible is far from being straightforward. This is due not only to the inherent electro-optical antagonism of TCOs but also to the actual fabrication approaches. Indeed, although many (N, μ) couples have been reported for dense polycrystalline ITO films prepared by standard physical vapor deposition (PVD) processes,[13] none fulfills an acceptable compromise. In particular, carrier densities as high as $(1-2) \times 10^{21}$ cm^{-3}, obtained by Sn doping to levels of 5−10 at %, promote resistivities as low as about 10^{-4} Ω·cm, which is relevant for photovoltaic and electromagnetic shielding applications, but have deleterious effects on the optical properties due to a plasma resonance close to the visible range. Reducing N to $10^{18}-10^{19}$ cm^{-3} for shifting plasma effects toward deeper IR cannot be considered here since σ becomes so low that it cannot be compensated by an increase of mobility, even if monocrystalline layers—almost free of grain boundaries—would be considered.

To overcome the current difficulties related to the optimization of the electro-optical properties of ITO, and in TCOs in general, this work aims at proposing novel solutions in the production of these materials. Regarding the preparation of thin films, different techniques have been reported.[5] Most of them are based on PVD techniques, such as electron-beam evaporation,[14] magnetron sputtering,[15,16] or pulsed laser deposition.[17] However, these processes generally require heating the substrates at relatively high temperatures (>300 °C) to ensure reasonable transmittance and conductivity, which can lead to the formation of intermixing layers, adhesion problems of the coatings, and substantial increase of production costs at industrial scale. Thanks to the great deal of control of the ion energy, flux and species combined with the possibility to operate at low pressure, ion beam sputtering (IBS) appears as an alternative and attractive technique for low-temperature deposition of ITO films with excellent properties ($\rho = 1.5 \times 10^{-4}$ Ω·cm, visible transmittance > 80%).[18,19] In addition to the choice of the growth process, the geometry is also an important parameter to take into account with a view to improving the film properties. In particular, the bottom-up fabrication of nanostructured films by oblique angle deposition (OAD) or glancing angle deposition (GLAD) has attracted much attention in the recent years. In this setup, incident particles arrive obliquely at the surface of the substrate, which leads to the formation of porous layers with tilted nanocolumns due to the so-called shadowing effect.[20,21] This approach, very attractive from the optical point of view, has been applied in the past decade to finely tune the refractive indexes of SiO_2 and/or TiO_2 layers and integrate them to obtain broad-band antireflective coatings over the entire visible and near-infrared spectrum.[22] Some studies report the OAD deposition of nanostructured ITO films by means of electron-beam evaporation[23−26] or magnetron sputtering.[27,28] However, as far as we know, no works to date are dealing with IBS deposition of ITO in the oblique geometry. To fill this knowledge gap, with the ambition of achieving tin-doped indium oxides with controlled nanostructure and endowed with enhanced antireflective capabilities in the near-infrared (NIR) range without compromising too much the carrier density, the present paper purposes on the exploration of the possibilities offered by the fabrication at room temperature of ITO thin films by combining IBS and OAD processes.

EXPERIMENTAL SECTION

Ion Beam Sputtering Deposition at Oblique Angles. Tin-doped indium oxide nanostructured films were fabricated at room temperature on silicon substrate by ion beam sputtering deposition in a Nordiko chamber, which includes two radio-frequency sources. The primary source was used to produce Ar or Xe ions accelerated at 1.2 keV (with a current of 80 mA) to sputter a 15 cm diameter water-cooled sintered ceramic target of ITO containing a nominal concentration of 10 wt % SnO_2 and inclined by an angle of 45° relative to the primary ion flux. Prior to the deposition, the chamber pressure was 2×10^{-6} Pa. During the process, oxygen was introduced in the chamber through the assistance gun with a flow of 5 sccm and the background pressure was maintained to 2×10^{-2} Pa. Oblique deposition was performed by placing the substrates on a laboratory-made substrate holder specially designed to allow the growth at different angles α from 50 to 85° (α represents the angle between the substrate normal and the incident vapor flux).

Morphological, Structural, and Compositional Analyses. After deposition, the general cross-sectional or top-view morphologies of the films were studied by scanning electron microscopy (SEM) using a field emission gun 7001F-TTLS JEOL microscope at an accelerating voltage of 20 kV. X-ray diffraction (XRD) experiments were performed using a Seifert XRD 3000 diffractometer fitted with a copper source and a 1 mm beam collimator to study the structure and texture of the different samples. To obtain additional insights into their nanostructure, transmission electron microscopy (TEM) experiments were conducted in an FEI Talos F200S analytical microscope operated at 200 kV and equipped with a Super-X energy-dispersive X-ray spectrometry (EDX) system that includes two silicon drift detectors. Local compositional analyses were performed by combining high-angle annular dark-field imaging (HAADF) and EDX acquisitions using the scanning (STEM) mode. The EDX spectrum images were recorded through the Thermo Scientific Velox user interface using an energy dispersion of 10 eV/channel over 4096 channels, to reach the In and Sn K-lines located near 25 keV. For comparison purpose, the very same experimental and fitting conditions were used for all of the investigated samples. Cross-sectional specimens were thinned down by mechanical polishing using a tripod apparatus up to less than 10 μm, followed by Ar ion milling in a GATAN PIPS system (3.5 keV, ±7° incidence). To minimize irradiation damage, the final step was performed at 2.5 keV, ±5° during 5 min up to electron transparency. Before insertion into the column of the TEM device, the prepared sample lamellae were cleaned in a plasma cleaner to remove residual hydrocarbon contamination.

Optical Characterizations. All ITO films deposited on silicon were characterized by standard spectroscopic ellipsometry at incident angles of 65, 70, and 75° (SE) and spectral

DOI: 10.1021/acs.jpcc.9b02885
J. Phys. Chem. C 2019, 123, 14036−14046

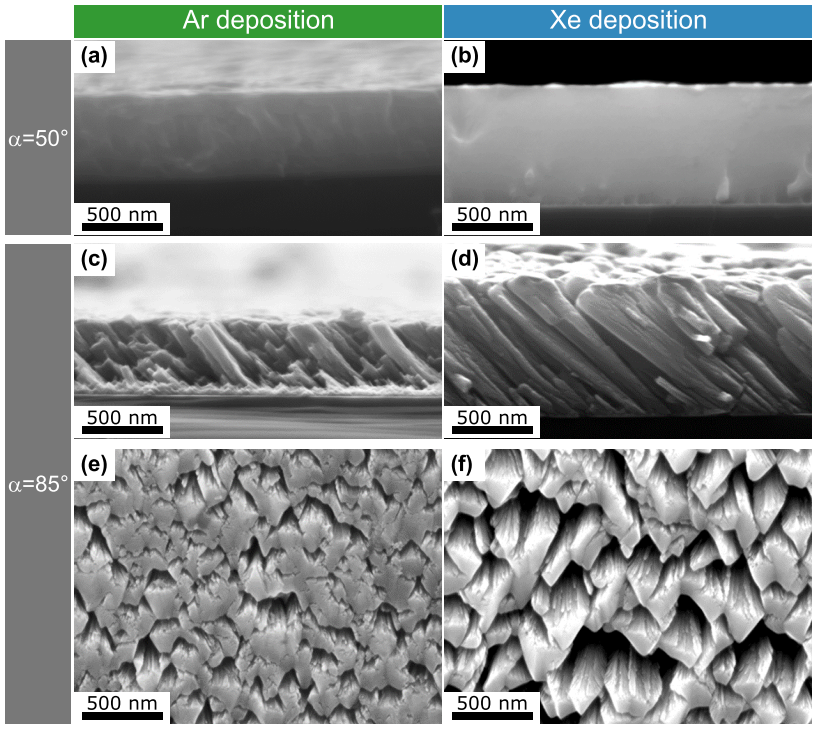

Figure 1. SEM cross-sectional views (a–d) and top views (e, f) of ITO films deposited during 120 min under different conditions: deposition angles α = 50° (a, b) and α = 85° (c–f), with Ar (a, c, e) and Xe (b, d, f). Note that the images have been recorded at the same magnification for comparison purpose.

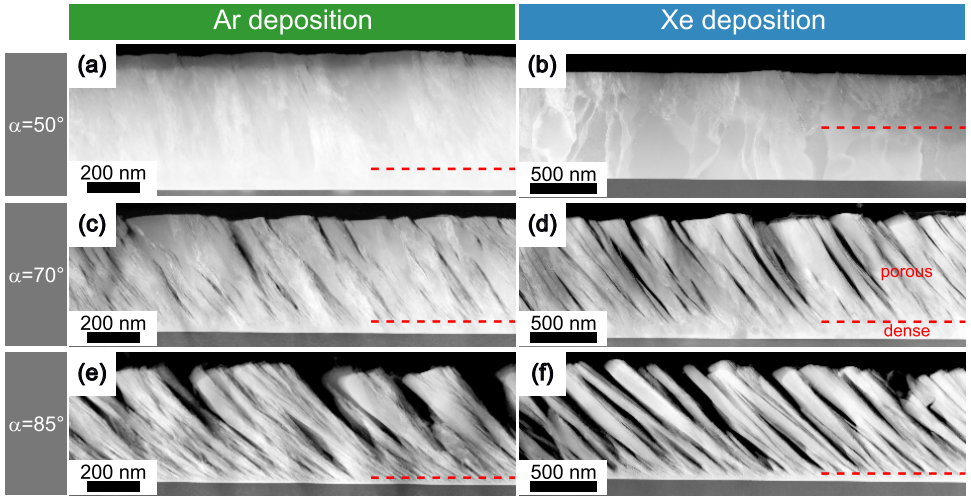

Figure 2. STEM-HAADF cross-sectional views of ITO films prepared during 120 min in different conditions: Ar IBS deposition with (a) α = 50°, (c) α = 70°, and (e) α = 85°; Xe IBS deposition with (b) α = 50°, (d) α = 70°, and (f) α = 85°. The dashed lines highlight the interfaces observed at high deposition angle between the bottom dense layer and the potential top porous layer (note here that the scales are different for Ar-deposited and Xe-deposited films).

reflectometry at normal incident angle (SR), both in the ultraviolet to near-infrared range (UV–vis–NIR) and in the IR range. UV–vis–NIR and IR SE were performed with a J. A. Woollam M2000XI and IR-Vase Mark II, respectively, and UV–vis–NIR and IR SR with a Varian Cary 5000 and a Bruker Tensor 27 FTIR, respectively.

■ RESULTS AND DISCUSSION

General aspects related to the nanostructure (morphology, structure, composition) and optical properties of these films will be addressed in detail by combining various techniques (X-ray diffraction, electron microscopy, spectroscopic ellipsometry, and reflectometry). An original approach based on the implementation of the complex film nanostructure into a two-layer optical model will allow the local extraction of relevant morphological (porosity) and electro-optical (refractive indexes, carrier densities, and mobilities) parameters not easily accessible by other techniques. It will be key to improve the knowledge of the IBS-OAD ITO films, from the role played by the growth parameters (sputter ions, deposition angle) up to the understanding of their properties.

DOI: 10.1021/acs.jpcc.9b02885
J. Phys. Chem. C 2019, 123, 14036–14046

Morphology. Figure 1 presents the SEM images of ITO films recorded after ion beam sputtering deposition at extreme angles of the series, during 120 min, using either Ar or Xe ions. As can be seen in Figure 1a,b, depositions at $\alpha = 50°$ give rise, at first glance, to the formation of dense films for both ions. The morphology is greatly modified when α increases, with the formation of porous and nanocolumnar layers as observed on cross-sectional (Figure 1c,d) and top views (Figure 1e,f) for growth performed at $\alpha = 85°$.

Complementary STEM-HAADF imaging of the films brings to light additional morphological details of the films, with the evidence of a two-layer character for each film. Indeed, a dense layer presenting a uniform HAADF contrast is always detected in the bottom part of the films (Figure 2). It can be observed in particular that the extension of this compact layer depends on both the growth angle and the type of ions, since Xe deposition and smaller α give rise to a thicker dense layer. Furthermore, a second layer showing more pronounced fluctuations of intensity is exhibited in the top part of each film. This top layer can be highly porous for deposition angles $\alpha > 50°$ and exposes a varying thickness depending on the deposition process as same as the bottom dense layer. This two-layer aspect will be discussed in more detail in Optical Properties and Modeling.

As expected, we noted that the tilt angle β of the nanocolumns relative to the substrate normal (extracted from SEM and TEM observations) increases with α (Figure 3). It is

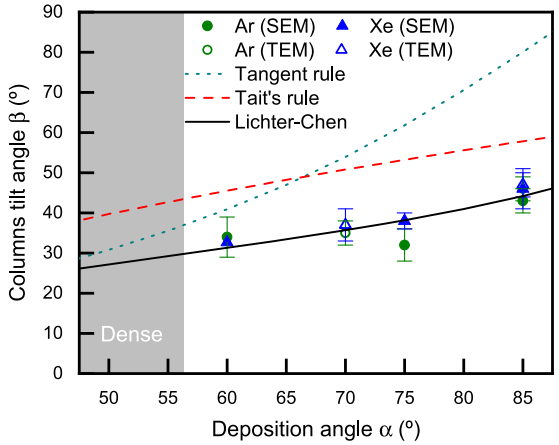

Figure 3. Evolution of column's tilt angle β (measured from SEM and/or STEM-HAADF) after IBS deposition during 120 min using Ar or Xe ions at different deposition angles. The experimental β values have been compared to different analytic models: tangent rule,[29] Tait's rule,[30] and Lichter−Chen expression[31] (using the diffusivity- and deposition rate-dependent parameter $\Phi = 0.6$).

however important to mention that the common empirical ballistic approaches such as the tangent[29] and Tait's[30] rules fail in describing correctly the experimental evolution and magnitude of β versus α. A better description of the β values is actually found with the Lichter and Chen expression[31] using a parameter $\Phi = 0.6$, which points out a diffusivity and deposition rate dependence. Our β values also match very well with those reported by Alvarez et al.[32] for ITO films deposited by electron evaporation at oblique angles. In this study, the authors demonstrated that surface trapping processes can modify the geometrical shadowing process and the development of the columnar growth. These observations therefore suggest that additional mechanisms, more complex than simple ballistic approaches, must be taken into account to understand the formation of ITO coatings by IBS at oblique angles.

Besides the deposition angle, the species used to sputter the target (Ar or Xe) have a significant impact on some morphological features of the ITO layers. According to SEM and STEM-HAADF observations (Figures 1 and 2), deposition with Xe at high angles leads to the formation of ITO films containing sharper and more separated nanocolumns. The Xe-deposited films also seem to present a higher degree of porosity compared to the case of Ar, which will be confirmed later from the simulations of the optical measurements (see Optical Properties and Modeling and Figure 10a,b). Changing the type of sputtering ions while maintaining all other parameters unchanged has also a strong influence on the growth rates, since substantially thicker films are obtained with Xe (about 900 nm) than with Ar (about 600 nm) (see Figures 1 and 2 and later Figure 10). Nevertheless, the type of ions used to sputter the target has no significant influence on the column tilt angle β of the nanocolumns (Figure 3).

Composition. It is well known that the physical properties of ITO films can be strongly affected by the composition. In particular, the Sn doping level, the deviation from the nominal source composition, and the presence of impurities are very important issues to clarify. Note that for a coefficient of 0.1/0.9 weight fractions of the SnO_2 and In_2O_3 homogeneously mixed compounds, the expected solid solution to be formed might ideally have the following atomic concentrations: 3.67 at % of Sn, 35.61 at % of In, and 60.72 at % of O. In the present study, STEM-EDX experiments were carried out to determine, locally, the composition and establish any change in the samples. Elemental mappings performed on the Ar and Xe films deposited at different angles first revealed a uniform distribution of indium, oxygen, and tin species, without evidence of dopant segregation (Figure S1). Further quantitative evaluation of the EDX spectra was done with great care and in a systematic way using the Thermo Scientific Velox software to achieve reliable compositional measurements over the whole ITO films (see Supporting Information for more details). As shown in Figure S2, this approach ensures optimal fitting of the experimental data for reliable elemental quantification. The averaged elemental compositions extracted from the full films and their evolution relative to the deposition conditions (sputtering ions, deposition angle) are summarized in Figure 4. As can be observed, the measured Sn concentration is very close to the nominal value (about 3.7 at %) and remains almost constant for all of the investigated samples (values range roughly from 3.5 to 4.5 at %).

Deviations from the nominal composition can be evaluated from the Sn/In and O/(In + Sn) atomic ratios. According to Figure 4, the stability of Sn/In close to the nominal value (10.3%) suggests that the O/(In + Sn) deviations from target composition (ratio, ∼1.5) are mainly due to a change in oxygen concentration. As a general trend, we observe that the films deposited with Xe present a moderate oxygen deficiency (O/(In + Sn) ≈ 1.3), which remains constant over the whole deposition angle range. On the contrary, the Ar films deposited at low angle ($\alpha = 50°$) show a more pronounced oxygen deficiency (O/(In + Sn) ≈ 1.0), which is progressively reduced when α increases to reach an almost perfect match of ITO film elements distributions with respect to that of the target composition at $\alpha = 85°$. In these films, note that the fitting of the EDX spectra near 3 keV was improved by considering

DOI: 10.1021/acs.jpcc.9b02885
J. Phys. Chem. C 2019, 123, 14036−14046

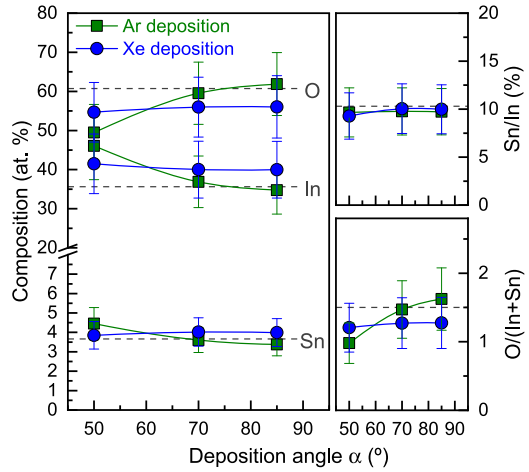

Figure 4. Average composition, and Sn/In and O/(In + Sn) atomic ratios of ITO films prepared by Ar and Xe IBS deposition at different angles (deposition time, 120 min). The dashed red lines indicate the nominal values according to the ITO target composition.

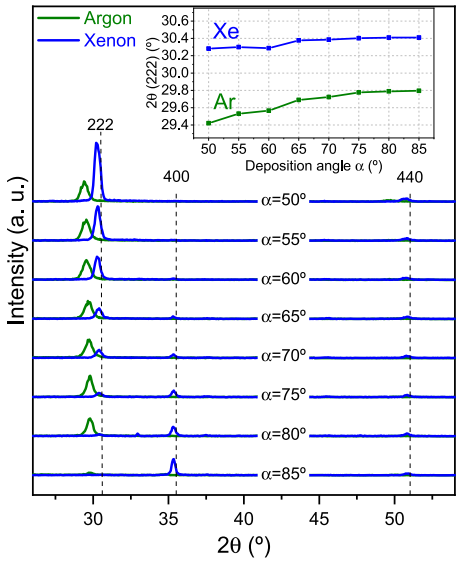

Figure 5. θ–2θ XRD diagrams of ITO layers after IBS deposition using Ar or Xe ions at different deposition angles α. The vertical dashed lines indicate the position of the 222, 400, and 440 reflections of bulk cubic-C-type In_2O_3 structure ($Ia\bar{3}$ space group) obtained from JCPDS 71-2194. Inset: evolution of the 2θ position of the 222 reflection.

small amounts of Ar entrapped during the IBS process: (0.7 ± 0.2) at % for α = 50°, (0.5 ± 0.2) at % for α = 70°, and (0.1 ± 0.1) at % for α = 85°. Note that this Ar content decreases with α following well a direct cosine law. In the case of Xe depositions, no Xe was detected inside the films. Such incorporation of sputtering ions into thin films prepared by IBS is well known and has been reported many times in other works.[33,34] This point will be discussed later at the end of this paper. Despite these compositional results have been obtained using the same conditions for the EDX acquisitions and processing, they must be considered carefully. This is particularly true for the quantification of light elements such as oxygen, which can give rise to errors in the absolute composition. Nevertheless, we believe that the relative changes evidenced between the samples of this study are reliable to establish general trends, which will be discussed in more detail later.

Structure. X-ray diffraction was used to investigate the structure of the films prepared at the different growth conditions. The presence of one or several main peaks on the θ–2θ diffractograms (Figure 5) first indicates that all of the layers are crystalline after deposition at room temperature. The main features located at $2\theta \approx 30.3°$ and $2\theta \approx 35.3°$ match pretty well with the 222 and 400 reflections of In_2O_3 cubic-C phase (space group $Ia\bar{3}$) reported in JCPDS 71-2194, respectively. For Xe-deposited films, the presence of a weak 440 peak at $2\theta \approx 50.7°$ that remains unchanged over the whole deposition angle range is also evidenced. Depending on the deposition angle, different behaviors are observed. For $\alpha < 65°$, all of the films are mainly (111)-textured. At higher α angles, clear differences in the crystallographic orientation appear depending on the process ions. Although the (222) planes are preserved over the full α range in the case of Ar deposition, a progressive switching in the preferential growth planes from (222) to (400) is detected for Xe deposition as α increases. Since no additional peak was evidenced for the sample prepared with Ar at α = 85°, the intensity loss of the main 222 diffraction feature can be attributed to a misorientation of the (111) planes relative to the surface. Regarding the position of the peaks in Figure 5, we realized that the 222 reflection for the set of Xe samples presents a slight shift of about 0.2–0.3° toward smaller 2θ values compared to the pure In_2O_3 cubic-C phase ($2\theta \approx 30.6°$, according to JCPDS 71-2194). This effect may be ascribed to an increase of the lattice parameter due to the larger repulsive forces provided by the substitution of Sn^{4+} ions on the indium sites.[35,36] In the case of Ar depositions, the 222 reflection is broader and it presents a more pronounced shift relative to pure cubic-C In_2O_3 (around 1°). Nevertheless, the amplitude of this peak displacement cannot be fully explained by an increase of the Sn content.[36] This idea is also supported by EDX measurements showing that the Sn concentration remains almost constant in all of the films (Figure 4). Alternatively, we may expect that Ar deposition could lead to higher amounts of growth defects due to the so-called "atomic peening" effect, giving rise to large residual stresses as previously reported for Y_2O_3 thin films prepared by IBS.[34] Following this idea, the progressive reduction of the 222 peak shift when α increases (especially for Ar sputtering) would suggest a reduction in the amount of growth defects formed in the films and therefore a gain in their crystalline quality.

To apprehend these structural differences at a smaller scale, complementary TEM experiments have been conducted. Conventional bright-field images of ITO layers prepared at α = 50° point out that IBS deposition with Xe leads to a better crystallinity (larger grains, lesser amount of grain boundaries, and perturbed regions) than with Ar (Figure 6a,b). Moreover, in Figure 6a,b, two layers with different amounts of defects can actually be identified: a low defective layer at the bottom (thickness of roughly 50–100 nm in the case of Ar, about 400 nm in the case of Xe) and a more defective layer on top. This aspect will be confronted later to optical simulations reported in Optical Properties and Modeling and then discussed. The films deposited at higher angles follow similar trends in terms of crystallinity, as confirmed by the bright-field TEM images presented in Figure 6c,d for the growth at α = 85° (note here that the films are thinner than those shown previously since

DOI: 10.1021/acs.jpcc.9b02885
J. Phys. Chem. C 2019, 123, 14036–14046

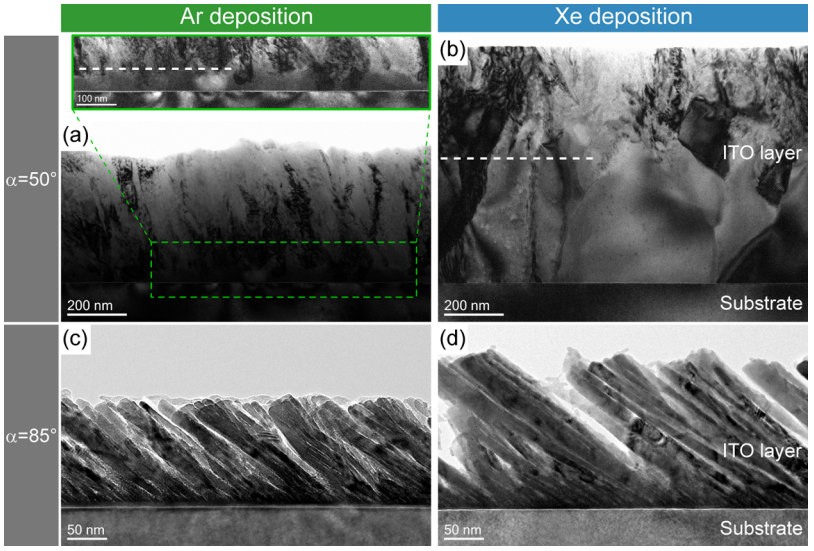

Figure 6. Bright-field TEM observations of ITO films prepared by Ar and Xe IBS at different angles. (a, b): Deposition at α = 50° (during 120 min). The inset in (a) shows a magnified and contrast-enhanced view of the substrate/film interfacial region. The dashed lines highlight the interfaces between two layers with different amounts of defects. Depositions at α = 85° during 40 min for Ar (c) and during 30 min for Xe (d).

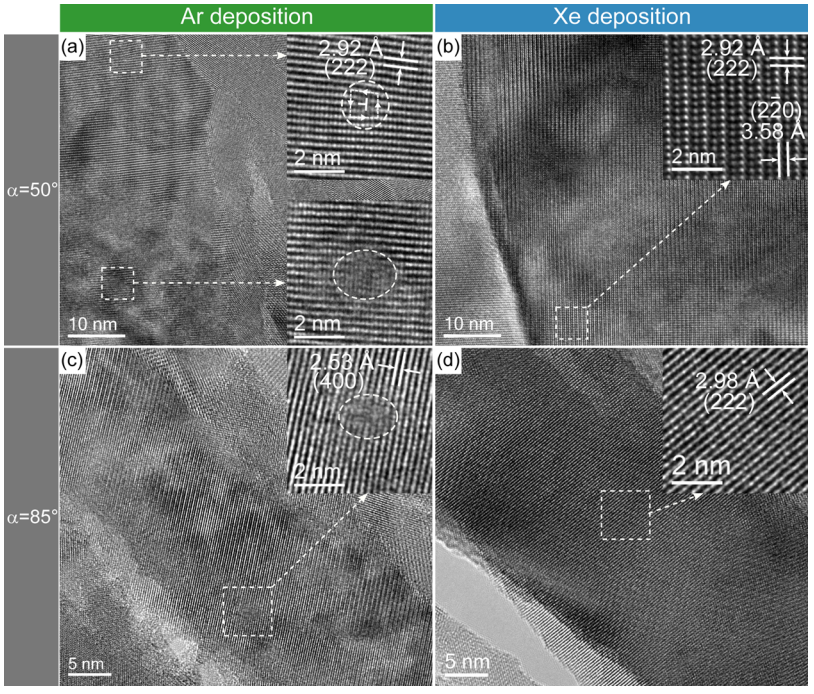

Figure 7. HRTEM images of the ITO films prepared by Ar and Xe IBS at different angles. (a, b): Deposition at α = 50°. (c, d): Deposition at α = 85°. The insets show magnified views of intragrain regions.

they were prepared with shorter deposition time: 40 min with Ar, 30 min with Xe).

The high-resolution TEM (HRTEM) images recorded in the top part of these films confirm the difference of crystallinity at the nanoscale. In the case of films deposited with Ar at low and high angles, small grains (<20 nm in size) and larger amount of grain boundaries are observed (Figure 7a–c). A close examination of the HRTEM images also evidenced the presence of intragrain extended defects (see closed dashed lines) that may be ascribable to dislocations (see, for example, the Burgers circuit in Figure 7a). On the contrary, Xe-deposited layers contain larger grains behaving as almost single-crystalline slanted nanorods at high deposition angle (Figure 7b–d). At the higher deposition angle, note that the nanocolumns prepared with Xe preferentially grow along the [111] crystal direction of ITO.

Optical Properties and Modeling. The reflectance spectra of the ITO films deposited on Si are shown in Figure 8, and several observations can be made. First, all spectra exhibit regular oscillations of the reflectance in the visible range (400–800 nm), as expected for a transparent thin film, which are limited on the UV side by a direct band gap absorption of ITO ($\lambda_g \approx$ 360 nm), and above a few microns by a free-carrier absorption. Second, increasing the deposition angle α results in an overall decrease of the reflectance in the visible range for both Ar- and Xe-deposited films. This effect is due to the

DOI: 10.1021/acs.jpcc.9b02885
J. Phys. Chem. C 2019, 123, 14036–14046

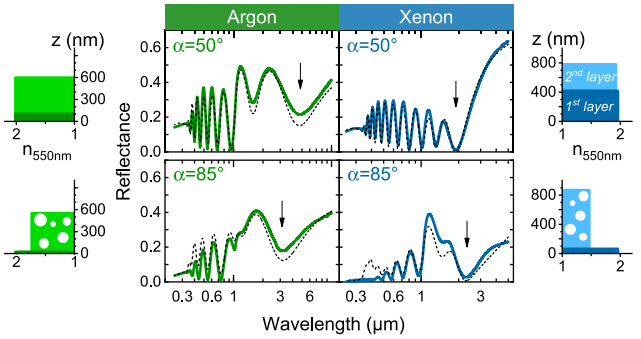

Figure 8. Reflectance measured (thick colored line) and simulated with the two-layer optical model (black dashed line) for Ar-deposited ITO (green, left) and for Xe-deposited ITO (blue, right) at an oblique angle α of 50 and 85°. The black arrow points out the onset of free-carrier-dominated reflectance. The corresponding optical model is represented near each curve, where the effective optical index n at λ = 550 nm, including the effect of porosity, is plotted versus the distance z to the substrate.

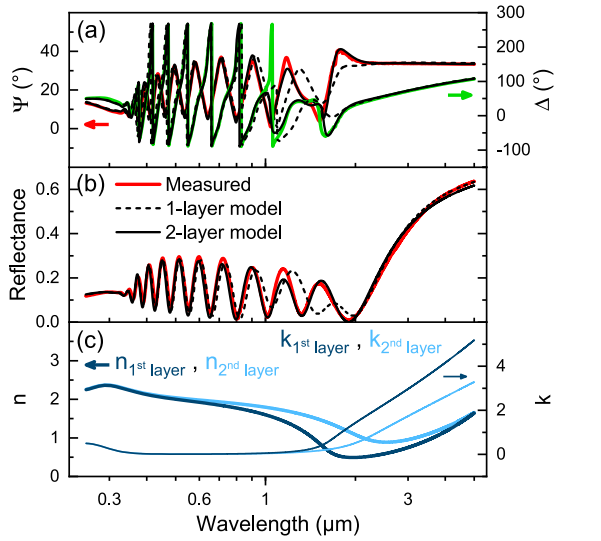

Figure 9. Optical properties of Xe-deposited film at α = 50°. (a) Ellipsometric angles Ψ (red, left axis) and Δ (green, right axis) measured at 70° incident angle. (b) Reflectance at normal incident angle (red). For both (a) and (b), the corresponding best fits using the two-layer optical model are shown as a dark continuous line. The best fits using a model with only one layer are also shown for comparison (dark dashed line). (c) Optical index n (thick line, left axis) and extinction coefficient k (thin line, right axis) for the first layer (dark colored) and the second layer (light colored) extracted from the two-layer optical model. Here, the second layer has no porosity and only the DO parameters differ between the two layers.

increasing proportion of porosity inside the film, reducing its effective optical index and thus providing an antireflective effect. Third, the onset of free-carrier absorption (see the vertical arrow in Figure 8) appears at a wavelength λ_{onset} around 4 μm for Ar- and 2 μm for Xe-deposited films, indicating a much smaller carrier density in the Ar case. When α increases, the λ_{onset} value decreases for Ar deposition, indicating a slight increase of carrier density, while it increases slightly for Xe, indicating a slight decrease of carrier density. Finally, strong and irregular oscillations in the reflectance spectra of all samples appear for λ ranging from roughly 1 to 3 μm. Such behavior is not expected for a thin transparent film with optical indexes varying smoothly with λ. This is instead a signature of a more complex layer stack as detailed thereafter.

To gain insight into the observed optical properties, a model has been developed and fitted onto our experimental data using the J. A. Woollam CompleteEASE software. All four measurements (UV−vis−NIR/IR SE and SR) were put together and fitted simultaneously with the very same optical model, providing a very robust uniqueness of the model-fit parameters hence extracted. The optical properties of ITO were reproduced using a three-oscillator model: (i) a Tauc−Lorentz oscillator (TLO) centered close to 3.5 eV ($\lambda_g \approx$ 360 nm) modeling the direct band gap absorption of ITO; (ii) a Gaussian oscillator (GO) arbitrarily centered out of the measurement range at 8 eV to model all UV interband transitions; and (iii) a Drude oscillator (DO) modeling the free-carrier optical behavior in the NIR range. The optical properties of the silicon substrate were modeled using the optical constants available in the J. A. Woollam database, which have been checked to show perfect agreement with one of our bare silicon substrates.

Different models were considered to simulate the optical properties of the ITO films. As a first attempt, a single-layer model including porosity was taken into consideration. However, despite this approach provides a very nice match to our experimental data in both the UV−vis and IR ranges, it was finally discarded since it systematically failed to reproduce them in the NIR range, close to the plasma frequency of the DO, as illustrated in Figure 9a,b. Other more complex models including porosity and/or carrier density gradients were also tested without further success. Finally, the best optical model chosen in this study comprise a 280 μm thick silicon substrate and the ITO film divided into two layers: the first layer at the bottom is always considered as dense, while porosity can be introduced in the second top layer in the framework of a Bruggeman effective medium approximation (BEMA). We emphasize here that only this two-layer optical model provided a good match with both the SE and SR data from the UV to the IR range (see Figure 9), being at the same time fully consistent with the SEM and TEM observations. Also note that this modeling further includes backside reflection on the substrate, surface roughness, and thickness inhomogeneity to account the real film morphologies.

The optical constants in the UV−vis range (TLO and GO parameters) were considered the same for both layers, and also kept constant regardless of the deposition angle α, for the sake of simplicity. Only the DO parameters (carrier density Ne and mobility μ) are thus allowed to differ between the two layers, to represent the strong contrast of the optical indexes between them in the 1−3 μm wavelength range. We further assumed that the properties of the first dense layer are not affected by the deposition angle α. The DO parameters of the first dense layer (carrier density Ne_1 and mobility μ_1) were also kept fixed to the ones of the first layer of the α = 50° sample for each sample batch (Ar or Xe), as under given deposition conditions, the dense layer is expected to have similar properties: Ne_1 (Ar) = 3.2 × 10^{20} $e^-\cdot cm^{-3}$ and μ_1 (Ar) = 7.0 $cm^2\cdot V^{-1}\cdot s^{-1}$; Ne_1 (Xe) = 6.0 × 10^{20} $e^-\cdot cm^{-3}$ and μ_1 (Xe) = 22.0 $cm^2\cdot V^{-1}\cdot s^{-1}$. As an example, Figure 9 presents the SE and SR measurements obtained for the Xe film deposited at α = 50° together with the corresponding modeling and the optical indexes (n, k) of the two layers.

The use of this optical model to fit the experimental optical measurements then allowed to extract simultaneously the

DOI: 10.1021/acs.jpcc.9b02885
J. Phys. Chem. C 2019, 123, 14036−14046

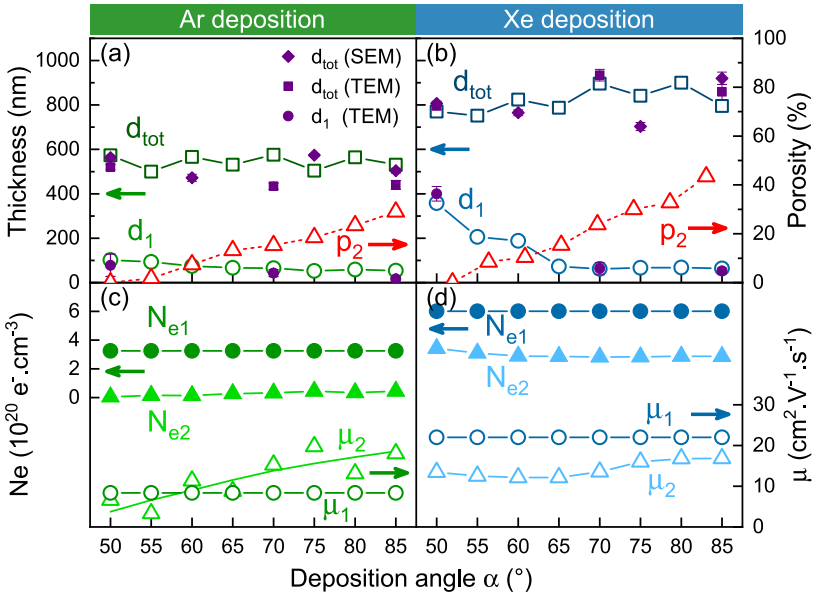

Figure 10. Parameters extracted from the fitting of the optical measurements using the two-layer model, for Ar- and Xe-deposited films, respectively. (a, b): Thickness of the first dense layer d_1 (open circles), total film thickness d_{tot} (open squares), and porosity p_2 of the second layer (open triangles). The thicknesses measured by SEM and TEM are also depicted in close symbols. (c, d): Carrier densities (Ne_1 and Ne_2 in close symbols) and mobilities (μ_1 and μ_2 in open symbols) of the two layers from DO.

thicknesses d_1 and d_2 of the two layers, as well as the porosity p_2 and the DO parameters Ne_2 and μ_2 of the second layer. In Figure 8, the simulated reflectance (dashed line) is shown together with the measured one (full line) for selected samples. The resulting thicknesses and optical indexes at λ = 550 nm of the two layers are also schemed nearby. The relevant fit parameters extracted from the two-layer optical model are displayed in Figure 10. We can note that despite some discrepancies ascribable to thickness nonuniformity are visible, the total film thickness $d_{tot} = d_1 + d_2$ extracted for the optical model shows an overall good agreement with SEM- and TEM-based measurements. In addition, the thickness d_1 of the first layer matches with the one measured by SEM or TEM over the full deposition angle range. This important point confirms that the two-layer optical model is suitable and physically meaningful to describe the optical properties of the OAD-IBS ITO films, and to extract other critical parameters such as the porosity, the refractive index, and the carrier density.

Regarding the porosity p_2 of the second layer, a sharp and almost linear increase is observed with α for both sample batches, from p_2 = 0 for α = 50° up to about 29% for Ar and 43% for Xe for α = 85°. This actually points out that depositions with Xe provide much more porous ITO coatings than with Ar, which is confirmed by the SEM and STEM-HAADF observations in Figures 1 and 2. The increase of porosity with the deposition angle has been commonly observed in the literature for OAD electron-beam-evaporated ITO.[23−25] Nevertheless, it must be mentioned that our IBS-deposited films are denser, since electron-beam evaporation of ITO at α = 85° leads, for example, to porosities as high as 85% according to ref 23. As a consequence, a simple model based only on geometrical arguments related to the shadowing effect, as proposed by Poxson et al.,[23] cannot be applied to predict the porosity evolution versus α of our IBS ITO films.

The fact that the second layer is not porous for α = 50° (p_2 = 0) agrees with the bright-field TEM images (Figure 6) since both Ar- and Xe-deposited films can actually be divided into two layers of different crystallinities. This is consistent with the larger carrier densities extracted in the bottom, less defective region of the films ($Ne_1 = 3.2 \times 10^{20}$ e$^-$·cm^{-3} against $Ne_2 \approx 0.5 \times 10^{19}$ e$^-$·cm^{-3} for Ar deposition, $Ne_1 = 6.0 \times 10^{20}$ e$^-$·cm^{-3} against $Ne_2 \approx 3.4 \times 10^{20}$ e$^-$·cm^{-3} for Xe deposition; see Figure 10c,d), since higher crystallinity is known to increase the number of free electrons in ITO.[37,38] Furthermore, this relationship between crystallinity and Ne is supported by the larger carrier concentrations extracted in the less defective Xe-deposited films (as compared to Ar-deposited films). Note that the bottom layer of the films prepared with Xe, almost defect-free and made of large grains, exhibits a carrier density ($Ne_1 = 6.0 \times 10^{20}$ e$^-$·cm^{-3}) similar to that of the optimal In_2O_3:SnO_2 alloy (90:10% wt) around 14×10^{20} e$^-$·cm^{-3}.[39] Upon increasing the deposition angle α, the first layer becomes thinner and thinner for both Ar and Xe. Nevertheless, it does not totally disappear even at α = 85° (d_1 = 54 nm for Ar, d_1 = 64 nm for Xe), as confirmed by TEM. Surprisingly, the carrier density Ne_2 shows a small increase with α for Ar, whereas it slightly decreases for Xe. This behavior could be linked to an improved crystallinity of Ar films with α, which can be inferred from XRD data (Figure 4), as mentioned previously in the section Structure. Regarding the mobility μ_2 in the second layer, it appears to be almost constant with α for Xe films (μ_2 (Xe) ≈ 15 cm^2·V^{-1}·s^{-1}) and slightly lower than μ_1 (Xe) = 22 cm^2·V^{-1}·s^{-1}. For Ar films, this parameter increases smoothly with α, from μ_2 (Ar, α = 50°) = 6 cm^2·V^{-1}·s^{-1} to μ_2 (Ar, α = 85°) = 15 cm^2·V^{-1}·s^{-1}. These values, related to the free-carrier mobility inside the grains, thus indicate a lower mobility for the Ar films, which may be linked to the poorer crystallinity evidenced by TEM. However, in contrast to the carrier densities Ne_1 and Ne_2, which are very robust fitting parameters, the mobilities present a much higher sensitivity to the slight variations of the fit procedure, with estimated uncertainties of ±5 cm^2·V^{-1}·s^{-1}. Therefore, their absolute values as well as their variations should not be overinterpreted. It is to be mentioned that the present two-layer optical model is fully

DOI: 10.1021/acs.jpcc.9b02885
J. Phys. Chem. C 2019, 123, 14036−14046

isotropic. The anisotropy stemming from the inclined columns yields a birefringent behavior.[40] This should be further addressed in the framework of generalized ellipsometry, which will be the goal of a future work.

Discussion about the Nanostructural and Electro-Optical Differences in ITO Films. As shown throughout this paper, the nanostructure and the electro-optical properties of the ITO films deposited by IBS at oblique angles exhibit a strong dependence on the growth conditions and particularly on the nature of the sputtering ions. As a general trend, Xe-deposited ITO films are thicker and present larger amounts of porosity, a better crystallinity (bigger grains, and lesser grain boundaries and intragrain defects), and superior carrier densities and mobilities compared to Ar-deposited films prepared in very similar conditions. A better understanding about the origin of these films specificities can be addressed from Monte-Carlo simulations to gain further information related to the basic mechanisms involved during the sputtering process, in particular on the effect of the mass of primary ions. For that purpose, the Stopping and Range of Ions in Matter (SRIM) package[41] was used to reproduce the IBS experimental conditions. The main results of these calculations shown in Table 1 (see caption for more details) indicate that the type of primary ions has a limited influence on the sputtering yields and energies (some tens of eV) of the sputtered atoms, but on the contrary, this parameter has a strong effect on the energy and amount of ions that are reflected on the target. It appears clearly that ions with lower mass, such as Ar, are significantly more subjected to backscattering on the target (17%) and are also more energetic (hundreds of eV) than heavier ions like Xe. Therefore, Ar ions are more prone to amplify the "atomic peening" effect and induce an "intrinsic" ion assist during IBS deposition. These Ar particles impinging on the growing films can therefore give rise to the sputtering of the material coating, resulting in a decrease of the effective growth rate.[33] They may also enhance the surface diffusion[42] resulting in less porosity due to the broadening of the nanocolumns,[43] consistent with the experiments. Finally, Ar species reflected on the target are more susceptible to be trapped into the growing films and to generate knock-on events that can create disorder into the crystal lattice. This latter point also agrees with our experiments since the incorporation of rare gas into the films and the formation of more defective layers have been evidenced when Ar was employed as primary ion. These considerations could explain why *Ne* and μ values are substantially smaller in Ar-IBS films. Indeed, when the structure is highly disordered, as in the case of Ar deposition, Sn may not be effective as a dopant[44] and scattering by neutral impurities may become dominant.[45,46] Inherent ion assistance due to backscattered ions is also expected to play a major role in the evolution of the structure, composition, and properties observed with the deposition angle. The higher energies involved during Ar deposition could, for example, explain why the crystal orientation along the denser (111) planes does not follow the flux of incident particles, as generally expected.[47] At low α, the strong oxygen deficiency of the ITO film prepared with Ar could be ascribed to a preferential resputtering of oxygen atoms at the surface of the growing film since the energies of backscattered Ar largely exceed the formation energies of oxygen vacancies in ITO (about 23−24 eV in In_2O_3 and SnO_2 according to ref 48). Since the atmosphere was kept in similar conditions for all of the depositions, the progressive rise of oxygen content and the strain relaxation (see 222 peak position in Figure 5) observed when α increases could be attributed to an enhancement of the geometric shadowing effect that may prevent efficiently the irradiation of neighboring areas, as commonly reported for surface nano-patterning processes using ion beams.[49,50] The decrease of the Ar content observed at the same time is strengthening this idea. A reduction in the number of backscattered ions captured at the substrate surface, directly linked to the projected surface and following a cosine law,[51] could also explain this Ar content decrease. In the case of Xe deposition, this shadowing effect should be more limited since the nanocolumns appear more separated, which was confirmed by the almost constant composition and interplanar (222) distances observed in these films for different deposition angles. Finally, the differences in the bombardment promoted by reflected ions could explain the development of preferred [111] orientation in the films even at high deposition angles for Ar films.

Table 1. Extracted Data from SRIM Calculations[a]

	Ar	Xe
amount of backscattered ions (%)	17	7
sputtering yield of In (atoms/ion)	2.4	2.5
sputtering yield of Sn (atoms/ion)	0.2	0.2
sputtering yield of O (atoms/ion)	3.9	4.1
mean energy of backscattered ions (eV)	218	46
mean energy of In atoms (eV)	23	15
mean energy of Sn atoms (eV)	27	17
mean energy of O atoms (eV)	17	12

[a]Input parameters: 500 000 Ar or Xe ions accelerated at 1.2 keV onto an In:Sn:O target (relative composition of 36:4:60 at %; density, 7.14 $g{\cdot}cm^{-3}$) with an incident angle of 45°.

CONCLUSIONS

In this work, the fabrication of porous tin-doped indium oxide thin films at room temperature has been explored for the very first time using ion beam sputtering deposition at oblique angles and relying on the use of different and complementary characterization techniques at different scales. To go deeper into the understanding of these systems, an original two-layer optical model taking into account the nonconventional films nanostructure has been proposed to reproduce the optical measurements and to evaluate locally some features not easily accessible by other techniques, including porosity, refractive indexes, as well as in-grain carrier densities and mobilities. Actually, it was shown that the studied films must be decomposed into two layers with different electro-optical properties, which is attributed to the shadowing as well as to the presence of growth defects and impurities due to the atomic peening. This singular approach has been crucial to evidence the relationships existing between the deposition parameters, the nanostructure and electro-optical properties of the ITO films. This work indicates that combining IBS and OAD is relevant to deposit crystalline ITO films with controlled porosities directly at room temperature. During this process, both the ion species used to sputter the target and the deposition angle have a strong impact on the structure, composition, and electro-optical properties of these films. In particular, it appears that the intrinsic ion assistance promoted by the bombardment of high-energy backscattered particles can be modulated by changing the mass of primary ions (Ar or Xe) and by playing on the geometric shadowing at the film

DOI: 10.1021/acs.jpcc.9b02885
J. Phys. Chem. C 2019, 123, 14036−14046

surface through the control of the deposition angle. The appropriate choice of these two parameters enables the fine-tuning of the ITO film porosity, structure (grain size, amount of defects, preferred crystallographic orientation), and properties (optical reflectivity, in-grain electrical transport), with great interests to cover a variety of technological needs. For transparent and conductive optical applications that would require a good compromise between broad-band antireflective capabilities over the extended visible range and electrical transport, deposition with Xe must clearly be preferred to Ar. Indeed, Xe IBS-OAD allows preparing ITO films covering a wider range of porosity levels (from about 0 to 43% for deposition angles between 50 and 85°), which offer more flexibility in the design of broad-band low-reflectivity surfaces. It also provides layers with better crystalline quality that permit to achieve superior carrier density and mobilities. In the near future, the electro-optical properties of these films will be scrutinized through in situ thermal annealing experiments that will combine temperature-dependent ellipsometry and anisotropic temperature-dependent Hall measurements. The anisotropic optical properties of the OAD films, investigated in the framework of generalized ellipsometry, could also give us further insight into the microstructure of our films, including the shape of the inclined nanocolumns and porosities. These approaches will be essential to elucidate the changes in scattering mechanisms ascribable to in-grain and grain boundaries as a function of the deposition conditions, as well as to find optimization paths in view of implementing these promising IBS-OAD ITO coatings in future transparent and conductive optics.

■ ASSOCIATED CONTENT

Supporting Information

The Supporting Information is available free of charge on the ACS Publications website at DOI: 10.1021/acs.jpcc.9b02885.

STEM-EDX analyses of ITO thin films: elemental mapping and composition extraction (PDF)

■ AUTHOR INFORMATION

Corresponding Authors

*E-mail: bertrand.lacroix@uca.es (B.L.).

*E-mail: fabien.paumier@univ-poitiers.fr (F.P.).

ORCID

B. Lacroix: 0000-0001-7916-6377

A. J. Santos: 0000-0003-3776-7080

F. M. Morales: 0000-0002-8341-2478

Present Address

⊥Helmholtz-Zentrum Berlin für Materialien und Energie, 14109 Berlin, Germany (F.M.).

Author Contributions

The manuscript was written through contributions of all authors. All authors have given approval to the final version of the manuscript.

Notes

The authors declare no competing financial interest.

■ ACKNOWLEDGMENTS

This work was partially supported by the French "Nouvelle Aquitaine" Region and by European Structural and Investment Funds (ERDF reference P-2016-BAFE-209): IMATOP project. The "Talent Attraction Program" of the University of Cádiz is acknowledged for supporting B. Lacroix contract code E-11-2017-0117214. A. J. Santos also acknowledges the financial support of the IMEYMAT Institute as well as the Ministerio de Ciencia, Innovación y Universidades and Ministerio de Educación y Formación Profesional in Spain for the concessions of grants (ICARO-173873 and FPU16-04386).

■ REFERENCES

(1) Liu, H.; Avrutin, V.; Izyumskaya, N.; Özgür, Ü.; Morkoç, H. Transparent Conducting Oxides for Electrode Applications in Light Emitting and Absorbing Devices. *Superlattices Microstruct.* **2010**, *48*, 458−484.

(2) Fortunato, E.; Ginley, D.; Hosono, H.; Paine, D. C. Transparent Conducting Oxides for Photovoltaics. *MRS Bull.* **2007**, *32*, 242−247.

(3) Minami, T. Transparent Conducting Oxide Semiconductors for Transparent Electrodes. *Semicond. Sci. Technol.* **2005**, *20*, S35−44.

(4) Lewis, B. G.; Paine, D. C. Applications and Processing of Transparent Conducting Oxides. *MRS Bull.* **2000**, *25*, 22−27.

(5) Dawar, A. L.; Joshi, J. C. Semiconducting Transparent Thin-Films: Their Properties and Applications. *J. Mater. Sci.* **1984**, *19*, 1−23.

(6) Gordon, R. G. Criteria for Choosing Transparent Conductors. *MRS Bull.* **2000**, *25*, 52−57.

(7) Coutts, T. J.; Young, D. L.; Li, X. Characterization of Transparent Conducting Oxides. *MRS Bull.* **2000**, *25*, 58−65.

(8) Moroni, M.; Lupo, E.; Marra, E.; Cenedese, A. Hyperspectral Image Analysis in Environmental Monitoring: Setup of a New Tunable Filter Platform. *Procedia Environ. Sci.* **2013**, *19*, 885−894.

(9) Gomez, R. B. Hyperspectral Imaging: A Useful Technology for Transportation Analysis. *Opt. Eng.* **2002**, *41*, 2137−2143.

(10) Yuen, P. W. T.; Richardson, M. An Introduction to Hyperspectral Imaging and Its Application for Security, Surveillance and Target Acquisition. *Imaging Sci. J.* **2010**, *58*, 241−253.

(11) Hass, G.; Heaney, J. B.; Toft, A. R. Transparent Electrically Conducting Thin Films for Spacecraft Temperature Control Applications. *Appl. Opt.* **1979**, *18*, 1488−1489.

(12) Ginley, D. S.; Hosono, H.; Paine, D. C. *Handbook of Transparent Conductors*; Springer Science + Business Media: New York, 2010.

(13) Ellmer, K.; Mientus, R. Carrier Transport in Polycrystalline ITO and ZnO:Al II: The Influence of Grain Barriers and Boundaries. *Thin Solid Films* **2008**, *516*, 5829−5835.

(14) Hamberg, I.; Granqvist, C. G. Evaporated Sn-Doped In_2O_3 Films: Basic Optical Properties and Applications to Energy-Efficient Windows. *J. Appl. Phys.* **1986**, *60*, R123−R159.

(15) Ray, S.; Banerjee, R.; Basu, N.; Batabyal, A. K.; Barua, A. K. Properties of Tin Doped Indium Oxide Thin Films Prepared by Magnetron Sputtering. *J. Appl. Phys.* **1983**, *54*, 3497−3501.

(16) Shigesato, Y.; Takaki, S.; Haranou, T. Crystallinity and Electrical Properties of Tin-Doped Indium Oxide Films Deposited by DC Magnetron Sputtering. *Appl. Surf. Sci.* **1991**, *48*−*49*, 269−275.

(17) Kim, H.; Gilmore, C. M.; Piqué, A.; Horwitz, J. S.; Mattoussi, H.; Murata, H.; Kafafi, Z. H.; Chrisey, D. B. Electrical, Optical, and Structural Properties of Indium Tin Oxide Thin Films for Organic Light-Emitting Devices. *J. Appl. Phys.* **1999**, *86*, 6451−6461.

(18) Kim, D.; Han, Y.; Cho, J.-S.; Koh, S.-K. Low Temperature Deposition of ITO Thin Films by Ion Beam Sputtering. *Thin Solid Films* **2000**, *377*−*378*, 81−86.

(19) Han, Y.; Kim, D.; Cho, J.-S.; Koh, S.-K.; Song, Y. S. Tin-Doped Indium Oxide (ITO) Film Deposition by Ion Beam Sputtering. *Sol. Energy Mater. Sol. Cells* **2001**, *65*, 211−218.

(20) Hawkeye, M. M.; Brett, M. J. Glancing Angle Deposition: Fabrication, Properties, and Applications of Micro- and Nanostructured Thin Films. *J. Vac. Sci. Technol., A* **2007**, *25*, 1317−1335.

(21) Barranco, A.; Borras, A.; Gonzalez-Elipe, A. R.; Palmero, A. Perspectives on Oblique Angle Deposition of Thin Films: From Fundamentals to Devices. *Prog. Mater. Sci.* **2016**, *76*, 59−153.

(22) Xi, J. Q.; Schubert, M. F.; Kim, J. K.; Schubert, E. F.; Chen, M.; Lin, S. Y.; Liu, W.; Smart, J. A. Optical Thin-Film Materials with Low Refractive Index for Broadband Elimination of Fresnel Reflection. *Nat. Photonics* **2007**, *1*, 176−179.
(23) Poxson, D. J.; Mont, F. W.; Schubert, M. F.; Kim, J. K.; Schubert, E. F. Quantification of Porosity and Deposition Rate of Nanoporous Films Grown by Oblique-Angle Deposition. *Appl. Phys. Lett.* **2008**, *93*, No. 101914.
(24) Zhong, Y.; Shin, Y. C.; Kim, C. M.; Lee, B. G.; Kim, E. H.; Park, Y. J.; Sobahan, K. M. A.; Hwangbo, C. K.; Lee, Y. P.; Kim, T. G. Optical and Electrical Properties of Indium Tin Oxide Thin Films with Tilted and Spiral Microstructures Prepared by Oblique Angle Deposition. *J. Mater. Res.* **2008**, *23*, 2500−2505.
(25) Leem, J. W.; Yu, J. S. Glancing Angle Deposited ITO Films for Efficiency Enhancement of a-Si:H/μc-Si:H Tandem Thin Film Solar Cells. *Opt. Express* **2011**, *19*, A258−A268.
(26) Yang, C.-S.; Chang, C.-M.; Chen, P.-H.; Yu, P.; Pan, C.-L. Broadband Terahertz Conductivity and Optical Transmission of Indium-Tin-Oxide (ITO) Nanomaterials. *Opt. Express* **2013**, *21*, 16670−16682.
(27) Leem, J. W.; Yu, J. S. Influence of Oblique-Angle Sputtered Transparent Conducting Oxides on Performance of Si-Based Thin Film Solar Cells. *Phys. Status Solidi A* **2011**, *208*, 2220−2225.
(28) Yao, Y.-C.; Tsai, M.-T.; Hsu, H.-C.; She, L.-W.; Cheng, C.-M.; Chen, Y.-C.; Wu, C.-J.; Lee, Y.-J. Use of Two-Dimensional Nanorod Arrays with Slanted ITO Film to Enhance Optical Absorption for Photovoltaic Applications. *Opt. Express* **2012**, *20*, 3479−3489.
(29) Nieuwenhuizen, M. J.; Haanstra, H. B. Microfractography of Thin Films. *Philips Tech. Rev.* **1966**, *27*, 87−91.
(30) Tait, R. N.; Smy, T.; Brett, M. J. Modelling and Characterization of Columnar Growth in Evaporated Films. *Thin Solid Films* **1993**, *226*, 196−201.
(31) Lichter, S.; Chen, J. Model for Columnar Microstructure of Thin Solid Films. *Phys. Rev. Lett.* **1986**, *56*, 1396−1399.
(32) Alvarez, R.; Lopez-Santos, C.; Parra-Barranco, J.; Rico, V.; Barranco, A.; Cotrino, J.; Gonzalez-Elipe, A. R.; Palmero, A. Nanocolumnar Growth of Thin Films Deposited at Oblique Angles: Beyond the Tangent Rule. *J. Vac. Sci. Technol., B: Nanotechnol. Microelectron.: Mater., Process., Meas., Phenom.* **2014**, *32*, No. 041802.
(33) Meyer, F.; Louchier, D.; Stambouli, V.; Pellet, C.; Schwebel, C.; Gautherin, G. Ion Beam Sputtering Deposition of Tungsten: Energy and Mass Effects of Primary Ions. *Appl. Surf. Sci.* **1989**, *38*, 286−294.
(34) Lacroix, B.; Paumier, F.; Gaboriaud, R. J. Crystal Defects and Related Stress in Y_2O_3 Thin Films: Origin, Modeling, and Consequence on the Stability of the C-Type Structure. *Phys. Rev. B* **2011**, *84*, No. 014104.
(35) González, G. B.; Cohen, J. B.; Hwang, J. H.; Mason, T. O.; Hodges, J. P.; Jorgensen, J. D. Neutron Diffraction Study on the Defect Structure of Indium-Tin-Oxide. *J. Appl. Phys.* **2001**, *89*, 2550−2555.
(36) Thirumoorthi, M.; Thomas Joseph Prakash, J. Structure, Optical and Electrical Properties of Indium Tin Oxide Ultra Thin Films Prepared by Jet Nebulizer Spray Pyrolysis Technique. *J. Asian Ceram. Soc.* **2016**, *4*, 124−132.
(37) Jung, Y. S. A Spectroscopic Ellipsometry Study on the Variation of the Optical Constants of Tin-Doped Indium Oxide Thin Films during Crystallization. *Solid State Commun.* **2004**, *129*, 491−495.
(38) Tuna, O.; Selamet, Y.; Aygun, G.; Ozyuzer, L. High Quality ITO Thin Films Grown by Dc and RF Sputtering without Oxygen. *J. Phys. D. Appl. Phys.* **2010**, *43*, No. 055402.
(39) Nadaud, N.; Lequeux, N.; Nanot, M.; Jové, J.; Roisnel, T. Structural Studies of Tin-Doped Indium Oxide (ITO) and $In_4Sn_3O_{12}$. *J. Solid State Chem.* **1998**, *135*, 140−148.
(40) Harris, K. D.; Van Popta, A. C.; Sit, J. C.; Broer, D. J.; Brett, M. J. A Birefringent and Transparent Electrical Conductor. *Adv. Funct. Mater.* **2008**, *18*, 2147−2153.
(41) Ziegler, J. F.; Ziegler, M. D.; Biersack, J. P. SRIM - The Stopping and Range of Ions in Matter. *Nucl. Instrum. Methods Phys. Res., Sect. B* **2010**, *268*, 1818−1823.
(42) Makeev, M. A.; Barabási, A.-L. Ion-Induced Effective Surface Diffusion in Ion Sputtering. *Appl. Phys. Lett.* **1997**, *71*, 2800−2802.
(43) Vick, D.; Friedrich, L. J.; Dew, S. K.; Brett, M. J.; Robbie, K.; Seto, M.; Smy, T. Self-Shadowing and Surface Diffusion Effects in Obliquely Deposited Thin Films. *Thin Solid Films* **1999**, *339*, 88−94.
(44) Gessert, T. A.; Williamson, D. L.; Coutts, T. J.; Nelson, A. J.; Jones, K. M.; Dhere, R. G.; Aharoni, H.; Zurcher, P. The Dependence of the Electrical Properties of Ion Beam Sputtered Indium Tin Oxide on Its Composition and Structure. *J. Vac. Sci. Technol., A* **1987**, *5*, 1314−1315.
(45) Shigesato, Y.; Paine, D. C.; Haynes, T. E. Study of the Effect of Ion Implantation on the Electrical and Microstructural Properties of Tin-Doped Indium Oxide Thin Films. *J. Appl. Phys.* **1993**, *73*, 3805−3811.
(46) Mergel, D.; Qiao, Z. Correlation of Lattice Distortion with Optical and Electrical Properties of In_2O_3:Sn Films. *J. Appl. Phys.* **2004**, *95*, 5608−5615.
(47) Ensinger, W. Growth of Thin Films with Preferential Crystallographic Orientation by Ion Bombardment during Deposition. *Surf. Coatings Technol.* **1994**, *65*, 90−105.
(48) Hou, Q.; Buckeridge, J.; Lazauskas, T.; Mora-Fonz, D.; Sokol, A. A.; Woodley, S. M.; Catlow, C. R. A. Defect Formation in In_2O_3 and SnO_2: A New Atomistic Approach Based on Accurate Lattice Energies. *J. Mater. Chem. C* **2018**, *6*, 12386−12395.
(49) Chini, T. K.; Datta, D. P.; Bhattacharyya, S. R. Ripple Formation on Silicon by Medium Energy Ion Bombardment. *J. Phys. Condens. Matter* **2009**, *21*, No. 224004.
(50) Kumar, M.; Datta, D. P.; Basu, T.; Garg, S. K.; Hofsäss, H.; Som, T. Temporal Evolution on SiO_2 Surface under Low Energy Ar^+-Ion Bombardment: Roles of Sputtering, Mass Redistribution, and Shadowing. *J. Phys. Condens. Matter* **2018**, *30*, No. 334001.
(51) Siad, A.; Besnard, A.; Nouveau, C.; Jacquet, P. Critical Angles in DC Magnetron Glad Thin Films. *Vacuum* **2016**, *131*, 305−311.

DOI: 10.1021/acs.jpcc.9b02885
J. Phys. Chem. C 2019, 123, 14036−14046

Publication VI

Porosity control for plasma-assisted molecular beam epitaxy of GaN nanowires

V. J. Gómez, A. J. Santos, E. Blanco, B. Lacroix, R. García,

D. L. Huffaker, F. M. Morales

Crystal Growth and Design 19 (2019) 2461-2469

CRYSTAL GROWTH & DESIGN

Article

Cite This: Cryst. Growth Des. 2019, 19, 2461−2469

pubs.acs.org/crystal

Porosity Control for Plasma-Assisted Molecular Beam Epitaxy of GaN Nanowires

Víctor J. Gómez,*[,†,#] Antonio J. Santos,[‡,§] Eduardo Blanco,[‡,∥] Bertrand Lacroix,[‡,§] Rafael García,[‡,§] Diana L. Huffaker,[†,⊥] and Francisco M. Morales[‡,§]

[†]School of Engineering, Cardiff University, CF24 3AA, Cardiff, United Kingdom

[‡]IMEYMAT: Institute of Research on Electron Microscopy and Materials, University of Cádiz, 11510 Puerto Real, Cádiz, Spain

[§]Department of Materials Science and Metallurgic Engineering, and Inorganic Chemistry, Faculty of Sciences, University of Cádiz, 11510 Puerto Real, Cádiz, Spain

[∥]Department of Condensed Matter Physics, Faculty of Sciences, University of Cádiz, 11510 Puerto Real, Cádiz Spain

[⊥]School of Physics and Astronomy, Cardiff University, CF24 3AA, Cardiff, United Kingdom

Supporting Information

ABSTRACT: We report on the bottom-up fabrication, by plasma-assisted molecular beam epitaxy, of monocrystalline GaN solid, hollow, and c-shape nanowires deposited in a compact fashion. The shape exhibited by these nanostructures varies from solid to c-shape and hollow nanowires. They were epitaxially grown with their [0001] directions perpendicular with respect to different surfaces of Si substrates. Advanced studies of these GaN nanostructures were carried out by means of selected-area electron diffraction and scanning and high-resolution transmission electron microscopy evidencing their structure and epitaxial alignments with respect to the silicon. Through a comprehensive analysis of the growth conditions (substrate temperature and Ga and N* fluxes) we demonstrate that a local Ga-limited regime is the mechanism behind the particular shape of these nanostructures. Additionally, spectroscopic ellipsometry studies, applying a model based on Bruggeman effective medium approximations and taking into account several aspects related to the nature of these GaN nanostructures, were carried out to obtain valuable information about the evolution of the optical constants and the porosity along the layer. This work shows a way to control the porosity and shape of GaN nanowires by varying the growth conditions, which could open new horizons in the development of GaN nanostructures for future applications.

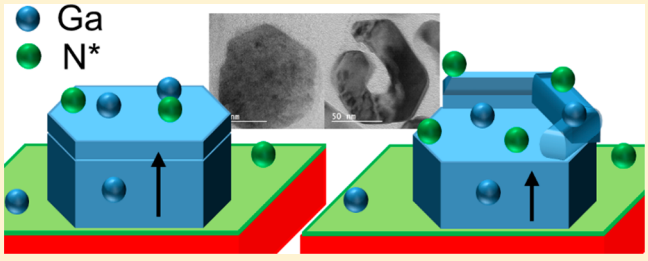

INTRODUCTION

Research on GaN nanostructures, such as nanowires (NWs) and nanoporous films (NPFs), has attracted substantial interest thanks to their high surface-to-volume ratio, and, in case of NWs, their strain-free nature.[1] The attractiveness of GaN NPFs resides in their significant strain relaxation[2,3] and enhanced surface Raman scattering.[4] Comparing with their compact counterparts, GaN NPFs have demonstrated improved properties in diverse applications such as photoelectrochemical water splitting,[5−7] supercapacitors for energy storage,[8,9] light emitting diodes (LEDs),[2,3,10−13] distributed Bragg reflectors,[11] or mechanic removal of films from the substrate.[14,15] The research on NPFs is not limited to GaN: different materials such as nanoporous InGaN,[16−19] Si,[20] carbon membranes,[21] and WO_3[22] have demonstrated a great potential for photoelectrochemical water splitting[18,20,21] and photocatalytic fuel cells.[22]

A vast majority of reports on the synthesis of NPFs are focused on different kind of etching of thin films or GaN−sapphire templates such as electroless etching,[3,4] electrochemical etching,[6,10,17] or high-temperature annealing.[8,9] The fabrication of ordered NPFs has been demonstrated using inductively coupled plasma (ICP) etching with an anodic alumina template as etching mask.[23] However, to the best of our knowledge very few reports on the growth of GaN NPFs can be found. Recently, Aguilo and co-workers reported the growth of GaN NPFs by chemical vapor deposition[13] and its application on LEDs. The main drawbacks of the etching (top-down) approach are the difficulties of controlling the porosity level and shapes on the films. Therefore, a way to produce high-quality NPFs in a bottom-up approach with direct control over the composition, porosity, and shape as well as low-cost routes to scale it to large areas for industrial transfer would be highly desirable.

In this Article, we present the growth of high-quality single crystalline GaN self-assembled NWs by plasma-assisted molecular beam epitaxy (MBE). GaN nanostructures were synthesized in a closed-packed manner that emulates the

Received: January 30, 2019
Revised: March 7, 2019
Published: March 15, 2019

DOI: 10.1021/acs.cgd.9b00146
Cryst. Growth Des. 2019, 19, 2461−2469

behavior of a NPF, combining the advantages offered by GaN NWs with the technological attractiveness of NPFs. The shape of the grown nanostructures varies from solid (SNW) to c-shape (CNW) and hollow (HNW) nanowires. By means of transmission electron microscopy (TEM) we show that wurtzite GaN S-, C- and H-NWs are grown along the [0001] direction, and epitaxially aligned with the underlying Si substrate. We demonstrate that a Ga-limited growth regime at the tips of the nanostructures is the mechanism behind their particular shapes. Consequently, we show control over the amount of porosity by tuning of the growth conditions. The porosity level is assessed through a comprehensive analysis of their optical properties by means of spectroscopic ellipsometry (SE).

EXPERIMENTAL SECTION

All studied samples were grown on chemically cleaned p-type Si(111) or (100) substrates in a Veeco Gen930 molecular beam epitaxy (MBE) reactor equipped with a radiofrequency nitrogen plasma source and a sumo Knudsen effusion cell for Ga. The substrates employed were (111) ± 0.5° and (001) ± 0.5° oriented, single side polished, and prime grade manufactured by Sil'Tronix. Before transferring into the growth chamber, the substrates were outgassed at 250 °C during 12 h. Prior to growth, the Si substrates were heated in the growth chamber to 900 °C for 30 min in order to remove the native oxide. The temperature was then slowly decreased (5 °C/min) until a clear 7 × 7 surface reconstruction was observed (860 °C) at the reflection high-energy electron diffraction (RHEED) pattern.[24] Then, the substrates were intentionally nitridated by exposing the surface to active nitrogen at 860 °C during 10 min under $\phi_{N^*} = 14 \times 10^{14} \frac{at}{cm^2\ s}$ generating a 2 nm-thick β-Si_3N_4 layer (Figure S1, Supporting Information). The growth conditions for the samples can be found in Table 1.

Table 1. Growth Conditions for the Samples Referred in This Study

	impinging fluxes ($\times 10^{14}$ at/cm^2 s^1)			
sample	Ga	N*	T_{subs} (°C)	substrate
T1	8	11	800	Si(111)
T2	8	11	825	Si(111)
T2′	8	11	825	Si(100)
T3	8	11	850	Si(111)
G1	4	11	825	Si(111)
G3	10	11	825	Si(111)
N1	11	11	850	Si(111)
N2	11	14	850	Si(111)
N3	11	19	850	Si(111)
N4	11	22	850	Si(111)
N5	11	27	850	Si(111)

The surface morphology and sample thickness were assessed by means of scanning electron microscopy (SEM) using a Zeiss Gemini 1540XB SEM microscope. For the transmission electron microscopy (TEM) analyses, the samples were prepared in cross-sectional (XTEM) and plan-view (PVTEM) orientations and thinned to electron transparency by tripod mechanical polishing followed by Ar^+ ion milling at 3.5 keV, ±7° incidence with a PIPS system from GATAN. The high-resolution TEM (HRTEM) and selected area electron diffraction (SAED) results were collected in a JEOL 2100 microscope equipped with a LaB_6 filament at an electron accelerating voltage of 200 kV. The energy dispersive X-ray spectra (EDS) and high-angle annular dark-field (HAADF) images were acquired using a FEI Talos F200S TEM operated in scanning TEM (STEM) mode. A variable angle spectroscopic ellipsometer equipped with an automatic rotating analyzer (J.A. Woollam V-VASE) was used to measure the ellipsometric angles, amplitude ratio (Ψ), and phase difference (Δ) between the reflected polarized light p and s components, at different angles of incidence, in the range of 0.5−5 eV. The samples' back surfaces had been previously scratched, so as to avoid incoherent back-surface reflection.

RESULTS AND DISCUSSION

Samples T2 and T2′ were chosen for the morphological and structural analysis. Both samples were grown with the same conditions but on different substrates, Si(111) for sample T2 and Si(100) for T2′. Figure 1a,b shows a cross-section SEM micrograph of samples T2 and T2′, respectively, taken with an inclination of 15°, which exhibit a high density of nanostructures with an average height of (667 ± 17) and (734 ± 8) nm, diameters of (120 ± 5) and (134 ± 5) nm, and wall thicknesses of (16 ± 1) and (19 ± 1) nm, respectively. It can also be appreciated that these columnar nanostructures are grown straight and parallel to the surface normal direction on both substrates. The top morphology of these specimens is a combination of solid NWs (SNWs) with well-developed hexagonal facets, most likely m-planes (density on samples T2 and T2′ of ∼4 × 10^8 and ∼1 × 10^8 cm^{-2}), hollow NWs (HNWs) with a hexagonal to dodecagonal shape, most likely a mixture of m- and a-planes (∼3 × 10^8 and 2 × 10^8 cm^{-2}), and c-shape NWs (CNWs, ∼3 × 10^9 cm^{-2} on both samples). The different nanostructures are illustrated on the top-view SEM micrograph of samples T2 (Figure 1c) and T2′ (Figure 1d). HAADF-XTEM studies were carried out on sample T2 to elucidate up to which extent the nanostructures are hollow or solid. As can be seen from Figure 1e, the highlighted CNW seems to be a kind of rolled film partially opened longitudinally. The great contrast between what we consider external and internal walls makes us think that these NWs are hollow. Note that the intensity on the HAADF images is proportional to the product of the effective atomic mass (the higher, the brighter) and the quantity of projected material. Considering pure GaN (see Supporting Information section 2 for energy dispersive X-ray spectroscopy, EDS) and that tripod polishing gives lamellae very uniform width, then different intensities are directly related with the local emptiness or compactness of the nanostructure. In Figure 1f, a brighter nanostructure with more homogeneous contrast can be observed (highlighted on the left side of this figure), so according to the previous explanation, it is most-likely a SNW. In addition, an increased intensity can be seen at the base of the nanostructures (black dashed rectangle on Figure 1f) than at the tips, suggesting that there is more GaN material on the bases of the nanostructures (closer to the substrate) than at the tips of the HNWs and CNWs. Analysis of the intensity of the HAADF-XTEM micrograph of sample T2 (Figure S3, Supporting Information) confirms the intensity decrease with increasing the distance from the substrate. This fact, combined with the observed and commented NWs-type surface densities, support the idea that most of the uncompact NWs are actually composed by solid bases (or initially SNWs) that evolve some of them into hollow or most of them into c-shape structures as the growth proceeds (Figure S4, Supporting Information).

To probe the microstructure of the rods, we performed HR-XTEM experiments on samples T2 and T2′ (Figure 2a,b), along the [10$\bar{1}$0] and the [11$\bar{2}$0] GaN directions, respectively, close to the interfaces among Si, β-Si_3N_4, and GaN. The

DOI: 10.1021/acs.cgd.9b00146
Cryst. Growth Des. 2019, 19, 2461−2469

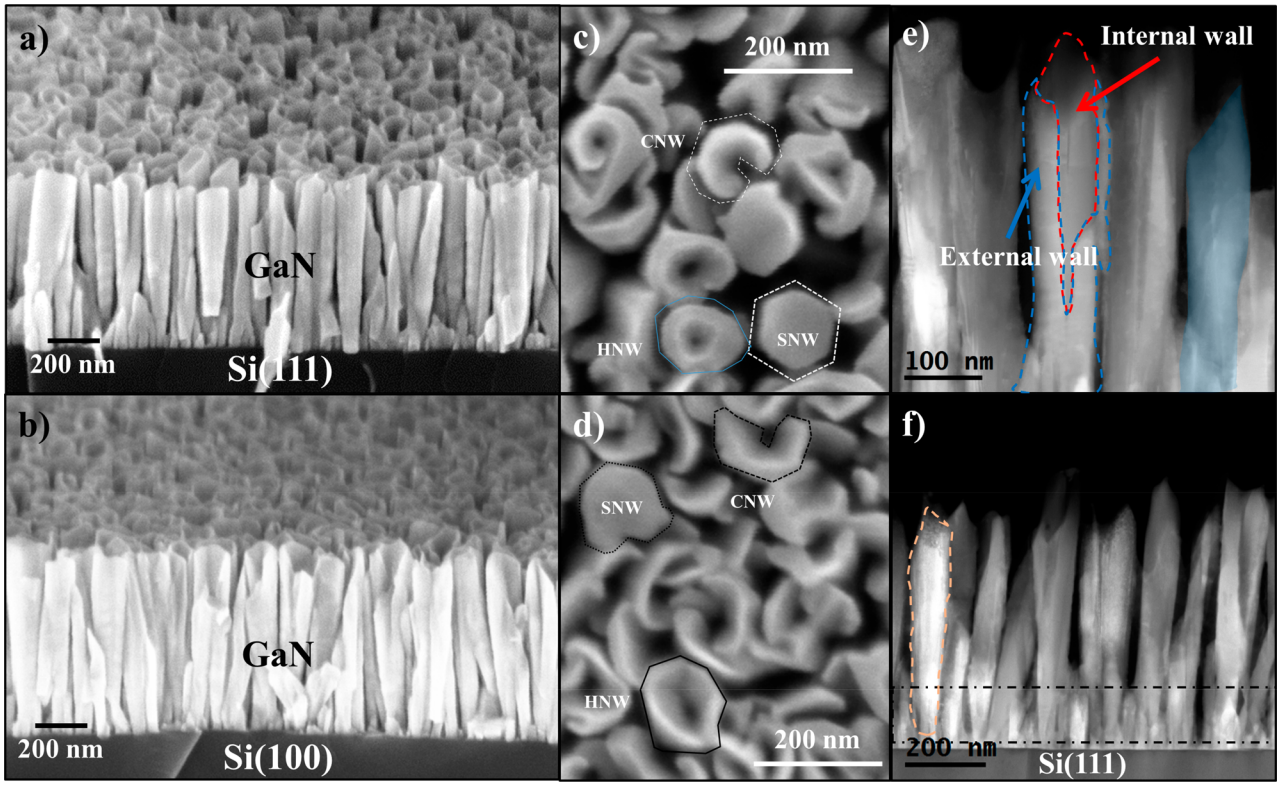

Figure 1. Cross-sectional SEM micrographs of (a) sample T2 and (b) sample T2′ taken at an inclination of 15°, and parallel to the Si{110} cleavage edge. Top-view SEM micrograph of samples (c) T2 and (d) T2′ that illustrate the morphology of the SNWs, HNWs, and CNWs. (e,f) HAADF-XTEM micrographs of the GaN nanostructures taken along the [11$\bar{2}$0] GaN zone axis on sample T2: dashed lines around internal (red) and external (blue) walls of a CNW, a brighter SNW (light orange), and GaN nanostructures bases (dashed-black rectangle) are included for clarity.

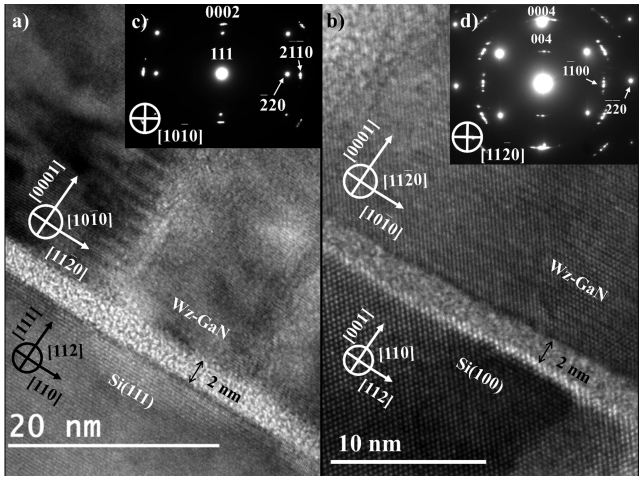

Figure 2. Cross-section HR-TEM images of GaN nanostructures on (a) Si(111) (sample T2) along the [10$\bar{1}$0] zone axis and (b) Si(100) (sample T2′) along the [11$\bar{2}$0] zone axis. Both micrographs show an amorphized 2 nm-thick β-Si_3N_4 interlayer. SAED patterns acquired over (c) sample T2 along the [10$\bar{1}$0] zone axis and (d) sample T2′ along the [11$\bar{2}$0] zone axis. Relevant reflections are marked for clarity on certain diffraction spots of both SAED patterns. Probing diameter of ∼700 nm on both SAED patterns.

nitridation technique explained in the experimental section gives rise to a 2 nm-thick β-Si_3N_4 in both cases. The nanostructures are revealed to be single-crystalline wurtzite GaN. According to Figure 2a,b the GaN nanostructures grow with the *c*-axis perpendicular to the Si(111) and Si(100) planes. This observation concurs with SEM micrographs shown above (Figure 1a,b). For the samples grown on Si(111) it also coincides with results reported by other groups.[25−27] In the case of Si(100) substrates, NWs grown with the c-direction perpendicular to the Si(100) plane agrees with previously reported results.[26,28] However, Shetty and co-workers reported similar mixture of nanostructures grown on Si(100)[29] with different alignment. They were tilted between 10° and 45° with respect to the Si(100) plane normal. In order to inspect the general epitaxial alignment between the GaN nanostructures and the underlying Si substrates in our specimens, SAED patterns, for more extended interface regions than those inspected by HRTEM, were collected (Figure 2c,d). The diffraction spots related to GaN are arced due to the presence of a small tilt among the nanostructures (smaller for sample T2). A slight twist of some NWs with respect to surface normal cannot be disregarded, against a perfect heteroepitaxy, since only (0001) fringes are resolved on the GaN when the Si atomic columns are perfectly aligned with the electron-beam and thus resoluble by phase-contrast. Nevertheless, the SAED patterns reveal a general coherency between surface and nanowires lattices, then the epitaxial relationship is defined as GaN(0001)||Si(111) and GaN(10$\bar{1}$0)||Si(112) for GaN on Si(111), and GaN(0001)||Si(001) and GaN(11$\bar{2}$0)||Si(110) for GaN on Si(100). Moreover, this is the commonly reported epitaxial alignment for III-nitrides (thin films and NWs) on Si(111).[25,27,30,31]

To gain deeper insight on the microstructure of the GaN rods we performed HR-PVTEM on a single SNW (Figure

DOI: 10.1021/acs.cgd.9b00146
Cryst. Growth Des. 2019, 19, 2461−2469

3a,b) and a single CNW (Figure 3d). The top-view of the SNW reveals a single crystalline GaN structure (confirming the

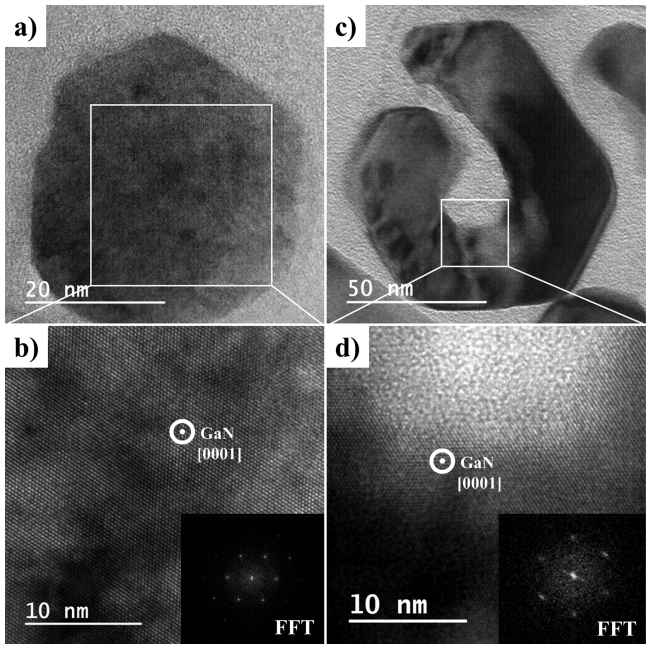

Figure 3. Top-view HR-PVTEM micrographs of a SNW (a) and enlarged area (b), and a CNW (c) and enlarged area (d) taken along the [0001] GaN zone axis. FFT images of both top-view HR-TEM micrographs of the SNW and the CNW are shown in their respective insets.

observations done in Figure 2a) with a hexagonal symmetry of atomic columns projected along the [0001] direction. The SNW shows a well-developed hexagonal shape with $\{10\bar{1}0\}$ side facets. In the case of the CNW (Figure 3d), the micrograph reveals a single crystalline CNW with five well-developed external side facets (most likely $\{10\bar{1}0\}$ facets) together with a sixth opened one, forming an open hexagon. The internal facets are parallel to the external $\{10\bar{1}0\}$ side facets. In this specific case the wall thickness is (30.1 ± 0.5) nm. Insets of Figure 3b,d are the fast Fourier transform (FFT), equivalent to a diffractogram, of the HR-TEM images of the SNW and the CNW, respectively. Both FFT images indicate a 6-fold symmetry fingerprint of the wurtzite crystal structure in the polar direction, on both kinds of nanostructures.

The natural question arising now is what is the mechanism behind the formation of HNWs and CNWs? Three different explanations can be found in the literature for the spontaneous formation of such structures: I. The screw dislocation driven model;[29,32] II. the reduction of the nucleation barrier along the NW top facet boundary by introducing high Si-flux;[33] III. the growth under a locally (on the tips) Ga-limited regime.[7,34,35]

Morin and co-workers[32] reported on the spontaneous formation of ZnO nanotubes driven by screw dislocations. In addition, Shetty et al.[29] found the role of screw dislocations to be crucial for the formation of the internal facets on the HNWs and CNWs. To investigate the role of screw-type dislocations on the shape of the nanostructures, we carried out TEM studies in two-beam diffraction-contrast conditions with g = 0002. Dislocations with total or partial screw component were found in a very low percentage of the studied nanostructures (<5%), suggesting that there should be another mechanism behind the formation of HNWs and CNWs. The second model proposed can be disregarded by the fact that no Si flux was employed during the growth of the present nanostructures, and the used temperatures cannot justify Si sublimation or out-diffusion from the substrate. However, it is worth mentioning that the morphology of the structures reported by Bolshakov and co-workers[33] is similar to the morphology exhibited by Samples T2 and T2′. Regarding the third mechanism, we performed a comprehensive study of the growth conditions (substrate temperature and Ga and N* fluxes), and their influence on the morphology of the nanostructures seem to be clear as it will be presented hereafter.

To probe the role of the local growth regime, we need to identify the effect of the different parameters on the local growth conditions. Once identified, we can design proper experiments. The number of Ga atoms arriving to the tip of the nanostructure per unit of time and unit of area is given by

$$\phi_{\mathrm{Ga}}^{\mathrm{loc}} = \phi_{Ga} + \phi_{\mathrm{Ga}}^{\mathrm{diff}} + \phi_{\mathrm{GaN}}^{\mathrm{dec}} - \phi_{\mathrm{Ga}}^{\mathrm{des}} \quad (1)$$

Being ϕ_{Ga} the Ga flux arriving directly to the tip, i.e., the flux effusing from the K-cell, $\phi_{\mathrm{Ga}}^{\mathrm{diff}}$ accounts for the Ga atoms diffused from the substrate to the side-walls and from the side-walls to the tip, $\phi_{\mathrm{GaN}}^{\mathrm{dec}}$ is the contribution from the decomposition of the nanostructure itself, leaving Ga atoms on the tip. It is defined as

$$\phi_{\mathrm{GaN}}^{\mathrm{dec}} = C \exp\left\{-\frac{E_{\mathrm{dec}}}{k_{\mathrm{B}}T}\right\} \quad (2)$$

Fernandez-Garrido and co-workers[36] reported $C = (2.4 \pm 0.2) \times 10^{29} \frac{\mathrm{at}}{\mathrm{cm}^2\,\mathrm{s}}$ to be the decomposition pre-exponential factor and E_{dec} the activation energy for the decomposition process, with values ranging from 3.1 to 3.6 eV.[36] $\phi_{\mathrm{Ga}}^{\mathrm{des}}$ accounts for the evaporation of Ga from the tip, given by the expression:

$$\phi_{\mathrm{Ga}}^{\mathrm{des}} = \mathrm{A}(\phi_{\mathrm{Ga}} + \phi_{\mathrm{Ga}}^{\mathrm{diff}} + \phi_{\mathrm{GaN}}^{\mathrm{dec}}) \exp\left\{-\frac{E_{\mathrm{des}}}{k_{\mathrm{B}}T}\right\} \quad (3)$$

where A is the desorption pre-exponential factor and E_{des} the activation energy for the desorption process. Bruno and co-workers reported $E_{\mathrm{des}} = (2.85 \pm 0.02)$ eV for Ga desorbing from GaN(0001) surface.[37] According to the empirical work of Brandt and co-workers[38] the activation energy for desorption is lower for the $\{0001\}$ planes than for the $\{10\bar{1}0\}$ planes. Therefore, a higher desorption rate on the top facets than on the side- and internal- walls is expected. To modify the local conditions, we can alter directly I. the total Ga atoms lost by adjusting the substrate temperature; II. the amount of arriving Ga atoms by varying the temperature of the Ga effusion cell and therefore the impinging Ga flux (ϕ_{Ga}); and III. the quantity of impinging N* atoms by tuning the plasma conditions (power or flux of pure N_2).

Effect of the Substrate Temperature. The variation of the substrate temperature has a direct effect on the amount of Ga desorbed from the surface and on the GaN decomposed. Note that the decomposition of GaN leaves liquid Ga on the surface that can be either reincorporated to the lattice with the excess of N* or desorbed from the surface. Figure 4 (a1−a3) shows the effect of the growth temperature, from a nanowall network grown (Figure 4 a1) at 800 °C to a low density

DOI: 10.1021/acs.cgd.9b00146
Cryst. Growth Des. 2019, 19, 2461−2469

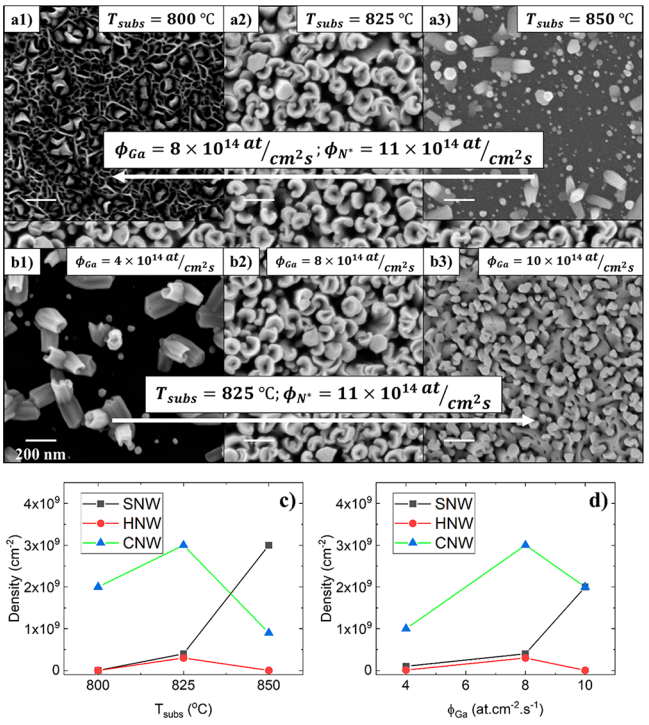

Figure 4. Top view SEM micrographs of GaN nanostructures grown on Si(111) at different substrate temperatures (T1, a1; T2, a2; T3, a3) and different impinging Ga flux (ϕ_{Ga}) (G1, b1; T2, a2 and b2; G3, b3). The white arrow points toward higher ϕ_{Ga}^{loc} values. Parameters kept constant are indicated over the white arrows. Density of the different nanostructures vs (c) substrate temperature and (d) ϕ_{Ga}. All the micrographs share a 200 nm scale bar. Note that micrographs a2 and b2 are the same.

packed SNWs at 850 °C (Figure 4 a3). Figure 4c illustrates the density of the nanostructures with respect to the substrate temperature. A further reduction of the substrate temperature will reduce the Ga losses increasing the Ga available on the surface, therefore, promoting a more compact growth. At temperatures above 850 °C the losses will become higher, thus resulting in no growth.

Effect of the Impinging Ga Flux (ϕ_{Ga}). The variation of the impinging Ga flux has a direct effect on the amount of Ga arriving to the tip of the nanostructures. Figure 4 (b1–b3) shows the results of the variation of the Ga flux. By increasing the ϕ_{Ga}, the amount of Ga atoms arriving to the tip of the nanostructures is increased modifying the local growth conditions. At the lowest ϕ_{Ga} (Figure 4 b1) the surface is characterized by the presence of doublets and triplets of CNWs (nanostructures with a common origin). At this condition, Ga is the limiting reactant and the nanostructures are mainly of the CNW type. An increase in the amount of Ga reaching the sample results first in an increase on the density of nanostructures covering the surface, being dominant the HNW and CNW types, and, by further increasing, evolves to a more compact network of SNW. This variation on the density of the nanostructures as a function of the ϕ_{Ga} value is plotted on Figure 4d.

Effect of the N* Flux (ϕ_{N^*}). The variation of the pure N_2 flux has a direct effect on the amount of active nitrogen arriving to the surface and hence the top of the nanostructures. Figure 5a shows the effect of increasing the active nitrogen flux. At the lowest ϕ_{N^*} (Figure 5 a1) there is not enough N* overpressure to counteract the effects of the GaN decomposition and Ga desorption, resulting in a very low density of nanostructures. As the ϕ_{N^*} increases, the surface is first saturated with nanostructures (Figure 5 a2), and then, by further increasing the ϕ_{N^*}, CNWs become dominant over the SNWs (Figure 5

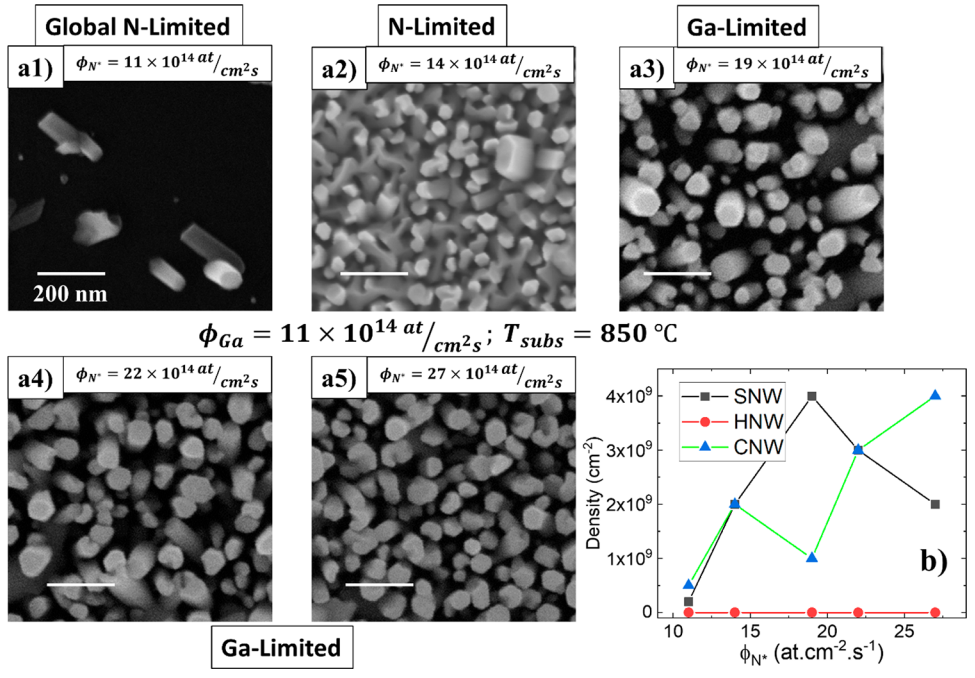

Figure 5. Top-view SEM micrographs of GaN nanostructures grown on Si(111) for (a1–a5) different pure N_2 fluxes (samples N1 to N5). Parameters kept constant are indicated below panel a3. All the micrographs share a 200 nm scale bar. (b) Density of nanostructures vs pure N_2 flux.

DOI: 10.1021/acs.cgd.9b00146
Cryst. Growth Des. 2019, 19, 2461–2469

a3 to a5). The length of the nanostructures increases with the ϕ_{N^*} until it saturates at $\phi_{N^*} = 19 \times 10^{14} \frac{at}{cm^2\,s}$, reaching the regime where Ga is the limiting reactant. Once reached, the Ga-limited regime shape of the nanostructures is progressing from a majority of SNWs to a majority of CNWs, as it is demonstrated in Figure 5b.

Samples T3, G1, and N1 present a surface composed by a mixture of clusters, tilted NWs, tripods, tetrapods, and multipods (Figures 4 a3,b1 and 5 a1). In the case of samples T3 and N1, the higher temperature (850 °C) produces an increase in the GaN decomposition and Ga desorption rates impossible to stabilize with the given ϕ_{N^*}, whereas in the sample G1 the impinging Ga flux is directly reduced. In the self-assembled growth of nanowires, two different regimes can be distinguished; a nucleation phase and a growth phase. The nucleation phase of GaN NWs is different than in standard crystal growth in the sense that GaN NWs do not nucleate directly in the form of wires. The nucleation phase comprises two successive periods: an initial incubation of stable nuclei in the form of clusters, followed by a transition period leading to shape transformations that eventually ends up with GaN NWs stable nuclei. During the growth phase the stable NW nuclei grow axially and radially. The nonoptimal growth conditions for those three samples affect primarily the nucleation phase, increasing the incubation time dramatically and reducing the density of nuclei. During the transition period, and together with the limited incorporation of Ga into the crystal, the nuclei cannot reach the typical stable NW nuclei shape,[39] thus forming metastable nuclei with a nonconventional shape. During the subsequent growth phase, the metastable nuclei will elongate in the axial and radial directions and will end up in a mixture of tilted NWs, clusters, tripods, tetrapods, and multipods in general (Figures 4 a3,b1 and 5 a1). The processes governing the particular shape of an individual NW are complex and out of the scope of this Article. However, we think that it is a combination of the shape of any individual metastable nucleus, i.e., the particular orientation of their free surfaces, and the evaporation and reincorporation of the Ga atoms.

To understand the morphology evolution leading to the formation of S-, H-, and CNWs, we are going to focus on the evolution of the stable NW nucleus formed after the nucleation stage. Depending on the amount of Ga atoms with respect to the amount of N* arriving to the tip, three different growth regimes can be distinguished:

When $\phi_{Ga}^{loc} = \phi_{N^*}$, the growth proceeds in the axial direction with a negligible change in radius. This is the regime for growth of SNWs with flat top facet.[39]

When $\phi_{Ga}^{loc} > \phi_{N^*}$, the Ga atoms diffusing from the side-walls to the top facet accumulate on the m-plane to c-plane edges, and each NW starts growing radially as well as axially. The NW will continue increasing its radius until new equilibrium conditions are reached, self-regulating itself.[40]

When $\phi_{Ga}^{loc} < \phi_{N^*}$, three competing processes take place: the incorporation of Ga atoms on the top facet, the evaporation of Ga atoms from the top facet (c-plane) and side-walls (m-planes), and the incorporation of atoms on the m-plane to c-plane edges.

According to the empirical work of Brandt and co-workers,[38] the activation energy for desorption is lower for the {0001} planes than for the $\{10\bar{1}0\}$ planes. Therefore, a higher desorption rate on the top facets than on the side-walls is expected. Taking that into account, less Ga atoms are expected to remain on the top facet than on the side-walls. In addition to the direct flux coming from the k-cell, Ga atoms will diffuse from the side-walls to the top facet. When arriving to the top facet, the higher concentration of N*, as compared to the Ga concentration, will reduce the diffusion length of the Ga atoms promoting their incorporation on less favorable sites such as the m-plane to c-plane edges. As the growth proceeds, the Ga atoms continue to incorporate on the edges. It is worth mentioning that, at the temperatures of those experiments, the GaN decomposition rate is not negligible; therefore, GaN is decomposed and Ga atoms can either evaporate or reincorporate into the crystal. Under these conditions, it is expected that the atoms incorporated on the edges will act as nucleation sites for the new arriving atoms, thus leaving a mixture of S-, H-, and CNWs.

This comprehensive analysis of the shape of the nanostructures with respect to the growth conditions (growth temperature, ϕ_{Ga} and ϕ_{N^*}) demonstrates unambiguously that the mechanism behind their particular shape is the growth under local Ga-limited conditions. This mechanism has been pointed out to be behind the growth of ordered arrays of GaN nanotubes[34] on a Ti-masked diamond substrate. In their case the local conditions on the tip were tuned by controlling the geometrical design of the mask (small period and large diameter). In addition, Park and co-workers[7] reported the growth of ordered arrays of GaN HNWs by MBE when using a low ϕ_{Ga}. Therefore, our findings are compatible with existing literature, provide an exhaustive growth map, and complement the already established theory on the growth of self-induced GaN NWs.[1,39−41]

Spectroscopic ellipsometry analyses were performed on samples N3, N4, and N5 to find out the impact of growth under Ga-limited conditions on both the total porosity and the evolution of the optical constants along the GaN nanostructure in a larger scale. Herein, the term porosity will be defined as the percentage of air/voids in the GaN material. For reference, 0% porosity will be associated with a compact solid GaN thin film, composed by 100% GaN and 0% air.

Analyses were carried out considering a wavelength range from 250 to 2500 nm (5−0.5 eV), and the angles of incidence were varied between 55 and 75°. The spot size of the light beam used was 3 mm, which was always positioned in the central region of the sample. The depolarization was registered in all cases, and it was included in the fitting process. As a first approach, the average porosity of each film was obtained by a pure Bruggeman effective medium approximation (BEMA) model, incorporating a mix of wurtzite GaN from the Woollam software library[42] and voids to describe the GaN nanowires layer, and assuming that individual nanowires exhibit the same behavior as the dense material. The calculated porosities show an increase of the voids proportion from 56% for sample N3 to 66% on sample N5, which could be associated with a boost in the density of CNWs.

Figure 6a shows the ellipsometric BEMA model enhanced by separating the in-plane (X, Y) and out-of-plane (Z) optical responses (uniaxial anisotropy). The out-of-plane depolarization factor was fitted to $q_z \approx 0$, with the sum of q_x and q_y being the difference of q_z from 1, due to the columnar morphology (perpendicular to the substrate) of the nanostructures.[43−45] In order to reproduce the morphology of the GaN porous film, it

DOI: 10.1021/acs.cgd.9b00146
Cryst. Growth Des. 2019, 19, 2461−2469

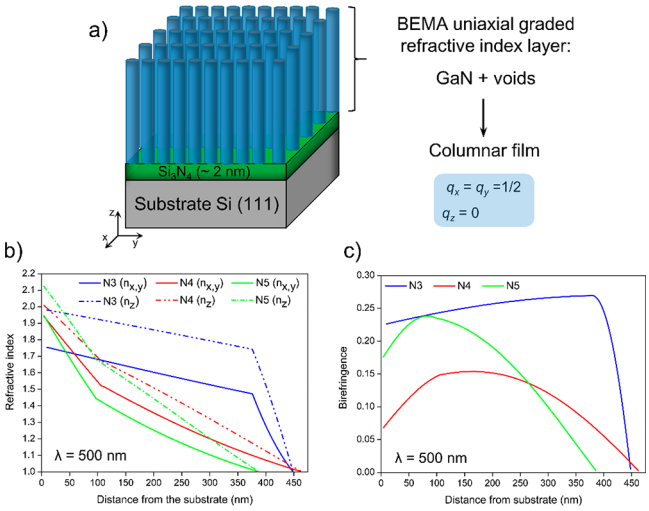

Figure 6. (a) Ellipsometric BEMA model of the GaN nanowire film. (b) In-plane (solid lines) and out-of-plane (dashed lines) refractive index and (c) birefringence, $n_e - n_o$, evolution versus the position within the thickness of layer at 500 nm wavelength.

was also assumed a variation in the refractive indexes (n) of the GaN nanostructure along the Z direction (a graded-index layer) so that it decreases, up to $n = 1$ on the surface, as we move away from the substrate. Such variation is originated by internal changes in the structure of the nanowires rather than by modifications in the number of nanowires per surface unit. Furthermore, layer thickness nonuniformity was obtained from the depolarization registered during the experiments. Additionally, a 2 nm thin layer of silicon nitride (Si_3N_4), located between the substrate and the nanowire layer, was also considered in the optical model. Making all these considerations and fixing the porosity values obtained from the pure BEMA aforementioned, the defined model shows a good agreement for the modeled and the experimental spectra, obtaining good mean square errors (MSE) including depolarization (see Supporting Information Figure S4 for the experimental and modeled ellipsometric measurements). Note that the thicknesses predicted by the model ((446 ± 0.24), (460 ± 0.50), and (383 ± 0.25) for N3, N4, and N5, respectively) differ slightly from those measured by SEM ((402 ± 18), (385 ± 26), and (367 ± 14) nm for N3, N4, and N5, respectively), being bigger for N3 and N4 samples. These differences could be related to the nonuniformity of thickness, which in turn is responsible for the measured depolarization. This nonuniformity along the spot size reaches to the 18% for N3 sample and 22% for N4 and is significantly lower for sample N5 where it is 6%.

The results obtained from the BEMA model let us know some further information about the studied systems. First of all, it can be noted that GaN nanostructure layers have a high porosity, which leads to lower refractive indexes when compared to a massive GaN (see Supporting Information Figure S5 for refractive index vs wavelength). Moreover, it can also be observed that this refractive index decreasing is more pronounced for greater N_2 fluxes, which would demonstrate a direct correlation between the effect of the total density of nanostructures and the SNWs to CNWs proportion in the refractive index. Figure 6b–c summarizes the evolution of the refractive index of uniaxial anisotropic GaN nanowire layers along the out-of-plane direction. Here, it can be found that the refractive index in the Z direction is in all samples greater than those corresponding to the in-plane directions, being the difference between both (birefringence) stronger for lower total densities of NWs and higher concentrations of SNWs. It is important to highlight that N4 and N5 samples present a faster drop in n within the first 100 nm, which could be related to a structural change from SNWs to CNWs, i.e., at the beginning all the NWs would have a solid base, which could develop the c-shape or not depend on the growth conditions. This would be also in agreement with the aforementioned accumulation of material on the bases of these nanostructures. Therefore, taking this into account, it could be said that the concentration of CNWs is higher in N5 than in the N4 sample because the decrease of n is sharper in the region close to the substrate. By contrast to this, N3 sample exhibits a constant and softer n decrease except in the zone close to the surface, after 370 nm, which could be associated with the nonuniformity in thickness (18% in this case). This fact makes us think this last layer would be fundamentally composed of SNWs. Moreover, the low initial value of both $n_{x,y}$ and n_z in N3 sample is due to its smaller total density of NWs (see Figure 5a3,b).

CONCLUSIONS

In this Article, we performed a thorough study of GaN-on-Si nanostructures growth by PAMBE. HR-TEM analysis showed single crystalline SNWs, HNWs, and CNWs epitaxially aligned with the underlying Si substrate and their effect on the morphology of the nanostructures. We have pointed out that the growth under local Ga-limited conditions is the mechanism behind the particular morphology of the nanostructures. Our findings are compatible with existing literature, provide an exhaustive growth map, and complement the already established theory on the growth of self-induced GaN NWs. The porosity of the samples as well as the evolution of the optical constants along their thickness were obtained from the fitting of the ellipsometry measurements to the BEMA uniaxial model. By tuning the growth conditions, the density and shape of the nanostructures, and thus the porosity, can be controlled. The particular morphology of the samples presented in this Article together with the demonstrated control over the porosity level will potentially open new horizons in the development of GaN nanostructures for future applications.

ASSOCIATED CONTENT

Supporting Information

The Supporting Information is available free of charge on the ACS Publications website at DOI: 10.1021/acs.cgd.9b00146.

Intentional nitridation, compositional analysis, intensity analysis of HAADF-XTEM micrograph of sample T2, additional TEM micrographs C-NWs at their interface region with Si, and ellipsometry modeling of GaN nanoporous film (PDF)

AUTHOR INFORMATION

Corresponding Author

*E-mail: victor.gomez@ftf.lth.se.

ORCID

Víctor J. Gómez: 0000-0003-2364-8814
Antonio J. Santos: 0000-0003-3776-7080
Francisco M. Morales: 0000-0002-8341-2478

DOI: 10.1021/acs.cgd.9b00146
Cryst. Growth Des. 2019, 19, 2461–2469

Present Address
[#]Solid State Physics, Lund University, Box 118, S-221 00 Lund, Sweden.

Author Contributions
The manuscript was written through contributions of all authors. All authors have given approval to the final version of the manuscript.

Notes
The authors declare no competing financial interest.

■ ACKNOWLEDGMENTS

The authors would like to acknowledge the financial support provided by Sêr Cymru National Research Network in Advanced Engineering and Materials. V.J.G. acknowledge Dr. P. Caroff and Dr. M. Kesaria for fruitful discussions. A.J.S. would like to thank the IMEYMAT Institute and the Spanish Ministerio de Educación y Cultura for the concessions of grants (ICARO-173873 and FPU16-04386). The "Talent Attraction Program" of the University of Cádiz is acknowledged by supporting B.L., contract code E-11-2017-0117214. University of Cádiz and IMEYMAT are also acknowledged for financing the mutual facilities available at the UCA R&D Central Services (SC-ICYT), the UCA project reference "PUENTE PR2018-040″, and the IMEYMAT project reference "AGREGADOR 2018-1".

■ REFERENCES

(1) Knelangen, M.; Consonni, V.; Trampert, A.; Riechert, H. In Situ Analysis of Strain Relaxation during Catalyst-Free Nucleation and Growth of GaN Nanowires. *Nanotechnology* **2010**, *21*, 245705.
(2) Vajpeyi, A. P.; Tripathy, S.; Chua, S. J.; Fitzgerald, E. A. Investigation of Optical Properties of Nanoporous GaN Films. *Phys. E* **2005**, *28*, 141−149.
(3) Najar, A.; Gerland, M.; Jouiad, M. Porosity-Induced Relaxation of Strains in GaN Layers Studied by Means of Micro-Indentation and Optical Spectroscopy. *J. Appl. Phys.* **2012**, *111*, 093513.
(4) Williamson, T. L.; Guo, X.; Zukoski, A.; Sood, A.; Díaz, D. J.; Bohn, P. W. Porous GaN as a Template to Produce Surface-Enhanced Raman Scattering-Active Surfaces. *J. Phys. Chem. B* **2005**, *109*, 20186−20191.
(5) Ryu, S. W.; Zhang, Y.; Leung, B.; Yerino, C.; Han, J. Improved Photoelectrochemical Water Splitting Efficiency of Nanoporous GaN Photoanode. *Semicond. Sci. Technol.* **2012**, *27*, 015014.
(6) Benton, J.; Bai, J.; Wang, T.; Kingdom, U. Nanoporous GaN for Enhanced Solar Hydrogen Production. *Proc. SPIE* **2014**, 91760.
(7) Park, J.; Mandal, A.; Kang, S.; Chatterjee, U.; Kim, J. S. Hydrogen Generation Using Non- Polar Coaxial InGaN/GaN Multiple Quantum Well Structure Formed on Hollow n-GaN Nanowires. *Sci. Rep.* **2016**, *6*, 31996.
(8) Zhang, L.; Wang, S.; Shao, Y.; Wu, Y.; Sun, C.; Huo, Q.; Zhang, B.; Hu, H.; Hao, X. One-Step Fabrication of Porous GaN Crystal Membrane and Its Application in Energy Storage. *Sci. Rep.* **2017**, *7*, 44063.
(9) Yu, J.; Zhang, L.; Shen, J.; Xiu, Z.; Liu, S. Wafer-Scale Porous GaN Single Crystal Substrates and Their Application in Energy Storage. *CrystEngComm* **2016**, *18*, 5149−5154.
(10) Lee, K. J.; Kim, S.-J.; Kim, J.-J.; Hwang, K.; Kim, S.-T.; Park, S.-J. Enhanced Performance of InGaN/GaN Multiple-Quantum-Well Light-Emitting Diodes Grown on Nanoporous GaN Layers. *Opt. Express* **2014**, *22*, A1164.
(11) Shiu, G. Y.; Chen, K. T.; Fan, F. H.; Huang, K. P.; Hsu, W. J.; Dai, J. J.; Lai, C. F.; Lin, C. F. InGaN Light-Emitting Diodes with an Embedded Nanoporous GaN Distributed Bragg Reflectors. *Sci. Rep.* **2016**, *6*, 29138.
(12) Hsu, W.-J.; Chen, K.-T.; Huang, W.-C.; Wu, C.-J.; Dai, J.-J.; Chen, S.-H.; Lin, C.-F. InGaN Light Emitting Diodes with a Nanopipe Layer Formed from the GaN Epitaxial Layer. *Opt. Express* **2016**, *24*, 11601.
(13) Carvajal, J. J.; Mena, J.; Aixart, J.; Díaz, F.; Aguiló, M. Rectifiers, MOS Diodes and LEDs Made of Fully Porous GaN Produced by Chemical Vapor Deposition. *ECS J. Solid State Sci. Technol.* **2017**, *80*, 143−148.
(14) Huang, S.; Zhang, Y.; Leung, B.; Yuan, G.; Wang, G.; Jiang, H.; Fan, Y.; Sun, Q.; Wang, J.; Xu, K.; et al. Mechanical Properties of Nanoporous GaN and Its Application for Separation and Transfer of GaN Thin Films. *ACS Appl. Mater. Interfaces* **2013**, *5*, 11074−11079.
(15) Huo, Q.; Shao, Y.; Wu, Y.; Zhang, B.; Hu, H.; Hao, X. High Quality Self-Separated GaN Crystal Grown on a Novel Nanoporous Template by HVPE. *Sci. Rep.* **2018**, *8*, 1−8.
(16) Abud, S. H.; Hassan, Z.; Yam, F. K. Enhancement of Structural and Optical Properties of Porous In0.27Ga0.73N Thin Film Synthesized Using Electrochemical Etching Technique. *Int. J. Electrochem. Sci.* **2012**, *7*, 10038−10046.
(17) Radzali, R.; Hassan, Z.; Zainal, N.; Yam, F. K. Nanoporous InGaN Prepared by KOH Electrochemical Etching with Different Light Sources. *Microelectron. Eng.* **2014**, *126*, 107−112.
(18) Soto Rodriguez, P. E. D.; Nash, V. C.; Aseev, P.; Gómez, V. J.; Kumar, P.; Alvi, N. U. H.; Sánchez, A.; Villalonga, R.; Pingarrón, J. M.; Nötzel, R. Electrocatalytic Oxidation Enhancement at the Surface of InGaN Films and Nanostructures Grown Directly on Si(111). *Electrochem. Commun.* **2015**, *60*, 158−162.
(19) Abud, S. H.; Hassan, Z.; Yam, F. K. Fabrication and Characterization of Metal-Semiconductor-Metal Photodetector Based on Porous InGaN. *Mater. Chem. Phys.* **2014**, *144*, 86−91.
(20) Xing, Z.; Ren, F.; Wu, H.; Wu, L.; Wang, X.; Wang, J.; Wan, D.; Zhang, G.; Jiang, C. Enhanced PEC Performance of Nanoporous Si Photoelectrodes by Covering HfO2 and TiO2 Passivation Layers. *Sci. Rep.* **2017**, *7*, 43901.
(21) Wang, H.; Min, S.; Ma, C.; Liu, Z.; Zhang, W.; Wang, Q.; Li, D.; Li, Y.; Turner, S.; Han, Y.; Zhu, H.; Abou-Hamad, E.; Hedhili, M. N.; Pan, J.; Yu, W.; Huang, K. W.; Li, L. J.; Yuan, J.; Antonietti, M.; Wu, T. Synthesis of Single-Crystal-like Nanoporous Carbon Membranes and Their Application in Overall Water Splitting. *Nat. Commun.* **2017**, *8*, 13592.
(22) Xia, L.; Bai, J.; Li, J.; Zeng, Q.; Li, X.; Zhou, B. A Highly Efficient BiVO4/WO3/W Heterojunction Photoanode for Visible-Light Responsive Dual Photoelectrode Photocatalytic Fuel Cell. *Appl. Catal., B* **2016**, *183*, 224−230.
(23) Wang, Y. D.; Chua, S. J.; Sander, M. S.; Chen, P.; Tripathy, S.; Fonstad, C. G. Fabrication and Properties of Nanoporous GaN Films. *Appl. Phys. Lett.* **2004**, *85*, 816−818.
(24) Suzuki, T.; Hirabayashi, Y. First Observation of the Si(111)-7 × 7<->1 × 1 Phase Transition by the Optical Second Harmonic Generation. *Jpn. J. Appl. Phys.* **1993**, *32*, L610−L613.
(25) Wierzbicka, A.; Zytkiewicz, Z. R.; Kret, S.; Borysiuk, J.; Dluzewski, P.; Sobanska, M.; Klosek, K.; Reszka, A.; Tchutchulashvili, G.; Cabaj, A.; Lusakowska, E. Influence of Substrate Nitridation Temperature on Epitaxial Alignment of GaN Nanowires to Si(111) Substrate. *Nanotechnology* **2013**, *24*, 035703.
(26) Calleja, E.; Ristić, J.; Fernández-Garrido, S.; Cerutti, L.; Sánchez-García, M. A.; Grandal, J.; Trampert, A.; Jahn, U.; Sánchez, G.; Griol, A.; Sánchez, B. Growth, Morphology, and Structural Properties of Group-III-Nitride Nanocolumns and Nanodisks. *Phys. Status Solidi B* **2007**, *244*, 2816−2837.
(27) Gačević, Ž.; Bengoechea-Encabo, A.; Albert, S.; Torres-Pardo, A.; Gonzalez-Calbet, J. M.; Calleja, E. Crystallographically Uniform Arrays of Ordered (In) GaN Nanocolumns Crystallographically Uniform Arrays of Ordered (In) GaN Nanocolumns. *J. Appl. Phys.* **2015**, *117*, 035301.
(28) Fan, S.; Shih, I.; Mi, Z. A Monolithically Integrated InGaN Nanowire/Si Tandem Photoanode Approaching the Ideal Bandgap Configuration of 1.75/1.13 EV. *Adv. Energy Mater.* **2017**, *7*, 1600952.
(29) Shetty, S.; Kesaria, M.; Ghatak, J.; Shivaprasad, S. M. The Origin of Shape, Orientation, and Structure of Spontaneously Formed

DOI: 10.1021/acs.cgd.9b00146
Cryst. Growth Des. 2019, 19, 2461−2469

Wurtzite GaN Nanorods on Cubic Si(001) Surface. *Cryst. Growth Des.* **2013**, *13*, 2407−2412.
(30) Gómez, V. J.; Gačević, Z.; Soto-Rodríguez, P. E. D.; Aseev, P.; Nötzel, R.; Calleja, E.; Sánchez-García, M. A. Comparative Study of Single InGaN Layers Grown on Si(111) and GaN(0001) Templates: The Role of Surface Wetting and Epitaxial Constraint. *J. Cryst. Growth* **2016**, *447*, 48−54.
(31) Dadgar, A.; Veit, P.; Schulze, F.; Bläsing, J.; Krtschil, A.; Witte, H.; Diez, A.; Hempel, T.; Christen, J.; Clos, R.; Krost, A. MOVPE Growth of GaN on Si - Substrates and Strain. *Thin Solid Films* **2007**, *515*, 4356−4361.
(32) Morin, S. A.; Bierman, M. J.; Tong, J.; Jin, S. Mechanism and Kinetics of Spontaneous Nanotube Growth Driven by Screw Dislocations. *Science* **2010**, *328*, 476−480.
(33) Bolshakov, A. D.; Mozharov, A. M.; Sapunov, G. A.; Shtrom, I. V.; Sibirev, N. V.; Fedorov, V. V.; Ubyivovk, E. V.; Tchernycheva, M.; Cirlin, G. E.; Mukhin, I. S. Dopant-Stimulated Growth of GaN Nanotube-like Nanostructures on Si(111) by Molecular Beam Epitaxy. *Beilstein J. Nanotechnol.* **2018**, *9*, 146−154.
(34) Schuster, F.; Hetzl, M.; Weiszer, S.; Garrido, J. A.; De La Mata, M.; Magen, C.; Arbiol, J.; Stutzmann, M. Position-Controlled Growth of GaN Nanowires and Nanotubes on Diamond by Molecular Beam Epitaxy. *Nano Lett.* **2015**, *15*, 1773−1779.
(35) Wei, P. C.; Chen, L. C.; Chen, K. H. Surface Diffusion Controlled Formation of High Quality Vertically Aligned InN Nanotubes. *J. Appl. Phys.* **2014**, *116*, 124301.
(36) Fernández-Garrido, S.; Koblmüller, G.; Calleja, E.; Speck, J. S. In Situ GaN Decomposition Analysis by Quadrupole Mass Spectrometry and Reflection High-Energy Electron Diffraction. *J. Appl. Phys.* **2008**, *104*, 033541.
(37) Bruno, G.; Losurdo, M.; Kim, T. H.; Brown, A. Adsorption and Desorption Kinetics of Ga on GaN(0001): Application of Wolkenstein Theory. *Phys. Rev. B: Condens. Matter Mater. Phys.* **2010**, *82*, 075326.
(38) Brandt, O.; Sun, Y. J.; Däweritz, L.; Ploog, K. H. Ga Adsorption and Desorption Kinetics on M-Plane GaN. *Phys. Rev. B: Condens. Matter Mater. Phys.* **2004**, *69*, 165326.
(39) Consonni, V. *Wide Band Gap Semiconductor Nanowires 1: Low-Dimensionality Related Effects and Growth*; Consonni, V., Feuillet, G., Baptist, R., Eds.; Wiley, 2014; pp 177−213.
(40) Kaganer, V. M.; Fernández-Garrido, S.; Geelhaar, L.; Calleja, E.; Sabelfeld, K. K.; Grandal, J.; Gotschke, T.; Brandt, O. Self-Regulated Radius of Spontaneously Formed GaN Nanowires in Molecular Beam Epitaxy. *Nano Lett.* **2013**, *13*, 3274−3280.
(41) Consonni, V.; Hanke, M.; Knelangen, M.; Geelhaar, L.; Trampert, A.; Riechert, H. Nucleation Mechanisms of Self-Induced GaN Nanowires Grown on an Amorphous Interlayer. *Phys. Rev. B: Condens. Matter Mater. Phys.* **2011**, *83*, 035310.
(42) Adachi, S. *Optical Constants of Crystalline and Amorphous Semiconductors*; Springer Science; Springer: Boston, MA, 1999.
(43) Kaminska, K.; Amassian, A.; Martinu, L.; Robbie, K. Growth of Vacuum Evaporated Ultraporous Silicon Studied with Spectroscopic Ellipsometry and Scanning Electron Microscopy. *J. Appl. Phys.* **2005**, *97*, 013511.
(44) Jones, S. B.; Friedman, S. P. Particle Shape Effects on the Effective Permittivity of Anisotropic or Isotropic Media Consisting of Aligned or Randomly Oriented Ellipsoidal Particles. *Water Resour. Res.* **2000**, *36*, 2821−2833.
(45) Gospodyn, J.; Sit, J. C. Characterization of Dielectric Columnar Thin Films by Variable Angle Mueller Matrix and Spectroscopic Ellipsometry. *Opt. Mater. (Amsterdam, Neth.)* **2006**, *29*, 318−325.

DOI: 10.1021/acs.cgd.9b00146
Cryst. Growth Des. 2019, 19, 2461−2469

Publication VII

Simultaneous optical and electrical characterization of GaN nanowire arrays by means of vis-IR spectroscopic ellipsometry

A. J. Santos, B. Lacroix, E. Blanco, S. Hurand, V. J. Gómez, F. Paumier, T. Girardeau, D. L. Huffaker, R. García, F. M. Morales

The Journal of Physical Chemistry C 124 (2020) 1535−1543

THE JOURNAL OF PHYSICAL CHEMISTRY C

Article

Cite This: J. Phys. Chem. C 2020, 124, 1535−1543

pubs.acs.org/JPCC

Simultaneous Optical and Electrical Characterization of GaN Nanowire Arrays by Means of Vis-IR Spectroscopic Ellipsometry

Antonio J. Santos,[†,‡] Bertrand Lacroix,[†,‡] Eduardo Blanco,[‡,§] Simon Hurand,[∥] Víctor J. Gómez,[⊥,@] Fabien Paumier,[∥] Thierry Girardeau,[∥] Diana L. Huffaker,[⊥,#] Rafael García,[†,‡] and Francisco M. Morales*[,†,‡]

[†]Department of Materials Science and Metallurgical Engineering and Inorganic Chemistry, Faculty of Sciences, University of Cádiz, 11510 Puerto Real, Cádiz, Spain

[‡]IMEYMAT: Institute of Research on Electron Microscopy and Materials, University of Cádiz, 11510 Puerto Real, Cádiz, Spain

[§]Department of Condensed Matter Physics, Faculty of Sciences, University of Cádiz, 11510 Puerto Real, Cádiz, Spain

[∥]Institut Pprime, UPR 3346 CNRS-Université de Poitiers-ENSMA, SP2MI, 86962 Futuroscope-Chasseneuil, France

[⊥]School of Engineering, Cardiff University, CF24 3AA Cardiff, United Kingdom

[#]School of Physics and Astronomy, Cardiff University, CF24 3AA Cardiff, United Kingdom

Supporting Information

ABSTRACT: We report an original and straightforward method for both optical and electrical characterization of vertical GaN nanowire arrays epitaxially grown on silicon through visible-infrared spectroscopic ellipsometry methods. For the initial purpose of adding new inputs to the ellipsometry model, focused ion-beam tomography experiments were conducted to extract porosity/depth profiles of these systems. To reproduce the optical free-carrier behavior in the infrared, the ellipsometric data acquired were fitted to an anisotropic Bruggeman model including Tauc-Lorentz and Drude oscillators, which enabled the determination of carrier density and in-grain mobility. The nice agreement of these results with those obtained by combining Hall effect measurements, X-ray diffraction, and transmission electron microscopy studies supported the validity of the proposed method, opening new horizons in the characterization of nanowire-based semiconducting layers.

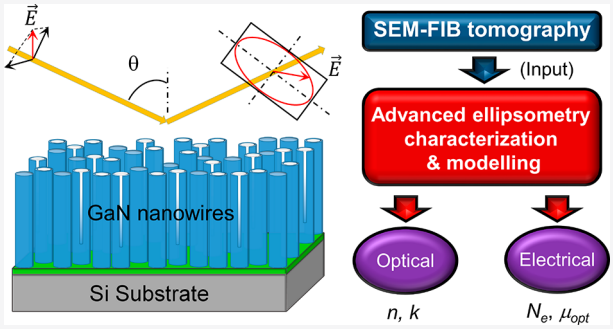

INTRODUCTION

Gallium nitride (GaN) nanowire (NW) arrays grown by plasma-assisted molecular beam epitaxy (PAMBE) have recently attracted the attention of the scientific community due to their high crystalline quality and low defect density[1−4] and their unique electrical and optical properties.[5−7] By tuning the growth conditions, the size and arrangement of the nanowires, and thus the porosity, can be controlled so as to modulate the optical and electrical properties of the system.[5,8−11] Thanks to its high surface-to-volume ratio, tunable refractive index and bandgap, high light extraction efficiency and quantum efficiency, GaN arrays have been erected as a promising material not only for the development of optoelectronic and optical devices such as field-effect transistors (FETs),[12,13] light-emitting diodes (LEDs),[6,14] laser diodes,[15] and detectors,[16] but also for photoelectrochemical water splitting[17,18] and energy storage[19] applications.

While the optical characterization of GaN nanowire and nanorod arrays through spectroscopic ellipsometry (SE),[9,10] polarized-goniometry,[20] or reflectivity spectroscopy[11] is well reported in the literature, the characterization of electrical properties related to conductivity, like carrier concentration and mobility, presents some difficulties associated with the geometry of this kind of structure.[4,21] Up to now, the majority of the studies are focused on Hall effect and field effect measurements performed on single nanowires after fabricating multiple contacts.[22−25] However, given the challenges aforementioned, very few studies based on the electrical characterization of complete nanowire films have been reported at the time of the submission of this work.[26−28] Hence, the development of novel and alternative methodologies for the electrical characterization of nanowire layers, such as noncontact THz spectroscopic measurements,[29] is crucial.

In this work, we report an alternative and straightforward way for both optical and electrical characterization of high-quality single crystalline GaN self-assembled NW films by means of visible-IR spectroscopic ellipsometry (SE), which is a

Received: November 11, 2019
Revised: December 20, 2019
Published: December 27, 2019

DOI: 10.1021/acs.jpcc.9b10556
J. Phys. Chem. C 2020, 124, 1535−1543

cheap, fast, and nondestructive technique that can be used as a systematic characterization tool even for industrial processes. These porosity-controlled layers of GaN nanostructures were grown in a compact fashion by PAMBE. The porosity profiles along the layer thickness, which are not constant due to the presence of different nanostructure shapes from solid (SNW) to c-shape (CNW) and hollow (HNW) nanowires, were extracted through focused ion-beam (FIB) tomography reconstructions (slice and view). In order to reproduce the SE measurements, these porosity profiles were incorporated into an optical model through an effective-medium approximation in the framework of an anisotropic Bruggeman model, in which the optical constants of GaN are modeled by a combination of a Tauc-Lorentz oscillator and a Drude oscillator. This approach not only allows one to determine porosity, thickness, and optical constants of GaN NW films but also carrier densities and optical mobilities. The validity of the defined model is supported by combining Hall effect measurements, X-ray diffraction (XRD), and transmission electron microscopy (TEM) techniques including high-resolution (HRTEM) and energy-dispersive X-ray spectroscopy (EDX).

EXPERIMENTAL SECTION

Wurtzite GaN nanowire layers were grown on chemically cleaned p-type Si(111) or (100) substrates by PAMBE along the [0001] direction and epitaxially aligned with the underlying Si substrate, following the same procedure as the one described in a previous study.[10] For 3D reconstructions, two different systems were used to acquire FIB-SEM tomography data sets: a Scios 2 DualBeam microscope from Thermo Scientific and a CrossBeam 350 microscope from ZEISS. Those data sets consist of stacks of SEM images recorded using backscattered electrons and an acceleration voltage of 1.4 kV. The optical and electrical properties of each sample were evaluated by standard vis-IR spectroscopic ellipsometry at incident angles of 65°, 75°, and 85°. These measurements were performed with a J. A. Woollam M2000XI (from 400 to 1700 nm) and J. A. Woollam IR-VASE Mark II (from 1700 to 24000 nm), respectively. In order to confirm the veracity of the electrical properties obtained through vis-IR SE experiments, room temperature Hall Effect measurements were conducted using a Van der Pauw Ecopia AMP-55 Hall measurement system in the presence of a magnetic field. The crystallographic structure was investigated by X-ray diffraction (XRD) experiments which were performed using a Seifert XRD 3000 diffractometer fitted with a copper source and a 1 mm beam collimator. To obtain additional insights into the nanostructure, high-resolution transmission electron microscopy (TEM) experiments were conducted in a FEI Talos F200S analytical microscope operated at 200 kV and equipped with a Super-X energy-dispersive X-ray spectrometry (EDX) system that includes two silicon drift detectors. Local compositional analyses were performed by combining high-angle annular dark-field imaging (HAADF) and EDX acquisitions using the scanning (STEM) mode. Electron-transparent cross-sectional FIB lamellae were prepared for TEM observations by using the aforementioned FIB systems.

RESULTS AND DISCUSSION

With the additional purpose of examining the effect of substrate orientation on optical and electrical properties, the samples selected for this study were T2 and T2′ (following the nomenclature of ref 10.), i.e., the same growth conditions but different substrate orientations: Si(111) and Si(100), respectively.

These two samples are composed by a mixture of three different kind of NWs: SNWs filled and with hexagonal facets, HNWs, with solid bases which evolve into hollow structures when reaching a critical thickness, and CNWs, similar to HNWs but partially opened longitudinally. More in-depth studies of the structure and morphology of these three types of nanowires as well as the effect that growth conditions have on both the overall porosity and the optical properties of such systems can be found in ref 10. Due to the presence of this variety of nanostructures, the porosity profile along the Z direction turns uncertain and nonlinear, hindering the optical characterization of these systems.[30] In order to overcome this difficulty, representative areas of T2 and T2′ samples were explored with the aim of extracting their porosity profiles by performing FIB tomography experiments. In this regard, two different FIB systems (Thermo Scientific Scios 2 DualBeam and ZEISS CrossBeam 350) were employed to carry out 3D reconstructions and analyses of T2 and T2′ volumes, respectively (see Supporting Information Section I for a detailed description of the experimental data acquisition, segmentation, 3D reconstruction, and porosity profile extraction).

Figure 1a,b displays volume visualizations of T2 and T2′ samples respectively together with their porosity profiles along the surface normal (Figure 1c,d). Note that the planar views obtained by data segmentation at depths close to the surface reveal the characteristic morphologies of GaN NWs (SNW, HNW, and CNW). As a first approach, a significant difference between the porosity profiles of both specimens can be appreciated. Whereas one of them (T2) experiences a first stage in which the porosity remains constant with the depth, followed by a progressive increase in porosity, the other (T2′) first experiments a slight decrease in porosity up to reaching a critical thickness from which it increases sharply. Furthermore, there are also differences in the total thickness of both samples (around 550 and 750 nm for T2 and T2′, respectively). In this way, the shapes of these two profiles only can be explained by considering that nanowires are composed by solid (filled) bases that evolve (or not) into hollow structures (HNW or CNW), justifying the initial step of constant porosity (first 300 nm of thickness) in sample T2. These results are consistent with the assumptions made in previous works.[10] On the other hand, the preliminary drop in porosity in sample T2′ could be associated with the broadening of solid bases that occur after attaining 100−150 nm thickness.

Once the evolution of the porosity along the NW layer is known, vis-IR SE experiments were performed in areas close to 3D reconstructions with the purpose of conducting a full, accurate, and comparable characterization of these systems. To do so, visible and infrared spectroscopic ellipsometry measurements were performed at incidence angles of 65°, 75°, and 85°. Both spectra were acquired separately and then were spliced and treated with the WVASE software from J. A. Woollam. In a first stage of the study, the data acquired were fitted to an Anisotropic Bruggeman Effective Medium Approximation (ABEMA) model composed by a mixture of wurtzite GaN, whose optical constants are modeled by the ones obtained for high-quality single-crystalline α-GaN layers[31] and void. A 2 nm-thick layer of silicon nitride (Si_3N_4) located between the Si

DOI: 10.1021/acs.jpcc.9b10556
J. Phys. Chem. C 2020, 124, 1535−1543

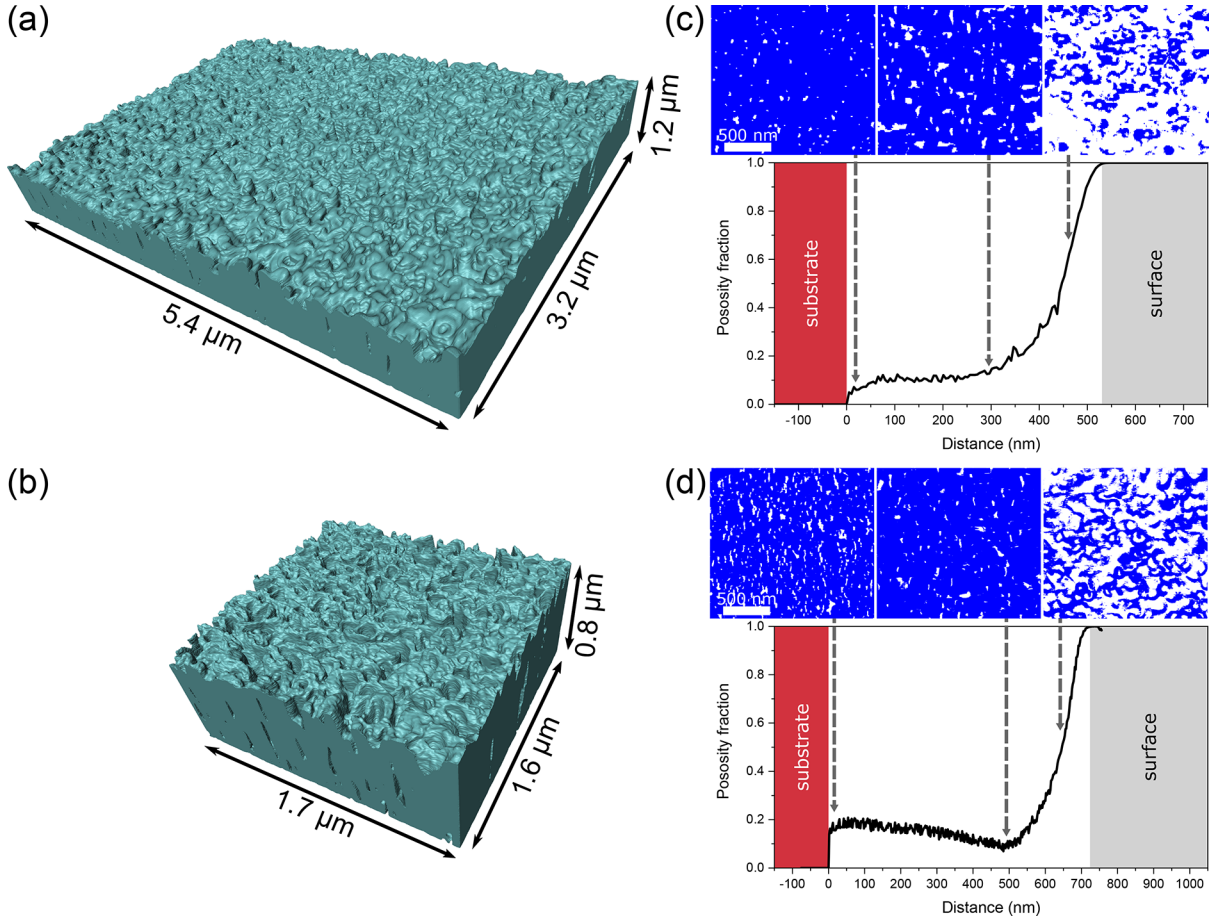

Figure 1. 3D reconstructions of the NW arrays in (a) T2 and (b) T2′ samples through FIB tomography. Volume sizes are 5440 × 3222 × 1230 nm^3 and 1744 × 1602 × 834 nm^3, respectively. Porosity profiles of (c) T2 and (d) T2′ samples extracted along the surface normal together with some planar views obtained by data segmentation at different depths (GaN material and voids are shown in blue and white colors, respectively). Note that these images were cut to show the same field of view in both samples, for comparison.

substrate and the nanowire layer was also included in the optical model. With the aim of reflecting the columnar geometry of the film with NWs growing perpendicular to the substrate, the depolarization factor in the extraordinary (out-of-plane) direction (q_z) was fixed to 0, whereas the ordinary or in-plane ones (q_x and q_y) were fixed at 1/2 (uniaxial anisotropy).[32,33] Moreover, the porosity profiles extracted by FIB tomography 3D reconstructions were incorporated into the model in order to reproduce the variation in the refractive index (n) along the Z direction (as a function based graded-index layer). On the other side, the anisotropy associated with the wurtzite GaN structure was considered negligible compared to the anisotropy associated with the columnar structure. Indeed, wurtzite GaN has a uniaxial structure, and its intrinsic birefringence, which is the difference $\Delta n = n_z - n_{x,y}$ between extraordinary optical index n_z and ordinary one $n_{x,y}$ is of the order of 0.02 (in absolute terms) in the visible range according to ref 31 (see Figure S8). On the other hand, by modeling GaN as an isotropic material and implementing it into the ABEMA model above-mentioned, the birefringence in the visible range is around 0.1 in the visible range as one can see on Figure 2c,d, that is, 5 times higher than the intrinsic birefringence of wurtzite GaN. We may therefore neglect the intrinsic uniaxial structure of GaN and conclude that the observed anisotropy is mainly due to the elongated shape of the NWs.

Despite the fact that this model provides a fine agreement to the experimental data in the visible range, it fails to reproduce the absorption in the IR range, as can be seen in Figure 2a,b. Indeed, the presence of a weak but non-negligible level of doping in the GaN results in free carrier absorption in the IR range. In order to model correctly this absorption, we replace the tabulated optical constants from ref 31 for wurtzite GaN by a combination of two oscillators: (i) a Tauc-Lorentz Oscillator (TLO) modeling the direct band gap (E_g) absorption of GaN[34] and (ii) a Drude Oscillator (DO) modeling the free-carrier behavior in the IR range[35] (a scheme of the optical model is presented in Figure S2). From 1.5 to 3 eV, that is, in the visible range, the parameters of the TLO were adjusted onto the values of the dielectric constants for wurtzite GaN from ref 31. The advantage of using a Tauc-Lorentz oscillator over, for example, a simple Lorentz oscillator, is to impose a more realistic value of zero for ε_2 below the gap. Also, a TLO permits the combination with another oscillator, here a Drude oscillator, unlike, for example, a simple Cauchy model. In this way, a DO was incorporated to represent free-carrier absorption by fitting the ellipsometry data in the lower energy region, considering an effective mass (m^*) of 0.20 for wurtzite GaN,[36] while the free carrier density $N_{e(opt)}$ and optical mobility μ_{opt} are the parameters to be fitted. Indeed, the Drude model is appropriate to characterize samples with carrier

DOI: 10.1021/acs.jpcc.9b10556
J. Phys. Chem. C 2020, 124, 1535−1543

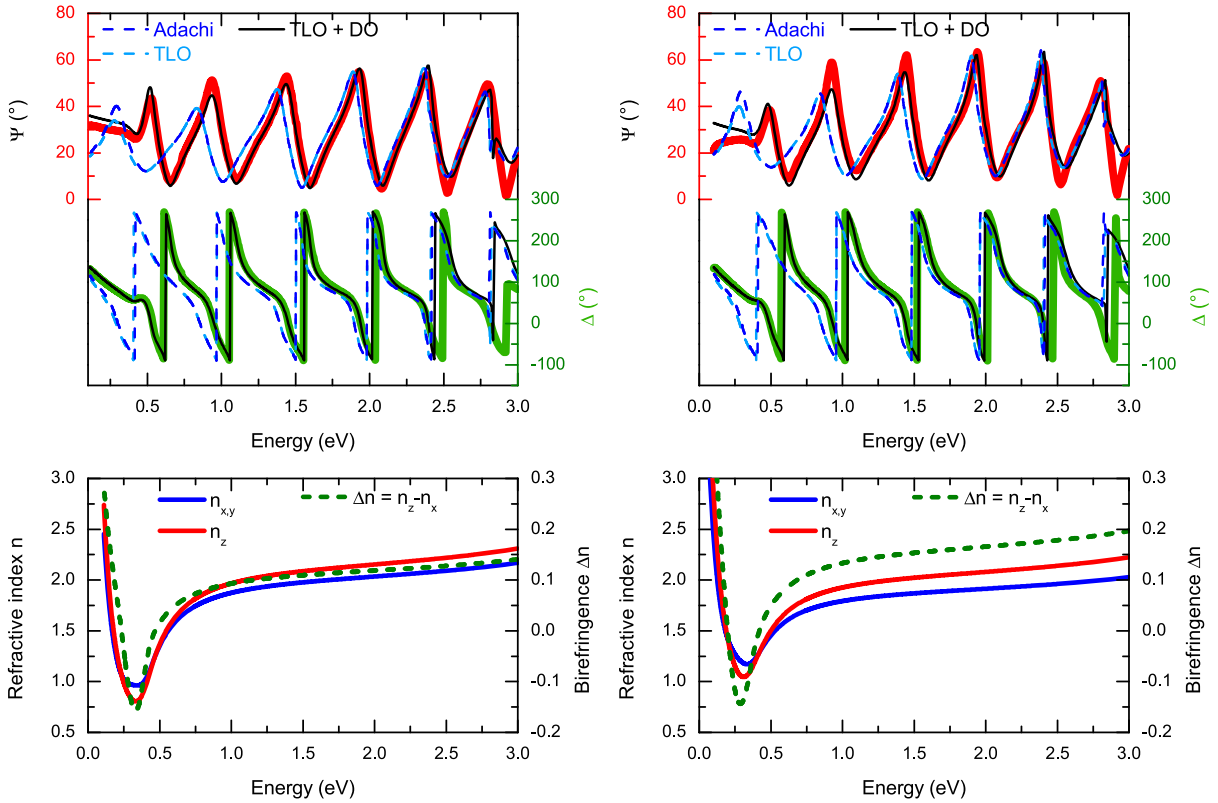

Figure 2. Measured spectroscopic ellipsometry angles Ψ (red) and Δ (green) for (a) T2 and (b) T2′ samples at an incident angle of 65°. Thick solid lines represent the experimental measurements. Thin solid black lines represent the best-fit achieved using the SE model (ABEMA including TLO + DO). For comparison, dashed lines represent the best-fit obtained with an ABEMA model with only a TLO (light blue) or using Adachi et al. (ref 31.) data (dark blue) for GaN. In-plane (blue solid lines) and out-of-plane (red solid lines) refractive indices and birefringence (dashed green lines) of (c) T2 and (d) T2′ samples obtained from simulations using the SE model.

concentrations down to 10^{18} cm^{-3} when infrared spectroscopic ellipsometry is used.[37]

The fittings obtained for T2 and T2′ samples after incorporating TLO and DO models are shown in Figure 2a,b, respectively, together with the fitting obtained by using either a TLO alone (TLO) or the data from ref 31 (Adachi) for GaN. As one can see, a TLO alone or Adachi data provide a quite good description of the measured Ψ and ΔSE values in the visible range. However, while approaching the IR range, a shift in energy between the modeled and measured oscillations of Ψ and Δ is noticeable. Moreover, they predict oscillations below 0.4 eV that are not observed. The addition of a Drude oscillator to the model resolves these issues: the modeled oscillations of Ψ and Δ remain in phase with the measured ones even in the IR range, and their cutoff at 0.4 eV is correctly predicted. We emphasize here that this cutoff provides a very robust criterion to fit the carrier density: the Mean Square Error (MSE) increases by 10% when a relative change of 10% of $N_{e(opt)}$ is applied to the model (see Figure S6). With this criterion, the relative uncertainty on the fitted value of $N_{e(opt)}$ is

Table 1. Summary of the Electrical Characterization of T2 and T2′ Samples through Hall Effect Measurements and Vis-IR SE[a]

	sample T2	sample T2′
Hall voltage, V_H (V)	$(-4.4 \pm 0.2) \times 10^{-6}$	$(-4.4 \pm 0.9) \times 10^{-6}$
sheet resistance, R_s (Ω)	111.5 ± 0.1	1881.2 ± 6.0
Hall carrier density, $N_{e(Hall)}$ (e^-/cm^3)	$(1.6 \pm 0.1) \times 10^{20}$	$(1.2 \pm 0.3) \times 10^{20}$
Hall mobility, μ_{Hall} (cm^2/V s)	6.8 ± 0.3	0.4 ± 0.1
optical carrier density, $N_{e(opt)}$ (e-/cm^3)	$(1.3 \pm 0.1) \times 10^{20}$	$(1.1 \pm 0.1) \times 10^{20}$
optical mobility, μ_{opt} (cm^2/V s)	45 ± 5	34 ± 5

[a]Hall effect experiments were conducted by supplying a current of 100 μA and inducing a magnetic field of 0.58 T. The thicknesses considered for these calculations were obtained from 3D reconstructions (Figure 1).

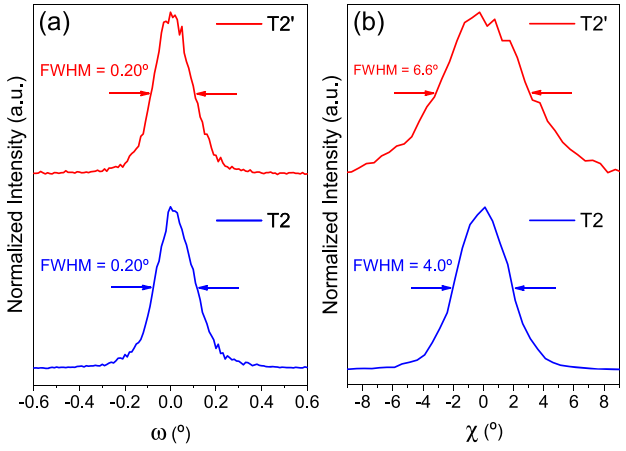

Figure 3. XRD rocking curves: (a) ω-scans and (b) χ-scans of the GaN 0002 reflection for T2 (blue lines) and T2′ (red lines) samples.

DOI: 10.1021/acs.jpcc.9b10556
J. Phys. Chem. C 2020, 124, 1535−1543

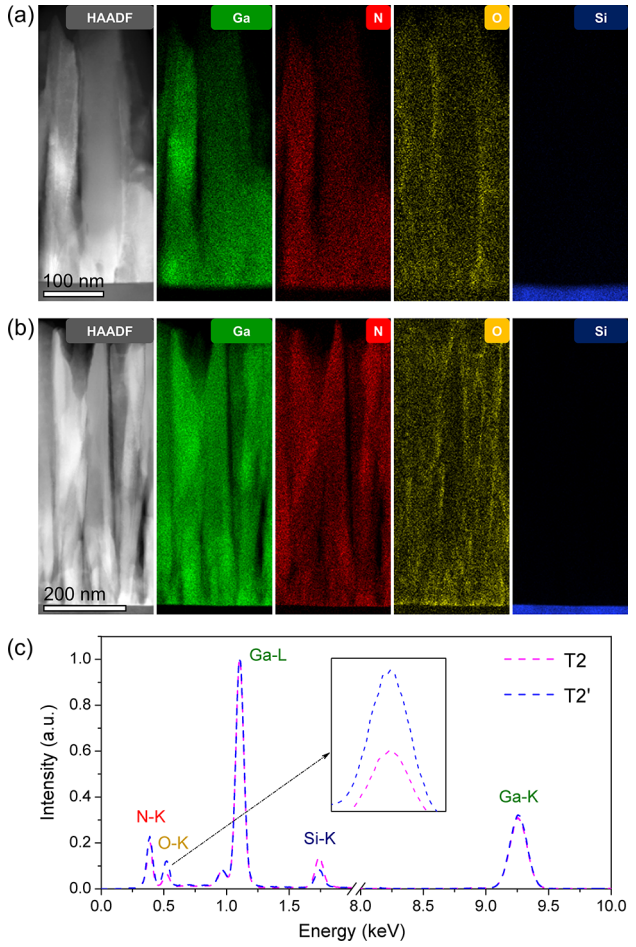

Figure 4. STEM-HAADF and EDX elemental maps of (a) T2 and (b) T2′ samples obtained for Ga, N, O, and Si atoms. (c) EDX spectra, normalized at the Ga-L$_\alpha$ peak (1098 eV), for T2 (magenta dashed line) and T2′ (blue dashed line) samples. The inset corresponds to the feature of the O−K$_\alpha$ peak (525 eV).

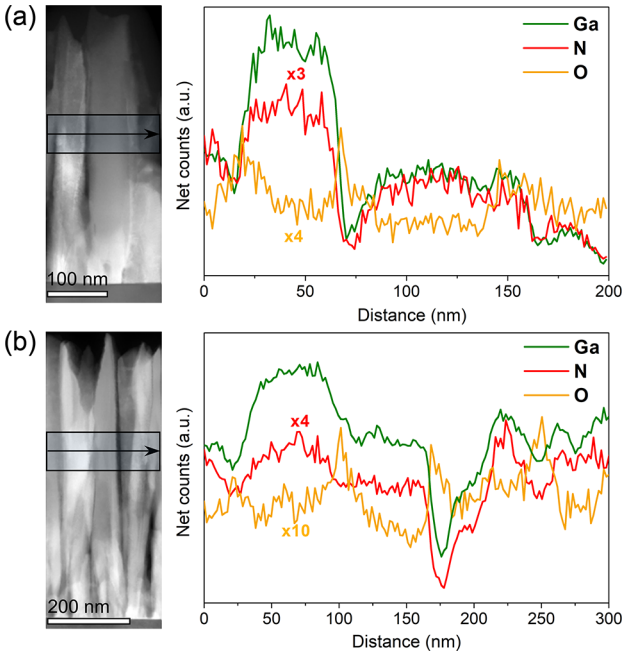

Figure 5. STEM-HAADF and Ga, N, and O EDX elemental profiles for (a) T2 and (b) T2′ samples. Note that such profiles were integrated across the NWs following the direction indicated by the arrows.

±10% for values of $N_{e(opt)}$ as low as 1×10^{18} e/cm^3. That is, ± 0.1×10^{20} e/cm^3 for a fitted value of $N_{e(opt)} = 1.3 \times 10^{20}$ e/cm^3 for sample T2.

The evolutions of the in-plane and out-of-plane refractive indices along with the birefringence of T2 and T2′ NW layers, obtained from the enhanced ellipsometry model over the vis-IR range, are displayed in Figure 2c,d, respectively. As expected, the refractive indices of both samples in the visible spectrum are smaller than that of bulk GaN due to the presence of voids. Nevertheless, both layers start to experience a metallic behavior at energies around 0.4 eV which corresponds to the onsets of free-carrier absorption, leading to an increase in refractive indices. Also note that, from visible to near-infrared, the refractive indices in the Z direction are greater than that corresponding to the in-plane one. Likewise, the values of birefringence obtained in this spectral range let us evidence that the optical anisotropy in T2′ is stronger than in T2.

Additionally, the DO parameters ($N_{e(opt)}$ and μ_{opt}) provided by the SE model are $N_{e(opt)}$ (T2) = $(1.3 \pm 0.1) \times 10^{20}$ e$^-$/cm^3 and μ_{opt} (T2) = 45 ± 5 cm^2/V s; $N_{e(opt)}$ (T2′) = $(1.1 \pm 0.1) \times 10^{20}$ e$^-$/cm^3 and μ_{opt} (T2′) = 34 ± 5 cm^2/V s. Note that the doping level of both samples is surprisingly high, taking into account that they were not intentionally doped. With regard to the optical mobility, the values extracted from the SE model are in good agreement with the electrical mobility obtained in the literature by four-point measurement for single GaN NWs.[4,38] Besides, these results are also consistent with the values of mobility obtained from the Hilsum equation[39] adapted for the case of GaN NWs,[40] that is, 32.2 cm^2/V s for T2 and 33.2 cm^2/V s for T2′ considering the doping level predicted by the SE model. This is because the optical measurements performed supply intragranular information, which is equivalent to the mean of a set of measurements carried out on different single NWs.

In order to confirm the values of carrier density and mobility predicted by SE as well as to validate the defined model, room temperature Hall Effect measurements were conducted. For this purpose, four contacts were placed at the corners of squared-shaped samples which were cut in such way that the same areas as in previous experiments were studied.

An overview of the results obtained from the Hall effect measurements for T2 and T2′ samples can be found in Table 1. The negative sign of the Hall voltage indicates that the majority of the carriers were electrons for both samples (n-type semiconductor). Moreover, the values of carrier densities measured are in accordance with those predicted by SE, which confirms the high n-doping level. However, great differences between the electrical behavior of T2 and T2′ samples are observed. As can be seen, sample T2′ exhibits a greater opposition to the flow of electric current than T2 (just over 1 order of magnitude). It should be also noted that the mobility measured by Hall effect, in addition to being surprisingly low, does not correspond with the one predicted by the SE model. The latter is expected since SE provides information related to the free-carrier mobility within grains (μ_{opt}), while the Hall effect give us information about the total mobility of the layer (μ_{Hall}), including the effects of grain boundaries as well as the porosity of the structure. Conversely, $N_{e(Hall)}$ values are not

DOI: 10.1021/acs.jpcc.9b10556
J. Phys. Chem. C 2020, 124, 1535−1543

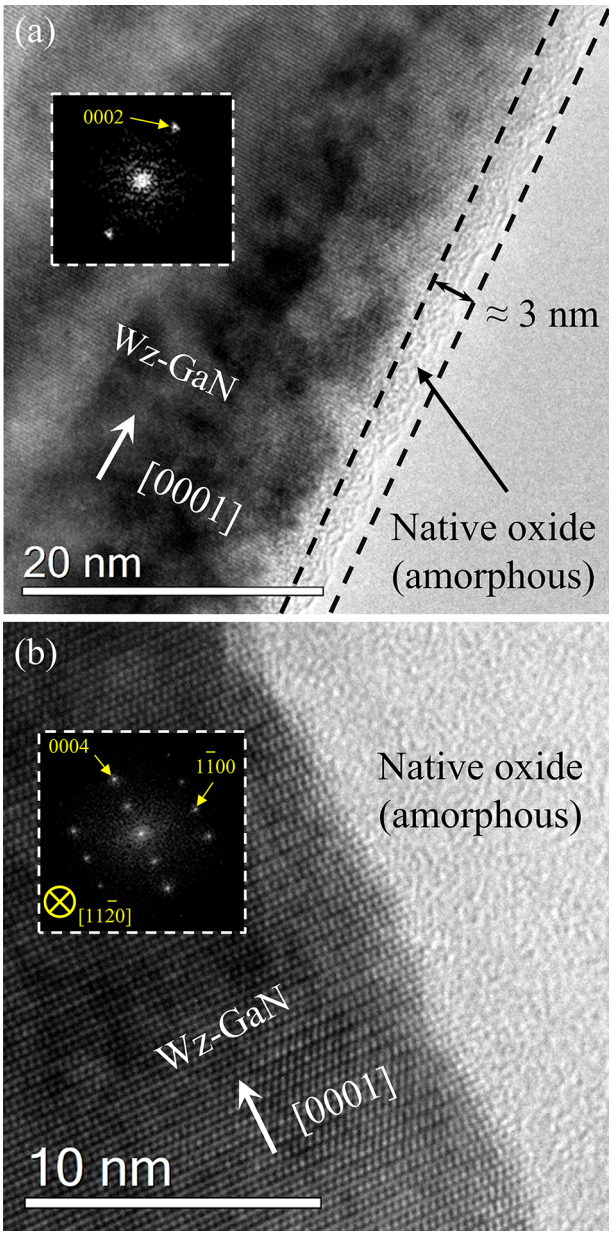

Figure 6. High-resolution TEM micrographs and corresponding FFT diffractions of single nanowires of (a) T2 and (b) T2′ samples. Note that these TEM observations were conducted on two FIB lamellae prepared by using the same SEM-FIB systems as for FIB tomography experiments.

affected by the porosity,[41] so it is relevant to compare them directly with those resulting from SE ($N_{e(opt)}$). Thus, μ_{Hall} values suggest that the mobility in GaN NW arrays is dominated by intergrain barriers.

This assumption is also supported by the shape analyses of XRD rocking curves (ω and χ-scans) of 0002 GaN diffraction peaks. As can be appreciated in Figure 3a, the full width at half-maximum (fwhm) values of the ω-scans are rather small for T2 and T2′ samples (0.20° in both cases) which not only indicates the good crystal quality of nanowires (low density of dislocations) but also a good epitaxial alignment between the GaN nanostructure and the single-crystalline Si substrate (the out-of-plane epitaxial relationship is GaN(0001)||Si(111) for T2 and GaN(0001)||Si(001) for T2′). In addition, χ-scans (Figure 3b) reveal that the slight misorientation of the (0002) planes along the growth direction (tilt) is more significant in T2′ than in T2.

Once we come to this point, it is time to account for the unintentional high doping concentration of the GaN NW layers. With the aim of elucidating the origin of the doping, EDX chemical analyses were carried out in both samples. The Thermo Scientific Velox user interface was used for data acquisition and processing. Quantification of the EDX data was performed using the standardless method. In order to minimize errors during this step, intensities of the different peaks were extracted with a great care after background subtraction with a multipolynomial approach. Since this approach can lead to inaccuracy in the quantitative composition determination, especially for low Z elements like O and N, qualitative analyses were conducted. STEM high-angle annular dark field imaging (HAADF) and EDX elemental maps (see Figure 4a,b) reveal a remarkable presence of oxygen distributed throughout both films. Note that the oxygen signal becomes greater on the edges of the nanowires, where projections only bring contributions of the surrounding material, suggesting that oxygen is mainly accumulated at NW surfaces (see elemental profiles obtained for both samples in Figure 5a,b). Likewise, EDX normalized spectra (Figure 4c) of both samples reveal that the amount of oxygen in T2′ is larger than the one detected in T2. In this context, it is well-known that high concentrations of oxygen in GaN can cause high levels of electron concentration.[42−45] Therefore, in consideration of these results, it could be assumed that the observed GaN NWs doping is linked to oxygen impurities.

By contrast, the explanation for the low total mobility of such GaN nanostructures is more complex. In addition to the effect of porosity, which acts by reducing the volume in which the current flows,[46] two additional reasons could contribute to this phenomenon: (i) surface state trapping and (ii) the formation of native oxide on the surface. Generally, electrical properties of nanowire-structured semiconductors are sensitive to the status of their surfaces. One of the main problems of nanostructured systems is the decrease in the carrier mobility due to the scattering from the surface states. Furthermore, this effect becomes even more significant for the case of NWs because of their high surface-to-volume ratio, which leads to free carriers within the wire being trapped at surface traps.[16,47] Nonetheless, this phenomenon would only affect the mobility inside nanowires which was proved not to be responsible for the low total mobility of the studied systems.

Another consequence of the great surface-to-volume ratio is the formation of amorphous layers of native oxide surrounding the nanowires when they are exposed to air. This issue has been previously reported by other authors[21,48] resulting in a detrimental effect on electrical properties since this oxide shell acts as a barrier for the motion of electrons among nanowires. According to similar studies,[49,50] this fact might also provide an explanation for the high levels of electron concentration in these GaN nanostructures: part of the oxygen atoms could diffuse from the oxide layer into the GaN nanowire at room temperature, originating oxygen impurities. HRTEM micrographs and fast Fourier transform (FFT) diffractions of isolated wurtzite GaN nanowires of T2 (Figure 6a) and T2′ (Figure 6b) samples evidence this formation of amorphous layers of native oxide on the surface. Note that the amount of oxide generated on the surface of the nanowire belonging to T2′ is considerably larger than that observed in the NW of T2. The latter, in addition to supporting the results obtained

DOI: 10.1021/acs.jpcc.9b10556
J. Phys. Chem. C 2020, 124, 1535−1543

through EDX analyses, could be associated with a major susceptibility to oxidation of T2′ compared to the T2 sample, leading to a minor mobility of the T2′ sample as Hall effect measurements revealed. Thus, we propose that both the native oxide layer formed on cylinder-like surfaces and porosity are the limiting factors on the global mobility of GaN nanowire array films.

After reaching these conclusions, it is clear that the surface-to-volume ratio plays a vital role in both optical and electrical properties of GaN NW arrays. The insertion of porosity allows one to cut down the effective refractive index of the layer. However, increasing the porosity implies greater surface-to-volume ratios, which has been proven to have a detrimental effect on the electron mobility because the formation of native oxide shells within the semiconducting layers is favored when the surface exposed to air is greater.[51] Hence, by tuning the growth conditions, the porosity of the nanostructures can be controlled, making these systems more appropriate for optical or electrical applications.

CONCLUSIONS

In summary, optical and electrical properties of GaN nanowire arrays grown on Si (111) and Si (100) by PAMBE were simultaneously explored by means of an innovative methodology based on vis-IR spectroscopic ellipsometry. For a better description of these nanostructures, porosity profiles extracted by FIB tomography reconstructions were implemented into an ABEMA model where the optical constants of GaN were modeled by a multioscillator approach (TLO and DO) which enabled us to determine the carrier density and intragrain mobility of such nanostructures. These results evidenced electron concentrations of about 10^{20} cm^{-3} and optical mobilities comparable to the one reported for individual GaN nanowires (30−50 cm^2/V s). Hall effect measurements, XRD, and transmission electron microscopy (STEM-EDX and HRTEM) studies not only provided a confirmation of the results predicted by the SE model but also let us elucidate that the oxygen impurity was the responsible for the high doping level and that the total mobility of such GaN arrays was mainly limited by the combined effect of porosity and surface oxidation of individual nanowires.

ASSOCIATED CONTENT

Supporting Information

The Supporting Information is available free of charge at https://pubs.acs.org/doi/10.1021/acs.jpcc.9b10556.

Three-dimensional FIB-SEM tomography reconstructions (experimental data acquisition; data processing; alignment, rotation, cropping, and denoising; segmentation and porosity quantification), optical modeling (optical model; fitting procedure; relevance of the Drude Oscillator; lowest detectable carrier concentration; uncertainty of the fit parameters; intrinsic anisotropy of GaN; and plasmonic effects) and additional references (PDF)

AUTHOR INFORMATION

Corresponding Author

*E-mail: fmiguel.morales@uca.es.

ORCID

Antonio J. Santos: 0000-0003-3776-7080

Bertrand Lacroix: 0000-0001-7916-6377

Víctor J. Gómez: 0000-0003-2364-8814

Francisco M. Morales: 0000-0002-8341-2478

Present Address

[@]V.J.G.: Solid State Physics, Lund University, Box 118, S-221 00 Lund, Sweden.

Author Contributions

The manuscript was written through contributions of all authors. All authors have given approval to the final version of the manuscript.

Notes

The authors declare no competing financial interest.

ACKNOWLEDGMENTS

The authors would like to express their gratitude to Ellen Backen, applications scientist from Thermo Fisher Scientific, for the images registered at the Scios 2 HiVac system at Nanoport (Eindhoven). We would also like to acknowledge ZEISS corporations for technical assistance as well as the loaning of the CrossBeam 350 system and the data acquisition. The authors also acknowledge the support provided by the PRIMEO (Partnership for Research and Innovation in Emerging Materials for phOtonics) lab. A.J.S. would like to thank the IMEYMAT Institute and the Spanish Ministerio de Educación y Cultura for the concessions of grants (ICARO-173873 and FPU16-04386). The "Talent Attraction Program" of the University of Cádiz is acknowledged by supporting B.L. contract code E-11-2017-0117214. University of Cádiz and IMEYMAT are also thanked by financing the mutual facilities available at the UCA R&D Central Services (SC-ICYT), the UCA project reference "PUENTE PR2018-040", and the IMEYMAT project reference "AGREGADOR 2018-1". The authors would like to acknowledge the financial support provided by Sêr Cymru National Research Network in Advanced Engineering and Materials. This work was also supported by the IMATOP project funded by "Nouvelle Aquitaine" Region and by the European Structural and Investment Funds (ERDF reference P-2016-BAFE-209).

REFERENCES

(1) Sobanska, M; Zytkiewicz, Z R; Calabrese, G; Geelhaar, L; Fernandez-Garrido, S Comprehensive Analysis of the Self-Assembled Formation of GaN Nanowires on Amorphous Al_xO_y: In Situ Quadrupole Mass Spectrometry Studies. *Nanotechnology* **2019**, *30* (15), 154002.

(2) Bolshakov, A. D.; Mozharov, A. M.; Sapunov, G. A.; Shtrom, I. V.; Sibirev, N. V.; Fedorov, V. V.; Ubyivovk, E. V.; Tchernycheva, M.; Cirlin, G. E.; Mukhin, I. S. Dopant-Stimulated Growth of GaN Nanotube-like Nanostructures on Si(111) by Molecular Beam Epitaxy. *Beilstein J. Nanotechnol.* **2018**, *9* (1), 146−154.

(3) Schlager, J. B.; Sanford, N. A.; Bertness, K. A.; Barker, J. M.; Roshko, A.; Blanchard, P. T. Polarization-Resolved Photoluminescence Study of Individual GaN Nanowires Grown by Catalyst-Free Molecular Beam Epitaxy. *Appl. Phys. Lett.* **2006**, *88* (21), 213106.

(4) Mansfield, L. M.; Bertness, K. A.; Blanchard, P. T.; Harvey, T. E.; Sanders, A. W.; Sanford, N. A. GaN Nanowire Carrier Concentration Calculated from Light and Dark Resistance Measurements. *J. Electron. Mater.* **2009**, *38* (4), 495−504.

(5) Pauzauskie, P. J.; Yang, P. Nanowire Photonics. *Mater. Today* **2006**, *9* (10), 36−45.

(6) Chen, C. Y.; Zhu, G.; Hu, Y.; Yu, J. W.; Song, J.; Cheng, K. Y.; Peng, L. H.; Chou, L. J.; Wang, Z. L. Gallium Nitride Nanowire Based Nanogenerators and Light-Emitting Diodes. *ACS Nano* **2012**, *6* (6), 5687−5692.

DOI: 10.1021/acs.jpcc.9b10556
J. Phys. Chem. C 2020, 124, 1535−1543

(7) Barrigón, E.; Heurlin, M.; Bi, Z.; Monemar, B.; Samuelson, L. Synthesis and Applications of III−V Nanowires. *Chem. Rev.* **2019**, *119* (15), 9170−9220.
(8) Park, Y. S.; Lee, G.; Holmes, M. J.; Chan, C. C. S.; Reid, B. P. L.; Alexander-Webber, J. A.; Nicholas, R. J.; Taylor, R. A.; Kim, K. S.; Han, S. W.; et al. Surface-Effect-Induced Optical Bandgap Shrinkage in GaN Nanotubes. *Nano Lett.* **2015**, *15* (7), 4472−4476.
(9) Lee, J. H.; Lee, B.; Kang, J. H.; Lee, J. K.; Ryu, S. W. Optical Characterization of Nanoporous GaN by Spectroscopic Ellipsometry. *Thin Solid Films* **2012**, *525*, 84−87.
(10) Gómez, V. J.; Santos, A. J.; Blanco, E.; Lacroix, B.; García, R.; Huffaker, D. L.; Morales, F. M. Porosity Control for Plasma-Assisted Molecular Beam Epitaxy of GaN Nanowires. *Cryst. Growth Des.* **2019**, *19* (4), 2461−2469.
(11) Chen, H.-Y.; Lin, H.-W.; Wu, C.-Y.; Chen, W.-C.; Chen, J.-S.; Gwo, S. Gallium Nitride Nanorod Arrays as Low-Refractive-Index Transparent Media in the Entire Visible Spectral Region. *Opt. Express* **2008**, *16* (11), 8106.
(12) Cha, H. Y.; Wu, H.; Chandrashekhar, M.; Choi, Y. C.; Chae, S.; Koley, G.; Spencer, M. G. Fabrication and Characterization of Pre-Aligned Gallium Nitride Nanowire Field-Effect Transistors. *Nanotechnology* **2006**, *17* (5), 1264−1271.
(13) Wu, H.; Cha, H. Y.; Chandrashekhar, M.; Spencer, M. G.; Koley, G. High-Yield GaN Nanowire Synthesis and Field-Effect Transistor Fabrication. *J. Electron. Mater.* **2006**, *35* (4), 670−674.
(14) Yeh, P. C.; Hwa, M. C.; Yu, J. W.; Wu, H. M.; Tsai, H. L.; Lai, C. M.; Huang, J. J.; Yang, J. R.; Peng, L. H. Photon-Assisted Tunneling in GaN Nanowire White Light Emitting Diodes. *Phys. Status Solidi Curr. Top. Solid State Phys.* **2009**, *6* (S2), S538−S540.
(15) Gradečak, S.; Qian, F.; Li, Y.; Park, H. G.; Lieber, C. M. GaN Nanowire Lasers with Low Lasing Thresholds. *Appl. Phys. Lett.* **2005**, *87* (17), 173111.
(16) Sun, J.; Han, M.; Gu, Y.; Yang, Z. xing; Zeng, H. Recent Advances in Group III−V Nanowire Infrared Detectors. *Adv. Opt. Mater.* **2018**, *6* (18), 1800256.
(17) Ryu, S. W.; Zhang, Y.; Leung, B.; Yerino, C.; Han, J. Improved Photoelectrochemical Water Splitting Efficiency of Nanoporous GaN Photoanode. *Semicond. Sci. Technol.* **2012**, *27* (1), 015014.
(18) Park, J.-H.; Mandal, A.; Kang, S.; Chatterjee, U.; Kim, J. S.; Park, B.-G.; Kim, M.-D.; Jeong, K.-U.; Lee, C.-R. Hydrogen Generation Using Non- Polar Coaxial InGaN/GaN Multiple Quantum Well Structure Formed on Hollow n-GaN Nanowires. *Sci. Rep.* **2016**, *6*, 31996.
(19) Zhang, L.; Wang, S.; Shao, Y.; Wu, Y.; Sun, C.; Huo, Q.; Zhang, B.; Hu, H.; Hao, X. One-Step Fabrication of Porous GaN Crystal Membrane and Its Application in Energy Storage. *Sci. Rep.* **2017**, *7*, 1−9.
(20) Henneghien, A.-L.; Tourbot, G.; Daudin, B.; Lartigue, O.; Désières, Y.; Gérard, J.-M. Optical Anisotropy and Light Extraction Efficiency of MBE Grown GaN Nanowires Epilayers. *Opt. Express* **2011**, *19* (2), 527.
(21) Gurwitz, R.; Shalish, I. Method for Electrical Characterization of Nanowires. *Nanotechnology* **2011**, *22* (43), 435705.
(22) Motayed, A.; Vaudin, M.; Davydov, A. V.; Melngailis, J.; He, M.; Mohammad, S. N. Diameter Dependent Transport Properties of Gallium Nitride Nanowire Field Effect Transistors. *Appl. Phys. Lett.* **2007**, *90* (4), 043104.
(23) Storm, K.; Halvardsson, F.; Heurlin, M.; Lindgren, D.; Gustafsson, A.; Wu, P. M.; Monemar, B.; Samuelson, L. Spatially Resolved Hall Effect Measurement in a Single Semiconductor Nanowire. *Nat. Nanotechnol.* **2012**, *7* (11), 718−722.
(24) Huang, Y.; Duan, X.; Cui, Y.; Lieber, C. M. Gallium Nitride Nanowire Nanodevices. *Nano Lett.* **2002**, *2* (2), 101−104.
(25) Hultin, O.; Otnes, G.; Borgström, M. T.; Björk, M.; Samuelson, L.; Storm, K. Comparing Hall Effect and Field Effect Measurements on the Same Single Nanowire. *Nano Lett.* **2016**, *16* (1), 205−211.
(26) Roddaro, S.; Nilsson, K.; Astromskas, G.; Samuelson, L.; Wernersson, L. E.; Karlström, O.; Wacker, A. InAs Nanowire Metal-Oxide-Semiconductor Capacitors. *Appl. Phys. Lett.* **2008**, *92* (25), 253509.
(27) Chen, Z. H.; Tang, Y. B.; Liu, Y.; Yuan, G. D.; Zhang, W. F.; Zapien, J. A.; Bello, I.; Zhang, W. J.; Lee, C. S.; Lee, S. T. ZnO Nanowire Arrays Grown on Al:ZnO Buffer Layers and Their Enhanced Electron Field Emission. *J. Appl. Phys.* **2009**, *106* (6), 064303.
(28) Wen, X.; Wu, W.; Ding, Y.; Wang, Z. L. Seedless Synthesis of Patterned ZnO Nanowire Arrays on Metal Thin Films (Au, Ag, Cu, Sn) and Their Application for Flexible Electromechanical Sensing. *J. Mater. Chem.* **2012**, *22* (19), 9469−9476.
(29) Parkinson, P.; Dodson, C.; Joyce, H. J.; Bertness, K. A.; Sanford, N. A.; Herz, L. M.; Johnston, M. B. Noncontact Measurement of Charge Carrier Lifetime and Mobility in GaN Nanowires. *Nano Lett.* **2012**, *12* (9), 4600−4604.
(30) Zangooie, S.; Woollam, J. A. Ellipsometric Characterization of Thin Porous GaAs Layers. *J. Mater. Sci. Lett.* **2000**, *19*, 2171−2173.
(31) Adachi, S. *Optical Constants of Crystalline and Amorphous Semiconductors*; Springer Science: Boston, MA, 1999.
(32) Jones, S. B.; Friedman, S. P. Particle Shape Effects on the Effective Permittivity of Anisotropic or Isotropic Media Consisting of Aligned or Randomly Oriented Ellipsoidal Particles. *Water Resour. Res.* **2000**, *36* (10), 2821−2833.
(33) Kaminska, K.; Amassian, A.; Martinu, L.; Robbie, K. Growth of Vacuum Evaporated Ultraporous Silicon Studied with Spectroscopic Ellipsometry and Scanning Electron Microscopy. *J. Appl. Phys.* **2005**, *97* (1), 013511.
(34) Jellison, G. E.; Modine, F. A. Parameterization of the Optical Functions of Amorphous Materials in the Interband Region. *Appl. Phys. Lett.* **1996**, *69* (3), 371−373.
(35) Fujiwara, H.; Kondo, M. Effects of Carrier Concentration on the Dielectric Function of ZnO:Ga and In_2O_3:Sn Studied by Spectroscopic Ellipsometry: Analysis of Free-Carrier and Band-Edge Absorption. *Phys. Rev. B: Condens. Matter Mater. Phys.* **2005**, *71* (7), 1−10.
(36) Drechsler, M.; Hofmann, D. M.; Meyer, B. K.; Detchprohm, T.; Amano, H.; Akasaki, I. Determination of the Conduction Band Electron Effective Mass in Hexagonal Gan. *Jpn. J. Appl. Phys.* **1995**, *34*, L1178−L1179.
(37) Fujiwara, H. *Spectroscopic Ellipsometry: Principles and Applications*; John Wiley & Sons Inc: Chichester, 2007.
(38) Chang, C. Y.; Chi, G. C.; Wang, W. M.; Chen, L. I. C.; Chen, K. H.; Ren, F.; Pearton, S. J. Electrical Transport Properties of Single GaN and InN Nanowires. *J. Electron. Mater.* **2006**, *35* (4), 738−743.
(39) Hilsum, C. Simple Empirical Relationship between Mobility and Carrier Concentration. *Electron. Lett.* **1974**, *10* (13), 259−260.
(40) Benner, O.; Blumberg, C.; Arzi, K.; Poloczek, A.; Prost, W.; Tegude, F. J. Electrical Characterization and Transport Model of N-Gallium Nitride Nanowires. *Appl. Phys. Lett.* **2015**, *107*, 082103.
(41) Orton, J. W.; Powell, M. J. The Hall Effect in Polycrystalline and Powdered Semiconductors. *Rep. Prog. Phys.* **1980**, *43* (11), 1263−1307.
(42) Xie, Z.; Sui, Y.; Buckeridge, J.; Sokol, A. A.; Keal, T. W.; Walsh, A. Prediction of Multiband Luminescence Due to the Gallium Vacancy-Oxygen Defect Complex in GaN. *Appl. Phys. Lett.* **2018**, *112* (26), 262104.
(43) Seifert, W.; Franzheld, R.; Butter, E.; Sobotta, H.; Riede, V. On the Origin of Free Carriers in High-conducting N-GaN. *Cryst. Res. Technol.* **1983**, *18* (3), 383−390.
(44) Kumar, M.; Poulose, A. C.; Nakajima, Y.; Sakthikumar, D.; Kumar, V.; Singh, R. Anomalous Emission from Oxygen Incorporated GaN Nanowires. *Phys. E* **2018**, *104*, 187−191.
(45) Slack, G. A.; Schowalter, L. J.; Morelli, D.; Freitas, J. A. Some Effects of Oxygen Impurities on AlN and GaN. *J. Cryst. Growth* **2002**, *246* (3−4), 287−298.
(46) Feenstra, R. M.; Wood, C. E. C. *Porous Silicon Carbide and Gallium Nitride*; John Wiley & Sons Inc: Chichester, 2008.

DOI: 10.1021/acs.jpcc.9b10556
J. Phys. Chem. C 2020, 124, 1535−1543

(47) Shalish, I.; Temkin, H.; Narayanamurti, V. Size-Dependent Surface Luminescence in ZnO Nanowires. *Phys. Rev. B: Condens. Matter Mater. Phys.* **2004**, *69* (24), 1−4.
(48) Watkins, N. J.; Wicks, G. W.; Gao, Y. Oxidation Study of GaN Using X-Ray Photoemission Spectroscopy. *Appl. Phys. Lett.* **1999**, *75* (17), 2602−2604.
(49) Pearton, S. J.; Cho, H.; LaRoche, J. R.; Ren, F.; Wilson, R. G.; Lee, J. W. Oxygen Diffusion into SiO_2-Capped GaN during Annealing. *Appl. Phys. Lett.* **1999**, *75* (19), 2939−2941.
(50) Jakiela, R.; Dumiszewska, E.; Caban, P.; Stonert, A.; Turos, A.; Barcz, A. Oxygen Diffusion into GaN from Oxygen Implanted GaN or Al_2O_3. *Phys. Status Solidi Curr. Top. Solid State Phys.* **2011**, *8* (5), 1513−1515.
(51) Santos, A. J.; Lacroix, B.; Maudet, F.; Corvisier, A.; Paumier, F.; Dupeyrat, C.; Girardeau, T.; García, R.; Morales, F. M. Surface Oxidation of Amorphous Si and Ge Slanted Columnar and Mesoporous Thin Films: Evidence, Scrutiny and Limitations for Infrared Optics. *Appl. Surf. Sci.* **2019**, *493*, 807−817.

DOI: 10.1021/acs.jpcc.9b10556
J. Phys. Chem. C 2020, 124, 1535−1543

Manuscript VIII

Exploring the possibilities and alternatives offered by the application of (S)TEM methods for the study of porous nanostructured coatings

A. J. Santos, B. Lacroix, F. Maudet, F. Paumier, S. Hurand, C. Dupeyrat, V. J. Gómez, D. L. Huffaker, T. Girardeau, R. García, F. M. Morales

Under review in Microscopy and Microanalysis

Exploring the Possibilities and Alternatives Offered by the Application of (S)TEM Methods for the Study of Porous Nanostructured Coatings

Antonio J. Santos[1,2,*], Bertrand Lacroix[1,2], Florian Maudet[3], Fabien Paumier[3], Simon Hurand[3], Cyril Dupeyrat[4], Víctor J. Gómez[5,†], Diana L. Huffaker[5,6], Thierry Girardeau[3], Rafael García[1,2], Francisco M. Morales[1,2,*]

[1] Department of Materials Science and Metallurgic Engineering, and Inorganic Chemistry, Faculty of Sciences, University of Cádiz, Spain.

[2] IMEYMAT: Institute of Research on Electron Microscopy and Materials of the University of Cádiz, Spain.

[3] Institut Pprime, UPR 3346 CNRS-Université de Poitiers-ENSMA, SP2MI, 86962 Futuroscope-Chasseneuil cedex, France.

[4] Safran Electronics and Defense, 26 avenue des Hauts de la Chaume, 86280 Saint-Benoît, France.

[5] School of Engineering, Cardiff University, CF24 3AA, Cardiff, United Kingdom.

[6] School of Physics and Astronomy, Cardiff University, CF24 3AA, Cardiff, United Kingdom.

* Corresponding author: antonio.santos@uca.es; fmiguel.morales@uca.es

ABSTRACT

Nanostructured films offer the ability of modifying surface properties, even more, when they can generate layers with controlled porosity. The lower implicit integrity of these (multi)layers when

compared to their compact counterparts, hinders the attainment of electron-transparent sections of submicron thicknesses (lamellae), which becomes one of the main reason for the scarcity of studies thorough (scanning-)transmission electron microscopy ((S)TEM). Aware of this opportunity, some comprehensive (S)TEM studies are conducted on different coatings deposited at oblique angles as well as GaN nanowire arrays, enabling the realization of several pioneering works presented here, which are essential to complete the characterization of such porosity-controlled coatings. Topics as diverse as the preparation of electron-transparent specimens and the advanced characterization of their structures, morphologies, interfaces and compositions are addressed thanks to the implementation of new breakthroughs in (S)TEM, which allow to obtain high resolution imaging, spectroscopies, or tomography, at both microscopic and nanoscopic levels. This works aims not only to establish (S)TEM as a reference tool for the advanced structural, chemical and morphological characterization of porous nanostructured skins, but also to open new horizons, providing better and new insights and thus allowing the optimization of the fabrication and design of such architectures.

KEYWORDS: Porous thin film; TEM sample preparation; HRTEM; iDPC-STEM; STEM-EDX; STEM-EELS; STEM-HAADF tomography.

1. Introduction

Surface engineering is an area of Materials Science & Technology that has lately attracted great interest thanks to the possibility of modifying the properties of the material that is covered by providing some characteristics that make it ideal for a determined application (Albella, 2018; Davim, 2012). In this light, many different approaches have emerged, being the design and manufacturing of porosity-controlled coatings one of the most appealing, since they endow materials with improved and additional functionalities of interest in many fields such as energy (Li et al., 2016; Dislaki et al., 2018), catalysis (Dubey et al., 2016; Abate et al., 2006), optics (Maudet et al., 2019; Maudet, Lacroix, Santos, Paumier, Paraillous, Hurand, Corvisier, Marsal, et al., 2020; Maudet, Lacroix, Santos, Paumier, Paraillous, Hurand, Corvisier, Dupeyrat, et al., 2020; Toccafondi et al., 2014; Prikulis et al., 2015; Santos et al., 2019) and electronics (Lacroix et al., 2019; Santos et al., 2020).

In recent times, coatings elaborated by means of oblique angle deposition (OAD) have become a widespread practice for attaining 3D micro- and mesoporous architectures of controlled structure and properties. Through this bottom-up approach, the deposition of tilted columnar and porous films is achieved thanks to the shadowing effect that occurs when the incident flux of particles arrives at an oblique angle (Hawkeye & Brett, 2007; van Kranenburg & Lodder, 1994; Robbie & Brett, 1997; Hawkeye et al., 2014; He & Zhao, 2011; Barranco et al., 2016). In this regard, OAD methods allow not only to deposit many types of materials (single elements, compounds with changing stoichiometries, metals, oxides, semiconductors, dielectrics, etc.) but also to sculpt, with a nanoscopic precision, a variety of complex architectures with controlled geometries (slanted, zig-zag, or helical structures; periodic arrays; etc.) simply by adjusting the deposition

parameters during the deposition. Likewise, the manufacture of fine-controlled nanoporous films by molecular beam epitaxy (MBE) or chemical vapour deposition (CVD) methods has also shown to be a good approach, even though the architectures achieved by these two techniques are different from those generated by OAD methods, being the most significant those formed by nanorods (NRs) or nanowires (NWs) of semiconducting materials (Gómez et al., 2019; Tyagi et al., 2019; Sun et al., 2018; Cha et al., 2009). Within the framework of the development of nanostructures for ultra-high performance multifunctional devices, OAD and MBE techniques have proved to be powerful tools since both permit to tune the effective refractive index (*n*) of the deposited film by controlling the porosity of the system, enabling to manufacture broadband omnidirectional graded-refractive-index antireflective (AR) coatings (Maudet et al., 2019; Santos et al., 2020; Maudet, Lacroix, Santos, Paumier, Paraillous, Hurand, Corvisier, Dupeyrat, et al., 2020; Maudet, Lacroix, Santos, Paumier, Paraillous, Hurand, Corvisier, Marsal, et al., 2020; Lacroix et al., 2019; Gómez et al., 2019; Xi et al., 2007; Kennedy & Brett, 2003; Tian et al., 2017; Chang et al., 2011). Nevertheless, in order to take maximum benefits from these two approaches, a fine description at different scales of the elaborated systems is needed.

From the outset of these technologies, various techniques have been used to characterize such nanostructured films at different scales. In the case of the OAD structures, scanning electron microscopy (SEM) (Alvarez et al., 2016; El Beainou et al., 2017; Chu et al., 2017), atomic force microscopy (AFM) (Jain et al., 2013; Esfandiar et al., 2013), X-ray diffraction (XRD) (Larson & Zhao, 2016; Shetty & Karimi, 2012), or X-ray photoelectron spectroscopy (XPS) (Polat et al., 2014; Salazar et al., 2017) studies have been extensively applied to obtain information about the structure, morphology and composition of such systems, which are relevant data to take into account for having a better description of their growth mechanisms and properties. It is however

worth to point out that these techniques mentioned above provide microstructural information with a limited spatial resolution: several microns in the case of XRD and XPS and up to a few nanometers in the case of AFM (lateral resolution) and SEM. According to Hawkeye et al. (Hawkeye & Brett, 2007), “the future development of OAD technology requires further study of fundamental growth processes as well as continued investigation and optimization of the physical properties of OAD fabricated films”. Therefore, in order to advance on the knowledge of the fundamental processes involved in the generation of such type of nanostructured films and to go further into their performances optimization, it is now becoming essential to apply, in a systematic way, characterization methodologies that allow a fine description of these systems. In this context, transmission electron microscopy (TEM), and its related techniques, postulates as the appropriate candidate, which is known to be a powerful and fast-growing analytical tool to probe not only the local structure but also the local chemistry and morphology of materials.

In the past few years, the integration of efficient and multiple signal detectors combined with the arrival of aberration correctors for the electron lenses have enabled significant improvements related to elemental detection sensitivity and dramatic reduction of the attainable resolution limits below the Angstrom, opening up new possibilities and challenges in the characterization of materials (Wang, 2011; McMullan et al., 2014; Hosokawa et al., 2013). However, although it has become a mainstay in the repertoire of characterization techniques for materials scientists, it should be noted that TEM still has difficulties to establish itself as a reference tool for apprehending topics related to nanoporous structures. Most of these difficulties come from the collection of electron-transparent sections of open (multi)layers of submicron thicknesses (lamellae), which becomes especially challenging compared to their compact equivalents. Besides, a thorough review of the state of the art dealing with the OAD processes indicates that

only a few studies have concerned the application of TEM, most are restricted to very basic TEM analyses, including, mainly, conventional TEM imaging, electron diffraction, or high-resolution TEM (see the recent references (Phae-ngam et al., 2019; Liedtke-Grüner et al., 2019; Liedtke et al., 2017, 2018; Qi et al., 2019; Auer & Ye, 2017; Amaya et al., 2017; Nuchuay et al., 2017) as example), and do not take advantage of the full potential of the ultimate generation electron microscopes including high spatial resolution imaging and spectroscopies or tomography for example.

On the other side, semiconducting nanowire films grown by MBE methods have also been broadly studied through SEM, photoluminescence spectroscopy (PL) or even TEM (Zhao & Mi, 2017; Debnath et al., 2008; Reznik et al., 2018; Zhao et al., 2019; Koval et al., 2019; Morkötter et al., 2013; Anyebe et al., 2020; Abdel All et al., 2020; Novikov et al., 2010). Nevertheless, as with the OAD systems, these works are limited to high-resolution and electron diffraction TEM studies of very narrow areas, being often observed the side faces and interfaces of individual NWs but not being explored the entire film or different representative areas, which can be associated to the aforementioned difficulties that the achievement of electron-transparent sheets of regular widths for nanoporous structures implies.

In this work, comprehensive studies by transmission and scanning-transmission electron microscopies ((S)TEM) were conducted on nanostructured porosity-controlled coatings, enabling several major advances, which were fundamental to reach important conclusions on the research of: (i) OAD systems of different nature, materials and architectures, providing not only a better insight of their structures and properties but also allowing the optimization of the fabrication and design of such architectures; and (ii) MBE films with variable morphologies and tunable optical and electrical properties of arrays of GaN hollow and/or compact nanowires. Issues as the

preparation of electron-transparent specimens and the advanced characterization of their structures, morphologies, interfaces and compositions are discussed thanks to the implementation of new innovations in (S)TEM, which allow to obtain high resolution imaging, spectroscopies, or tomography, at both microscopic and nanoscopic levels.

2. Materials and methods

2.1. Sample fabrication

2.1.1. OAD films

A variety of OAD coatings prepared using different conditions and materials have been studied. Silicon dioxide (SiO_2) and titanium dioxide (TiO_2) OAD thin films were fabricated at room temperature in an electron-beam evaporator placed into a physical vapour deposition (PVD) vacuum chamber (base pressure $2x10^{-6}$ mbar). Such (multi)layers were deposited at different angles of incidence (α) relative to the substrate normal from 50° to 85°, without substrate rotation, by adjusting the angle of the substrate holder with respect to a fixed evaporation direction. Since this deposition chamber is not equipped with an in-situ adjustable orientation sample-holder, bilayer and trilayer systems were made in two and three steps respectively with an azimuthal rotation of $\Phi = 180°$ in between on silicon substrates. For a more in-depth description of deposition parameters of some of these systems, see references 8 and 9.

Indium tin-doped oxide (ITO) OAD films were fabricated at different angles α from 50 to 85° on silicon substrates by ion beam sputtering (IBS) deposition in a Nordiko chamber at room temperature with a base pressure of $2x10^{-6}$ Pa. The IBS chamber includes two radio-frequency sources: the first one was used to produce Ar or Xe ions accelerated at 1.2 keV, while the second one was employed as oxygen assistance gun with a flow of 5 sccm and the background pressure

was maintained to $2x10^{-2}$ Pa. Further information on the IBS-OAD deposition of ITO films can be found elsewhere in reference 13.

2.1.2. Nanowire films by MBE

High-quality single crystalline GaN self-assembled NW films were grown on chemically cleaned p-type Si(111) or (100) substrates in a Veeco Gen930 molecular beam epitaxy (MBE) reactor along the [0001] direction and epitaxially aligned with the underlying Si substrate, following the same procedure as the one described in reference 21.

2.2. (S)TEM studies

To observe these materials under an electron beam, cross-sections (XTEM) of the specimens were prepared by two different methods: (i) a progressive thinning down by a tripod polisher (Model 590 Tripod Polisher®) up to few microns, followed by Ar^+ ion-milling at an acceleration energy of 3.5 keV in a Gatan Precision Ion Polishing System (PIPS)-691 at ±7º milling angles (double-beam mode); (ii) the collection of electron-transparent lamellae using two different focused ion beam (FIB) systems: a Thermo Scientific Scios 2 DualBeam, and a ZEISS CrossBeam 350. Afterwards, such structures were studied by means of some advanced characterization techniques including high-angle annular dark field imaging (HAADF), electron tomography (ET), integrated differential phase contrast (iDPC) and local compositional analyses by EDX (energy-dispersive X-ray spectroscopy) and EELS (electron energy-loss spectroscopy). On this purpose, five different (S)TEM microscopes were used: JEOL 2100 LaB_6, JEOL 2010, FEI Talos F200S, FEI Talos F200X G2 and a double aberration-corrected FEI Titan Cubed Themis 60-300 microscope, working all of them at an accelerating voltage of 200 kV.

3. Results and discussion

Many nanoporous OAD and MBE systems of different nature, architecture and hardness will be here explored through the application of a wide variety of (S)TEM methods, giving special emphasis to (i) the most adequate procedures for the collection of electron-transparent sheets, (ii) overall studies of the structures and morphologies generated at micro- and nanoscale, (iii) atomic-resolution imaging of crystalline structures, (iv) chemical analyses by combining imaging and spectroscopies techniques, and (v) the 3D reconstruction of such structures by (S)TEM tomography.

3.1. Preparation of electron-transparent lamellae for (S)TEM observations

As previously mentioned, the fact that very few TEM based studies found for nanostructured thin films is closely linked to the difficulties encountered during the TEM sample preparation process. Besides, it becomes evident that the TEM sample preparation process of porous multilayer structures of dissimilar stiffness, such as the OAD ones, will be even more hindered. In order to lead the way for further TEM studies of porous nanostructured coatings, the challenging collection of electron-transparent lamellae of porous (multi)layers of different materials, architectures and hardness with methods of thinning down by tripod polishing plus ion milling, or focused ion beams (FIB) is here addressed. Moreover, the benefits and drawbacks of each sample preparation method are explored, paying special attention to aspects such as the homogeneity of the thinned lamella, the contamination during preparations, or the final thickness achieved.

3.1.1. Tripod polishing

As it is well-known, the TEM sample preparation process is a destructive method whose purpose is to collect an ultrathin specimen of a few nanometer-thick so that a beam of electrons is

transmitted through it interacting with the specimen and forming the image. Traditionally, cross-section (XTEM) and planar-view (PVTEM) TEM sample preparation processes have been faced in many ways, although the majority of them share the following steps of cutting, grinding/polishing, dimpling and ion-milling (Weaver, 1997; Mccaffrey & Barna, 1997; Bradley et al., 1987; Flutie, 1985; Sáfrán & Grenet, 2002). Considering the relative weakness of the porous samples to be here studied, it is desirable to avoid the mechanical dimpling process since it would be quite severe (Unal et al., 1990). Keeping this in mind, flat-type polishing of cross-sectional specimens were prepared using a tripod polisher, which allows to carefully thin down the specimen up to a few microns with a high control of micrometric steps applied on feet, evolving a much softer mechanical thinning than that achieved with heavy holders (as the Gatan Disc Grinder) and SiC sandpapers (as those of Struers), avoiding the dimpling stage and reducing the time required for the final thinning step by ion milling (Cha et al., 2016).

As can be seen in **Figure 1(a)**, specimen slats were cut into volume sizes of 2.5 mm x 0.8 mm. After that, two of these slats were glued (facing the porous films each other) using M-Bond 610 adhesive (Micro-Measurements). Once the epoxy adhesive is cured, the stacked specimen is fixed on the outer edge of the Pyrex glass stub, which is mounted on the tripod polisher by means of an L-bracket, using thermal wax, placing the plane formed by the two porous films perpendicular to the Pyrex glass surface. Once the thermal wax is cooled down, the excess is removed by applying acetone carefully. The latter is very important since the aspect and thickness of the specimen after each polishing step will be checked through an optical microscope which has the spindle of a micrometer attached that controls the thickness of the sample by means of the difference of focus between the polished surface of the sample and the Pyrex glass surface (free of thermal wax).

Before starting the polishing, it is necessary to level the tripod polisher which is done by manipulating the micrometers installed in its structure allowing to adjust the height of its supporting feet. Next, the both sides of the specimen are polished using 15, 6, 3, 1, and 0.5 μm grain diamond lapping films (South Bay Technology) by removing the material equivalent to three times the grain size from the previous stage (the "rule of three") (Voyles et al., 2003). Here is very important to keep both specimen and diamond discs clean during polishing since otherwise bits of the sample that is being polished off or the remains of bigger diamond grains will cause scratches. In order to prevent that, the sample is cleaned between each polishing step by compressed air, while the remains of specimen retained on the diamond lapping films are removed after each step by using fresh paper towels. The specimen is polished until its thickness reaches 10-15 μm, then gluing a TEM grid on its top surface by applying small droplets of the M-Bond adhesive and letting it curing. Finally, the thinned specimen is easily removed from the Pyrex glass together with the glued grid by the immersion of the L-bracket in acetone. The aspect of a sample after polishing is shown in **Figure 1(b)**.

The supported sample is later undergone to a low-energy ion milling (3-3.5 kV) using a Gatan 691 PIPS system working at double beam mode (±7º milling angles). It must be taken into account that the milling parameters depend on the specimen material. Therefore, the milling conditions here provided can vary slightly depending on the characteristics of specimen to be prepared. **Figure 1(c)** displays the final aspect of a sample after half an hour of ion milling. As can be seen here, it was not carried out an excessive ion milling stage and that is the reason why the electron transparent region presents an elongated shape and not the so characteristic hole. Indeed, a minimal and smooth ion milling is always recommended not only to reduce sample damage but also to prevent the amorphization of the electron transparent area. This is helped by

using a tripod polisher since, unlike the traditional polishing plus dimpling, it enables to thin down the specimen stack homogeneously up to 5-10 μm, reducing the time required for the ion milling step and favouring the generation of homogeneous electron transparent regions. The above emphasises with the homogeneously distributed yellow hue of both silicon substrate sheets that can be seen in the inset of **Figure 1(c)**, which reveal that the final thickness of the sample is suitable and that the ionic attack has occurred homogeneously and well-aligned.

3.1.2. FIB methods

FIB–TEM specimen preparation technique is another simple and straightforward alternative to collect electron-transparent lamellae of thin films. This technique not only provides the capability to prepare TEM samples with minimum levels of damage and contamination but is also capable of preparing samples either along particular orientations or in specific areas with a few nanometer precision (Li et al., 2006). From the beginning of this technique, the preparation of FIB-TEM samples of fragile or ultra-fine specimens has become a challenging issue. Nevertheless, the new cutting-edge techniques developed in recent years have helped to face these difficulties (Dinh et al., 2018; Xu et al., 2018; Pan et al., 2018). Following, the validity to prepare electron transparent lamellae of porous systems by means of FIB methods is here scrutinised.

Figure 2 displays a TEM lamella fabricated by means of a FIB system. As can be seen in the picture, the lamella was thinned after lift-out with the aim of attaining ultra-thin regions, which is vital for collecting adequate high-resolution TEM images. The inset of **Figure 2** reveals a very good electron-transparent region for HRTEM observations after polishing at low energy but it implies an extra cost to pay: as can be noticed in the silicon substrate, a directional curtaining

occurs as a result of the aforementioned polishing, giving rise to an irregular electron transparent region which could limit the conducting of some studies (i.e. to carry out 3D reconstructions by means of electron tomography methods). This does not mean that the FIB lift-out plus final thinning is not the most suitable approach to fabricate electron-transparent foils of porous thin films, but quite the opposite, since it sometimes becomes in the only one alternative to prepare them. In general, both tripod polishing and focused ion beams are good approaches to prepare electron-transparent sheets of porous coatings. Nevertheless, what is certain and evident is that, depending on the characteristics of the specimen to be studied and the TEM techniques to be applied, one approach can result more appropriate than the other one.

3.1.3. Selection of the most appropriate sample preparation process: advantages and drawbacks of both methods

Once evidenced that tripod polishing and FIB methods are both good approaches to collect electron-transparent regions of porous and delicate thin films, the next step will be to analyse which of these two alternatives would be the most appropriate one depending on the (S)TEM study to be conducted.

For this purpose, the advantages and disadvantages of one and other method are reviewed in **Table 1**. Initially, both methods will be compared from the point of view of the time invested to carry out a TEM preparation. As seen in previous sections, the tripod polishing method is a procedure that includes several stages, which have to be addressed systematically and thoroughly to achieve a satisfactory final result. Therefore, the preparation of a sample through this method usually takes, at best, 1-2 days for a trained person, but materials costs are low. In contrast, FIB

sample preparation is more straightforward, faster (a specialized technician could carry out a FIB preparation in a few hours) and cleaner than the tripod polishing, since this method allows a lamella to be lifted out and thinned in the absence of glue, water, or other solvents. For that matter, it must be highlighted that such solvents have been proved to contribute to the oxidation of porous thin films of metalloids such as silicon and germanium but without affecting their structure and morphology (Santos et al., 2019). Nevertheless, the time saved in FIB preparations is countered by the fact that the price of a preparation as well as the level of expertise required to carry out such experiment are both remarkably higher.

Now it is time to focus on the final appearance of the samples prepared by both methods. **Figure 3** shows the STEM-EELS relative thickness map (for more information about this technique, refer to section 3.4) of a SiO_2 OAD bilayer prepared for TEM observations by means of tripod polishing plus ion-milling. As can be here appreciated, the thickness of the observable region remains incredibly constant ($t/\lambda \approx 0.3$ in the central part of the nanocolumns, which corresponds to about 36 nm assuming an electron mean free path of 120 nm according to our experimental conditions and to the Malis equation (Malis et al., 1988)), which is maintained longitudinally along approximately 4 μm. Thus, here is not only evidenced that the tripod polishing successes in preparing electron-transparent foils of porous multilayer systems with suitable thicknesses for HRTEM studies but also allows to obtain regions of homogenous thickness extended to large areas, which make this kind of preparation the most suitable alternative when (S)TEM tomography or spectroscopy studies are needed. Besides, a specimen prepared by tripod polishing provides up to four regions of electron transparency which enables to explore larger sample areas. However, all the above mentioned is subject to certain limitations: although the tripod polishing procedure is well-defined, there are some factors that are going to influence the

preparation of a particular specimen such as for instance the ability and care when dealing with the sample or the unique features of each film. This does not ensure that the result achieved through this method is always going to be the same but quite the opposite: both the aspect and the final thickness of the sample cannot be totally controlled in real time which can lead to situations in which the porous film subject to study is smashed, without knowing it, during one of the stages that tripod polishing implies or that, by strictly applying the method, the final thickness achieved for a sample is not the same as the one achieved for another of the same or different characteristics. In this sense, and for the purpose of making sure that a sample prepared by tripod polishing has not been significantly affected or damaged after the sample preparation process, an optional action could be to verify the prepared samples in a SEM microscope, verifying multiple samples at the same time and not individually since it could considerably increase the sample preparation costs and times (limited accessibility to SEM). In exchange, the tripod polishing weaknesses are precisely the strengths of the FIB preparation method, which is a process that allows a robust live control of the thickness and appearance of the TEM lamella. Moreover, the FIB method is the best alternative to prepare TEM lamellae of specific areas or orientations (which can be an issue of special interest when studying OAD coatings) with minimal damage and contamination, although, as seen before, it fails in its attempt to achieve homogeneous thicknesses after a final thinning at low energy. Likewise, it should not be neglected the effect of the protective layer of platinum deposited on the surface of a sample prior to FIB preparation (see **Figure 2**). Although the purpose of the Pt-layer is to protect the surface from incurring FIB induced damage, it can hinder subsequent analysis, especially on the surface. For instance, the appearance of unwanted peaks in spectroscopy which can hide or overlap relevant signals.

FIB-induced damage and ion implantation should also be addressed here, which both depend on preparation parameters like ion voltage, incident angle, substrate composition and ion species. In this sense, conventional Ga^+ FIB processing is well known to produce amorphisation and Ga^+ implantation during FIB milling (Rubanov & Munroe, 2004; Tong et al., 2016). In this regard, some alternative solutions such as using low energy argon ion milling (Nowakowski et al., 2017), Xe^+ PFIB systems (Liu et al., 2020; Zhong et al., 2020), or focused-electron-beam-induced etching by chlorine (Roediger et al., 2011) have been shown to be capable of removing Ga^+ implantation and amorphous damage from TEM specimens.

Another aspect to be taken into account is the budgetary limitations that a laboratory or research centre may have. The cost of a sophisticated FIB system implies an important investment that might not be assumable for all. In that case, tripod polishing postulates as the most affordable alternative to tackle the TEM specimen preparation of porous films due to its facility to be implemented in any laboratory without assuming a large investment. Likewise, it is interesting to highlight that, although it implies a higher cost of acquisition and commissioning, a FIB lamella provides much less areas of electron transparency that the one provided by a specimen prepared by tripod polishing.

Therefore, considering all the arguments previously referred, it is recommended, as a first approach, to address the preparation of nanostructured porous films by tripod polishing. On the other hand, the FIB preparation is only urged in the following cases: (i) when tripod polishing preparation fails; (ii) when the amount of material to be studied is so small that does not allow a tripod polishing preparation; (iii) when it is essential to reduce the presence of pollutants during preparation; (iv) to prepare specimens along particular orientations or specific areas; and (v) to

prepare ultra-thin films for HRTEM observations when thickness non-uniformity does not undermine the studies to be performed.

3.2. Structure and morphology at micro- and nanoscale

Once established the most suitable routes to prepare electron-transparent foils of porous systems for TEM observations, the contribution that the application of each of the (S)TEM methods offer to the study of OAD and MBE nanowire porous nanostructures will be evaluated hereafter. In this sense, the capabilities of conventional transmission electron microscopy (CTEM) methods as a tool to explore the structure and morphology of such systems at different scales will first be explored.

After deposition, a widespread routine adopted by scientific community is to verify the overall look of the deposited nanostructure through SEM methods (Tyagi et al., 2019; Debnath et al., 2008; Barranco et al., 2016; Hawkeye & Brett, 2007). Even though the above could be considered as an appropriate preliminary approach, the comprehensive characterization of such morphologies and structures must be complemented by additional studies that allow to obtain, for instance, more detailed information on how the nanostructured film evolves as the deposition progresses or about how the transition between layers occurs. In this sense, TEM microscopy postulates as the most viable option because it is a very powerful and versatile tool that allows obtaining very valuable information for simulations (Dervaux et al., 2017) or providing new inputs to optical models (Maudet et al., 2019).

Figure 4 displays some bright-field (BF) TEM micrographs of different OAD mono-, bi- and trilayer systems, placing special emphasis on the aspect of the generated interfaces. It is worth to mention that all these specimens were prepared for TEM observations by means of tripod

polishing. As can be seen, unlike SEM routines, TEM surveys not only allow to obtain general information about layer thicknesses and column tilt angles (β), but also allow to investigate how the transition between layers occurs or even determine the crystalline or amorphous nature of such porous coatings. In this sense, it is evidenced that the PVD-OAD deposition of SiO_2 and TiO_2 films gives rise to the generation of amorphous systems whose transitions between layers are characterised by being sharp and without generating intermixing layers, unlike what revealed in previous studies where an intermixing layer of about 50 nm thick was found at a Ge/MgF_2 interface (Maudet et al., 2019). Moreover, such micrographs also reveal that the tips of the lower columns behave as growth nuclei for the formation of new columns in upper layers.

Figure 5 shows two bright-field TEM micrographs IBS-OAD ITO columns deposited at $\alpha = 85^{o}$ using Xe and Ar ions. Note that, in this case, these TEM studies allowed to observe a great difference between the shape of the columns displayed in **Figure 5(a)**, which present a side sawtooth shape, and those found for the columns contained in **Figure 5(b)**, whose shapes are more regular. In view of the above, it can be assumed that such remarkable differences in the morphology of both systems must be closely linked to the nature of the ions sputtered during the deposition (Xe or Ar), which is in agreement with what was stated in a previous work in which it was determined that the selection of a particular sputtering ion has an effect not only on the overall nanostructure generated but also on the electro-optical properties of such ITO films (Lacroix et al., 2019).

On the other hand, studies of the structure and morphology of GaN nanowire films by means of CTEM methods can be also found in ref. 21. All the examples provided until now have evidenced the ability of the TEM as a tool to inspect the structure and morphology of porous thin films with a great level of detail. Nevertheless, even though similar studies could have been

performed by using a SEM microscope, these examples are just a small proof of all the possibilities that TEM microscopy can offer. In the following sections, the real potential of the TEM applied to the study of thin films will be revealed.

3.3. Crystal structure surveys

When a thin film presents a crystalline organization of its atoms, the orientation of its grains can determine the macroscopic properties of the system. These crystalline features are commonly explored by the scientific community through X-ray diffraction methods which allow to identify preferential crystal orientations or to determine the epitaxial alignment between the porous thin film and the underlying substrate (Collado et al., 2016; Abadias et al., 2019; Shi et al., 2018; Upadhyaya et al., 2020). However, even though XRD studies normally provide overall diffraction statistics, which is especially suitable to study single crystalline systems, this technique does not allow to survey how the orientation of crystalline planes evolves along the layer thickness. This limitation can be overcome by combining high-resolution TEM (HRTEM) and selected area electron diffraction (SAED) methods, which not only allow to replicate the studies conducted by XRD but also to assess the crystal structure of a thin film locally. A preliminary proof of this can be found in ref. 21 in which the crystal structure of GaN nanowires as well as their epitaxial relationships were determined by combining HRTEM and SAED.

Another example of the validity and versatility of the TEM as a tool to carry out comprehensive structural characterizations of porous coatings at different levels is shown in **Figure 6** which reveals the nanostructural and crystallographic changes that an ITO OAD film (deposited by Xe IBS at $\alpha = 50^{o}$) experiences along its layer thickness. On the one side, **Figure 6(a)** shows a remarkable difference between the nanostructure at the bottom part of the film, formed by bigger

and more homogeneous grains, and some minor regions at the upper one, where arrays of slanted columns can be located (see the detail in **Figure 6(c)** and **(d)**). Such study also reveals, thanks to HRTEM nanographs and FFT spectra performed at the top (**Figure 6(b)**) and bottom (**Figure 6(d)**) of the layer, the crystallographic changes that the ITO OAD film experiments along its layer thickness. These results are consistent with the assumptions reached in previous works, in which HRTEM images also revealed the presence of intragrain extended defects and dislocations at the top part of Ar-deposited IBS-OAD ITO films, underlining once again the remarkable difference between the films deposited with Ar (more subjected to backscattering and more energetic) and Xe ions (Lacroix et al., 2019). In other words, the previous assumptions based on the division of the ITO OAD film into two layers of different morphology and crystallinity are here supported since, apart from the morphological differences aforementioned, a sharp switching in the preferential growth planes from (222) (bottom layer) to (440) (top layer) was evidenced as the film thickness increases for this specific deposition angle. This latter could also explain the significant difference between the optical and electrical behaviour of the upper region with respect to lower one. A complete study combining such structural TEM analyses with X-ray diffraction pole figure is currently in progress to understand the texture evolution of these ITO films with the deposition angle.

Before ending this section, it must be highlighted that atomic resolution TEM imaging can also be applied to figure out certain material properties. A clear example is polarity, which is an important feature, especially for III-nitrides such as GaN, since it has a significant effect on surface roughness (Rouviere et al., 1998) and reactivity (Losurdo et al., 2004; Weyher et al., 1997), electron mobility (Dimitrov et al., 2000; Rajan et al., 2005) and dopant incorporation (Tuomisto et al., 2005; Ng & Cho, 2002). Many authors have examined the polarity of III-

nitrides by wet etching (Muto et al., 2005), X-ray photoelectron diffraction (Romanyuk et al., 2016), or using different TEM related techniques (De La Mata et al., 2012; Schuster et al., 2014; Woo et al., 2015; Sarwar et al., 2016; Naresh-Kumar et al., 2019; Rajak et al., 2019; Zhao et al., 2018). Among the TEM methods, aberration-corrected STEM combined with HAADF and annular bright field (ABF) has become one of the best strategies for directly displaying (not with the highest clarity for lighter atoms) the polarity of group III-nitride films manufactured in very different ways.

Figure 7 illustrates an atomic resolution micrograph of a single crystalline GaN nanowire in $[11\bar{2}0]$ orientation which was collected by means of a technique called integrated differential phase contrast STEM (iDPC-STEM) imaging (Lazić & Bosch, 2017; Lazić et al., 2016; Yücelen et al., 2018) using an aberration corrected microscope. This recently introduced direct phase imaging technique allows to image the phase of the transmission function of a sample enabling live imaging of both light and heavy elements together at sub-Å resolution. This technique, which requires ultra-thin sample thicknesses and ultimate Cs-corrected microscopes to achieve good results, is especially favoured when applied to the study of porous thin films since they have, thanks to their large surface-to-volume ratio compared to their compact counterpart, more regions of optimal thickness which are located at the edges of such nanostructures. Accordingly, as displayed in **Figure 7**, Gallium and Nitrogen dumbbells in GaN nanowire arrays were resolved thanks to the implementation of the iDPC-STEM technique, demonstrating the Ga-polarity of such nanostructures (Ga atoms on top of the double atom layers).

3.4. Chemical compositional analyses by imaging and spectroscopies

Until now, the potential and versatility of TEM methods to perform extensive structural characterizations of porous thin films at different levels has been solidly proved. Nevertheless, the capabilities and alternatives that the STEM mode offers for studying the chemical features of materials have not yet been fully explored.

On the one hand, when operating in STEM mode under dark field conditions, the image obtained using a HAADF detector will be due solely and exclusively to electrons that have been incoherently scattered from their path through matter at a sufficiently high angle. Since the HAADF detector is very sensitive to differences of the element irradiated based on the atomic number (Z-contrast), the resulting STEM-HAADF image will present an intensity approximately proportional to the square of the atomic number of the scanned region, as the heavier atoms will have a greater capacity to scatter electrons at higher angles due to bigger electrostatic interactions between their nuclei and the electron beam. This means that qualitative information about the chemical composition of a sample can be obtained, since the contrast in the HAADF images will be associated with a difference in the effective atomic number. Nonetheless, it must be considered that variations in thickness also significantly affect the intensity of the HAADF signal, which should be taken into account so as not to misinterpret the information contained in the HAADF image.

An example of this kind of studies can be seen in **Figure 8(a)** which displays a STEM-HAADF micrograph conducted in a TiO_2/SiO_2 OAD trilayer system together with the HAADF signal profile acquired along individual columns belonging to each of the layers. As can be appreciated, the HAADF signal becomes more intense in the TiO_2 layer (brighter contrast) than in both SiO_2 layers, which is, in principle, reasonable since titanium (Z = 22) has a greater atomic number than silicon (Z = 14). Moreover, the HAADF profile reveals a very similar HAADF intensity for

both SiO_2 layers compared to the one recorded for the TiO_2 layer, which also suggests that the thickness of the thinned TEM sample is quite homogeneous (note that this sample was prepared for TEM observations by tripod polishing). In this sense, it is worth mentioning that this same STEM imaging technique was implemented in previous studies to identify hollow and solid GaN nanowires thanks to the fact that the HAADF intensity is also proportional to the quantity of projected material (see ref. 21).

Nevertheless, what really makes the TEM a very powerful analytic tool is the combination of STEM imaging and spectroscopy. In this sense, the most common TEM-based spectroscopy techniques are Energy Dispersive X-ray Spectroscopy (EDX or EDS) and Electron Energy Loss Spectroscopy (EELS). Based on X-rays emitted as a result of the interaction of the primary electron beam with the atoms that constitute a material, the EDX technique allows to identify and quantify the elemental constituents of a sample by the analysis of the resulting X-ray energies which are characteristic of specific elements. This analytical technique is especially useful when is applied to the study of porous thin films since not only allows to uncover, by means of spectrum images (SIs), the quantitative distribution of the elements that compose a sample but also to know additional relevant information like how the interfaces are developed (Maudet et al., 2019) or if the porous nanostructure is subjected to the spontaneous oxidation of its exposed surfaces (Santos et al., 2019, 2020).

An evidence of the capability of this analytical tool is presented in **Figure 8**, in which the EDX elemental maps and profiles of a TiO_2/SiO_2 OAD trilayer (**Figure 8(a)**) are displayed together with the EDX integrated spectra and associated atomic quantifications of each layer (**Figure 8(b)**). EDX spectra were recorded over 100×100 nm^2 areas and large integration times (several minutes, collecting a total of 1137 frames) using current probes of about 450 pA, beam

convergence angles of 16 mrad, dwell times of 5 µs and dispersions of 5 eV/channel over 4000 channels. The FEI Velox™ software was used for STEM-EDX data acquisition and processing. EDX elemental quantifications of TiO_2 and SiO_2 OAD layers were performed by using the standardless method (i.e. based on theoretical sensitivity factors). Although the accuracy of this approach is rarely considered better than 10% (Egerton & Malac, 2005), especially for low Z elements like O, the measurement uncertainties attained here (below 5%) support the validity of the standardless quantification since the atomic proportions obtained are very close to the ideal stoichiometry (66.9 at. % of O, 33.1 at. % of Si for SiO_2 layers; 65.6 at. % of O, 34.4 at. % of Ti for TiO_2 layer). Additionally, it should be also noted that the combination of EDX elemental maps and profiles (**Figure 8(a)**) also provides valuable information on how the transition between layers takes place (intermixing thickness, composition, etc.).

On the other hand, another alternative way to carry out elemental quantifications at nanometer scale consists of measuring the loss of energy from the inelastic interactions between the electron beam and a thin specimen. That loss of energy will be associated with different characteristic electronic transitions of the constituent elements of a sample, allowing their identification and quantification. This is the basis of the EELS technique which, compared to EDX, provides improved signal, spatial resolution, energy resolution and sensitivity for low atomic number elements (Bertoni et al., 2008; Egerton & Malac, 2005). In addition to the above-mentioned, EELS information can also be used to characterize chemical bonding configurations, oxidation states, valence and conduction band electronic properties or even sample thickness (see **Figure 3**). Special mention must be made of the low-loss EELS region, which not only contains valuable information about the chemical composition and electronic structure but also about the optical properties of a specimen, opening an alternative way to locally probe the optical behavior of

porous thin films. Taking advantage of such capacities, EELS analysis were conducted in previous works not only for the sake of demonstrating the formation of core-shell-type nanostructures in Ge OAD layers as a consequence of the spontaneous surface oxidation of such porous architectures but also for determining the oxidation state of the oxide generated in the same way as XPS surveys (see Ref. 12). Likewise, it is worth mentioning that similar local STEM-EELS analysis were also performed on IBS-OAD ITO films with the aim of examining the distribution of In, Sn and O along the diameter of such ITO nanocolumns. However, the overall overlapping of the EELS signals coming from the different elements and compounds made the obtained results inconclusive.

3.5. 3D reconstructions: STEM-HAADF tomography

Electron Tomography (ET) is a technique that allows to reconstruct the three-dimensional structure of a specimen from a set of two-dimensional images recorded at various tilt angles (tilt-series) which are then processed off-line using different reconstruction algorithms (Weyland & Midgley, 2004; Midgley & Dunin-Borkowski, 2009; Goris et al., 2013; van Aarle et al., 2015; Chen et al., 2014; Kübel et al., 2005). Among the different ET variants, STEM tomography has become established as one of the most powerful. As 3D characterizations at the nanoscale represent valuable insights into the design of nanomaterials, STEM tomography examinations of thin films are becoming increasingly popular for material scientists, being the HAADF signal preferred to BF because of its monotonic dependence on the sample thickness (Midgley et al., 2001; Friedrich et al., 2005). Applied to the characterization of porosity-controlled thin films, STEM-HAADF tomography reconstructions can supply relevant geometric features (3D morphologies and textures, distribution and interaction between nanostructures, porosity profiles,

anisotropy, etc.) which will enable a better understanding of how growth events occur as well as evaluate the influence they have on the properties of the coating.

Figure 9(a) displays the STEM-HAADF electron tomography 3D reconstruction of a TiO_2/SiO_2 OAD trilayer system together with the extracted porosity profile along the surface normal (**Figure 9(b)**). For a detailed description of the experimental data acquisition, segmentation, 3D reconstruction, and porosity profile extraction, refer to Supplementary Material Section I. According to the literature, needle-geometry samples accomplished by focused ion beams have been proved to be the most suitable approach for TEM tomographic experiments, since this geometry prevents thickness changes when tilting the sample (Hernández-Saz et al., 2013). Nonetheless, the good appearance of the 3D reconstruction presented here also suggests that tripod polishing is also a suitable approach to handle STEM tomography examinations. Note how the top views reveal the remarkable porosity and morphological texture changes when moving from one layer to another. Moreover, it must be highlighted that the information extracted from ET reconstructions not only provides additional insights into the nanostructure but also very useful inputs such as the porosity profile which can be used to describe the optical behaviour of a system. Good proof of this is reported in some of our previous works in which the 3D volume reconstructions of several porous films allowed us to assess the scattering behaviour of antireflective coatings by means of finite-difference time domain (FDTD) simulations (see Ref. 9) as well as to validate and improve optical models by implementing the porosity profiles extracted from STEM-HAADF tomographic reconstructions into ellipsometry effective-medium approximation models (see Ref. 8 and Ref. 14).

4. Conclusions

In this work, the possibilities and alternatives offered by the application of (S)TEM methods for a comprehensive and exhaustive characterization of porous nanostructured coatings were assessed. After identifying the tricky collection of porous TEM lamellae as one of the main reasons for the absence of advanced (S)TEM characterizations of such systems, two different TEM sample preparation strategies were tested. In this sense, both tripod polishing and focused ion beams were evidenced to be suitable approaches for preparing electron-transparent foils of porous thin films. Likewise, a comparative analysis on the most appropriate sample preparation option as a function of the (S)TEM study to be conducted was also met. Once this difficulty was overcome, several (S)TEM characterization techniques, such as HRTEM, SAED, STEM-HAADF, STEM-iDPC, STEM-EDX, STEM-EELS or ET, were implemented on several OAD and NW porous films. In this way, the implementation of new breakthroughs in (S)TEM imaging and spectroscopy allowed us to accomplish some of the pioneering studies presented here, highlighting the versatility and capabilities that TEM methods offer to the extensive characterization of porous nanostructures. Issues, such as (a) the morphology, porosity, crystal structure and composition of individual columns or nanowires, local regions and entire layers; (b) the nature, morphology, composition and thickness of transitions between layers; and (c) the 3D reconstruction of such porous structures were finely explored by (S)TEM methods, providing, at the same time, both local and overall data. Note that the above is not achieved by means other characterization techniques such as XPS, which only provides quantitative information about the first 1-5 nm thick of a sample, or XRD, which only gives global information, which may lead to an incomplete or misleading characterization of the coating. Furthermore, it was also emphasized the valuable contribution of TEM studies for the optical and

electrical characterization of such porous systems especially when combined with other techniques like spectrophotometric and Hall effect measurements and, particularly, spectroscopy ellipsometry.

Based on the evidences shown throughout this work, it is intended to make materials scientists aware of the niche of opportunity that (S)TEM methods represent for the advanced characterization of porous nanostructured systems, opening new horizons, since they allow to examine the structure and composition of materials at scales and levels of detail that other techniques do not reach, simplifying methodologies, as they allows to obtain, by using a single equipment, equivalent results to those that could be acquired thorough the combination of SEM, AFM, XPS and XRD analysis, and contributing to a better knowledge of growth mechanisms and properties.

ASSOCIATED CONTENT

Supplementary Material

Three-dimensional STEM-HAADF tomography reconstructions (experimental data acquisition; segmentation; 3D reconstruction; and porosity profile extraction) (PDF)

AUTHOR INFORMATION

Present Addresses

†Valencia Nanophotonics Technology Center, Universitat Politècnica de València, 46022 València, Spain.

ACKNOWLEDGMENT

A. J. Santos would like to thank the IMEYMAT Institute and the Spanish Ministerio de Educación y Cultura for the concessions of grants (ICARO-173873 and FPU16-04386). The "Talent Attraction Program" of the University of Cádiz is acknowledged by supporting B. Lacroix contract code E-11-2017-0117214. University of Cádiz and IMEYMAT are also agreed by financing the mutual facilities available at the UCA R&D Central Services (SC-ICYT), the UCA project reference "PUENTE PR2018-040", and the IMEYMAT project references "AGREGADOR 2018-1" and "LÍNEAS PRIORITARIAS PLP2019120-3". The authors would like to acknowledge the financial support provided by Sêr Cymru National Research Network in Advanced Engineering and Materials. This work was also partly carried out in the framework of the associate laboratory PRIMEO ("Partnership for Research and Innovation in Emerging Materials for phOtonics") between Safran Electronics & Defense and PPRIME Institute. It benefited from the partial support of the DGA (Direction Générale de l'Armement, the French Defense Procurement Agency), the "Nouvelle Aquitaine" Region and the European Structural and Investment Funds (ERDF reference P-2016 BAFE-209): IMATOP project.

REFERENCES

VAN AARLE, W., PALENSTIJN, W. J., DE BEENHOUWER, J., ALTANTZIS, T., BALS, S., BATENBURG,

K. J. & SIJBERS, J. (2015). The ASTRA Toolbox: A platform for advanced algorithm development in electron tomography. *Ultramicroscopy* **157**, 35–47.

ABADIAS, G., ANĞAY, F., MAREUS, R. & MASTAIL, C. (2019). Texture and stress evolution in HfN films sputter-deposited at oblique angles. *Coatings* **9,** 712.

ABATE, S., CENTI, G., PERATHONER, S. & FRUSTERI, F. (2006). Enhanced stability of catalytic membranes based on a porous thin Pd film on a ceramic support by forming a Pd-Ag interlayer. *Catalysis Today* **118**, 189–197.

ABDEL ALL, N., ALMOKHTAR, M. & EL GHOUL, J. (2020). Temperature dependence of photoluminescence from AlN/GaN-thin nanowires. *Journal of Materials Science: Materials in Electronics* **31**, 5033–5039.

ALBELLA, J. M. (2018). *Capas delgadas y modificación superficial de materiales*. Consejo Superior de Investigaciones Científicas.

ALVAREZ, R., GARCIA-MARTIN, J. M., GARCIA-VALENZUELA, A., MACIAS-MONTERO, M., FERRER, F. J., SANTISO, J., RICO, V., COTRINO, J., GONZALEZ-ELIPE, A. R. & PALMERO, A. (2016). Nanostructured Ti thin films by magnetron sputtering at oblique angles. *Journal of Physics D: Applied Physics* **49**, 045303.

AMAYA, C., PRÍAS-BARRAGÁN, J. J., APERADOR, W., HERNÁNDEZ-LANDAVERDE, M. A., RAMÍREZ-CARDONA, M., CAICEDO, J. C., RODRÍGUEZ, L. A., SNOECK, E., GÓMEZ, M. E. & ZAMBRANO, G. (2017). Thermal conductivity of yttria-stabilized zirconia thin films with a zigzag microstructure. *Journal of Applied Physics* **121**, 245110.

ANYEBE, E. A., KESARIA, M., SANCHEZ, A. M. & ZHUANG, Q. (2020). A comparative study of graphite and silicon as suitable substrates for the self-catalysed growth of InAs nanowires by MBE. *Applied Physics A: Materials Science and Processing* **126**, 427.

AUER, M. & YE, D. (2017). Facet-mediated growth of silver nanoparticles on biaxial calcium fluoride nanorod arrays. *Nanotechnology* **28**, 035301.

BARRANCO, A., BORRAS, A., GONZALEZ-ELIPE, A. R. & PALMERO, A. (2016). Perspectives on oblique angle deposition of thin films: From fundamentals to devices. *Progress in Materials Science* **76**, 59–153.

EL BEAINOU, R., MARTIN, N., POTIN, V., PEDROSA, P., YAZDI, M. A. P. & BILLARD, A. (2017). Correlation between structure and electrical resistivity of W-Cu thin films prepared by GLAD co-sputtering. *Surface and Coatings Technology* **313**, 1–7.

BERTONI, G. & VERBEECK, J. (2008). Accuracy and precision in model based EELS quantification. *Ultramicroscopy* **108**, 782–790.

BRADLEY, S. A., REDDY, J. F. & KING, W. E. (1987). Two Methods for Aligning a Mechanical Dimpling Device for TEM Sample Preparation. *Journal of Electron Microscopy Technique* **6**, 303–304.

CHA, H.-W., KANG, M.-C., SHIN, K. & YANG, C.-W. (2016). Transmission Electron Microscopy Specimen Preparation of Delicate Materials Using Tripod Polisher. *Applied Microscopy* **46**, 110–115.

CHA, H. G., KIM, C. W., KIM, Y. H., JUNG, M. H., JI, E. S., DAS, B. K., KIM, J. C. & KANG, Y. S.

(2009). Preparation and characterization of α-Fe_2O_3 nanorod-thin film by metal-organic chemical vapor deposition. *Thin Solid Films* **517**, 1853–1856.

CHANG, C.-H., DOMINGUEZ-CABALLERO, J. A., CHOI, H. J. & BARBASTATHIS, G. (2011). Nanostructured gradient-index antireflection diffractive optics. *Optics Letters* **36**, 2354.

CHEN, D., GORIS, B., BLEICHRODT, F., MEZERJI, H. H., BALS, S., BATENBURG, K. J., DE WITH, G. & FRIEDRICH, H. (2014). The properties of SIRT, TVM, and DART for 3D imaging of tubular domains in nanocomposite thin-films and sections. *Ultramicroscopy* **147**, 137–148.

CHU, H., SONG, S., LI, C. & GIBSON, D. (2017). Surface Enhanced Raman Scattering Substrates Made by Oblique Angle Deposition: Methods and Applications. *Coatings* **7**, 26.

COLLADO, V., MARTIN, N., PEDROSA, P., RAUCH, J. Y., HORAKOVA, M., YAZDI, M. A. P. & BILLARD, A. (2016). Temperature dependence of electrical resistivity in oxidized vanadium films grown by the GLAD technique. *Surface and Coatings Technology* **304**, 476–485.

DAVIM, J. P. (2012). *Materials and Surface Engineering: Research and Development*. Woodhead Publishing.

DEBNATH, R. K., MEIJERS, R., JEGANATHAN, K., RICHTER, T., STOICA, T., CALARCO, R. & LÜTH, H. (2008). Self-assembled growth of GaN nanowires. *Journal of Physics: Conference Series* **126**, 012026.

DERVAUX, J., CORMIER, P. A., MOSKOVKIN, P., DOUHERET, O., KONSTANTINIDIS, S., LAZZARONI, R., LUCAS, S. & SNYDERS, R. (2017). Synthesis of nanostructured Ti thin films by combining glancing angle deposition and magnetron sputtering: A joint experimental and modeling

study. *Thin Solid Films* **636**, 644–657.

DIMITROV, R., MURPHY, M., SMART, J., SCHAFF, W., SHEALY, J. R., EASTMAN, L. F., AMBACHER, O. & STUTZMANN, M. (2000). Two-dimensional electron gases in Ga-face and N-face AlGaN/GaN heterostructures grown by plasma-induced molecular beam epitaxy and metalorganic chemical vapor deposition on sapphire. *Journal of Applied Physics* **87**, 3375–3380.

DINH, T. M. C., BARNABÉ, A., BUI, M. A., JOSSE, C., HUNGRIA, T., BONNINGUE, C., PRESMANES, L. & TAILHADES, P. (2018). FIB plan view lift-out sample preparation for TEM characterization of periodic nanostructures obtained by spinodal decomposition in $Co_{1.7}Fe_{1.3}O_4$ thin films. *CrystEngComm* **20**, 6146–6155.

DISLAKI, E., ROBBENNOLT, S., CAMPOY-QUILES, M., NOGUÉS, J., PELLICER, E. & SORT, J. (2018). Coercivity Modulation in Fe–Cu Pseudo-Ordered Porous Thin Films Controlled by an Applied Voltage: A Sustainable, Energy-Efficient Approach to Magnetoelectrically Driven Materials. *Advanced Science* **5**, 1–8.

DUBEY, A., KOLEKAR, S. K., GNANAKUMAR, E. S., ROY, K., VINOD, C. P. & GOPINATH, C. S. (2016). Porous thin films toward bridging the material gap in heterogeneous catalysis. *Catalysis, Structure and Reactivity* **2**, 1–12.

EGERTON, R. F. & MALAC, M. (2005). EELS in the TEM. *Journal of Electron Spectroscopy and Related Phenomena* **143**, 43–50.

ESFANDIAR, A., SAVALONI, H. & PLACIDO, F. (2013). On the fabrication and characterization of graded slanted chiral nano-sculptured silver thin films. *Physica E: Low-Dimensional Systems*

and Nanostructures **50**, 88–96.

FLUTIE, R. E. (1985). TEM/STEM Sample Preparation for the Investigation of Solid State Structures: Applications to Electronic Devices and Computer Components. *MRS Proceedings* **62**, 105–112.

FRIEDRICH, H., MCCARTNEY, M. R. & BUSECK, P. R. (2005). Comparison of intensity distributions in tomograms from BF TEM, ADF STEM, HAADF STEM, and calculated tilt series. *Ultramicroscopy* **106**, 18–27.

GÓMEZ, V. J., SANTOS, A. J., BLANCO, E., LACROIX, B., GARCÍA, R., HUFFAKER, D. L. & MORALES, F. M. (2019). Porosity Control for Plasma-Assisted Molecular Beam Epitaxy of GaN Nanowires. *Crystal Growth and Design* **19**, 2461–2469.

GORIS, B., ROELANDTS, T., BATENBURG, K. J., HEIDARI MEZERJI, H. & BALS, S. (2013). Advanced reconstruction algorithms for electron tomography: From comparison to combination. *Ultramicroscopy* **127**, 40–47.

HAWKEYE, M. M. & BRETT, M. J. (2007). Glancing angle deposition: Fabrication, properties, and applications of micro- and nanostructured thin films. *Journal of Vacuum Science & Technology A: Vacuum, Surfaces, and Films* **25**, 1317.

HAWKEYE, M. M., TASCHUK, M. T. & BRETT, M. (2014). Glancing angle deposition of thin films. *Wiley*.

HE, Y. & ZHAO, Y. (2011). Advanced multi-component nanostructures designed by dynamic shadowing growth. *Nanoscale* **3**, 2361.

HERNÁNDEZ-SAZ, J., HERRERA, M. & MOLINA, S.I. (2013). Fabrication of needle-shaped specimens containing subsurface nanostructures for electron tomography. In *FIB Nanostructures* **20**, Wang Z. M. (Ed), pp 241-246. Springer.

HOSOKAWA, F., SAWADA, H., KONDO, Y., TAKAYANAGI, K. & SUENAGA, K. (2013). Development of Cs and Cc correctors for transmission electron microscopy. *Journal of Electron Microscopy* **62**, 23–41.

JAIN, R. K., GAUTAM, Y. K., DAVE, V., CHAWLA, A. K. & CHANDRA, R. (2013). A study on structural, optical and hydrophobic properties of oblique angle sputter deposited HfO_2 films. *Applied Surface Science* **283**, 332–338.

KENNEDY, S. R. & BRETT, M. J. (2003). Porous broadband antireflection coating by glancing angle deposition. *Applied optics* **42**, 4573–4579.

KOVAL, O. Y., SAPUNOV, G. A., FEDOROV, V. V. & MUKHIN, I. S. (2019). Growth and optical properties of GaPN/GaP heterostructure nanowire array. *Journal of Physics: Conference Series* **1400**, 055036.

VAN KRANENBURG, H. & LODDER, C. (1994). Tailoring growth and local composition by oblique-incidence deposition: a review and new experimental data. *Materials Science and Engineering R* **11**, 295–354.

KÜBEL, C., VOIGT, A., SCHOENMAKERS, R., OTTEN, M., SU, D., LEE, T. C., CARLSSON, A. & BRADLEY, J. (2005). Recent advances in electron tomography: TEM and HAADF-STEM tomography for materials science and semiconductor applications. *Microscopy and Microanalysis* **11**, 378–400.

DE LA MATA, M., MAGEN, C., GAZQUEZ, J., UTAMA, M. I. B., HEISS, M., LOPATIN, S., FURTMAYR, F., FERNÁNDEZ-ROJAS, C. J., PENG, B., MORANTE, J. R., RURALI, R., EICKHOFF, M., FONTCUBERTA I MORRAL, A., XIONG, Q. & ARBIOL, J. (2012). Polarity assignment in ZnTe, GaAs, ZnO, and GaN-AlN nanowires from direct dumbbell analysis. *Nano Letters* **12**, 2579–2586.

LACROIX, B., SANTOS, A. J., HURAND, S., CORVISIER, A., PAUMIER, F., GIRARDEAU, T., MAUDET, F., DUPEYRAT, C., GARCÍA, R. & MORALES, F. M. (2019). Nanostructure and Physical Properties Control of Indium Tin Oxide Films Prepared at Room Temperature through Ion Beam Sputtering Deposition at Oblique Angles. *Journal of Physical Chemistry C* **123**, 14036–14046.

LARSON, S. & ZHAO, Y. (2016). Tuning the composition of Bi_xW_yO nanorods towards zero bias PEC water splitting. *Nanotechnology* **27**, 1–12.

LAZIĆ, I. & BOSCH, E. G. T. (2017). *Analytical Review of Direct Stem Imaging Techniques for Thin Samples*. 1st ed. Elsevier Inc.

LAZIĆ, I., BOSCH, E. G. T. & LAZAR, S. (2016). Phase contrast STEM for thin samples: Integrated differential phase contrast. *Ultramicroscopy* **160**, 265–280.

LI, J., MALIS, T. & DIONNE, S. (2006). Recent advances in FIB-TEM specimen preparation techniques. *Materials Characterization* **57**, 64–70.

LI, X. J., SONG, Z. WEI, ZHAO, Y., WANG, Y., ZHAO, X. C., LIANG, M., CHU, W. G., JIANG, P. & LIU, Y. (2016). Vertically porous nickel thin film supported Mn_3O_4 for enhanced energy storage performance. *Journal of Colloid and Interface Science* **483**, 17–25.

LIEDTKE-GRÜNER, S., GRÜNER, C., LOTNYK, A., GERLACH, J. W., MENSING, M., SCHUMACHER, P. & RAUSCHENBACH, B. (2019). Crystallinity and texture of molybdenum thin films obliquely deposited at room temperature. *Thin Solid Films* **685**, 8–16.

LIEDTKE, S., GRÜNER, C., GERLACH, J. W., LOTNYK, A. & RAUSCHENBACH, B. (2018). Crystalline Ti-nanostructures prepared by oblique angle deposition at room temperature. *Journal of Vacuum Science & Technology B, Nanotechnology and Microelectronics: Materials, Processing, Measurement, and Phenomena* **36**, 031804.

LIEDTKE, S., GRÜNER, C., LOTNYK, A. & RAUSCHENBACH, B. (2017). Glancing angle deposition of sculptured thin metal films at room temperature. *Nanotechnology* **28**, 385604.

LIU, J., NIU, R., GU, J., CABRAL, M., SONG, M. & LIAO, X. (2020). Effect of Ion Irradiation Introduced by Focused Ion-Beam Milling on the Mechanical Behaviour of Sub-Micron-Sized Samples. *Scientific Reports* **10**, 1–8.

LOSURDO, M., GIANGREGORIO, M. M., CAPEZZUTO, P., BRUNO, G., NAMKOONG, G., DOOLITTLE, W. A. & BROWN, A. S. (2004). Interplay between GaN polarity and surface reactivity towards atomic hydrogen. *Journal of Applied Physics* **95**, 8408–8418.

MALIS, T., CHENG, S. C. & EGERTON, R. F. (1988). EELS log-ratio technique for specimen-thickness measurement in the TEM. *Journal of Electron Microscopy Technique* **8**, 193–200.

MAUDET, F., LACROIX, B., SANTOS, A. J., PAUMIER, F., PARAILLOUS, M., DUPEYRAT, C., GARCÍA, R., MORALES, F. M. & GIRARDEAU, T. (2019). Towards perfect MWIR transparency using oblique angle deposition. *Applied Surface Science* **470**, 943–950.

MAUDET, F., LACROIX, B., SANTOS, A. J., PAUMIER, F., PARAILLOUS, M., HURAND, S., CORVISIER, A., DUPEYRAT, C., GARCÍA, R., MORALES, F. M. & GIRARDEAU, T. (2020). On the importance of light scattering for high performances nanostructured antireflective surfaces. *Acta Materialia* **188**, 386–393.

MAUDET, F., LACROIX, B., SANTOS, A. J., PAUMIER, F., PARAILLOUS, M., HURAND, S., CORVISIER, A., MARSAL, C., GIROIRE, B., DUPEYRAT, C., GARCÍA, R., MORALES, F. M. & GIRARDEAU, T. (2020). Optical and nanostructural insights of oblique angle deposited layers applied for photonic coatings. *Applied Surface Science* **520**, 146312.

MCCAFFREY, J. P. & BARNA, A. (1997). Preparation of cross-sectional TEM samples for low-angle ion milling. *Microscopy Research and Technique* **36**, 362–367.

MCMULLAN, G., FARUQI, A. R., CLARE, D. & HENDERSON, R. (2014). Comparison of optimal performance at 300keV of three direct electron detectors for use in low dose electron microscopy. *Ultramicroscopy* **147**, 156–163.

MIDGLEY, P. A. & DUNIN-BORKOWSKI, R. E. (2009). Electron tomography and holography in materials science. *Nature Materials* **8**, 271–280.

MIDGLEY, P. A., WEYLAND, M., MEURIG THOMAS, J. & JOHNSON, B. F. G. (2001). Z-contrast tomography: A technique in three-dimensional nanostructural analysis based on Rutherford scattering. *Chemical Communications* 907–908.

MORKÖTTER, S., FUNK, S., LIANG, M., DÖBLINGER, M., HERTENBERGER, S., TREU, J., RUDOLPH, D., YADAV, A., BECKER, J., BICHLER, M., SCARPA, G., LUGLI, P., ZARDO, I., FINLEY, J. J., ABSTREITER, G. & KOBLMÜLLER, G. (2013). Role of microstructure on optical properties in

high-uniformity $In_{1-x}Ga_xAs$ nanowire arrays: Evidence of a wider wurtzite band gap. *Physical Review B - Condensed Matter and Materials Physics* **87**, 1–9.

MUTO, D., ARAKI, T., NAOI, H., MATSUDA, F. & NANISHI, Y. (2005). Polarity determination of InN by wet etching. *Physica Status Solidi (A) Applications and Materials Science* **202**, 773–776.

NARESH-KUMAR, G., BRUCKBAUER, J., WINKELMANN, A., YU, X., HOURAHINE, B., EDWARDS, P. R., WANG, T., TRAGER-COWAN, C. & MARTIN, R. W. (2019). Determining GaN Nanowire Polarity and its Influence on Light Emission in the Scanning Electron Microscope. *Nano Letters* **19**, 3863–3870.

NG, H. M. & CHO, A. Y. (2002). Investigation of Si doping and impurity incorporation dependence on the polarity of GaN by molecular beam epitaxy. *Journal of Vacuum Science & Technology B: Microelectronics and Nanometer Structures* **20**, 1217.

NOVIKOV, B. V., SEROV, S. Y., FILOSOFOV, N. G., SHTROM, I. V., TALALAEV, V. G., VYVENKO, O. F., UBYIVOVK, E. V., SAMSONENKO, Y. B., BOURAVLEUV, A. D., SOSHNIKOV, I. P., SIBIREV, N. V., CIRLIN, G. E. & DUBROVSKII, V. G. (2010). Photoluminescence properties of GaAs nanowire ensembles with zincblende and wurtzite crystal structure. *Physica Status Solidi - Rapid Research Letters* **4**, 175–177.

NOWAKOWSKI, P., BONIFACIO, C. S., CAMPIN, M. J., RAY, M. L. & FISCHIONE, P. E. (2017). Accurate Removal of Implanted Gallium and Amorphous Damage from TEM Specimens after Focused Ion Beam (FIB) Preparation. *Microscopy and Microanalysis* **23**, 300–301.

NUCHUAY, P., CHAIKEEREE, T., HORPRATHUM, M., MUNGKUNG, N., KASAYAPANAND, N., OROS,

C., LIMWICHEAN, S., NUNTAWONG, N., CHANANONNAWATHORN, C., PATTHANASETTAKUL, V., MUTHITAMONGKOL, P., SAMRANSUKSAMER, B., DENCHITCHAROEN, S., KLAMCHUEN, A., THANACHAYANONT, C. & EIAMCHAI, P. (2017). Engineered omnidirectional antireflection ITO nanorod films with super hydrophobic surface via glancing-angle ion-assisted electron-beam evaporation deposition. *Current Applied Physics* **17**, 222–229.

PAN, Y., ZHAO, Y., TAN, P. K., MAI, Z., RIVAL, F. & LAM, J. (2018). Problems of and solutions for coating techniques for tem sample preparation on ultra low-k dielectric devices after progressive-FIB Cross-section Analysis. *Proceedings of the International Symposium on the Physical and Failure Analysis of Integrated Circuits, IPFA*, pp. 1–5. Singapore.

PHAE-NGAM, W., HORPRATHUM, M., CHANANONNAWATHORN, C., LERTVANITHPHOL, T., SAMRANSUKSAMER, B., SONGSIRIRITTHIGUL, P., NAKAJIMA, H. & CHAIYAKUN, S. (2019). Oblique angle deposition of nanocolumnar TiZrN films via reactive magnetron co-sputtering technique: The influence of the Zr target powers. *Current Applied Physics* **19**, 894–901.

POLAT, D. B., KELES, O. & AMINE, K. (2014). Well-aligned, ordered, nanocolumnar, Cu-Si thin film as anode material for lithium-ion batteries. *Journal of Power Sources* **270**, 238–247.

PRIKULIS, J., TAMULEVIČIUS, T., POPLAUSKS, R., BERGS, G., APSITE, I., MALINOVSKIS, U., ACTINS, A. & ERTS, D. (2015). Optical properties of thin metal films with nanohole arrays on porous alumina-aluminum structures. *RSC Advances* **5**, 68143–68150.

QI, Z., TANG, J., HUANG, J., ZEMLYANOV, D., POL, V. G. & WANG, H. (2019). Li_2MnO_3 Thin Films with Tilted Domain Structure as Cathode for Li-Ion Batteries. *ACS Applied Energy Materials* **2**, 3461–3468.

RAJAK, P., ISLAM, M., JIMÉNEZ, J. J., MÁNUEL, J. M., ASEEV, P., GAČEVIĆ, CALLEJA, E., GARCÍA, R., MORALES, F. M. & BHATTACHARYYA, S. (2019). Unravelling the polarity of InN quantum dots using a modified approach of negative-spherical-aberration imaging. *Nanoscale* **11**, 13632–13638.

RAJAN, S., WONG, M., FU, Y., WU, F., SPECK, J. S. & MISHRA, U. K. (2005). Growth and electrical characterization of N-face AlGaN/GaN heterostructures. *Japanese Journal of Applied Physics, Part 2: Letters* **44**, 15–18.

REZNIK, R. R., KOTLYAR, K. P., SOSHNIKOV, I. P., KUKUSHKIN, S. A., OSIPOV, A. V. & CIRLIN, G. E. (2018). MBE growth and Structural Properties of InAs and InGaAs Nanowires with Different Mole Fraction of In on Si and Strongly Mismatched SiC/Si(111) Substrates. *Semiconductors* **52**, 651–653.

ROBBIE, K. & BRETT, M. J. (1997). Sculptured thin films and glancing angle deposition: Growth mechanics and applications. *Journal of Vacuum Science & Technology a-Vacuum Surfaces and Films* **15**, 1460–1465.

ROEDIGER, P., WANZENBOECK, H. D., WAID, S., HOCHLEITNER, G. & BERTAGNOLLI, E. (2011). Focused-ion-beam-inflicted surface amorphization and gallium implantation-new insights and removal by focused-electron-beam-induced etching. *Nanotechnology* **22**, 235302.

ROMANYUK, O., BARTOŠ, I., BRAULT, J., MIERRY, P. DE, PASKOVA, T. & JIŘÍČEK, P. (2016). GaN quantum dot polarity determination by X-ray photoelectron diffraction. *Applied Surface Science* **389**, 1156–1160.

ROUVIERE, J. L., WEYHER, J. L., SEELMANN-EGGEBERT, M. & POROWSKI, S. (1998). Polarity

determination for GaN films grown on (0001) sapphire and high-pressure-grown GaN single crystals. *Applied Physics Letters* **73**, 668–670.

RUBANOV, S. & MUNROE, P. R. (2004). FIB-induced damage in silicon. *Journal of Microscopy* **214**, 213–221.

SÁFRÁN, G. & GRENET, T. (2002). Novel method for the plan-view TEM preparation of thin samples on brittle substrates by mechanical and ion beam thinning. *Microscopy Research and Technique* **56**, 308–314.

SALAZAR, P., RICO, V. & GONZÁLEZ-ELIPE, A. R. (2017). Non-enzymatic hydrogen peroxide detection at NiO nanoporous thin film- electrodes prepared by physical vapor deposition at oblique angles. *Electrochimica Acta* **235**, 534–542.

SANTOS, A. J., LACROIX, B., BLANCO, E., HURAND, S., GÓMEZ, V. J., PAUMIER, F., GIRARDEAU, T., HUFFAKER, D. L., GARCÍA, R. & MORALES, F. M. (2020). Simultaneous Optical and Electrical Characterization of GaN Nanowire Arrays by Means of Vis-IR Spectroscopic Ellipsometry. *Journal of Physical Chemistry C* **124**, 1535–1543.

SANTOS, A. J., LACROIX, B., MAUDET, F., CORVISIER, A., PAUMIER, F., DUPEYRAT, C., GIRARDEAU, T., GARCÍA, R. & MORALES, F. M. (2019). Surface oxidation of amorphous Si and Ge slanted columnar and mesoporous thin films: Evidence, scrutiny and limitations for infrared optics. *Applied Surface Science* **493**, 807–817.

SARWAR, A. T. M. G., YANG, F., ESSER, B. D., KENT, T. F., MCCOMB, D. W. & MYERS, R. C. (2016). Self-assembled InN micro-mushrooms by upside-down pendeoepitaxy. *Journal of Crystal Growth* **443**, 90–97.

SCHUSTER, F., LAUMER, B., ZAMANI, R. R., MAGÉN, C., MORANTE, J. R., ARBIOL, J. & STUTZMANN, M. (2014). P-GaN/n-ZnO heterojunction nanowires: Optoelectronic properties and the role of interface polarity. *ACS Nano* **8**, 4376–4384.

SHETTY, A. R. & KARIMI, A. (2012). Texture mechanisms and microstructure of biaxial thin films grown by oblique angle deposition. *Physica Status Solidi (B) Basic Research* **249**, 1531–1540.

SHI, P., LI, X., ZHANG, Q., YI, Z. & LUO, J. (2018). Photocatalytic activity of self-assembled porous TiO_2 nano-columns array fabricated by oblique angle sputter deposition. *Materials Research Express* 5, 045018.

SUN, R., WANG, G. G. & PENG, Z. C. (2018). Fabrication and UV photoresponse of GaN nanowire-film hybrid films on sapphire substrates by chemical vapor deposition method. *Materials Letters* **217**, 288–291.

TIAN, L., LI, L., BAN, C., & WU, M. (2017). Fabrication and characterization of TiO_2 antireflection coatings with gradient-index. In *2017 IEEE 12th International Conference on Nano/Micro Engineered and Molecular Systems*, pp. 131–136. Los Angeles.

TOCCAFONDI, C., UTTIYA, S., CAVALLERI, O., GEMME, G., BARBORINI, E., BISIO, F. & CANEPA, M. (2014). Optical properties of nanogranular and highly porous TiO2 thin films. *Journal of Physics D: Applied Physics* **47**, 485301.

TONG, Z., JIANG, X., LUO, X., BAI, Q., XU, Z., BLUNT, L. & LIANG, Y. (2016). Review on FIB-Induced Damage in Diamond Materials. *Current Nanoscience* **12**, 685–695.

TUOMISTO, F., SAARINEN, K., LUCZNIK, B., GRZEGORY, I., TEISSEYRE, H., SUSKI, T., POROWSKI, S., HAGEMAN, P. R. & LIKONEN, J. (2005). Effect of growth polarity on vacancy defect and impurity incorporation in dislocation-free GaN. *Applied Physics Letters* **86**, 1–3.

TYAGI, P., RAMESH, C., YADAV, B. S., KUSHVAHA, S. S. & KUMAR, M. S. (2019). Laser molecular beam epitaxy of vertically self-assembled GaN nanorods on Ta metal foil: Role of growth temperature and laser repetition rate. *CrystEngComm* **21**, 5448–5454.

UNAL, O., HEUER, A. H. & MITCHELL, T. E. (1990). Preparation of crosssectional specimens of ceramic thermal barrier coatings for transmission electron microscopy. *Journal of Electron Microscopy Technique* **14**, 307–312.

UPADHYAYA, K., AYACHIT, N. & SHIVAPRASAD, S. M. (2020). Comparison of optoelectronic properties of epitaxial and non-epitaxial GaN nanostructures. *Journal of Materials Science: Materials in Electronics* **31**, 13756–13764.

VOYLES, P. M., GRAZUL, J. L. & MULLER, D. A. (2003). Imaging individual atoms inside crystals with ADF-STEM. *Ultramicroscopy* **96**, 251–273.

WANG, Z. L. (2011). Picoscale science and nanoscale engineering by electron microscopy. *Journal of Electron Microscopy* **60**, 269–278.

WEAVER, L. (1997). Cross-section TEM sample preparation of multilayer and poorly adhering films. *Microscopy Research and Technique* **36**, 368–371.

WEYHER, J. L., MÜLLER, S., GRZEGORY, I. & POROWSKI, S. (1997). Chemical polishing of bulk and epitaxial GaN. *Journal of Crystal Growth* **182**, 17–22.

WEYLAND, M. & MIDGLEY, P. A. (2004). Electron tomography. *Materials Today* **7**, 32–40.

WOO, S. Y., BUGNET, M., NGUYEN, H. P. T., MI, Z. & BOTTON, G. A. (2015). Atomic Ordering in InGaN Alloys within Nanowire Heterostructures. *Nano Letters* **15**, 6413–6418.

XI, J. Q., SCHUBERT, M. F., KIM, J. K., SCHUBERT, E. F., CHEN, M., LIN, S. Y., LIU, X. & SMART, J. A. (2007). Optical thin-film materials with low refractive index for broadband elimination of Fresnel reflection. *Nature Photonics* **1**, 176–179.

XU, Y., GU, L., LI, Y., MO, B. & LIN, Y. (2018). Combination of focused ion beam (FIB) and microtome by ultrathin slice preparation for transmission electron microscopy (TEM) observation. *Earth, Planets and Space* **70**, 150.

YÜCELEN, E., LAZIĆ, I. & BOSCH, E. G. T. (2018). Phase contrast scanning transmission electron microscopy imaging of light and heavy atoms at the limit of contrast and resolution. *Scientific Reports* **8**, 1–10.

ZHAO, B., LOCKREY, M. N., CAROFF, P., WANG, N., LI, L., WONG-LEUNG, J., TAN, H. H. & JAGADISH, C. (2018). The effect of nitridation on the polarity and optical properties of GaN self-assembled nanorods. *Nanoscale* **10**, 11205–11210.

ZHAO, S. & MI, Z. (2017). Recent advances on p-type III-nitride nanowires by molecular beam epitaxy. *Crystals* **7**, 18–26.

ZHAO, S., WANG, R., CHU, S. & MI, Z. (2019). Molecular beam epitaxy of III-Nitride Nanowires: Emerging applications from deep-ultraviolet light emitters and Micro-LEDs to artificial photosynthesis. *IEEE Nanotechnology Magazine* **13**, 6–16.

ZHONG, X., WADE, C. A., WITHERS, P. J., ZHOU, X., CAI, C., HAIGH, S. J. & BURKE, M. G. (2020). Comparing Xe^{+}pFIB and Ga^{+}FIB for TEM sample preparation of Al alloys: Minimising FIB-induced artefacts. *Journal of Microscopy* 1–12.

TABLES

Table 1. Advantages and disadvantages of tripod polishing and focused ion beams TEM sample preparation methods when applied to porous thin films.

<table>
<tr><th></th><th>Advantages</th><th>Disadvantages</th></tr>
<tr><td rowspan="3">Tripod polishing</td><td>Low running and material costs</td><td>Absence of in-situ control (blind process)</td></tr>
<tr><td>Larger electron-transparent areas of homogeneous thickness: suitable for performing any (S)TEM study</td><td rowspan="2">Possibility of specimen contamination during one of the preparation stages: promotion of unwanted oxidation of coatings</td></tr>
<tr><td>Easily adaptable and implementable to any lab</td></tr>
<tr><td rowspan="4">Focused ion beams</td><td rowspan="2">Straightforward, faster and cleaner</td><td>Sophisticated and expensive system which requires a high level of expertise</td></tr>
<tr><td>Need for post-lift thinning to attain ultra-thin regions: appearance of directional curtaining</td></tr>
<tr><td rowspan="2">Selection of specific areas and particular orientations: in-situ control</td><td>Pt-layer protective layer can hinder subsequent analysis</td></tr>
<tr><td>FIB-induced damage and ion implantation</td></tr>
</table>

FIGURE LEGENDS

Figure 1. Different stages involved in preparing delicate TEM specimens using the tripod method. (a) Scheme of a glued staked specimen before polishing. Pictures of the specimen, once attached to a 3 mm TEM molybdenum grid, after tripod polishing (b) and after ion milling (c). The inset of (c) places emphasis on the developed electron-transparent region.

Figure 2. STEM-HAADF overview of a FIB lamella of GaN nanowires. Note that the central part of the lamella was thinned and polished at low energy afterwards. The inset details the final aspect of the thinned region.

Figure 3. Large field-of-view (more than 4 μm width) STEM-EELS thickness-map of a SiO_2 bilayer (about 300 nm thick) deposited by OAD on a Si substrate (1^{st} layer with $\alpha = 65^{o}$, 2^{nd} layer with $\alpha = 85^{o}$). The colour scale represents the evolution of relative thickness of the specimen (t/λ) where t is specimen thickness and λ is the characteristic mean free path for inelastic scattering.

Figure 4. Bright-field TEM overview of different OAD systems deposited on silicon substrates. (a) SiO_2 OAD monolayer deposited at $\alpha = 85^{o}$. (b) SiO_2 OAD bilayer deposited at $\alpha = 65°$ and $\alpha = 85°$ with azimuthal rotation between the two layers of $\Phi = 180°$. (c) TiO_2/SiO_2 OAD trilayer deposited at α (TiO_2) = 70°, α (1^{st} SiO_2) = 50° and α (2^{nd} SiO_2) = 82° with azimuthal rotation between layers of $\Phi = 180°$. The insets of (a), (b) and (c) detail the features of the Si/SiO_2, SiO_2/SiO_2 and TiO_2/SiO_2 interfaces respectively, together with the corresponding FFT diffractogram of each layer.

Figure 5. Bright-field TEM micrographs of ITO-OAD columns prepared by (a) Xe and (b) Ar IBS at $\alpha = 85^{o}$.

Figure 6. Evolution of the crystallographic orientation of an ITO OAD film deposited by Xe IBS at α = 50º. (a) Cross-section bright-field TEM overall observation of the ITO OAD film. (b) High-resolution TEM micrograph of the Si/ITO OAD interface with the corresponding FFT of each layer. (c) Bright-field TEM detail of the top part of the film. (d) High-resolution TEM micrograph of the top part of the film together with the associated FFT diffractogram of the region.

Figure 7. iDPC-STEM image of a single crystalline GaN nanowire along the [$11\bar{2}0$] zone axis. Beam current was maintained below 30 pA, the dwell time is 5 µs, beam convergence angle is 21.4 mrad and the field of view is 12.6 nm. The resulting range of collection angles for the annular DF detector (DF4) is 15-57 mrad, with DPC and scan rotations of 8º and -3º, respectively. Note that the image is shown as it appears live on the screen without any post-processing. The image reveals the larger Ga atoms on top of the double atom layers (Ga-polar).

Figure 8. STEM-EDX analysis of a TiO_2/SiO_2 OAD trilayer deposited at α (TiO_2) = 70°, α (1^{st} SiO_2) = 50° and α (2^{nd} SiO_2) = 82° with azimuthal rotation between layers of Φ = 180°. (a) STEM-HAADF micrograph and elemental maps obtained for Si, Ti and O atoms together with the elemental profiles along the whole coating thickness and the HAADF profile collected along individual columns of each layer. (b) EDX integrated spectra and associated compositional quantitative analysis for each OAD layer.

Figure 9. (a) STEM-HAADF 3D reconstruction of a TiO_2/SiO_2 OAD trilayer. (b) Associated porosity profile extracted along the surface normal, together with some representative planar views of each layer obtained by data segmentation (voids are shown in black colours).

FIGURES

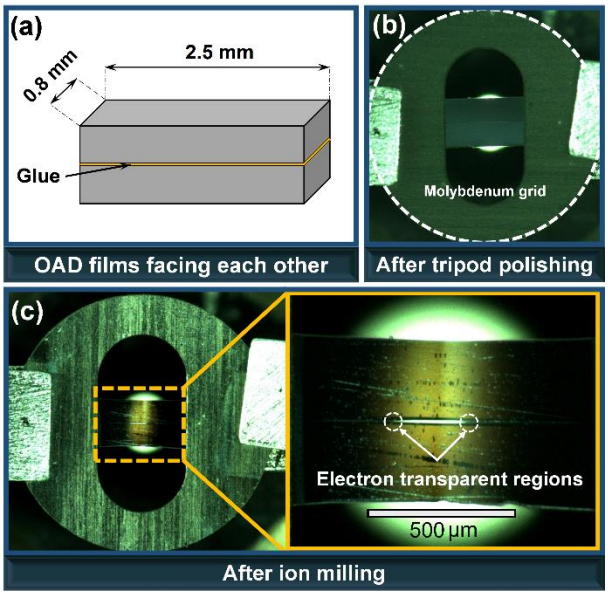

Fig. 1

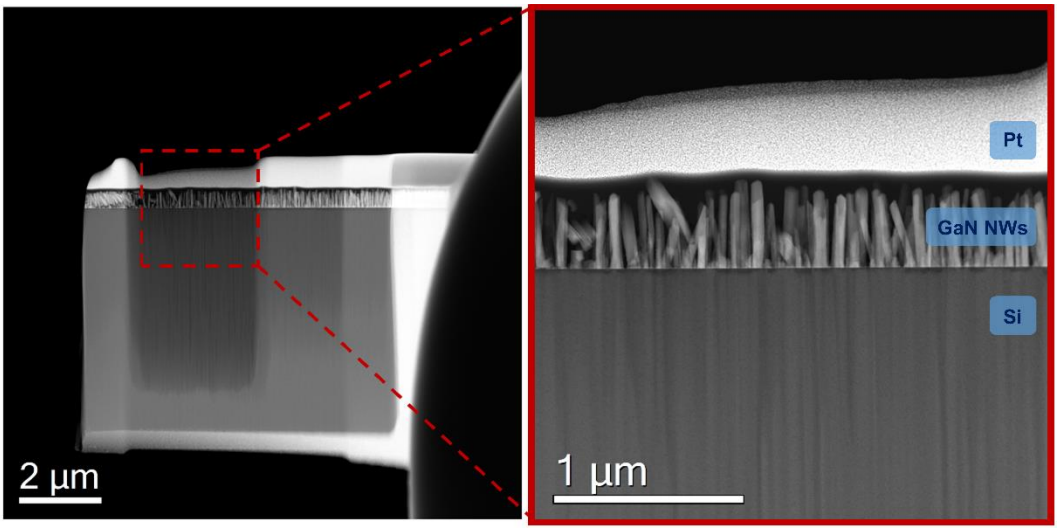

Fig. 2

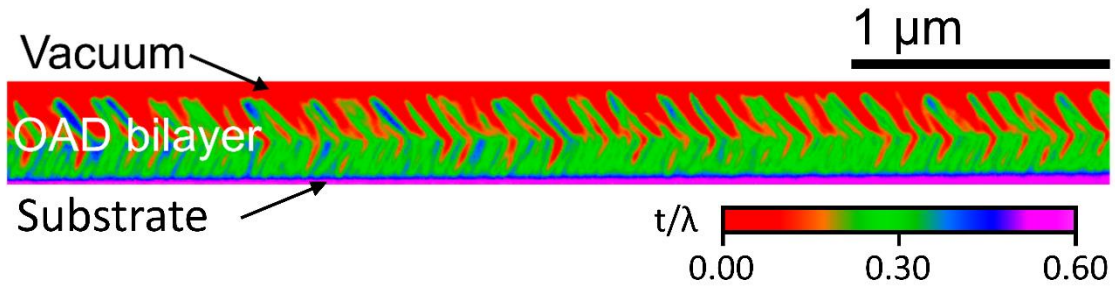

Fig. 3

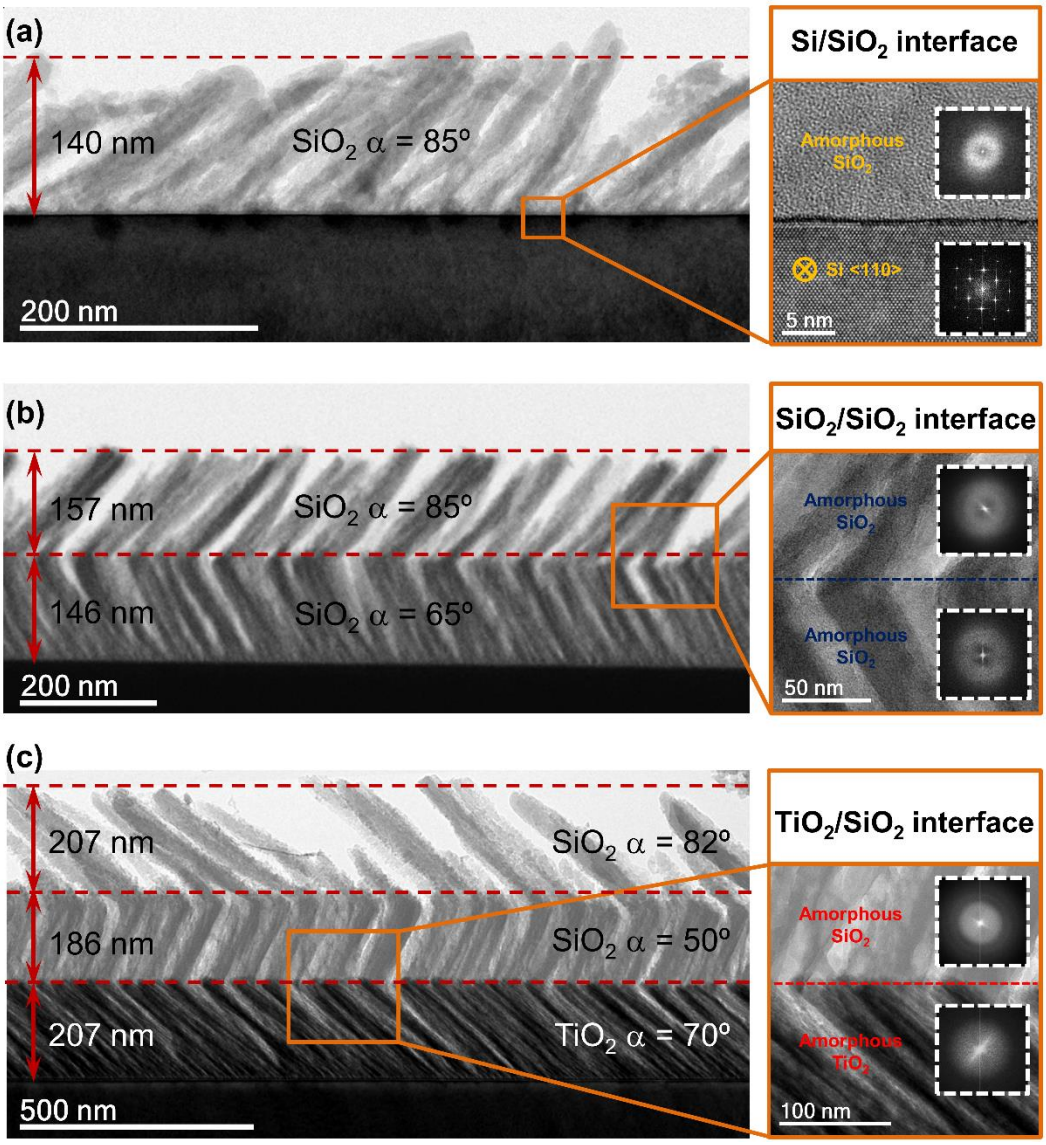
(a)
140 nm
SiO2 α = 85°
200 nm
Si/SiO2 interface
Amorphous SiO2
Si <110>
5 nm
(b)
157 nm
SiO2 α = 85°
146 nm
SiO2 α = 65°
200 nm
SiO2/SiO2 interface
Amorphous SiO2
Amorphous SiO2
50 nm
(c)
207 nm
SiO2 α = 82°
186 nm
SiO2 α = 50°
207 nm
TiO2 α = 70°
500 nm
TiO2/SiO2 interface
Amorphous SiO2
Amorphous TiO2
100 nm

Fig. 4

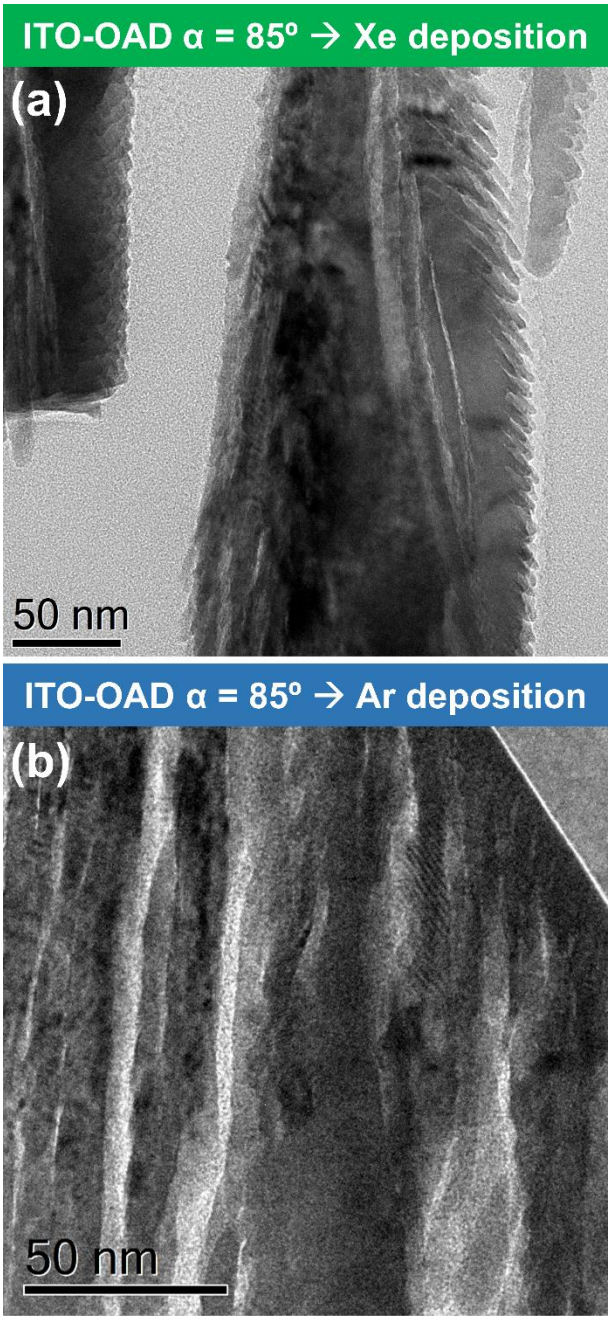
ITO-OAD α = 85° → Xe deposition
(a)
50 nm
ITO-OAD α = 85° → Ar deposition
(b)
50 nm

Fig. 5

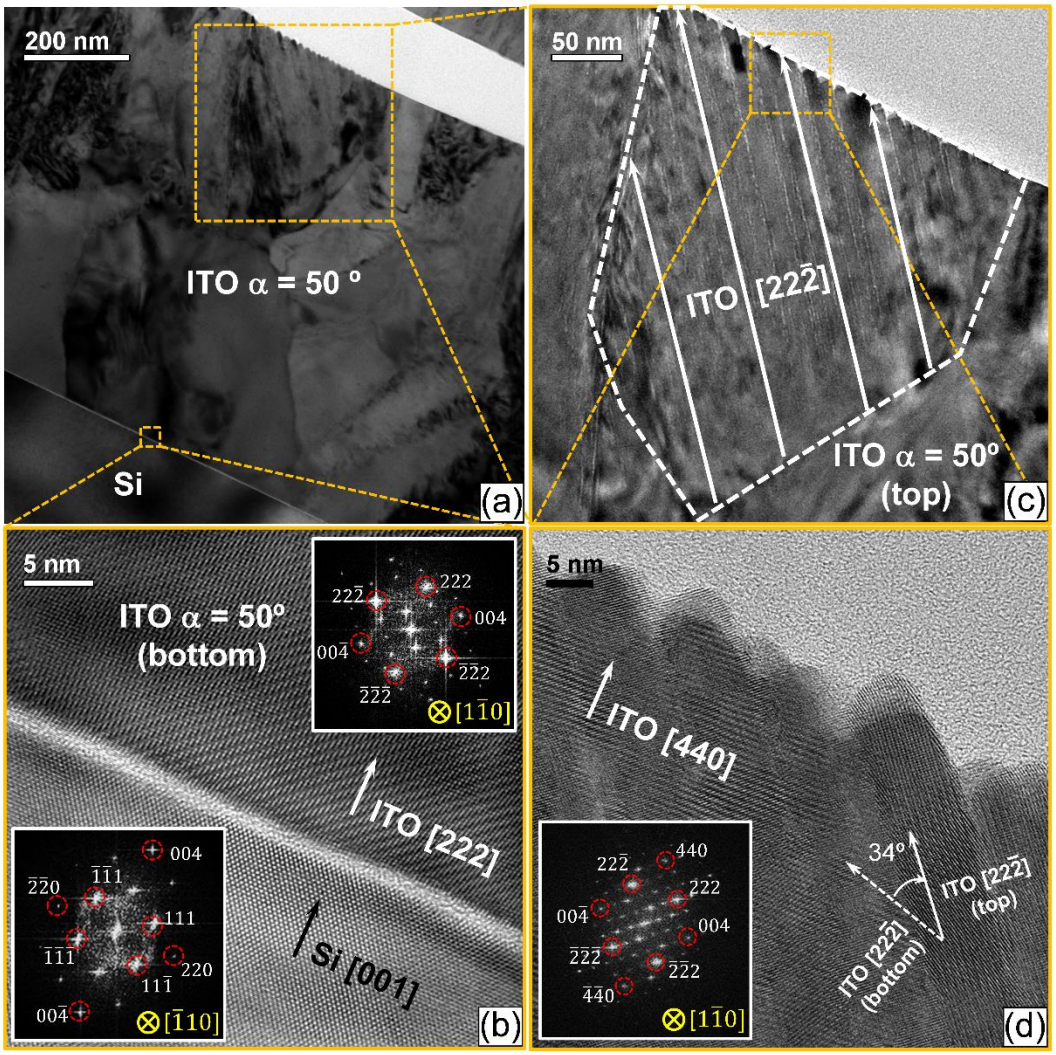
200 nm
ITO α = 50 °
Si
(a)
50 nm
ITO [22$\bar{2}$]
ITO α = 50°
(top)
(c)
5 nm
ITO α = 50°
(bottom)
22$\bar{2}$
222
004
00$\bar{4}$
$\bar{2}\bar{2}\bar{2}$
$\bar{2}$22
⊗[1$\bar{1}$0]
ITO [222]
Si [001]
004
$\bar{1}\bar{1}$1
$\bar{2}\bar{2}$0
111
$\bar{1}$11
220
11$\bar{1}$
00$\bar{4}$
⊗[$\bar{1}$10]
(b)
5 nm
ITO [440]
22$\bar{2}$
440
222
00$\bar{4}$
004
$\bar{2}\bar{2}\bar{2}$
$\bar{2}$22
$\bar{4}\bar{4}$0
⊗[1$\bar{1}$0]
34°
ITO [22$\bar{2}$]
(top)
ITO [22$\bar{2}$]
(bottom)
(d)

Fig. 6

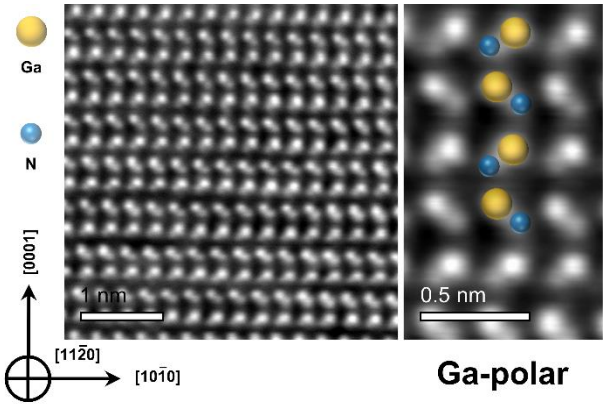
Ga
N
[0001]
[11$\bar{2}$0]
[10$\bar{1}$0]
1 nm
0.5 nm
Ga-polar

Fig. 7

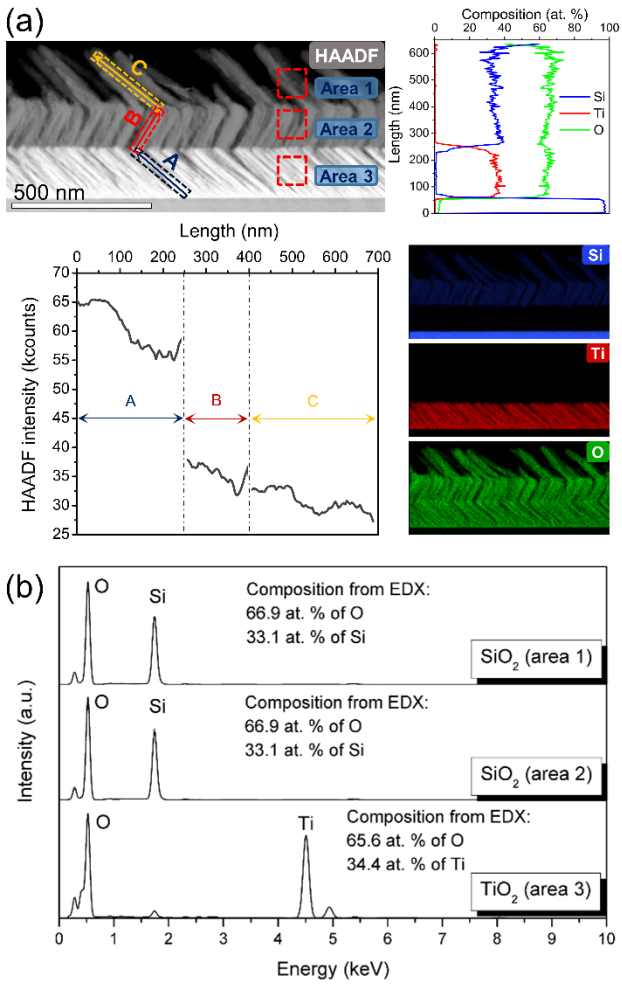
(a)
HAADF
Area 1
Area 2
Area 3
C
B
A
500 nm
Composition (at. %)
Length (nm)
Si
Ti
O
Length (nm)
HAADF intensity (kcounts)
A
B
C
Si
Ti
O
(b)
Intensity (a.u.)
O
Si
Composition from EDX:
66.9 at. % of O
33.1 at. % of Si
SiO2 (area 1)
SiO2 (area 2)
Ti
Composition from EDX:
65.6 at. % of O
34.4 at. % of Ti
TiO2 (area 3)
Energy (keV)

Fig. 8

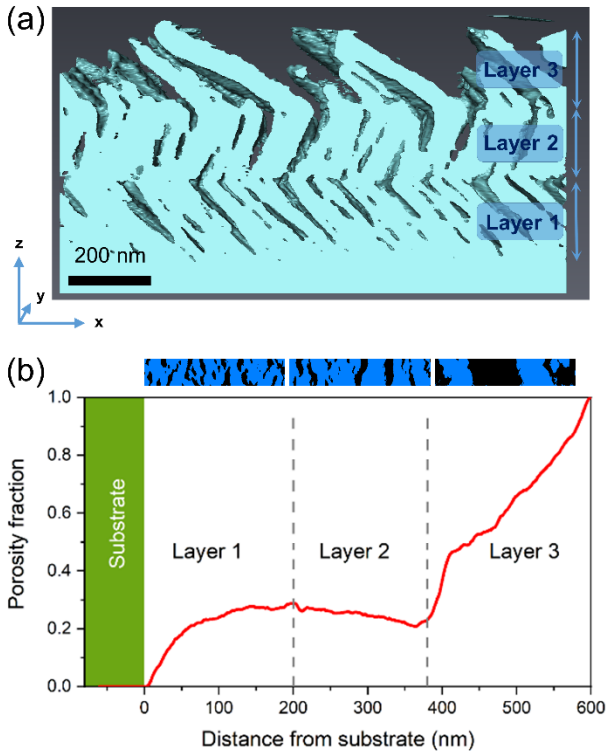
(a)
Layer 3
Layer 2
Layer 1
200 nm
z
y
x
(b)
Porosity fraction
1.0
0.8
0.6
0.4
0.2
0.0
Substrate
Layer 1
Layer 2
Layer 3
0
100
200
300
400
500
600
Distance from substrate (nm)

Fig. 9

GRAPHICAL ABSTRACT

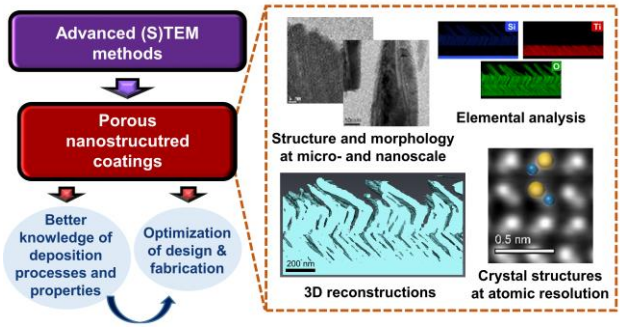

Manuscript IX

Controlled grain-size thermochromic VO_2 coatings by the fast oxidation of sputtered vanadium or vanadium oxide films deposited at glancing angles

A. J. Santos, B. Lacroix, M. Domínguez, R. García, N. Martin,

F. M. Morales

Under review in Applied Surface Science

Controlled grain-size thermochromic VO_2 coatings by the fast oxidation of sputtered vanadium or vanadium oxide films deposited at glancing angles

A. J. Santos[a, b, *], B. Lacroix[a, b], M. Domínguez[a, c], R. García[a, b], N. Martin[d] and F. M. Morales[a, b]

[a] *IMEYMAT: Institute of Research on Electron Microscopy and Materials of the University of Cádiz, Spain.*

[b] *Department of Materials Science and Metallurgic Engineering, and Inorganic Chemistry, Faculty of Sciences, University of Cádiz, Spain.*

[c] *Department of Condensed Matter Physics, Faculty of Sciences, University of Cádiz, 11510 Puerto Real, Cádiz, Spain.*

[d] *Institut FEMTO-ST, UMR 6174 CNRS, Université Bourgogne Franche-Comté, 15B, Avenue des montboucons 25030 Besançon Cedex, France.*

* Corresponding author: antonio.santos@uca.es

Abstract: An original oxidation strategy to attain thermochromic vanadium dioxide thin films is reported. This two-step procedure comprises the initial deposition of DC magnetron-sputtered vanadium or vanadium oxide films by the combination of glancing angle deposition and, if needed, reactive gas pulsing process, followed by fast oxidation of such layers in air atmosphere at high temperatures. Thanks to the careful control of the thermal treatment parameters, and taking advantage of the superior reactivity of the high surface-to-volume porous deposited structures, the formation of pure VO_2 (M1) layers was achieved. The comprehensive characterization of such oxidized systems by means of scanning electron microscopy, Raman spectroscopy and scanning-

transmission electron microscopy techniques such as electron energy-loss spectroscopy, not only confirmed the presence of the VO_2 (M1) phase, but also allowed to shed light on the key role that reaction time plays in the selective formation of vanadium dioxide films of adjustable grain size and crystallinity. The metal-to-insulator response of the accomplished VO_2 layers was finally evaluated by means of temperature dependent Kelvin probe force microscopy measurements, evidencing surface potential drops at heating, greater than those reported in the literature to date for VO_2 thin films. The present work sheds light on the simple and cost-effective fabrication of high-efficient VO_2 coatings for practical applications in smart windows or switching electronics.

Keywords: VO_2 thin film, glancing angle deposition, fast oxidation, metal-insulator transition, transmission electron microscopy, EELS spectroscopy, Raman spectroscopy, KPFM.

1. Introduction

Vanadium oxides (VO_x) have become one of the most extensively studied materials for many years due to their unique properties and technological applications. In this framework, vanadium (IV) oxide (VO_2) has specially attracted the attention of the scientific community since it experiments a reversible metal-to-insulator phase transition (MIT) between insulating monoclinic VO_2 (M1) to metallic rutile VO_2 (R) during heating at a temperature of ~68 ºC, which implies drastic changes in the optical and electrical properties [1–4]. This makes VO_2 an attractive thermochromic material for applications in smart windows [5–7], resistive switching elements [8,9], storage devices [10] and sensors [11].

Nevertheless, the fabrication of VO_2-based films has become a real challenging issue not only due to the complexity of the vanadium-oxygen reactive system but also because of the narrow stability range of VO_2, which can lead to the formation other more thermodynamically stable oxides such as V_2O_3 and V_2O_5, mixtures of various stoichiometries, or even the appearance of several VO_2 metastable crystalline polymorphs [2–4,12–14]. Hence, it is clear that the preparation of VO_2 films requires a precise control of the deposition parameters.

Many different approaches, such as sol–gel [15], pulsed laser deposition [16,17], chemical vapor deposition [18], and polymer-assisted deposition [19], have succeeded in synthesizing VO_x films with high VO_2 yields, although the complexity and high cost involved in all these methods become a critical limitation for practical applications. In this context, reactive direct current (DC) magnetron sputtering postulates as one of the most promising and simplest techniques for depositing large-areas of vanadium or vanadium oxide films at low temperature [5,20–24], so that by adjusting oxygen

injection times during the sputtering process, the proportions of V to O on the films can be controlled. As can be found in the literature [11,20,22–25], many different post-deposition annealing strategies, which are required to obtain VO_2 films with desired compositions and morphologies, have been extensively implemented on magnetron sputtered V or VO_x films. Several of these post-annealing treatments sometimes lack of precise control of key oxidation parameters like reaction temperatures and times or heating and cooling rates, either omitting or not proving accurate data on them, which seriously compromise their reproducibility. Others however, have the disadvantage of rigid experimental conditions that implies controlled O_2, N_2 or SO_2 partial pressures at high temperatures (> 450ºC) for reaction times longer than 1 hour. Therefore, the development of a simple, fast and cost-effective thermal treatment to carry out the effective oxidation of vanadium or vanadium oxide films for the fabrication of thermochromic VO_2 coatings has become a crucial issue.

In this paper, we report a simple and straightforward post-deposition oxidation strategy for the effective oxidation of DC magnetron-sputtered V or VO_x films to obtain thermochromic VO_2 (M1) nanostructured films of controlled crystallinity and grain size. Taking advantage of the great reactivity of these high surface-to-volume porous nanostructures, in addition to evaluate how oxidation occurs in systems of different morphology and composition, vanadium films were deposited by GLancing Angle Deposition (GLAD) whereas VO_x films were produced by combining GLAD and the Reactive Gas Pulsing Process (RGPP). Thanks to the accurate control of temperatures and reaction times, as well as heating rates, fast thermal treatment of these GLAD thin films was successfully performed in air atmosphere. Afterwards, all these oxidized systems were completely characterized by means of Raman spectroscopy, scanning

electron microscopy (SEM) and scanning-transmission electron microscopy (S)TEM techniques, including high-angle annular dark-field (HAADF) and high-resolution (HRTEM) imaging, as well as electron energy-loss spectroscopy (EELS), allowing us to unravel the key role that reaction time plays not only in the selective generation of different vanadium oxide phases but also in the formation of VO_2 (M1) layers of a diverse nature, morphology and thickness. Likewise, the effect of oxygen injection times on the subsequent oxidation of the vanadium oxide GLAD films prepared by RGPP was also investigated. Finally, in order to evaluate the MIT response of such oxidized coatings, the surface work functions of the best thermally treated V or VO_x samples were investigated through Kelvin probe force microscopy (KPFM) measurements [26].

2. Materials and Method

Films were deposited at room temperature by DC magnetron sputtering from a vanadium metallic target (51 mm diameter and 99.9 atomic % purity) in a homemade deposition chamber which was evacuated down to 10^{-5} Pa before each run by means of a turbomolecular pump backed by a primary pump. The target was sputtered with a constant current density J = 100 A m^{-2}. Single crystalline (100) silicon substrates were placed at 65 mm from the target surface. On the basis of previous studies [20], V or VO_x films were deposited by combining GLAD (GLancing Angle Deposition) and Reactive Gas Pulsing Process (RGPP), fixing the angle of incidence (α) relative to the substrate normal at 85°. Argon was injected at a mass flow rate of 2.40 sccm and the pumping speed was maintained at S = 13.5 L s^{-1}, whereas the oxygen gas was periodically supplied into the sputtering chamber. A rectangular pulsed signal was

employed for the oxygen flow rate with regard to time evolution. The pulsing period was set at P = 16 s. The maximum oxygen flow rate was q_{O_2Max} = 0.40 sccm. It corresponds to the critical flow required to avalanche the process in the compound sputtering mode. The minimum oxygen flow rate was q_{O_2min} = 0 sccm. Thus, the injection time of the oxygen gas was changed from t_{ON} = 0 to 8 s. The thickness of the vanadium film (t_{ON} = 0 s) was measured by profilometry, adjusting the deposition time to obtain a film thick enough (~700 nm) to investigate how the oxidation progresses when the subsequent thermal treatments are applied. This same deposition time was later fixed for films prepared with t_{ON} > 0 s.

After deposition, vanadium or vanadium oxide samples were thermally treated in a homemade reaction system consisting in an Al_2O_3 tube on a SiC resistors furnace able to reach 1500°C, with an attached concentric steel tube where a high-temperature steel covered k-type thermocouple inside which acts as an axle for a system of horizontal translation. At the end of the metallic tube nearby the furnace, the thermocouple crosses and fixes to a cylinder placed inside this tube, mechanized with a hitch to hang a combustion boat. Thus, the thermometer tip is always placed some millimeters over the center of this alumina crucible, allowing the temperature in the reaction zone to be life-tracked. The other end side also crosses and is fixed to another piece that is part of a handlebar used to slide the specimen holders inside and outside. In this way, by fixing a temperature in the center of the furnace, one is able to control the temperature increase (heating rate) by moving the boat more and more inside the furnace. Consequently, translation routines were prepared for reaching an average heating rate of 42ºC s^{-1}, as well as for adjusting longer or shorter reaction times at the desired temperature of 550ºC. Lastly, all the samples were cooled down in open-air atmosphere.

Cross-sectional and plan-view scanning electron microscopy (SEM) images were acquired using FEI Nova NanoSEM and FEI Teneo microscopes operated at 5 kV, to examine the general morphology and size of each film. To obtain additional insights into the nanostructure of such systems, high-resolution transmission electron microscopy (HRTEM), selected area electron diffraction (SAED) and high-angle annular dark-field imaging (HAADF) studies were carried out in two TEM microscopes (FEI Talos F200X and JEOL 2100 LaB_6), working both at an accelerating voltage of 200 kV. A Gatan Imaging Filter (GIF) Continuum system fitted in the Talos microscope was used for spatially-resolved EELS analysis in scanning mode. STEM-EELS 2D spectrum image (SI) data were acquired using a 2.5 mm diameter aperture and 0.05 eV/channel energy dispersion. The convergence and collection semi-angles were set to 10.5 and 20.0 mrad, respectively, and the probe current was about 150 nA. In this configuration, the energy resolution was 0.8 eV. In order to allow accurate chemical shift measurements, the Dual EELS mode was used to record nearly simultaneously both, low-loss, and V-$L_{2,3}$ in addition to O-K edges, at each pixel position. Dwell times of about 0.9 to 2 seconds per pixel were set to optimize the signal-to-noise ratio. Electron-transparent cross-sectional samples were prepared for TEM observations by means of both tripod polishing and focused ion beam (FIB) approaches. For this purpose, a tripod polisher (Model 590 Tripod Polisher®) was used to progressively thin the samples to a few microns, followed by Ar^+-ion milling in a Gatan PIPS system setting the acceleration energy of both guns to 3.5 keV (+7° top and −7° bottom). Alternatively, FIB lamellae were also prepared in a Zeiss Auriga FIB-SEM system.

Raman spectroscopy measurements were determined by using a dispersive Raman spectrometer (Jasco, model NRS7200) with a 100x objective coupled to a 532.19 nm

NdYAG laser excitation source. Raman spectra were recorded with a spectral resolution of 1 cm^{-1} in the range of 39–856 cm^{-1}. These wavenumbers are those where vanadium oxides show their characteristic Raman bands. Care was taken to avoid heat-induced phase changes in the samples, so laser power was set at 0.6 mW and Raman spectra were collected for 30 s with an average accumulation of two spectra.

Finally, KPFM measurements at increasing and decreasing temperatures were performed with a Bruker MultiMode 8-HR AFM system, equipped with a water-refrigerated scanner (model AS-130VT), that included a variable-temperature sample stage connected to a MultiMode High Temperature Heater controller (maximum temperature 250°C) from Digital Instruments/Veeco. A specialized probe holder that fits to a silicone rubber seal to form a controlled environment space for the tip and the sample, was used to perform these measurements. The sample temperature was previously calibrated by performing a heating/cooling experiment in which the sample was substituted by a K-type thermocouple glued with thermal paste to a metallic puck (similar to the one used to attach the sample to the scanner stage). Thus, the small difference between the scanner heater controller temperature and the real sample temperature can be easily estimated for every heating/cooling step. A specialized KPFM SiN probe from Bruker (type PFQNE-AL), with a nominal tip radius of 5 nm, was used to obtain both topographic, in the conventional tapping mode, and simultaneous surface potential images, in the Frequency Modulated-KPFM (FM-KPFM) mode. The work function of the tip was calibrated against gold using an Al/Au/Si test sample also from Bruker (reference PF-KPFM-SMPL) before and after the thermal cycle. Tip wearing during the KPFM experiment was minimum, as can be inferred from the fact that topographic images hardly show loss of lateral resolution, nor

the probe work function changed significantly after the heating/cooling cycle was completed. It should be noted that, to ensure that the same sample area was scanned at each temperature, the tip had to be relocated on the sample surface at every temperature step, to compensate for the AFM scanner thermal drift.

3. Results and discussion

3.1. Characterization of as-deposited thin films

Pure vanadium or vanadium oxide GLAD thin films were deposited on silicon substrates at $\alpha = 85°$ and oxygen was pulsed during the deposition, varying the oxygen injection time (t_{ON}) from 0 to 8 s. In this regards, five samples were deposited which were tagged as V0 (t_{ON} = 0s), V2 (t_{ON} = 2 s), V4 (t_{ON} = 4 s), V6 (t_{ON} = 6 s), and V8 (t_{ON} = 8 s). For the purpose of exploring the structure and the morphology of as-deposited thin films, Figure 1 shows cross-sectional and planar view SEM micrographs of samples V0 to V8. As can be seen, all samples exhibit a well-defined structure of inclined columns but the effect of the oxygen injection time is also evidenced. As reference, sample V0 presents columns slightly connected to each other, which gives rise to a porous structure about 700 nm thick. Nonetheless, as oxygen injection time increases, samples gradually become thicker (since deposition rate increases as well [20]) and columns are more and more narrow, which not only promotes the connection between the columns but also leads to a decrease in the total porosity. This is clearly observed in Fig. 1, specially for planar view images, which were taken at the same magnification. Furthermore, it was also found that all samples presented column tilt angle (β) values lower than expected according to common empirical ballistic approaches such as the tangent [27] ($\beta = 80°$) and Tait [28] ($\beta = 58°$) rules. However, it has been proved that

these empirical expressions have completely succeeded in accounting for the tilt angle of nanocolumns, when $\alpha > 50°$ [29], so that additional mechanisms, more complex than geometrical relationships, must be taken into account to understand the formation of such columnar structures. In general, it is assumed that the β angle value depends on the chemical nature of the deposited material, the deposition conditions, as well as well as the characteristics of the deposition reactor itself [30,31]. Likewise, a progressive decrease of the β angle can also be observed as oxygen injection time increases, which can be linked to the mean free path of the sputtered particles. The sputtering pressure, which increases with oxygen injection time, promotes the collisions between particles, leading to the widening of the particle flux that reaches the target and impinges the film. This phenomenon can give rise to maximum column angles β close to 20–30° for high incident angles, which could explain the effect observed here for RGPP samples.

Additionally, with the aim of disclosing the crystal structure, the predominant species present in the as-deposited films, and hence the effect of oxygen injection time, V0 and V8 samples were prepared for TEM observations. Figures 2(a) and (b) display the STEM-HAADF images of samples V0 and V8, respectively. As can be appreciated, the V0 overlayer presents a more porous structure when compared to that of V8, which is in agreement with the evidences stated before. Also noteworthy is the great difference between the β values for both samples, being indeed double for the non-oxidized one ($\beta = 52°$ for V0, and $\beta = 26°$ for V8). Besides, HRTEM images and their fast Fourier transform (FFT) for the top regions of samples V0 (Fig. 2(c)) and V8 (Fig. 2(d)) evidenced a remarkable difference between both samples at the nanoscale. On one side, the HRTEM studies not only demonstrate that the vanadium GLAD layer (V0) is crystalline after deposition at room temperature but also it is mainly composed by the

pure vanadium cubic phase. By contrast, the vanadium oxide GLAD layer (V8) presents a less crystalline structure, which could be explained due to the increase of the mean energy of the sputtered particles as the oxygen injection time increases [20]. Moreover, the HRTEM micrograph and its FFT (equivalent to a diffractogram of the crystalline structure) for sample V8 revealed interplanar distances and angles proper from those of the tetragonal $V_{16}O_3$ phase. Lastly, in order to check more extended regions than those inspected by HRTEM, selected area electron diffraction (SAED) patterns were collected for V0 and V8 samples (see Supplementary Material Section I) which, in addition to support the greatest crystallinity of sample V0, confirmed that the major phase in V0 sample was cubic vanadium (AMCSD 0011235) whereas the V8 sample was constituted by a mixture of cubic VO (ICDD 01-075-0048) and tetragonal $V_{16}O_3$ (ICDD 04-011-0169).

3.2. Thermal oxidation and subsequent characterization of pure vanadium films

Once disclosed the nature, morphology and structure of the as-deposited vanadium or vanadium oxide GLAD films, their fast heating was conducted to promote the formation of the VO_2 thermochromic phase. Note that, initially, only sample V0 was thermally treated since the aim of this first stage was to optimize reaction times that maximize the amounts of VO_2. In all cases, the reaction temperature (T_r) and heating rate (h_r) were fixed to 550ºC and 42ºC s^{-1}, respectively. In this light, the V0 sample was subjected to different reaction times (t_r) ranging from 1 to 300 seconds followed by the subsequent instantaneous cooling in air. A detailed scheme of the fast thermal treatment process can be found in Figure 3(a). Here, with the aim of demonstrating the high control achieved in our developed system, it is worth mentioning that all the displayed temperature

versus time tracks are those recorded during the thermal treatment. Thereupon, Raman spectroscopy analyses were performed on all the treated samples for the purpose of monitoring the rise of the different vanadium oxidized species as reaction time increases. Fig. 3(b) shows the Raman spectra collected for V0 samples heated at 550ºC and subjected to different reaction times (from 1 to 300 seconds). As seen, Raman signals given for samples treated during 1 and 15 seconds can be characterized, in addition to be quite noisy, to contain weak VO_2 (M1) peaks at ~194, 224, 262 and 612 cm^{-1}, as well as others at ~304 and 420 cm^{-1} which can be associated to the presence of VO_x ($1.67 < x < 2$) species [32]. The remaining Raman bands found in both samples might be attributed to metastable vanadium oxides whose Raman scattering data have not been reported yet. As reaction time increases, VO_2 (M1) Raman signature gradually becomes more significant, reaching a pure VO_2 (M1) signal for t_r = 45 s which perfectly matches with other Raman VO_2 spectra previously reported in the literature [32–35]. From this point forward, longer reaction times would only promote the formation of the α-V_2O_5 phase (according to Ref. [32]), turning into the predominant phase for t_r > 75 s. Thus, all of the above points out the fundamental role that the precise control of the thermal treatment parameters, and very specially the reaction time, plays in achieving the effective transformation of V into VO_2 (M1) thin films.

Furthermore, the structure and morphology of all these annealed samples were also explored by means of SEM. Figure 4 illustrates the top views of all the thermally treated V0 samples which not only allow to identify the different stages involved in the oxidation of such layers but also bring to light some characteristic features of both VO_2 and V_2O_5 phases. Here, a progressive widening of the grain size for reaction times between 1 and 45 seconds can be observed (for a more detailed overview of the grain

morphology after 1 and 15 seconds reaction times, refer to Supplementary Material Section II). Hence, it seems that the oxidation of vanadium GLAD V0 occurs from the top to the bottom of the layer, starting with the formation of small nuclei of VO_x ($x < 2$) that will later evolve into coarser grains of VO_2 (M1). Likewise, it also appears that the slanted columnar morphology so characteristic of the GLAD systems, which is the main responsible for the almost instantaneous and efficient oxidation of these films thanks to its large surface-to-volume ratios, is lost after thermal treatment. On the other hand, it is also noticed that $t_r > 60$ leads to the gradual growth of these grains along the axial direction, emerging a kind of micro-rods structure randomly distributed in all directions which is characteristic of the V_2O_5 [36,37]. In consequence, the porosity of the film increases again, but at the expense of its consistency and homogeneity.

In order to accomplish a comprehensive characterization of the fast thermally treated V0 samples, as well as to reinforce the assumptions previously made, TEM studies were performed on several selected samples. Figure 5(a), (b) and (c) display the bright-field TEM cross-sectional views for V0 samples after reaction times of 1, 45 and 300 seconds, respectively. In Fig. 5(a), two clear regions are distinguished: a first compact layer of about 120 nm thick composed by well-defined grains (to have a better insight of this first layer, refer to Supplementary Material Section III), and a second porous and thicker layer beneath (~ 520 nm) that preserves the GLAD morphology of the original system. This confirms the previous hypothesis that oxidation initiates on the surface of the film and progresses towards the substrate as the reaction time increases. Similarly, it is also evidenced that the GLAD morphology disappears as the oxidation of the film develops. Fig. 5(d) shows a HRTEM micrograph of a grain corresponding to the oxidized region (sublayer 1) of the V0 sample for $t_r = 1$ s, revealing atomic columns of

monoclinic VO_2 (M1) (ICCD 04-005-4338) oriented in the [011] zone axis, with families of planes and their parameters and angles highlighted. Thus, it could be asserted that the granular reaction product that progresses from the surface of the layer towards the substrate is the thermochromic VO_2 phase. The same applies to the V0 sample subjected to a reaction time of 45 seconds, although the size of the grains observed here, as well as the thickness of the oxidized layer (~ 400 nm), are both significantly greater (Fig. 5(b)). Note that the reduced thickness of the V0 sample for t_r = 45 s is not directly associated to thermal treatment itself, but rather to an excessive ion-milling during the FIB sample preparation. In this way, it seems that, until the 45-second reaction time is reached, the oxygen in-diffuses more and more, giving rise to the appearance of bigger and single-crystalline VO_2 grains. The above could explain the outstanding Raman VO_2 (M1) signal acquired for this sample. Likewise, the HRTEM images collected in this oxidized region (sublayer 1 of the V0 sample for t_r = 45 s) also show interplanar spacings and angles that match with the $[11\bar{2}]$ VO_2 (M1) orientation (Fig. 5(e)). Nonetheless, an unreacted buried layer of about 160 nm thick still remains. Overall, it must be highlighted that, for $t_r \leq 45$ s, homogeneous oxide layer thicknesses are generated, whereas the original total thickness of the layer is not significantly affected. Also note that the VO_2 thicknesses attained here (120 – 400 nm) are above those conventionally reported in the literature for optical applications in thermochromic smart windows [3,4,7,38]. Hence, the subsequent thermal treatments of thinner (< 100 nm) vanadium GLAD films at T_r = 550ºC, h_r = 42ºC s^{-1} and $t_r \leq 45$ s, could lead to the exclusive formation of pure VO_2 films of controlled grain size, which has been reported to have significant effects on the features of the MIT transition [39], thanks to the precise control of reaction times.

On the contrary, the V0 sample subjected to t_r = 300 s presents a structure quite different from those previously visualized (Fig. 5(c)). In this case, a unique layer can be distinguished, being its thickness almost three times thicker than the previous ones. This is clearly linked to an advanced oxidation of the film characterized by the oxygen enrichment, which leads us to think that V_2O_5 is the predominant specie in the sample. Indeed, the HRTEM image displayed in Fig. 5(f), which was collected from a representative region of V0 sample for t_r = 300 s, confirms this assumption since characteristic lattice distances and angles of the [012] V_2O_5 zone axis (ICDD 04-008-4555) were identified. Other features of this sample are the irregular shapes and thicknesses as well as the presence of big voids (see Supplementary Material Section IV), which could all compromise the consistency of the coating.

In order to go a little further in the characterization of such thermally treated samples, as well as to unravel the vanadium oxidation state within each of the layers previously distinguished, STEM-EELS analyses were carried out in V0 preparations subjected to t_r = 1, 45 and 300 s. Like in others 3d transition metals, the $L_{2,3}$ edge of vanadium exhibits a characteristic shape consisting in two sharp peaks usually separated by a few eV (known as “white lines”). Since those major features are due to electron transitions from 2p ($2p_{3/2}$ and $2p_{1/2}$, for L_3 and L_2, respectively) to unoccupied 3d states, the L_3/L_2 intensity ratio as well as the shift of the $L_{2,3}$ lines reveal the d-band occupancy, and consequently they are very sensitive to the valence state of the metal [40,41]. As a general trend, and especially in the case of V, an increase in the oxidation state leads to a shift of the $L_{2,3}$ edge towards higher energy loss as well as a decrease of the L_3/L_2 ratio [42–44]. Because the oxygen K-edge reflects the local density of states at the oxygen site, changes in its energy-loss near-edge structure can also be considered to determine

the oxidation levels. In the case of the V-O system, the O-K edge overlaps with the continuum region of V-$L_{2,3}$ edge, which hinders chemical quantification. However, monitoring the relative band shift between O-K and V-L_3 edges as well as the shape of the O-K edge, in particular modifications in the relative intensities of the e_g and t_{2g} pre-edge peaks can be insightful to reveal some changes of the V valence [45,46].

Figure 6 displays the extracted EELS signals containing both the V-$L_{2,3}$ and O-K pre-edge which were summed in small characteristic areas of V0 samples thermally treated at h_r = 42ºC s^{-1}, T_r = 550ºC, and t_r = 1, 45 and 300 s. For detailed information on the processing of the STEM-EELS 2D spectrum image datasets, see Supplementary Material Section V. As can be seen in Fig. 6(a), the EELS spectrum #1a collected from just one individual nanocolumn (brighter contrast on the HAADF image) is characteristic of metallic vanadium, since only the V-$L_{2,3}$ white lines separated by ΔE_L = 7.0 eV, with the L_3 peak located at 514.1 eV, are visible. Also note that peak positions and energy differences extracted from these and subsequent EELS spectra can be found in Table S.1 (Supplementary Material Section V). Between two nanocolumns, the EELS signal shows some modifications (spectrum #2a) since the $L_{2,3}$ lines are shifted towards the higher energies (L_3 position at 514.8 eV) and a single peak around 531.7 eV appears in the O-K pre-edge region. This feature is attributed to the e_g state arising from hybridization between O 2p and V 3d states [45,46]. Those observations, combined with the fact that the measured energy difference between the e_g and the V-L_3 peaks is ΔE = 16.9 eV, may reveal the V^{2+} valence state (VO) [44,47]. This indicates that, despite the V nanocolumns are mostly metallic, they may present a slightly oxidized surface due either to air exposure, as evidenced in other GLAD systems [48], or to the thermal annealing process itself. In the upper region of the film, measurements as the spectrum

#3a shows more pronounced changes characterized by a higher energy shift of the V-$L_{2,3}$ lines (L_3 position at 516.0 eV) and by the presence of two peaks in the O-K pre-edge region that corresponds to t_{2g} (around 528.6 eV) and e_g (around 530.8 eV) states coming from the O 2p and V 3d hybridization [45,46]. This increased shift of V-$L_{2,3}$ lines, but also the stronger t_{2g} contribution relative to e_g, the reduced energy difference between the e_g and the V-L_3 line (ΔE=14.7 eV) as well as the strong shoulders visible on the left sides of the L_3 and L_2 peaks (shown by the arrows) are fingerprints that allow to confirm the V^{4+} valence state (VO_2) [43,44].

When the annealing time increases up to 45 s (Fig. 6(b)), it is observed that the distribution of the oxidation states within the layer remains quite close to the previous case, but with a much deeper oxidized layer that extends up to about 400 nm from the surface. The EELS signals obtained in the upper part (spectrum #3b, where large grains are observed) and in the lower part (spectrum #2b, where both smaller grains and voids are observed) of this layer present very similar features than for the spectrum #3a (also see Table S1), confirming that the greater part of the films is in the V^{4+} valence state in agreement once again with the presence of VO_2. At the bottom part of the film (spectrum #1b), within about the first 160 nm of the layer, the EELS signals are quite similar to those of spectrum #2a, characteristic of a V^{2+} valence state.

By contrast, as evidenced in Fig. 6(c), 300 s reaction time leads to a complete modification of the oxidation state in the whole layer. All the EELS signals corresponding to regions located at different thicknesses within the coating present the same features that matches very well with a V^{5+} valence state (V_2O_5) according to the trends evidenced in the literature. As compared with the EELS signals of the previously identified VO_2 regions, the spectra shown in Fig. 6(c) present on the one hand V-$L_{2,3}$

white lines that are slightly shifted (0.5 eV) towards higher energies (L_3 position at about 516.6 eV), and on the other hand less separated O-K pre-edge peaks with a stronger t_{2g} contribution [43,45,46,49]. We can also mention that two weak shoulders are detected on the left side of the V-L_3 peak, indicating the presence of the vanadium pentoxide.

3.3. Thermal oxidation and subsequent characterization of vanadium oxide films

Once known how oxidation develops for pure vanadium GLAD films, it is time to explore how VO_x GLAD films deposited at different oxygen injection times behave when subjected to fast thermal treatments. In this way, provided the good outcomes obtained for the V0 sample, a thermal treatment consisting in a fast heating ramp of 42ºC s^{-1}, followed by keeping a constant temperature of 550ºC for 45 seconds, and a final cooling down in air atmosphere, was systematically applied to V2, V4, V6 and V8 samples. Figure 7 shows the planar view SEM images obtained for V2, V4, V6 and V8 samples after thermal treatments. As can be seen, all these samples present a granular structure quite similar to those presented in the V0 sample subjected to t_r = 45 s. However, remarkable differences are noticed. Proof of this is the undesired appearance, to a greater (samples V4 and V8) or lesser (samples V2 and V6) extent, of V_2O_5 micro-rod bundles on the surface, as well as the cracking (sample V6) or the final detachment (sample V8) of the coating (for a more detailed perception of such cracks and delaminations, refer to Supplementary Material Section VI). Note that the detachment of the V8 overlayer took place while it was cooled down in air. Thus, this phenomenon could be associated to the combined effect of the two following events. On the one

hand, it should not be forgotten that, as oxygen injection times increases, columns become taller and narrower, so the development of a more compact layer over such porous structures can result in a greater source of stress. Likewise, it should also be kept in mind that the species present in the sample V8 before the thermal treatment (VO and $V_{16}O_3$) were not the same as for sample V0. Thus, all this could lead to the outbreak of residual stresses at the different interfaces, probably favored by thermal expansion mismatches between layers, which can result in the development and propagation of cracks or, in the worst case, in the collapse of the physisorbed film, promoting the observed lack of adherence.

Figure 8(a) reveals the Raman spectroscopy studies carried out on V2, V4 and V6 samples. Note that Raman analyses could not be performed on the V8 sample as result of its detachment. The measured Raman spectra for V2 and V6 samples clearly show the characteristic Raman bands of the VO_2 (M1) phase together with a weak band at around ~340 cm^{-1} which is associated to the presence β-V_2O_5 [32]. By contrast, the Raman spectrum of the V4 sample not only indicates a clear VO_2 (M1) signature, but also a prominent signal of two overlapped bands at ~266 and 269 cm^{-1} which are characteristic to γ'-V_2O_5 and ε'-V_2O_5 pentoxide polymorphs [32]. All this is in agreement with the previously observed through SEM studies, which noticed the presence of the so characteristic V_2O_5 micro-rods, especially for the V6 sample. Therefore, in addition to the cracking and the detachment of the film, it seems that the thermally treated vanadium oxide GLAD samples also have the disadvantage of being less homogeneous than the V0, with the appearance of V_2O_5 micro-rod bundles on the surface. Notwithstanding, the results obtained for the V2 sample are quite promising.

So as to ultimately know how oxidation develops along the thickness of such porous vanadium oxide films, it was decided to explore the two most favorable samples so far, i.e., V2 and V6 samples, by means of TEM methods. Fig. 8(b) and (c) illustrate the cross-sectional bright-field overviews of V2 and V6 samples, respectively. Both samples clearly present three regions: a first sublayer located in the top part of the films (sublayer 1) characterized by large and single-crystalline grains; an intermediate region beneath (sublayer 2) consisting of grains of considerably smaller size; and a third most buried region (sublayer 3), in principle not oxidized, that preserves the features of the GLAD structures. Overall, some distinguishing characteristics of these two samples are a thicker first sublayer (~ 390 nm) for the V2 sample versus a greater intermediate thickness sublayer (~ 360 nm) for the sample V6. However, the size of the grains located in the so-called sublayer 1 of both samples is considerably bigger than those formed in the V0 sample for the same thermal treatment. Likewise, the oxidized layer thicknesses of V2 and V6 samples are ~ 570 nm and ~ 680 nm, respectively, which means that vanadium oxide GLAD films are more prone to oxidation than those of pure vanadium. All this could be explained by the fact that taller and smaller diameter columns, which is favored as oxygen injection time increases, imply greater surface-to-volume ratios, thus increasing the reactivity of the coating [48]. For this same reason, oxidation was more effective and progressed deeper in sample V6 than in V2. Instead, it should also be noticed that the original thickness of as-deposited V2 and V6 samples was not significantly affected after oxidation. In addition to the above, the HRTEM images collected from large-sized grains of V2 and V6 samples (Supporting Information Section VII) once more demonstrated the presence of the thermochromic VO_2 (M1) phase in the most surface layers.

In order to completely understand the effect that the deposition conditions can have on the oxidation process, and in particular the pulsed injection of oxygen, STEM-EELS analyses were also carried out in V2 and V6 oxidized samples as those shown in Figure 9(a) and (b), respectively. The EELS signals (see also Table S1 for more details) collected from the bottom part of the films, where the GLAD nanocolums are still visible, are similar and match well with a metallic V or poorly oxidized vanadium (VO), whereas the top part of the films reveal features that are clear fingerprints of VO_2. In the case of the V2 film, it is important to note that a thin intermediate sublayer (about 80 nm) has been identified on top of the nanocolumns, which shows EELS signal (spectrum #2 on Fig. 9(a)) with intermediate features (white line shift, energy difference ΔE, O-K pre-edge peak shapes) compared to VO and VO_2 and that matches with V^{3+} (V_2O_3) valence state according to the literature [43,47] . As a general trend, it can be observed that, as oxygen injection time increases more heterogeneous and thicker VO_2 layers are achieved after oxidation. However, as evidenced through Raman and EELS studies, they may develop V_2O_5 or V_2O_3 oxides up or down, respectively. Thus, it seems that a gradient of phases from more (V^{5+}) to less (V^{3+}) oxidized states, with an intermediate majoritarian V^{4+} valence region, following the V-O phase diagram trend [32], is developed along the film thickness in the direction from the surface (continuously exposed to O reactivity) to the interface with the substrate (where events promoted by O diffusion are more limited).

3.4. Metal-to-insulator response of the oxidized films

Finally, with the aim of evaluating the MIT of the oxidized samples, variable temperature KPFM was used to obtain the evolution of the work function (W_S) maps

with temperature. Figures 10(a) and (b) show the overlayed tridimensional images of topography and work function for the V0 sample subjected to t_r = 45 s at two different temperatures, below and above the MIT. In Fig. 10(c) the distribution of W_S values in both images, calculated from the KPFM values considering the tip work function, are represented. These values are fitted to a Gaussian function and, from the mean values found (peaks), it is clearly shown that a reduction in work function of about 0.16 eV takes place, as expected for this kind of transition [26].

A more detailed study was performed for the oxidized V2 sample (550ºC, h_r = 42ºC s^{-1} and t_r = 45 s), as shown in Figure 11, by scanning a 2 × 2 μm^2 area of this sample during a full heating and cooling cycle. The topography of this region is shown in Fig. 11(a), while Figs. 11(b)-(f) display the evolution of the work function maps with temperature during the heating/cooling cycle. These maps were derived from the KPFM images, taking into account the work function of the tip, and from them, the W_S distribution histograms can be represented and fitted to a Gaussian function (i.e., a normal distribution is again considered). The mean W_S values obtained at each temperature are represented in Fig. 11(g). Here, error bars length corresponds to the standard deviation of each Gaussian distribution fit. As expected, a hysteretic MIT, manifested as a reduction in work function of ~0.2 eV, which is considerably greater than those reported in the literature to date for VO_2 thin films [26], is clearly shown, with inflection points at around 78°C during heating and at around 73°C during cooling, and a thermal hysteresis width about $\Delta T \sim 5$°C.

In view of the foregoing, it is clearly demonstrated that the controlled and fast oxidation of V or VO_x GLAD films in air atmosphere leads to the attainment of high-performance VO_2 thermochromic layers. Hence, given the VO_2 thicknesses achieved here for the

different fast thermal treatments carried out, it is thought that the deposition and subsequent oxidation of vanadium or vanadium oxide GLAD film thicknesses similar to those required for optical applications in smart windows (< 100 nm) would give rise to the exclusive formation of VO_2 (M1) layers of adjustable grain size and crystallinity by controlling (a) oxygen injection times during deposition ($t_{ON} \leq 2$ s); and (b) reaction times ($t_r \leq 45$s) for thermal treatments conducted at 550ºC and $h_r = 42$ºC s^{-1}. In fact, these latest assumptions, which should be also contrasted through optical and electrical measurements, will be the focus of our future investigations.

4. Conclusions

In this work, a novel, simple and cost-effective approach for the fast oxidation of vanadium-based films to accomplish thermochromic VO_2 coatings of tunable grain size and crystallinity has been reported. For this purpose, porous V or VO_x layers were prepared by DC magnetron sputtering involving the glancing angle deposition (GLAD) and the reactive gas pulsing process (RGPP), keeping deposition angle $\alpha = 85°$ and pulsing the oxygen gas with t_{ON} = 0, 2, 4, 6 and 8 s. As a first step, thanks to the accurate control of the oxidation parameters as well as the great reactivity of the high surface-to-volume films deposited, the fast oxidation of pure vanadium samples was performed in air atmosphere at $h_r = 42$ºC s^{-1} and $T_r = 550$ºC, for reaction times (t_r) ranging from 1 to 300 s. Results collected for such oxidized systems through SEM and Raman spectroscopy not only allowed to explore the characteristic structure and morphology of the different oxide phase generated but also to optimize reaction times which maximize the highest amounts of the thermochromic VO_2 phase. Further TEM and STEM-EELS studies disclosed that $t_r \leq 45$ s guarantee the exclusive formation of

VO_2 (M1) superficial layers of different grain size and crystallinity with thicknesses between 120 – 400 nm.

By virtue of the foregoing, the subsequent fast oxidation of vanadium oxide samples at h_r = 42ºC s^{-1}, T_r = 550ºC, and t_r = 45 s was carried out. On this occasion, SEM images not only evidenced an earlier formation of V_2O_5 microrods on the surface of such samples, but also the cracking and film detachment for samples deposited with $t_{ON} \geq 6$ s. Furthermore, although the Raman spectroscopy analysis performed on thermally treated vanadium oxide samples clearly revealed the characteristic Raman bands of the VO_2 (M1) phase, several Raman bands corresponding to different V_2O_5 polymorphs were also detected. Nonetheless, TEM and STEM-EELS analyses confirmed the good results obtained for the oxidized sample deposited with t_{ON} = 2 s, and showed the formation of VO_2 (M1) multilayers of about 570 nm total thick. In such way, it was distinguished a most superficial layer composed by larger and single-crystalline VO_2 grains, and a second inner layer characterized by smaller grains.

Finally, the remarkable surface potential drops recorded by temperature dependent KPFM measurements of the best thermally treated vanadium or vanadium oxide samples confirmed the outstanding MIT response of the resultant VO_2 (M1) films. Therefore, it is demonstrated that the exclusive formation of high-performance VO_2 (M1) coatings of adjustable grain size and crystallinity can be achieved by the post-deposition oxidation of vanadium-based samples deposited at $\alpha = 85°$ and $t_{ON} \leq 2$ s when the subsequent fast thermal treatments are conducted in air atmosphere at h_r = 42ºC s^{-1}, T_r = 550ºC, $t_r \leq 45$ s.

ACKNOWLEDGEMENTS

A. J. Santos would like to thank the IMEYMAT Institute and the Spanish Ministerio de Educación y Cultura for the concessions of grants (ICARO-173873 and FPU16-04386). The “Talent Attraction Program” of the University of Cádiz is acknowledged by supporting B. Lacroix contract code E-11-2017-0117214. University of Cádiz and IMEYMAT are also agreed by financing the mutual facilities available at the UCA R&D Central Services (SC-ICYT), the UCA projects reference “PUENTE PR2018-040” and “PUENTE PR2020-003”, and the IMEYMAT project references “LÍNEAS PRIORITARIAS PLP2019120-3 and PLP2021120-1”. The regional government of Andalusia with FEDER cofunding also participates through the projects AT-5983 Trewa 1157178 and FEDER-UCA18-10788. M. Domínguez acknowledges financial support from the Spanish Ministerio de Ciencia e Innovación under project reference EQC2018-004704-P FEDER 2014-2020, “Modernización del Servicio de Microscopía de Fuerza Atómica (AFM) del IMEYMAT”.

REFERENCES

[1] J.B. Goodenough, The two components of the crystallographic transition in VO_2, J. Solid State Chem. 3 (1971) 490–500. doi:10.1016/0022-4596(71)90091-0.

[2] V. Devthade, S. Lee, Synthesis of vanadium dioxide thin films and nanostructures, J. Appl. Phys. 128 (2020) 231101. doi:10.1063/5.0027690.

[3] S. Wang, M. Liu, L. Kong, Y. Long, X. Jiang, A. Yu, Recent progress in VO_2 smart coatings: Strategies to improve the thermochromic properties, Prog. Mater. Sci. 81 (2016) 1–54. doi:10.1016/j.pmatsci.2016.03.001.

[4] K. Liu, S. Lee, S. Yang, O. Delaire, J. Wu, Recent progresses on physics and applications of vanadium dioxide, Mater. Today. 21 (2018) 875–896. doi:10.1016/j.mattod.2018.03.029.

[5] C. Batista, V. Teixeira, J. Carneiro, Structural and morphological characterization of magnetron sputtered nanocrystalline vanadium oxide films for thermochromic smart surfaces, J. Nano Res. 2 (2008) 21–30. doi:10.4028/www.scientific.net/JNanoR.2.21.

[6] X. He, C. Gu, F. Chen, X. Xu, Vanadium dioxide thin films for smart windows: optical design and performance improvement, Eighth Int. Conf. Thin Film Phys. Appl. 9068 (2013) 90680G. doi:10.1117/12.2054369.

[7] Z. Chen, Y. Gao, L. Kang, J. Du, Z. Zhang, H. Luo, H. Miao, G. Tan, VO_2-based double-layered films for smart windows: Optical design, all-solution preparation and improved properties, Sol. Energy Mater. Sol. Cells. 95 (2011) 2677–2684. doi:10.1016/j.solmat.2011.05.041.

[8] B.G. Chae, H.T. Kim, D.H. Youn, K.Y. Kang, Abrupt metal-insulator transition observed in VO_2 thin films induced by a switching voltage pulse, Phys. B

Condens. Matter. 369 (2005) 76–80. doi:10.1016/j.physb.2005.07.032.

[9] S.A. Corr, M. Grossman, J.D. Furman, B.C. Melot, A.K. Cheetham, K.R. Heier, R. Seshadri, Controlled reduction of vanadium oxide nanoscrolls: Crystal structure, morphology, and electrical properties, Chem. Mater. (2008) 6396–6404. doi.org/10.1021/cm801539f.

[10] T. Driscoll, H.T. Kim, B.G. Chae, B.J. Kim, Y.W. Lee, N.M. Jokerst, S. Palit, D.R. Smith, M. Di Ventra, D.N. Basov, Memory metamaterials, Science. 325 (2009) 1518–1521. doi:10.1126/science.1176580.

[11] A.K. Prasad, S. Amirthapandian, S. Dhara, S. Dash, N. Murali, A.K. Tyagi, Novel single phase vanadium dioxide nanostructured films for methane sensing near room temperature, Sens. Actuator B-Chem. 191 (2014) 252–256. doi:10.1016/j.snb.2013.09.102.

[12] A. Perucchi, L. Baldassarre, P. Postorino, S. Lupi, Optical properties across the insulator to metal transitions in vanadium oxide compounds, J. Phys. Condens. Matter. 21 (2009) 323202. doi:10.1088/0953-8984/21/32/323202.

[13] M.G. Krishna, Y. Debauge, A.K. Bhattacharya, X-ray photoelectron spectroscopy and spectral transmittance study of stoichiometry in sputtered vanadium oxide films, Thin Solid Films. 312 (1998) 116–122. doi:10.1016/s0040-6090(97)00717-7.

[14] E. Hryha, E. Rutqvist, L. Nyborg, Stoichiometric vanadium oxides studied by XPS, Surf. Interface Anal. 44 (2012) 1022–1025. doi:10.1002/sia.3844.

[15] M.M. Seyfouri, R. Binions, Sol-gel approaches to thermochromic vanadium dioxide coating for smart glazing application, Sol. Energy Mater. Sol. Cells. 159 (2017) 52–65. doi:10.1016/j.solmat.2016.08.035.

[16] H. Liu, O. Vasquez, V.R. Santiago, L. Diaz, A.J. Rua, F.E. Fernandez, Novel pulsed-laser-deposition - VO_2 thin films for ultrafast applications, J. Electron. Mater. 34 (2005) 491–496. doi:10.1007/s11664-005-0056-y.

[17] Y.L. Wang, X.K. Chen, M.C. Li, R. Wang, G. Wu, J.P. Yang, W.H. Han, S.Z. Cao, L.C. Zhao, Phase composition and valence of pulsed laser deposited vanadium oxide thin films at different oxygen pressures, Surf. Coat. Technol. 201 (2007) 5344–5347. doi:10.1016/j.surfcoat.2006.07.087.

[18] R. Binions, G. Hyett, C. Piccirillo, I.P. Parkin, Doped and un-doped vanadium dioxide thin films prepared by atmospheric pressure chemical vapour deposition from vanadyl acetylacetonate and tungsten hexachloride: The effects of thickness and crystallographic orientation on thermochromic properties, J. Mater. Chem. 17 (2007) 4652–4660. doi:10.1039/b708856f.

[19] J. Du, Y. Gao, H. Luo, L. Kang, Z. Zhang, Z. Chen, C. Cao, Significant changes in phase-transition hysteresis for Ti-doped VO 2 films prepared by polymer-assisted deposition, Sol. Energy Mater. Sol. Cells. 95 (2011) 469–475. doi:10.1016/j.solmat.2010.08.035.

[20] V. Collado, N. Martin, P. Pedrosa, J.Y. Rauch, M. Horakova, M.A.P. Yazdi, A. Billard, Temperature dependence of electrical resistivity in oxidized vanadium films grown by the GLAD technique, Surf. Coat. Technol. 304 (2016) 476–485. doi:10.1016/j.surfcoat.2016.07.057.

[21] H. Zhang, Z. Wu, D. Yan, X. Xu, Y. Jiang, Tunable hysteresis in metal-insulator transition of nanostructured vanadium oxide thin films deposited by reactive direct current magnetron sputtering, Thin Solid Films. 552 (2014) 218–224. doi:10.1016/j.tsf.2013.12.007.

[22] G. Rampelberg, B. De Schutter, W. Devulder, K. Martens, I. Radu, C. Detavernier, In situ X-ray diffraction study of the controlled oxidation and reduction in the V-O system for the synthesis of VO_2 and V_2O_3 thin films, J. Mater. Chem. C. 3 (2015) 11357–11365. doi:10.1039/c5tc02553b.

[23] Y.X. Ji, G.A. Niklasson, C.G. Granqvist, M. Boman, Thermochromic VO_2 films by thermal oxidation of vanadium in SO_2, Sol. Energy Mater. Sol. Cells. 144 (2016) 713–716. doi:10.1016/j.solmat.2015.10.012.

[24] P. Pedrosa, N. Martin, R. Salut, M. Arab Pour Yazdi, A. Billard, Controlled thermal oxidation of nanostructured vanadium thin films, Mater. Lett. 174 (2016) 162–166. doi:10.1016/j.matlet.2016.03.097.

[25] H.M.R. Giannetta, C. Calaza, C. Calaza, L. Fonseca, L. Fraigi, L. Fonseca, Vanadium oxide thin films obtained by thermal annealing of layers deposited by RF magnetron sputtering at room temperature, in Modern technologies for creating the thin-film systems and coatings, by N. Nikitenkov, InTechOpen, London (2017). doi.org/10.5772/67054.

[26] A. Sohn, T. Kanki, K. Sakai, H. Tanaka, D.W. Kim, Fractal nature of metallic and insulating domain configurations in a VO_2 thin film revealed by Kelvin probe force microscopy, Sci. Rep. 5 (2015) 1–7. doi:10.1038/srep10417.

[27] M.J. Nieuwenhuizen, H.B. Haanstra, Microfractography of thin films, Philips Tech. Rev. 27 (1966) 87–91.

[28] R.N. Tait, T. Smy, M.J. Brett, Modelling and characterization of columnar growth in evaporated films, Thin Solid Films. 226 (1993) 196–201. doi:10.1016/0040-6090(93)90378-3.

[29] J. Lintymer, J. Gavoille, N. Martin, J. Takadoum, Glancing angle deposition to

modify microstructure and properties of sputter deposited chromium thin films, Surf. Coat. Technol. 174 –175 (2003) 316–323. doi:10.1016/S0257-8972(03)00413-4.

[30] M.M. Hawkeye, M.J. Brett, Glancing angle deposition: Fabrication, properties, and applications of micro- and nanostructured thin films, J. Vac. Sci. Technol. A Vacuum, Surfaces, Films. 25 (2007) 1317. doi:10.1116/1.2764082.

[31] A. Barranco, A. Borras, A.R. Gonzalez-Elipe, A. Palmero, Perspectives on oblique angle deposition of thin films: From fundamentals to devices, Prog. Mater. Sci. 76 (2016) 59–153. doi:10.1016/j.pmatsci.2015.06.003.

[32] P. Shvets, O. Dikaya, K. Maksimova, A. Goikhman, A review of Raman spectroscopy of vanadium oxides, J. Raman Spectrosc. 50 (2019) 1226–1244. doi:10.1002/jrs.5616.

[33] Y. Li, S. Ji, Y. Gao, H. Luo, M. Kanehira, Core-shell VO_2 @TiO_2 nanorods that combine thermochromic and photocatalytic properties for application as energy-saving smart coatings, Sci. Rep. 3 (2013) 1370. doi:10.1038/srep01370.

[34] P. Vilanova-Martínez, J. Hernández-Velasco, A.R. Landa-Cánovas, F. Agulló-Rueda, Laser heating induced phase changes of VO_2 crystals in air monitored by Raman spectroscopy, J. Alloys Compd. 661 (2016) 122–125. doi:10.1016/j.jallcom.2015.11.174.

[35] D. Louloudakis, D. Vernardou, E. Spanakis, M. Suchea, G. Kenanakis, M. Pemble, K. Savvakis, N. Katsarakis, E. Koudoumas, G. Kiriakidis, Atmospheric pressure chemical vapor deposition of amorphous tungsten doped vanadium dioxide for smart window applications, Adv. Mater. Lett. 7 (2016) 192–196. doi:10.5185/amlett.2016.6024.

[36] M.M. Margoni, S. Mathuri, K. Ramamurthi, R.R. Babu, K. Sethuraman, Sprayed vanadium pentoxide thin films: Influence of substrate temperature and role of HNO_3 on the structural, optical, morphological and electrical properties, Appl. Surf. Sci. 418 (2017) 280–290. doi:10.1016/j.apsusc.2017.02.039.

[37] A. Baltakesmez, C. Aykaç, B. Güzeldir, Phase transition and changing properties of nanostructured V_2O_5 thin films deposited by spray pyrolysis technique, as a function of tungsten dopant, Appl. Phys. A Mater. Sci. Process. 125 (2019) 1–18. doi:10.1007/s00339-019-2736-0.

[38] C.O.F. Ba, S.T. Bah, M. D'Auteuil, V. Fortin, P. V. Ashrit, R. Vallée, VO_2 thin films based active and passive thermochromic devices for energy management applications, Curr. Appl. Phys. 14 (2014) 1531–1537. doi:10.1016/j.cap.2014.09.005.

[39] L. Kang, Y. Gao, Z. Zhang, J. Du, C. Cao, Z. Chen, H. Luo, Effects of annealing parameters on optical properties of thermochromic VO_2 films prepared in aqueous solution, J. Phys. Chem. C. 114 (2010) 1901–1911. doi.org/10.1021/jp909009w.

[40] T.G. Sparrow, B.G. Williams, C.N.R. Rao, J.M. Thomas, L_3/L_2 white-line intensity ratios in the electron energy-loss spectra of 3d transition-metal oxides, Chem. Phys. Lett. 108 (1984) 547–550. doi:10.1016/0009-2614(84)85051-4.

[41] O.L. Krivanek, J.H. Paterson, Elnes of 3d transition-metal oxides. I. Variations across the periodic table, Ultramicroscopy. 32 (1990) 313–318. doi:10.1016/0304-3991(90)90077-Y.

[42] W.G. Waddington, P. Rez, I.P. Grant, C.J. Humphreys, White lines in the $L_{2,3}$ electron-energy-loss and x-ray absorption spectra of 3d transition metals, Phys.

Rev. B. 34 (1986) 1467–1473. doi:10.1103/PhysRevB.34.1467.

[43] A. Gloter, V. Serin, C. Turquat, C. Cesari, C. Leroux, G. Nihoul, Vanadium valency and hybridization in V-doped hafnia investigated by electron energy loss spectroscopy, Eur. Phys. J. B. 22 (2001) 179–186. doi:10.1007/PL00011142.

[44] D.S. Su, M. Wieske, E. Beckmann, A. Blume, G. Mestl, R. Schlögl, Electron beam induced reduction of V_2O_5 studied by analytical electron microscopy, Catal. Lett. 75 (2001) 81–86. doi:10.1023/A:1016754922933.

[45] X.W. Lin, Y.Y. Wang, V.P. Dravid, P.M. Michalakos, M.C. Kung, Valence states and hybridization in vanadium oxide systems investigated by transmission electron-energy-loss spectroscopy, Phys. Rev. B - Condens. Matter. 47 (1993) 3477. doi:10.1126/science.267.5198.713.

[46] C. Hébert, M. Willinger, D.S. Su, P. Pongratz, P. Schattschneider, R. Schlögl, Oxygen K-edge in vanadium oxides: Simulations and experiments, Eur. Phys. J. B. 28 (2002) 407–414. doi:10.1140/epjb/e2002-00244-4.

[47] J. Li, B.D. Gauntt, J. Kulik, E.C. Dickey, Stoichiometry of nanocrystalline VO_x thin films determined by electron energy loss spectroscopy, Microsc. Microanal. 15 (2009) 1004–1005. doi:10.1017/S1431927609092770.

[48] A.J. Santos, B. Lacroix, F. Maudet, A. Corvisier, F. Paumier, C. Dupeyrat, T. Girardeau, R. García, F.M. Morales, Surface oxidation of amorphous Si and Ge slanted columnar and mesoporous thin films: Evidence, scrutiny and limitations for infrared optics, Appl. Surf. Sci. 493 (2019) 807-817. doi:10.1016/j.apsusc.2019.07.064.

[49] M. Abbate, H. Pen, M.T. Czyzyk, F.M.F. de Groot, J.C. Fuggle, Y.J. Ma, C.T. Chen, F. Sette, A. Fujimori, Y. Ueda, K. Kosuge, Soft X-ray absorption

spectroscopy of vanadium oxides, J. Electron Spectros. Relat. Phenomena. 62 (1993) 185–195. doi:10.1016/0368-2048(93)80014-D.

Figures and captions

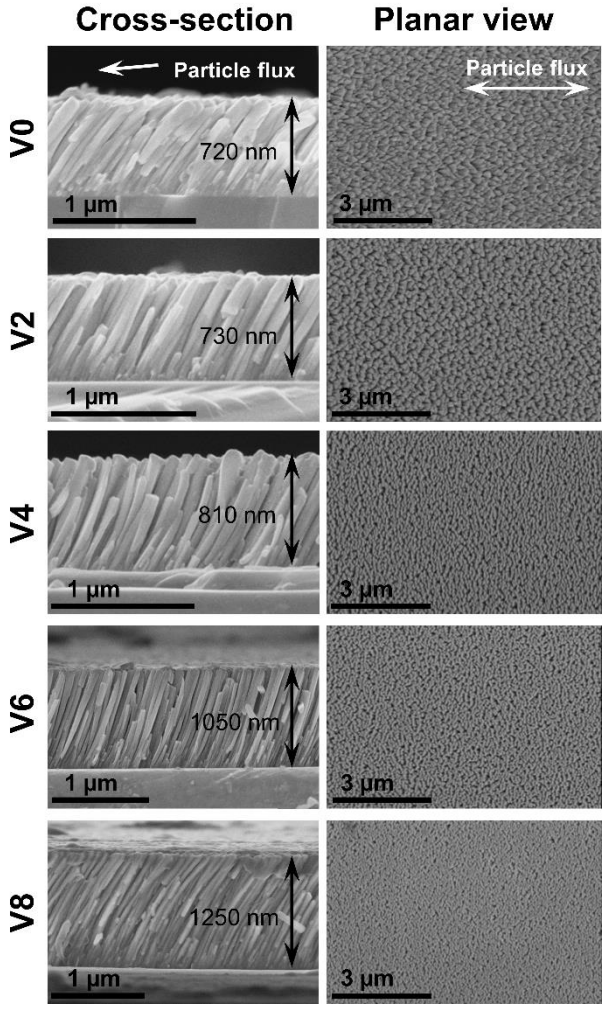

Fig. 1. SEM cross-section and planar view micrographs of the as-deposited vanadium or vanadium oxide GLAD films. The white arrows indicate the directions of the particle flux during GLAD deposition.

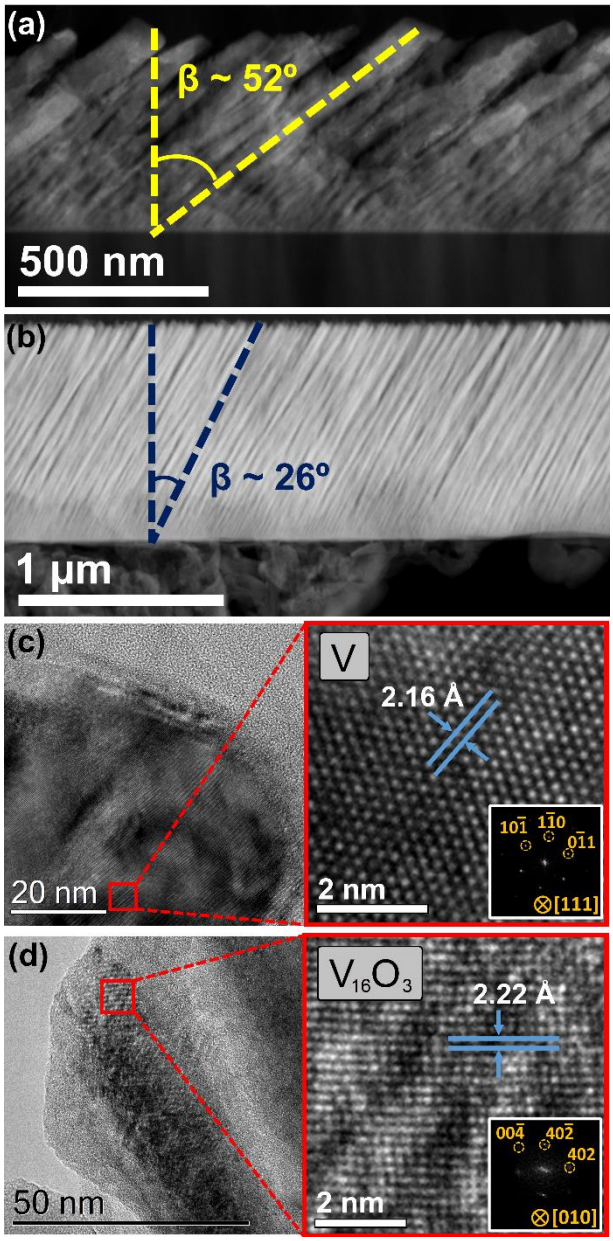

Fig. 2. TEM studies of the as-deposited V0 and V8 samples. Cross-section STEM-HAADF overviews of the (a) V0 and (b) V8 samples. High-resolution TEM micrographs of the (c) V0 and (d) V8 samples. The insets show magnified views of intragrain regions together with their corresponding FFT diffractions.

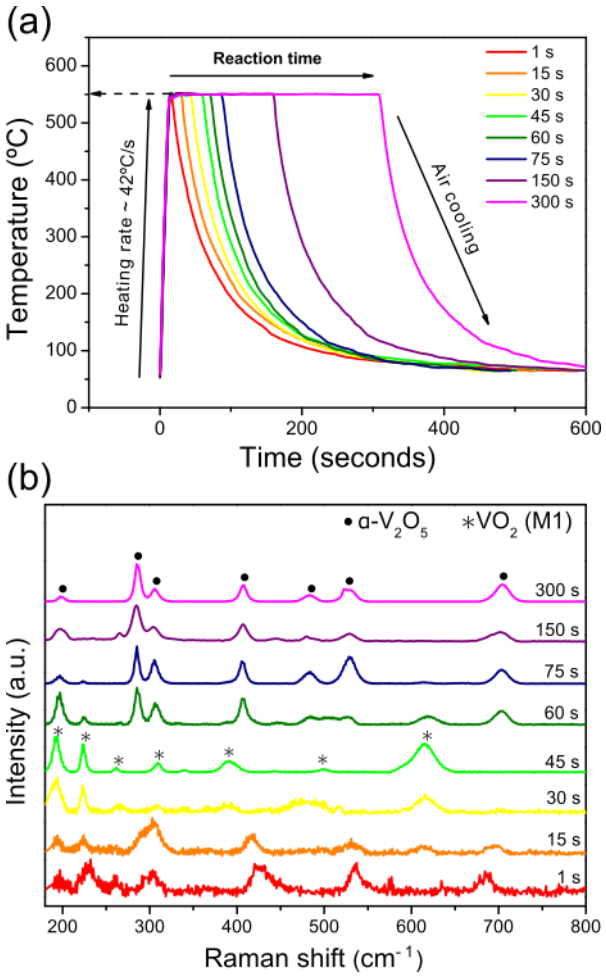

Fig. 3. (a) Temperature versus time tracks of many thermally treated V0 samples at 550ºC, h_r = 42ºC s^{-1}, and reaction times (t_r) ranging from 1 to 300 s. (b) Raman spectra of all the thermally treated V0 samples.

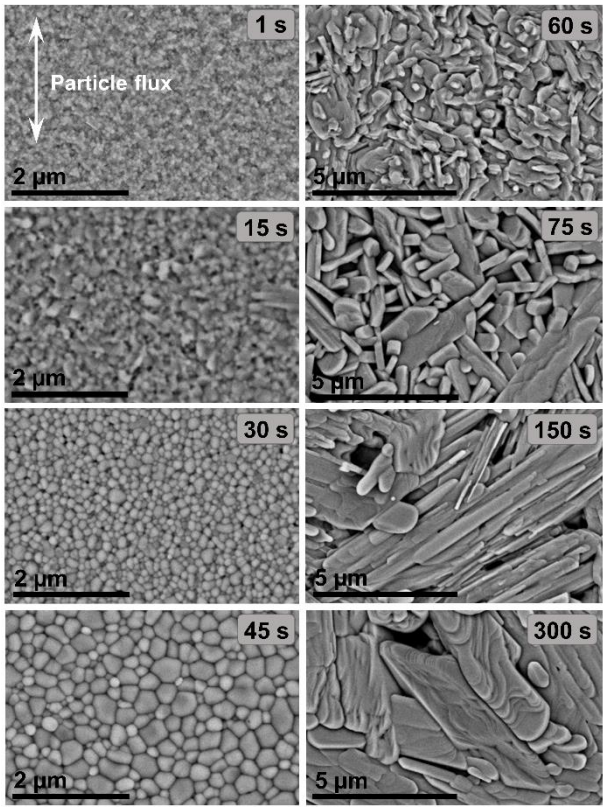

Fig. 4. SEM planar view of thermally treated V0 samples at 550ºC, h_r = 42ºC s^{-1}, and reaction times (t_r) ranging from 1 to 300 s as labelled in the images. The white arrow indicates the directions of the particle flux during GLAD deposition.

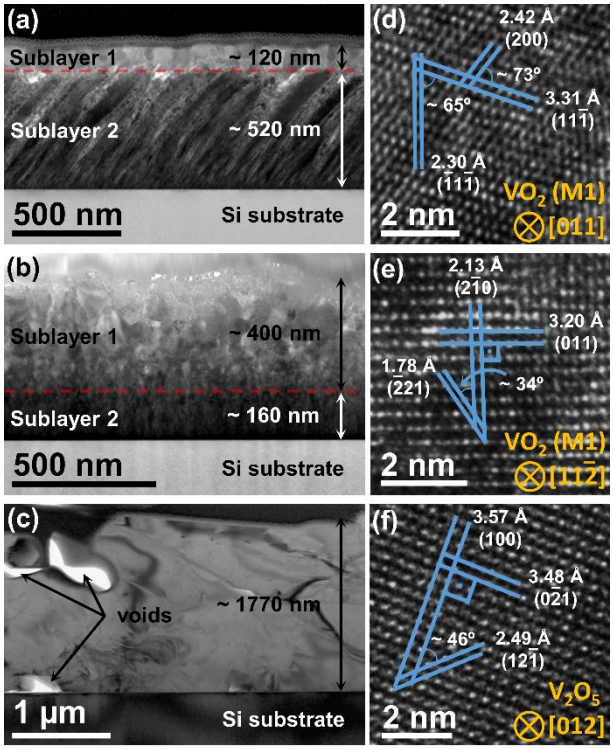

Fig. 5. TEM studies of thermally treated V0 samples. Bright-field (BF) TEM overview of V0 samples subjected to reaction times of (a) 1, (b) 45, and (c) 300 s. High-resolution TEM micrographs acquired from the upper regions of V0 samples subjected to reaction times of (d) 1 and (e) 45 s. (f) High-resolution TEM image of a representative region the of V0 sample subjected to a reaction time of 300 s.

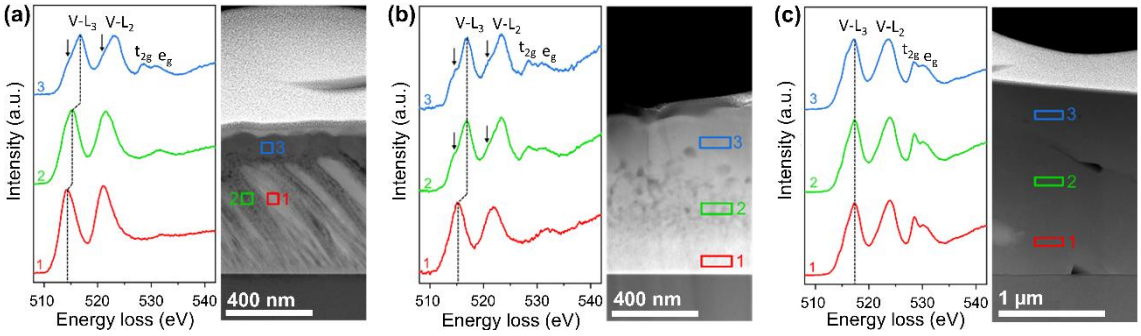

Fig. 6. EELS spectra recorded in different areas of thermally treated V0 samples at 550ºC, hr = 42ºC s^{-1}, and t_r = (a) 1 s, (b) 45 s, (c) 300 s. Images on the right corresponds to HAADF overviews. The spectra were previously aligned, and background-subtracted using a power law function.

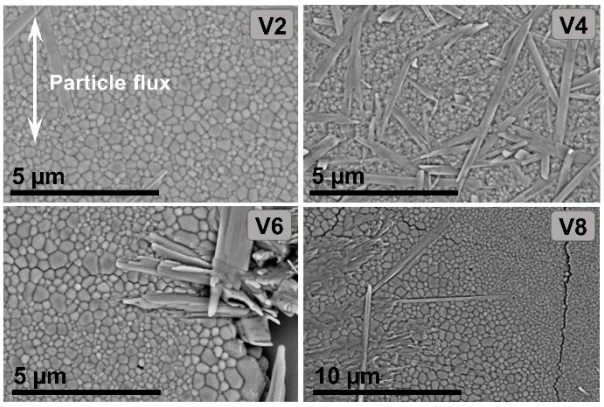

Fig. 7. SEM planar view of V2, V4, V6 and V8 samples after being thermally treated at 550ºC, h_r = 42ºC s^{-1} and t_r = 45 s.

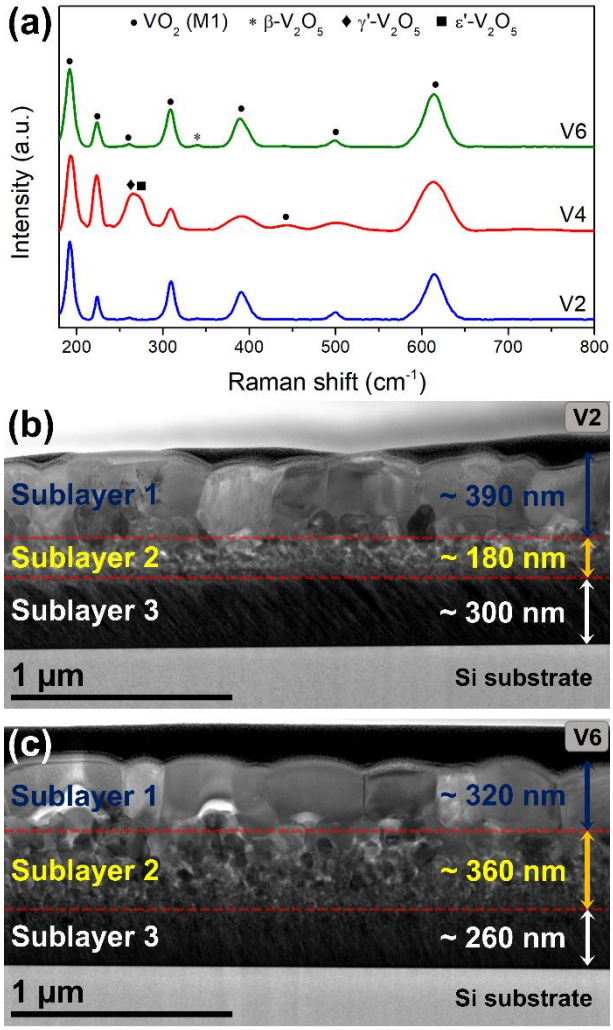

Fig. 8. (a) Raman spectra of V2, V4 and V6 samples after being thermally treated at 550ºC, h_r = 42ºC s^{-1} and t_r = 45 s. Bright-field (BF) TEM overview of (b) V2 and (c) V6 samples after being subjected to the abovementioned thermal treatment.

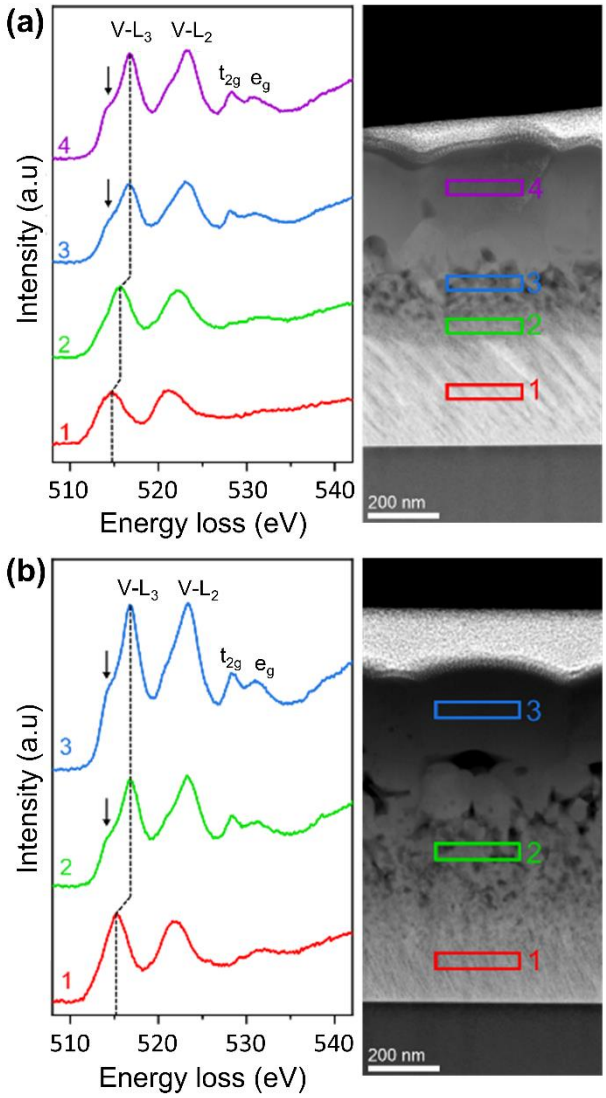

Fig. 9. EELS spectra recorded in different areas of V2 (a) and V6 (b) samples after thermal treatment at 550ºC, h_r = 42ºC s^{-1} and t_r = 45 s. Images on the right corresponds to HAADF overviews. The spectra were previously aligned, and background-subtracted using a power law function.

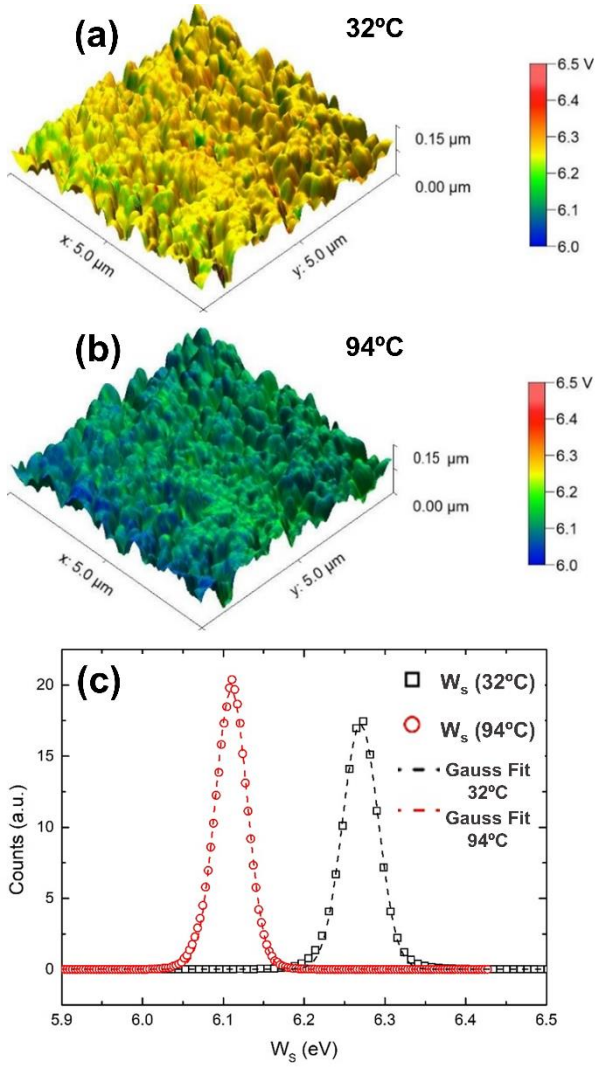

Fig. 10. Overlay of work function map and topography at two different temperatures, (a) below and (b) above MIT, for the V0 sample subjected to t_r = 45 s. (c) Distributions of work function values across these two maps; the mean (peak) values deduced from the Gauss fits are 6.27 eV at 32ºC and 6.11 eV at 94ºC, i.e., a value of ΔW_S = 0.16 eV for the MIT in this sample.

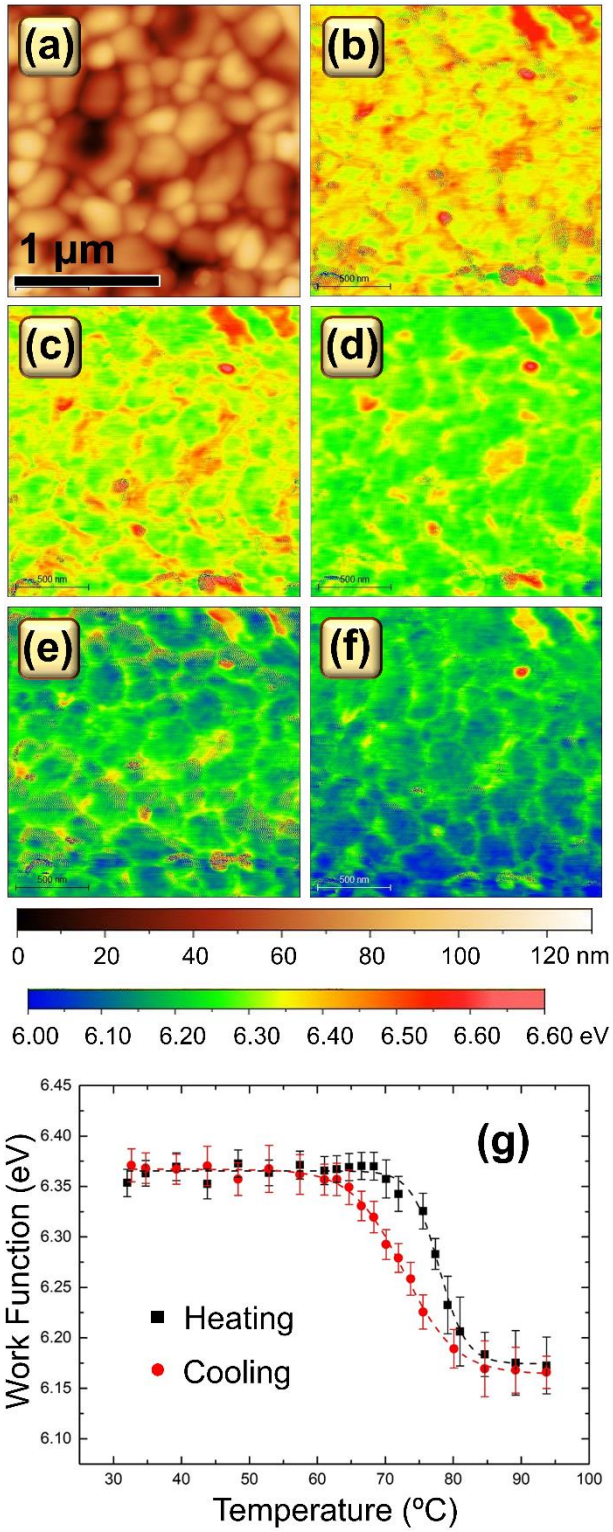

Fig. 11. Variable temperature KPFM measurements performed on the V2 sample after thermal treatment at 550ºC, h_r = 42ºC s^{-1} and t_r = 45 s. (a) AFM image of the region where the KPFM experiment was performed. (b) – (f) Work function maps for 70, 75,

78, 81 and 94°C, respectively, during heating. (g) Work function versus sample temperature during heating (black squares) and cooling (red circles) experiments performed on the V2 sample. These values are derived from the means of the Gaussian fits obtained from the distribution of surface potential values across the sample surface, taking into account the previously calibrated tip work function.